



The University of  
**Nottingham**

UNITED KINGDOM • CHINA • MALAYSIA

# Raman chemical and physical mapping of oral dosage forms

Francesco Tres, MSc

Thesis submitted to the University of Nottingham  
for the degree of Doctor of Philosophy

in the

Laboratory of Biophysics and Surface Analysis  
School of Pharmacy

October 2015

# *Acknowledgements*

I would like to express my deep gratitude to my supervisors Dr. Jonathan Burley, Dr. Jonathan Aylott and Dr. Stephen Wren. Dr. Jonathan Burley you have been an inspiring guidance in these four years and I thank you for your invaluable technical support. I also thank you for your optimism, encouragement and ability to get things done by smiling at people. Dr. Jonathan Aylott I thank you for providing full support for the project and for your helpful discussions on my future career. Dr. Jonathan Burley and Dr. Jonathan Aylott since the first day I never doubted about the project and our team. I also thank you both for the good times we had together in Macclesfield and congratulate Dr. Jonathan Aylott for beating the local chad playing pool after a long afternoon in the pub. Dr. Stephen Wren I deeply thank you for your constant support during the project and for your help during the time I spent in AstraZeneca. Working with you has been incredibly pleasant and I also thank you for bringing a number of experts from AstraZeneca into the project.

I wish to express my gratitude to the following people for their help and input with specific aspects of my work: Prof. Phil Williams for the kinetic modelling, Dr. Les Hughes for the magnetic resonance imaging experiments, Dr. Kevin Treacher and Jamie Patient for the rotating disk dissolution rate test, Dr. Jonathan Booth and Martin Kearns for using the hot melt extruder, and Dr. Steven Coombes for the  $^1\text{H}$  nuclear magnetic resonance experiments.

I would like to thank Dr. Claudia Matz for her warm support and wise words. Thanks to everyone in the CDT, especially my friends of the 2011 cohort (Naim, Jamie, Lee, Kathryn and Andreea), for all the trips to Macclesfield, conferences, parties, laughing and much more we shared together in these four years.

Finally I want to thank the special people of my life. Thanks mum, dad and Elena for being there when I need, for caring about me no matter what and for always being the people I can count on my life. Thanks also for trying to understand and showing interest in my work. Thanks Chiara for being my soulmate, for loving me and sharing your life with me. Thank you for your encouragement, for listening my boring monologues on work and problems, for spending several weekends waiting me outside the lab and for providing excellent ideas for the project. I surely could not have asked for a better team-mate than you.

# *Declaration*

I hereby declare that the work contained in this thesis titled “Raman chemical and physical mapping of oral dosage forms” is the result of my own work conducted at the University of Nottingham and AstraZeneca (Macclesfield) between October 2011 and September 2015, with the guidance of my supervisors Dr. Jonathan Burley, Dr. Jonathan Aylott and Dr. Stephen Wren.

# *Abstract*

A high number of new chemical entities emerging from the drug development process show pharmacological activity, but at the same time are characterised by poor dissolution and solubility profiles. As a result, there is a strong push to develop innovative formulations for the delivery of such compounds so that the desired oral bioavailability and pharmacological effects are achieved. An increasingly popular class of formulations to improve the dissolution properties of poorly soluble drugs is represented by amorphous solid dispersions, whereby the drug is molecularly dispersed in a carrier matrix. One of the key challenges for developing amorphous solid dispersions in real-world formulations is the understanding of the dissolution performance. Although this is very important, due to the fact that the dissolution performance limits the *in vivo* efficacy, the dissolution mechanisms by which the amorphous solid dispersions dissolve is still not fully understood.

This thesis investigates the dissolution performance of three solid dispersions model systems including felodipine, bicalutamide and indomethacin, all poorly soluble drugs, with copovidone, a water-soluble polymer. The complexity of the model systems increases through the chapters, starting by testing the dissolution of a well-documented poorly soluble drug model, i.e. felodipine, as a function of the drug loading (5% and 50% w/w) (Chapter 3). In Chapters 4 and 5 the dissolution of bicalutamide, which is known to exist in at least two different polymorphic forms (form I and form II), is investigated as a function of three drug loadings (5%, 30% and 50% w/w). Finally, the dissolution of indomethacin, which presents a pH-variable solubility and dissolution rate due to its weakly acidic nature ( $pK_a$  of 4.5), is probed as a function of both dissolution medium pH (pH 2 and 6.8) and drug loading (5%, 15%, 30%, 50%, 70% and 90% w/w) (Chapter 6).

The dissolution of amorphous solid dispersions and other oral dosage forms is commonly tested using the USP dissolution apparatuses (types I, II

and IV). These methods present a significant limitation, i.e. they can not provide any directly spatially-resolved chemical information on potential changes occurring to the solid form (e.g. amorphous to crystalline, polymorphs or solvation-related transformations).

In this thesis Raman spectroscopy is employed as primary analytical technique in an attempt to fill the gaps related to the understanding of the dissolution mechanisms of amorphous solid dispersions and the limitations of the conventional USP apparatuses. The novelty of this approach derives from collecting Raman data directly from the dosage form in real time and *in situ* during the course of the dissolution test using a flow-through cell placed below the Raman microscope. Temporally- and spatially-resolved chemical Raman maps are generated using a novel mathematical approach which derives from the use of concatenated maps to explicitly probe the chemical and physical changes as a function of time as well as space. In-line ultraviolet spectroscopy is also integrated to the Raman system to directly relate changes in dissolution behaviour to physicochemical changes that occur to the solid form during the dissolution test.

A wide range of other state-of-the-art analytical techniques is also used to complement the Raman data to obtain a clear picture of drug release from amorphous solid dispersions. This includes a combined magnetic resonance imaging/ultraviolet flow cell system to allow, similarly to the Raman/ultraviolet method, changes in dissolution profile to be related to physical changes occurring in the solid material, and for the first time quantitative suppressed-water  $^1\text{H}$  nuclear magnetic resonance spectroscopy was applied to amorphous solid dispersions.  $^1\text{H}$  nuclear magnetic resonance, due to the high chemical selectivity, provides quantitative data on both the drug and the polymer. Finally, the rotating disk dissolution rate test, i.e. a modified version of the conventional intrinsic dissolution rate test, is developed and employed for the first time to gain information, similarly to  $^1\text{H}$  nuclear magnetic resonance spectroscopy, on the dissolution rates of both the drug and the polymer.

The dissolution performance of all amorphous solid dispersion model systems is shown to be strongly affected by the drug loading. At low drug loading the drug and the polymer dissolve with the same rate from the molecular dispersion, pointing to a drug release dependent on the high water solubility of copovidone. At high drug loading, the dissolution rates of both the drug and the polymer are significantly slower and this is shown to be ascribed to the formation of an amorphous drug-rich shell around the compact, followed by the drug re-crystallisation. For the high drug loaded amorphous solid dispersions, the dissolution performance is strongly dependent on the physicochemical properties of the drug, i.e. low aqueous solubility and high hydrophobicity. The dissolution behaviour of the amorphous indomethacin solid dispersions is also found to be affected by the dissolution medium pH. Indomethacin from the amorphous solid dispersions with 15% or higher drug loading is released only at pH 6.8 due to the significant increase in its aqueous solubility at this pH.

# *Publications*

A copy of each peer-reviewed paper can be seen at the end of this thesis.

Tres, F.; Coombes, S. R.; Phillips, A. R.; Hughes, L. P.; Wren, S. A. C.; Aylott, J. W.; Burley, J. C. Investigating the Dissolution Performance of Amorphous Solid Dispersions Using Magnetic Resonance Imaging and Proton NMR. *Molecules* 2015, 20, 16404–16418.

Tres, F.; Patient, J. D.; Williams, P. M.; Treacher, K.; Booth, J.; Hughes, L. P.; Wren, S. A. C.; Aylott, J. W.; Burley, J. C. Monitoring the Dissolution Mechanisms of Amorphous Bicalutamide Solid Dispersions via Real-Time Raman Mapping. *Molecular Pharmaceutics* 2015, 12, 1512–1522.

Tres, F.; Treacher, K.; Booth, J.; Hughes, L. P.; Wren, S. A. C.; Aylott, J. W.; Burley, J. C. Real time Raman imaging to understand dissolution performance of amorphous solid dispersions. *Journal of Controlled Release* 2014, 188, 53–60.

Tres, F.; Treacher, K.; Booth, J.; Hughes, L. P.; Wren, S. A. C.; Aylott, J. W.; Burley, J. C. Indomethacin-copovidone extrudates: a mechanistic study of pH-dependent controlled release. To be submitted to *Journal of Controlled Release*.

# Contents

<b>Acknowledgements</b>	<b>i</b>
<b>Declaration</b>	<b>iii</b>
<b>Abstract</b>	<b>iv</b>
<b>Publications</b>	<b>vii</b>
<b>Contents</b>	<b>vii</b>
<b>List of Figures</b>	<b>xiii</b>
<b>List of Tables</b>	<b>xvi</b>
<b>List of Equations</b>	<b>xvii</b>
<b>Abbreviations</b>	<b>xviii</b>
<b>1 Introduction</b>	<b>1</b>
1.1 Poorly soluble drugs . . . . .	1
1.2 Solubility and dissolution rate . . . . .	5
1.3 Strategies of improving the dissolution properties . . . . .	6
1.3.1 Pro-drugs . . . . .	6
1.3.2 Salts . . . . .	6
1.3.3 Particle size reduction . . . . .	7
1.3.4 Amorphous forms and amorphous solid dispersions (ASDs) . . . . .	7
1.3.5 Polymorphs . . . . .	8
1.3.6 Co-crystals . . . . .	8
1.3.7 Microemulsions . . . . .	9
1.3.8 Cyclodextrins . . . . .	9
1.4 Amorphous solids . . . . .	10
1.4.1 Formation of the amorphous form . . . . .	10
1.4.2 Physical stability of the amorphous form . . . . .	10
1.5 Amorphous solid dispersions . . . . .	13
1.5.1 Preparation of amorphous solid dispersions . . . . .	13
1.5.2 Carrier materials . . . . .	14

---

1.5.3	Solid-state characterisation of amorphous solid dispersions . . . . .	15
1.5.3.1	Polarized light microscopy (PLM) . . . . .	15
1.5.3.2	X-ray powder diffraction (XRPD) . . . . .	16
1.5.3.3	Solid-state nuclear magnetic resonance (ss-NMR) . . . . .	16
1.5.3.4	Differential scanning calorimetry (DSC) . . . . .	17
1.5.3.5	Raman and infrared (IR) spectroscopy . . . . .	17
1.5.4	Physical stability during storage . . . . .	18
1.5.5	Dissolution performance in aqueous media . . . . .	21
1.6	Dissolution measurements . . . . .	23
1.6.1	Solution-based methods . . . . .	24
1.6.1.1	Quantitative suppressed-water $^1\text{H}$ nuclear magnetic resonance . . . . .	24
1.6.2	Solid-based methods . . . . .	24
1.6.2.1	Ultraviolet imaging . . . . .	24
1.6.2.2	Infrared and Raman spectroscopy . . . . .	25
1.6.2.3	Magnetic resonance imaging . . . . .	28
1.7	Motivation and aims of the work . . . . .	29
<b>2</b>	<b>Materials and experimental techniques</b>	<b>32</b>
2.1	Materials . . . . .	32
2.1.1	Copovidone . . . . .	32
2.1.2	Felodipine . . . . .	33
2.1.3	Bicalutamide . . . . .	34
2.1.4	Indomethacin . . . . .	34
2.2	Experimental techniques . . . . .	35
2.2.1	Hot melt extrusion . . . . .	35
2.2.2	X-ray powder diffraction . . . . .	36
2.2.3	Raman spectroscopy . . . . .	37
2.2.3.1	Principles of Raman spectroscopy . . . . .	37
2.2.3.2	Raman microscopy . . . . .	39
2.2.3.3	Raman mapping . . . . .	40
2.2.3.4	Data analysis . . . . .	41
2.2.4	Quantitative suppressed-water $^1\text{H}$ nuclear magnetic resonance spectroscopy . . . . .	43
2.2.5	Magnetic resonance imaging . . . . .	44
2.2.6	Rotating disk dissolution rate test . . . . .	45
<b>3</b>	<b>Raman mapping to understand the dissolution performance of amorphous felodipine extrudates</b>	<b>47</b>
3.1	Introduction . . . . .	47
3.2	Materials and methods . . . . .	48
3.2.1	Materials . . . . .	48

---

3.2.2	Preparation of the amorphous form of felodipine and the extrudates . . . . .	49
3.2.3	Analytical methods . . . . .	49
3.2.3.1	X-ray powder diffraction . . . . .	49
3.2.3.2	Rotating disk dissolution rate test . . . . .	49
3.2.3.3	Raman spectroscopy . . . . .	50
3.2.3.4	Optical imaging . . . . .	53
3.3	Results and discussion . . . . .	53
3.3.1	Optical imaging . . . . .	53
3.3.2	Rotating disk dissolution rate test . . . . .	55
3.3.3	Raman spectroscopy results . . . . .	58
3.3.3.1	Dry raw materials spectra: visual observation . . . . .	58
3.3.3.2	Dissolution experiments . . . . .	61
3.4	Conclusions . . . . .	70
<b>4</b>	<b>Monitoring the dissolution mechanisms of bicalutamide extrudates via Raman mapping</b>	<b>72</b>
4.1	Introduction . . . . .	72
4.2	Materials and methods . . . . .	73
4.2.1	Materials . . . . .	73
4.2.2	Samples preparation . . . . .	73
4.2.2.1	Preparation of the amorphous form and crystalline bicalutamide form II . . . . .	73
4.2.2.2	Preparation of the bicalutamide-copovidone extrudates . . . . .	74
4.2.3	Analytical methods . . . . .	74
4.2.3.1	X-ray powder diffraction . . . . .	74
4.2.3.2	Rotating disk dissolution rate test . . . . .	74
4.2.3.3	Raman spectroscopy . . . . .	75
4.2.3.4	Optical imaging . . . . .	75
4.3	Results and discussion . . . . .	76
4.3.1	Optical imaging and rotating disk dissolution rate . . . . .	76
4.3.2	Raman spectroscopy results . . . . .	80
4.3.2.1	Raman spectra of “dry” raw materials . . . . .	80
4.3.2.2	Raman spectroscopic mapping . . . . .	84
4.4	Conclusions . . . . .	91
<b>5</b>	<b>Magnetic resonance imaging and <sup>1</sup>H nuclear magnetic resonance for studying the dissolution of bicalutamide extrudates</b>	<b>92</b>
5.1	Introduction . . . . .	92
5.2	Materials and methods . . . . .	93
5.2.1	Materials . . . . .	93
5.2.2	Samples preparation . . . . .	93
5.2.3	Analytical methods . . . . .	94

---

5.2.3.1	X-ray powder diffraction . . . . .	94
5.2.3.2	Raman spectroscopy . . . . .	94
5.2.3.3	Magnetic resonance imaging ultraviolet-visible flow cell system . . . . .	94
5.2.3.4	<sup>1</sup> H nuclear magnetic resonance . . . . .	95
5.3	Results and discussion . . . . .	96
5.3.1	Solution-state assays . . . . .	96
5.3.1.1	Ultraviolet-visible flow cell experiments . . .	96
5.3.1.2	<sup>1</sup> H nuclear magnetic resonance . . . . .	99
5.3.2	Solid-state analysis . . . . .	101
5.3.2.1	Magnetic resonance imaging flow cell exper- iments . . . . .	101
5.4	Conclusions . . . . .	105
<b>6</b>	<b>Indomethacin-copovidone extrudates: a mechanistic study of pH-dependent controlled release</b>	<b>107</b>
6.1	Introduction . . . . .	107
6.2	Materials and methods . . . . .	109
6.2.1	Materials . . . . .	109
6.2.2	Samples preparation . . . . .	109
6.2.2.1	Preparation of the amorphous and $\alpha$ forms of indomethacin . . . . .	109
6.2.2.2	Preparation of the indomethacin-copovidone extrudates . . . . .	110
6.2.3	Analytical methods . . . . .	110
6.2.3.1	X-ray powder diffraction . . . . .	110
6.2.3.2	Rotating disk dissolution rate test . . . . .	110
6.2.3.3	Raman ultraviolet-visible flow cell system .	111
6.2.3.4	Optical imaging . . . . .	112
6.3	Results and discussion . . . . .	113
6.3.1	Optical imaging . . . . .	113
6.3.2	Rotating disk dissolution rate test . . . . .	117
6.3.3	Raman ultraviolet-visible flow cell experiments . . . .	122
6.3.3.1	Ultraviolet-visible . . . . .	122
6.3.3.2	Raman spectroscopy . . . . .	124
6.4	Conclusions . . . . .	132
<b>7</b>	<b>Conclusions and future work</b>	<b>133</b>
<b>A</b>	<b>Supplementary information part-I</b>	<b>139</b>
<b>B</b>	<b>Supplementary information part-II</b>	<b>140</b>
<b>C</b>	<b>Supplementary information part-III</b>	<b>144</b>

<b>D Supplementary information Part-IV</b>	<b>147</b>
--	------------

<b>Bibliography</b>	<b>150</b>
---------------------	------------

# List of Figures

1.1	The BCS . . . . .	3
1.2	The DCS . . . . .	4
1.3	Free energy/temperature diagram . . . . .	11
1.4	Crystallisation of the amorphous form . . . . .	12
1.5	Water vapour absorption diagram . . . . .	20
1.6	Spring and parachute model . . . . .	22
2.1	Chemical structures of drugs and copovidone . . . . .	33
2.2	Scheme of an extruder . . . . .	36
2.3	Raman scattering . . . . .	38
2.4	Raman microscope . . . . .	39
2.5	Confocal Raman microscopy . . . . .	40
2.6	Raman mapping . . . . .	41
2.7	Decay of the NMR signal . . . . .	45
2.8	Rotating disk system . . . . .	46
3.1	Raman flow cell . . . . .	51
3.2	Optical images of dissolution . . . . .	54
3.3	Swelling trend . . . . .	55
3.4	RDDR trends . . . . .	57
3.5	Raman spectra of raw materials . . . . .	59
3.6	Raman spectra of the 5% extrudate dissolution . . . . .	62
3.7	Raman spectra of the 50% extrudate dissolution . . . . .	63
3.8	HAC dendrogram . . . . .	65
3.9	MCR images during dissolution . . . . .	67
3.10	Re-crystallisation kinetic . . . . .	68
3.11	MCR images after dissolution . . . . .	69
3.12	XRPD pattern of the 50% extrudate residue . . . . .	70
4.1	Optical images of dissolution . . . . .	77
4.2	Swelling trend . . . . .	77
4.3	RDDR dissolution profiles . . . . .	79
4.4	Reference Raman spectra . . . . .	81
4.5	Structural conformations of forms I and II . . . . .	82
4.6	Raman spectra of the 5% extrudate during dissolution . . . . .	85
4.7	Raman MCR maps during dissolution . . . . .	87

---

4.8	Raman maps of the core and surface of the 50% extrudate . . . . .	88
4.9	XRPD pattern of the 50% extrudate residue . . . . .	88
4.10	Re-crystallisation kinetic model . . . . .	90
5.1	UV-Vis dissolution profiles . . . . .	97
5.2	Absorbance UV-Vis values at 350 nm . . . . .	98
5.3	$^1\text{H}$ NMR spectra . . . . .	100
5.4	Release profiles . . . . .	101
5.5	MRI images first experiment . . . . .	102
5.6	MRI images zoom . . . . .	103
5.7	Evolution of the compact dimensions . . . . .	104
5.8	Raman spectrum of the 30% extrudate residue . . . . .	105
6.1	Scheme of the body . . . . .	109
6.2	Scheme of the experimental configuration . . . . .	112
6.3	Photographs during the dissolution test . . . . .	113
6.4	Photographs of the extrudates with $\geq 15\%$ indomethacin . . . . .	114
6.5	Compact surface area as a function of time . . . . .	116
6.6	RDDR trends in pH 2 HCl . . . . .	119
6.7	RDDR trends in pH 6.8 phosphate buffer . . . . .	120
6.8	Partial RDDR at pH 6.8 as a function of the indomethacin weight fraction . . . . .	121
6.9	Dissolution profiles of indomethacin . . . . .	122
6.10	Raman spectra of raw materials . . . . .	125
6.11	Averaged Raman spectra of the dissolution experiment . . . . .	127
6.12	Schematic model of the dissolution mechanism . . . . .	128
6.13	Averaged Raman spectra of the high drug-loaded extrudates . . . . .	130
6.14	Phonon-mode Raman region of the 70% extrudate compact during dissolution . . . . .	131
6.15	XRPD pattern of the 100% amorphous residue . . . . .	131
A.1	XRPD patterns . . . . .	139
B.1	XRPD patterns of raw materials . . . . .	140
B.2	Raman spectra of the 50% extrudate dissolution . . . . .	141
B.3	Remaining time-point Raman maps . . . . .	142
B.4	Constrained kinetic model . . . . .	143
C.1	XRPD characterisation . . . . .	144
C.2	Raman characterisation . . . . .	145
C.3	$^1\text{H}$ NMR spectra of reference solutions . . . . .	145
C.4	MRI images second experiment . . . . .	146
D.1	XRPD patterns of indomethacin crystalline forms . . . . .	147
D.2	Raman spectra of indomethacin crystalline forms . . . . .	148
D.3	XRPD patterns of the extrudates . . . . .	149

---

D.4 Phonon mode region of raw materials . . . . . 149

# List of Tables

1.1	Solid dispersion products . . . . .	20
3.1	Partial RDDR values of felodipine and copovidone . . . . .	56
4.1	Raman acquisition details . . . . .	75
4.2	Partial RDDR values of bicalutamide and copovidone . . . . .	78
6.1	Partial RDDR values of indomethacin and copovidone . . . . .	117

# List of Equations

1.1 Noyes–Whitney equation . . . . .	5
2.1 Bragg equation . . . . .	36
2.2 Abbe equation . . . . .	40
3.1 Index of performance . . . . .	56

# Abbreviations

<b>ALS</b>	<b>A</b> lternating <b>L</b> east- <b>S</b> quares
<b>ASD</b>	<b>A</b> morphous <b>S</b> olid <b>D</b> ispersion
<b>ATR FT-IR</b>	<b>A</b> ttenuated <b>T</b> otal <b>R</b> eflectance <b>F</b> ourier <b>T</b> ransform- <b>I</b> nfra <b>R</b> ed
<b>BCS</b>	<b>B</b> iopharmaceuticals <b>C</b> lassification <b>S</b> ystem
<b>CARS</b>	<b>C</b> oherent <b>A</b> nti- <b>S</b> tokes <b>R</b> aman <b>S</b> cattering
<b>CCD</b>	<b>C</b> harge- <b>C</b> oupled <b>D</b> evice
<b>Copovidone</b>	Poly(vinyl pyrrolidone)-poly(vinyl acetate)
<b>DCS</b>	<b>D</b> evelopability <b>C</b> lassification <b>S</b> ystem
<b>FaSSIF</b>	<b>F</b> asted- <b>S</b> tate <b>S</b> mall <b>I</b> ntestinal <b>F</b> luid
<b>GI</b>	<b>G</b> astro <b>I</b> ntestinal
<b>hGH</b>	<b>H</b> uman <b>G</b> rowth <b>H</b> ormone
<b>HAC</b>	<b>H</b> ierarchical <b>A</b> gglomerative <b>C</b> lustering
<b>HPLC</b>	<b>H</b> igh <b>P</b> erformance <b>L</b> iquid <b>C</b> hromatography
<b>HPMC</b>	<b>H</b> ydroxy <b>P</b> ropyl <b>M</b> ethyl <b>C</b> ellulose
<b>HPMCAS</b>	<b>H</b> ydroxy <b>P</b> ropyl <b>M</b> ethyl <b>C</b> ellulose <b>A</b> cetate- <b>S</b> uccinate
<b>HME</b>	<b>H</b> ot <b>M</b> elt <b>E</b> xtrusion
<b>IDR</b>	<b>I</b> ntrinsic <b>D</b> issolution <b>R</b> ate
<b>LHS</b>	<b>L</b> eft <b>H</b> and <b>S</b> ide
<b>MCR</b>	<b>M</b> ultivariate <b>C</b> urve <b>R</b> esolution
<b>MRI</b>	<b>M</b> agnetic <b>R</b> esonance <b>I</b> maging
<b>MW</b>	<b>M</b> olecular <b>W</b> eight
<b>NCE</b>	<b>N</b> ew <b>C</b> hemical <b>E</b> ntity
<b>NSAID</b>	<b>N</b> on <b>S</b> teroidal <b>A</b> nti- <b>I</b> nflammatory <b>D</b> rug
<b>PAA</b>	<b>P</b> oly <b>A</b> crylic <b>A</b> cid

---

<b>PEG</b>	<b>P</b> oly <b>E</b> thylene <b>G</b> lycol
<b>PLA</b>	<b>P</b> oly <b>L</b> actic <b>A</b> cid
<b>PLGA</b>	<b>P</b> oly( <b>L</b> actic-co- <b>G</b> lycolic <b>A</b> cid)
<b>PLM</b>	<b>P</b> olarized <b>L</b> ight <b>M</b> icroscopy
<b>PCA</b>	<b>P</b> rincipal <b>C</b> omponent <b>A</b> nalysis
<b>PVP</b>	<b>P</b> oly( <b>V</b> inyl <b>P</b> yrrolidone)
<b>RDDR</b>	<b>R</b> otating <b>D</b> isk <b>D</b> issolution <b>R</b> ate
<b>RH</b>	<b>R</b> elative <b>H</b> umidity
<b>RHS</b>	<b>R</b> ight <b>H</b> and <b>S</b> ide
<b>SLAD</b>	<b>S</b> olubility <b>L</b> imited <b>A</b> bsorbable <b>D</b> ose
<b>ss-NMR</b>	<b>S</b> olid- <b>S</b> tate <b>N</b> uclear <b>M</b> agnetic <b>R</b> esonance
<b>USP</b>	<b>U</b> nited <b>S</b> tates <b>P</b> harmacopeia
<b>UV-Vis</b>	<b>U</b> ltra <b>V</b> iolet- <b>V</b> isible
<b>XRPD</b>	<b>X</b> - <b>R</b> ay <b>P</b> owder <b>D</b> iffraction

# Chapter 1

## Introduction

### 1.1 Poorly soluble drugs

Oral ingestion is the most commonly used and convenient route of drug administration due to high patient compliance, cost effectiveness and flexibility in the design of dosage forms.<sup>1</sup> However, the major challenge associated with the oral administration is the low bioavailability. The oral bioavailability depends on a number of factors such as the aqueous solubility, dissolution rate, drug permeability, first-pass metabolism and susceptibility to efflux mechanisms. For orally administered drugs the aqueous solubility is the most important factor to achieve an adequate bioavailability and the required pharmacological response. The drug molecules must be dissolved in the gastrointestinal (GI) fluids, absorbed through the GI membrane into the circulatory system and reach the target in sufficient quantity. For poorly soluble drugs the absorption step is solubility- and dissolution rate-limited.

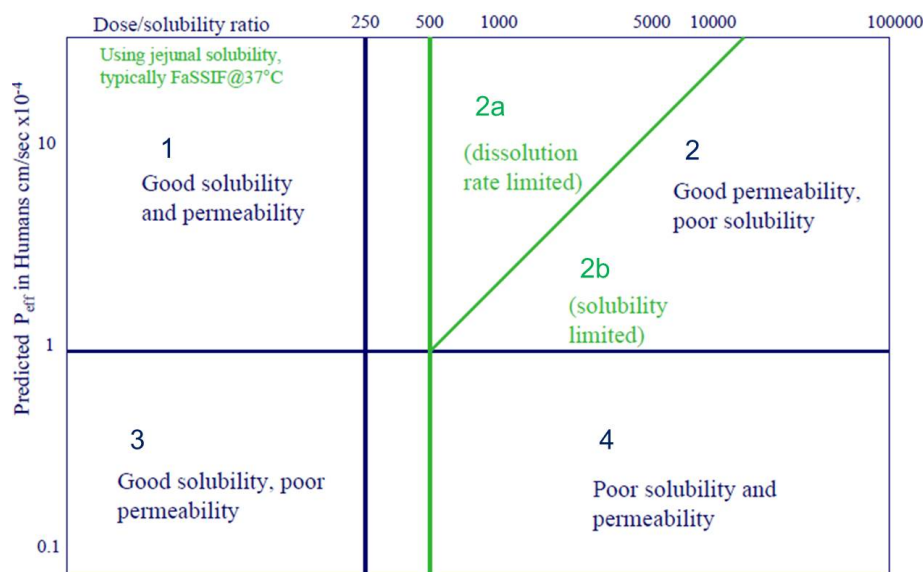
Approximately 70% of new chemical entities (NCEs) developed in the pharmaceutical industry show poor water solubility. This percentage can be even higher, as high as 90%, for certain drug categories.<sup>2</sup> For these

molecules the low aqueous solubility is a limiting factor to achieve the desired concentration in the systemic circulation and thus pharmacological response. Therefore, improving the oral bioavailability of poorly soluble drugs represents a major challenge to the pharmaceutical industry. One way to improve the oral bioavailability of poorly soluble drugs is to increase the drug concentration in the GI fluids and this can be obtained by increasing the water solubility, dissolution rate or a combination of both. One of the most important examples of improving the dissolution properties is represented by converting crystalline solids into amorphous solids.<sup>3</sup> In an amorphous material the three-dimensional long-range order which characterises crystalline materials is lost and as a consequence the energy barrier for drug molecules to go into solution is lowered.

In 1995 the biopharmaceutics classification system (BCS) was established to facilitate the development of oral drug products, classifying drug molecules according to their aqueous solubility and intestinal permeability.<sup>4</sup> As shown in Figure 1.1, a BCS class 1 drug is characterised by high solubility and high permeability, a class 2 has low solubility and high permeability, a class 3 has high solubility and low permeability and a class 4 is characterised by low solubility and permeability. Class 1 drugs are the most attractive candidates to progress to clinical trials as they are characterised by high solubility and permeability. The bioavailability of class 2 drugs (low solubility, high permeability) can be improved simply using formulation approaches that increase the concentration of the drug in the GI fluids, and this can be achieved by increasing the drug solubility or dissolution rate. The bioavailability of class 3 drugs (high solubility, low permeability) is permeability-rate limited, while the dissolution step is likely to be rapid. Class 4 drugs possess low solubility and permeability, therefore they are often poor candidates for drug development. Over the past few decades there has been a significant increase of drug candidates that have fallen into class 2 and class 4, therefore improving the dissolution properties is a pressing issue for the pharmaceutical industry.<sup>5</sup>

FIGURE 1.1: The BCS.<sup>6</sup>

In 2010 a revised classification system for oral drugs termed the developability classification system (DCS) was introduced using the BCS as a starting point.<sup>7</sup> While the BCS is designed as a regulatory classification for the assurance of bio-equivalence, the DCS more accurately categorises drugs according to the factors limiting the oral absorption and therefore provides a more appropriate classification system for the issues related to oral product development. The main deviation of the DCS from the BCS is the introduction of the solubility limited absorbable dose (SLAD) concept and the addition of two sub-classes for class 2 drugs (Figure 1.2). The SLAD is represented by the boundary between class 2a and class 2b and it is based on the idea that permeability and solubility are compensatory for class 2 drugs. For class 2a compounds (dissolution rate-limited), a solid dosage form containing the crystalline drug can be designed to achieve the complete oral absorption without the use of complex solubilisation technologies. This is a result of the compensatory nature of high permeability on low solubility. For this particular class, however, the drug release from a standard formulation and absorption will depend on a number of factors such as particle size, surface area and wettability.

FIGURE 1.2: The DCS.<sup>7</sup>

For class 2b compounds (solubility-limited), the drug will not be absorbed unless it is formulated in an already solubilised form. Therefore, class 2b represents a major challenge to formulators.

Griseofulvin (dose of 500 mg) is an example of solubility-limited class 2b compound. The solubility of griseofulvin in fasted state simulated intestinal fluid (FaSSIF) has been reported to be  $19 \mu\text{g} \cdot \text{mL}^{-1}$ , while absorption and permeability have been shown to be high.<sup>8</sup> Even when the drug is administered as micronised particles, there is not sufficient dissolution to obtain a complete absorption.<sup>9,10</sup> A solid dispersion of griseofulvin in poly(ethylene glycol) (PEG) has been used to obtain greater dissolution and oral absorption compared to the micronised drug.<sup>11</sup> However, the complete oral absorption for griseofulvin and other solubility-limited compounds is very challenging and requires careful selection of solubilising strategies. Mefenamic acid (dose of 250 mg) is a nonsteroidal anti-inflammatory drug (NSAID) with a solubility in FaSSIF of  $0.04 \text{ mg} \cdot \text{mL}^{-1}$  and a very high intestinal permeability.<sup>7,12</sup> According to the new DCS system, mefenamic acid is a borderline 2a/2b compound with a SLAD of 280 mg and a recommended maximum particle size of 42  $\mu\text{m}$ . For mefenamic acid, if the dissolution is sufficiently rapid, even from a formulation where the drug is not already

solubilised, a complete absorption will be observed due to the compensatory effect of high permeability on low solubility.

## 1.2 Solubility and dissolution rate

Aqueous solubility and dissolution rate are important properties to consider when developing drugs for oral administration. Solubility is an intrinsic property of a solid substance which occurs under dynamic equilibrium, i.e. solubility results from the simultaneous and opposing processes of dissolution and precipitation of solids. The dissolution rate is an extrinsic property and it is defined as the rate of solvation. Therefore, changing the chemical structure of a drug molecule (e.g. pro-drugs, salt formation) will change the solubility, whilst the dissolution rate can be changed through the use of formulation strategies (e.g. particle size reduction, complexation).

The correlation between solubility and dissolution rate is described by the Noyes–Whitney equation (Equation 1.1):<sup>13</sup>

$$\frac{dC}{dt} = k_D A (C_S - C_t) \quad (1.1)$$

where  $\frac{dC}{dt}$  is the dissolution rate,  $k_D$  is the dissolution rate constant (dependent on the stirring rate and the diffusion constant),  $A$  is the surface area of the solid,  $C_S$  is the solubility of the drug, and  $C_t$  is the drug concentration dissolved at time  $t$ . This equation shows that, all other factors being constant, the dissolution rate is proportional to the surface area of the solid and to the solubility of the drug. As a result, poorly soluble drugs will have a slow dissolution rate and poor bioavailability. A review of the current formulation strategies to improve the dissolution properties and oral bioavailability of poorly soluble drugs is outlined in the next sections.

## 1.3 Strategies of improving the dissolution properties

### 1.3.1 Pro-drugs

The pro-drug approach consists of functionalising a drug with hydrophilic moieties (e.g. phosphate ester groups), so that the solubility will increase.<sup>14</sup> After administration, the inactive substance is metabolised *in vivo* to produce the active drug. For example, amprenavir has been phosphorylated to produce fosamprenavir.<sup>14</sup> Fosamprenavir in the form of a calcium salt was shown to be approximately 10 times more soluble than amprenavir. Although this approach to improve the oral bioavailability has produced a number of commercially available products,<sup>15</sup> two main requirements must be satisfied. Firstly, the compound should have a suitable functional group to make a pro-drug. Secondly, an enzyme in the body is necessary to transform the pro-drug in its active form after administration. A more complex biopharmaceutical profile and poor chemical stability can be additional challenges.

### 1.3.2 Salts

Forming salts of ionisable drugs is one of the most common ways to increase the dissolution properties.<sup>16</sup> The improvement in dissolution compared to the free acid or free base under the pH conditions of the GI tract is due to the higher solubility of the free drug in the pH microclimate of the aqueous diffusion layer surrounding the solid generated by the counterion.<sup>17,18</sup> For example, the dissolution rates of doxycycline hydrochloride at pH 4 and 7 were found to be significantly higher compared to those of the free base form.<sup>16</sup> Similarly, the dissolution rates of sodium salicylate at pH 1.1, 2.1 and 7.0 were shown to be higher than those of salicylic acid.<sup>16</sup> The main disadvantage of this approach is that a drug must contain ionisable groups

(e.g. carboxylic acids, amines) to form a salt. In addition, salts can potentially revert into aggregates of their free acid or base forms, thus inhibiting the improvement in bioavailability.

### 1.3.3 Particle size reduction

It can be seen from Equation 1.1 that the surface area of the solid is a key parameter that directly affects the dissolution rate. Reducing the particle size of the drug will increase the surface area and therefore the dissolution rate. The amount of griseofulvin in the blood was found to be approximately doubled by reducing the particle size from 10 to 2.7  $\mu\text{m}$ .<sup>19</sup> Micro-nisation is a common method to reduce the particle size and it is done by milling techniques. Limitations of this technology include the formation of particles with poor flow properties and the generation of charged and cohesive particles which can rapidly aggregate.

### 1.3.4 Amorphous forms and amorphous solid dispersions (ASDs)

Converting a crystalline drug into an amorphous drug is considered one of the most important approaches to improve the dissolution properties of poorly soluble drugs.<sup>3</sup> For example, the dissolution of amorphous indomethacin and ritonavir were found to be 5 and 10 fold higher than that of their crystalline counterparts.<sup>20,21</sup> This increase in dissolution typically will result in an increase in oral absorption and bioavailability. Two classes of amorphous materials are relevant to the pharmaceutical science: pure amorphous solids and ASDs. As amorphous solids and ASDs are the main focus of this thesis, important physicochemical considerations for their preparation, stability and dissolution improvements will be specifically discussed in later sections (Sections 1.4 and 1.5).

### 1.3.5 Polymorphs

Drugs can exist in several different crystalline forms known as polymorphs. Polymorphism is defined as the ability of a compound to crystallise as more than one distinct crystal species. Polymorphs, due to their different packing arrangements, present significantly different physicochemical properties such as water solubility and dissolution rate, stability and compactability.<sup>22</sup> Selecting a polymorph with higher free energy can increase the dissolution rate and bioavailability compared to the thermodynamically stable form. Kobayashi et al. have shown that the dissolution rate and bioavailability were significantly different between carbamazepine polymorphs.<sup>23</sup> The dissolution rate of both anhydrides (form I and form III) was found to be 1.5 and 1.6 fold higher than that of the dihydrate form. The plasma concentration level of form I was shown to be approximately twice than that of form III and the dihydrate form. The main challenge is that metastable polymorphs can convert into the more stable form during manufacturing, storage as well as dissolution in the GI fluids, leading to unpredictable performances.<sup>24</sup> Polymorph screening is therefore a very important part of the pharmaceutical development.

### 1.3.6 Co-crystals

The definition of co-crystals is still under debate in literature, but in general they can be defined as a crystalline material that consists of two or more chemical species held together by non-covalent forces.<sup>25-27</sup> While according to some definitions the term co-crystal includes salts, the molecules in a co-crystal are not necessarily ionically bonded together, i.e. there is not proton transfer, but they are held together by other non-covalent forces, mostly through hydrogen bonding and  $\pi$ - $\pi$  stacking. As discussed for polymorphs, co-crystals often present superior physicochemical properties compared to those of each of the separate entities. The dissolution rate of a co-crystal which consists of a sodium channel blocker and saccharin was shown to be

18 fold higher compared to that of the pure crystalline form.<sup>28</sup> In addition, the plasma concentration level of the co-crystal was found to be 3 fold higher than that of the pure crystalline form. As with salt formation, however, co-crystals can suffer from selection problems (e.g. compatible functional groups are required for inter-molecular interactions).

### **1.3.7 Microemulsions**

Microemulsions are biphasic systems composed of two immiscible liquids with one dispersed through the other.<sup>29,30</sup> Microemulsions are stabilised by surfactants and can be used for parenteral, topical and oral administration. Hydrophobic and poorly soluble drugs are incorporated into the microemulsion, so that the dissolution step can be avoided. The bioavailability of a cyclosporine microemulsion has been found to be 6.5 fold higher compared to the conventional oral solution formulation.<sup>31</sup> The main drawback of this formulation strategy is the chemical and physical instability.

### **1.3.8 Cyclodextrins**

Cyclodextrins are cyclic oligosaccharides with a hydrophilic outer surface and a hydrophobic inner cavity capable of forming complexes with hydrophobic and poorly soluble drugs. They are not only used to improve the dissolution and bioavailability of poorly soluble drugs, but also for taste masking. Improvements in solubility from 1.8 to 200 fold for a number of drugs have been obtained when using cyclodextrin solutions over water.<sup>32</sup> The main limitation of cyclodextrins includes the potential nephrotoxicity after parenteral administration.<sup>33</sup>

## 1.4 Amorphous solids

### 1.4.1 Formation of the amorphous form

The amorphous phase can be defined as a disordered solid that lacks the three-dimensional long-range order present in the crystalline phase.<sup>34</sup> A classical free energy-temperature diagram (Figure 1.3) shows that, when the temperature is increased, there is a significant reduction in free energy of the crystal, until the melting temperature  $T_m$  is reached, where the crystal undergoes a spontaneous conversion to the liquid form. If the system is slowly cooled to below the  $T_m$  and there is sufficient time for nucleation and crystal growth to occur, the liquid phase will revert to the crystal. However, if the liquid is rapidly cooled and the crystallisation is avoided, the system will maintain the properties of the liquid phase as supercooled liquid. If the system is further cooled, the viscosity of the supercooled liquid increases and this results in a distinct discontinuity in the free energy-diagram, with the formation of the unstable glassy state. The temperature at which this change occurs is termed glass transition temperature  $T_g$ . The amorphous phase can therefore be prepared by melting the crystalline form and supercooling the system below the  $T_m$  and the  $T_g$ . This is indeed the basis for producing ASDs by hot melt extrusion (HME).

### 1.4.2 Physical stability of the amorphous form

Figure 1.3 also shows that the amorphous/glassy phase is in a higher free energy state at all temperatures compared to the crystalline phase. Therefore, the amorphous form will spontaneously crystallise over time. Such crystallisation will clearly negate the benefits of using the amorphous form for enhancing the dissolution properties of poorly water-soluble drugs. Aso et al. found that for several pharmaceuticals the molecular mobility and

the re-crystallisation tendency of the amorphous form significantly increases above the  $T_g$ .<sup>35</sup>

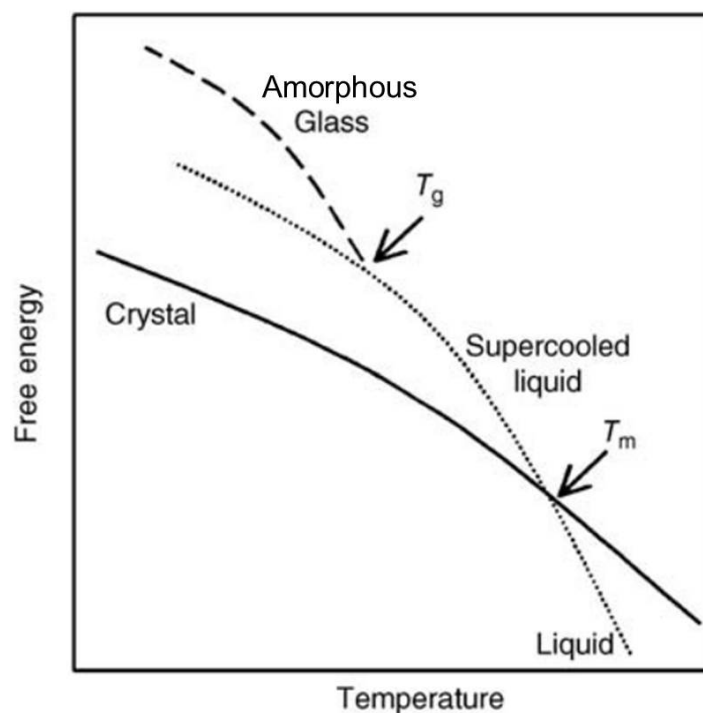


FIGURE 1.3: Effect of temperature on free energy for a single-component system.<sup>36</sup>

The  $T_g$  is therefore an important indicator of the physical stability of an amorphous material. Storing the amorphous material below the  $T_g$  should lower the risk of crystallisation due to the low molecular mobility. However, it has been reported that felodipine and nifedipine, while they have similar  $T_g$ s (46.4 °C for felodipine and 45.5 °C for nifedipine), they have a different re-crystallisation behaviour, with nifedipine re-crystallising far more readily than felodipine.<sup>37</sup> This was attributed to a higher thermodynamic driving force and lower activation energy for crystallisation in nifedipine. In addition, the presence of water in the storage conditions can lower the  $T_g$  of amorphous materials by plasticisation effect, increasing the rate of crystallisation.<sup>38</sup> The preparation method used to prepare the amorphous material has been demonstrated to significantly affect the thermodynamic properties and the re-crystallisation tendency. Karmwar et al. have prepared amorphous indomethacin using melt quenching, spray drying, ball milling and cryomilling.<sup>39</sup> They found that the physical stability of the

amorphous form decreased in the order: melt quenching > cryomilling > spray drying > ball milling. The drug particle size has been also shown to affect the physical stability and re-crystallisation tendency. Particles of amorphous felodipine with smaller size were shown to crystallise at faster rates compared to larger particles.<sup>40</sup>

Homogeneous nucleation and crystal growth from the liquid state can be used to describe the re-crystallisation of organic molecules from the amorphous state.<sup>41</sup> This model assumes that the molecules in the liquid state first undergo spontaneous nucleation, followed by the growth of crystallites. The free energy difference  $\Delta G$  between molecules in the amorphous state and those in the crystalline state is the thermodynamic driving force for nucleation and crystal growth (Figure 1.4). However, phase separation with the formation of new surfaces between the nuclei and the amorphous phase must occur prior to nucleation, and this process is thermodynamically unfavourable. Thus, there is an increase in  $\Delta G$  until a critical radius  $r$  of spherical nuclei is reached, above which the spontaneous nucleation occurs. Nucleation inhibitors can potentially prevent the system from reaching the critical nucleus radius, thus avoiding the crystal growth.

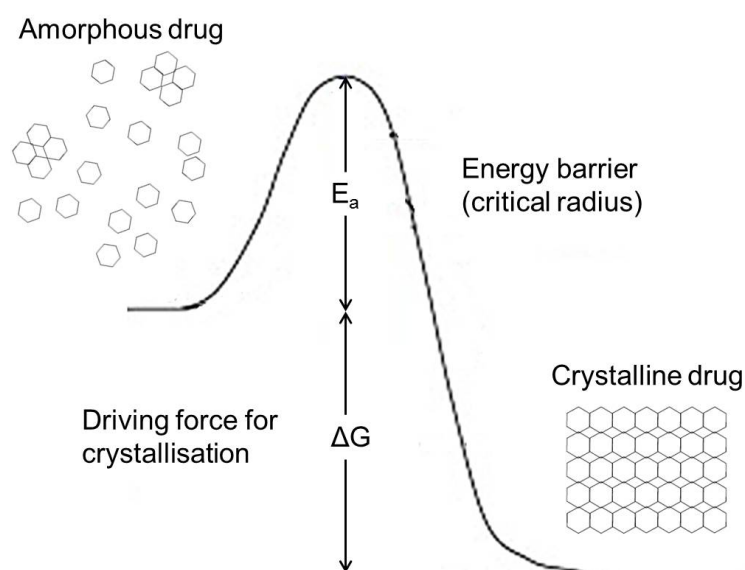


FIGURE 1.4: Energies associated with the crystallisation of amorphous materials.<sup>6</sup>

As mentioned before, the main advantages of the amorphous form compared to the crystal are the improved dissolution properties due to the lack of a well-ordered crystal lattice. However, amorphous pharmaceuticals, due to their physical instability, have the tendency to quickly re-crystallise during storage or when exposed to dissolution media,<sup>20</sup> leading to an unpredictable bioavailability. Nucleation inhibitors or molecules that reduce the molecular mobility of the system such as polymers can be used to improve resistance to crystallisation and enhance the dissolution properties.<sup>42</sup>

## 1.5 Amorphous solid dispersions

ASDs can be defined as single-phase amorphous mixtures of one or more active pharmaceutical ingredients (APIs) and a polymeric carrier.<sup>43</sup> The primary functions of the polymer are to provide stability of the amorphous form during storage against the solid-state crystallisation and to maintain the drug supersaturation in the dissolution medium by inhibiting the solvent-mediated crystallisation.<sup>44</sup>

### 1.5.1 Preparation of amorphous solid dispersions

ASDs can be prepared by two main methods: melt (fusion) and solvent evaporation. Melt (fusion) methods primarily include HME, direct capsule filling and compression moulding, while solvent evaporation methods mainly include spray drying and co-precipitation. In HME the material is melted/softened at elevated temperatures and continuously extruded to produce small fragments which are then milled and mixed with other formulation components.<sup>45</sup> The main advantages of HME are that it is a continuous and solvent-free process and that it can be scaled up to large-scale manufacturing. Disadvantages are related to the use of high temperatures which can lead to thermal degradation and to a poor mixing between the drug and the polymer because of the high viscosity of the liquid polymer.

Direct capsule filling consists of directly filling the gelatin capsules with the melt of solid dispersions, while in compression moulding the mixture of a drug and a polymer is compressed at elevated temperature. In spray drying a solution of a drug and a polymer is sprayed through a nozzle into a drying chamber where the solvent is rapidly evaporated.<sup>46</sup> The main advantages of spray drying are that the particle size of the material can be controlled and that the process can be easily scaled up for manufacturing. Disadvantages include potential degradation due to the solvent and difficulty in completely removing the solvent with consequent safety concerns. Co-precipitation consists of co-precipitating the drug and the carrier as microparticles by adding a non-solvent to the solution of the drug and the carrier.

### 1.5.2 Carrier materials

Typical materials for preparing ASDs are water-soluble or water-swelling polymers. When selecting a carrier it is important to consider the manufacturing method. For example, in HME the carrier must be thermally stable under the required process conditions. If the preparation is via spray drying, both the drug and the polymer should be sufficiently soluble in the required organic solvent. In addition, the selection of polymer carrier should also be evaluated based on the drug:polymer miscibility, mechanism of the inhibition of the crystal growth and the carrier ability to enhance the dissolution profiles of the dispersed drug. A lack of miscibility can induce drug re-crystallisation.<sup>47,48</sup> For example felodipine was found to be miscible with PVP and this polymer was very effective to inhibit the drug re-crystallisation.<sup>49</sup> In contrast, felodipine was shown to be only partially miscible with polyacrylic acid (PAA), and the drug quickly crystallised.<sup>48,50</sup> Itraconazole was found to be miscible with Eudragit E100 only up to a drug loading of 13%, while at higher drug loadings a drug-rich amorphous phase

and polymer-rich amorphous phase were observed using microthermal analysis.<sup>51</sup>

The most commonly used polymers for preparing ASDs include vinyl-pyrrolidone-based polymers such as poly(vinyl pyrrolidone) (PVP) and poly(vinyl pyrrolidone)-poly(vinyl acetate) (copovidone)<sup>52,53</sup> and cellulose-based polymers such as hydroxypropyl methylcellulose (HPMC) and hydroxypropyl methylcellulose acetate-succinate (HPMCAS).<sup>54</sup> Methacrylate-based polymers such as Eudragit are also used for a pH-dependent drug release.<sup>55</sup>

### **1.5.3 Solid-state characterisation of amorphous solid dispersions**

As previously discussed, the physical stability and the dissolution mechanisms of ASDs have been shown to be strongly affected by the solid-state properties, therefore the determination of the physical structure is of particular importance. In this section, common methods for solid-state characterisation of ASDs will be presented.

#### **1.5.3.1 Polarized light microscopy (PLM)**

PLM is a contrast-enhancing technique that probes birefringence, which is a phenomenon that most crystalline APIs display due to their anisotropic nature. Amorphous materials are isotropic and therefore they do not show birefringence. Crystalline domains appear as coloured and bright regions, while amorphous domains show a similar colour to the background. Using PLM it is possible to readily detect small quantities of crystalline material in an otherwise amorphous matrix. The key advantage of this technique is that small amounts of material are required. PLM has been employed in several studies to evaluate optimum polymers for ASDs and the recrystallisation behaviour of amorphous systems.<sup>41,49,56,57</sup> In one of these

studies, for example, PLM was employed to investigate the nucleation rate of amorphous indomethacin as a function of temperature.<sup>41</sup> In other studies, PLM has been used to evaluate the impact of polymer amount and storage conditions on the nucleation rate of felodipine.<sup>49,57</sup>

### 1.5.3.2 X-ray powder diffraction (XRPD)

XRPD is one of the most common methods to determine and quantify crystallinity in amorphous systems. The diffractogram of a crystalline material contains characteristic peaks, while that of an amorphous material is characterised by a broad halo. The limits of detection of crystallinity are typically in the range of 1–5% by weight for laboratory-based diffractometers,<sup>58</sup> while with synchrotron-based systems it is possible to achieve lower detection limits, as low as 0.2%.<sup>59</sup> XRPD has been employed in a number of reports to evaluate the solid-state structure of ASDs, including miscibility.<sup>49–51,60</sup> In one of these reports, XRPD was used to follow the crystallisation kinetics of amorphous felodipine solid dispersions as a function of polymer type (PVP *vs* HPMCAS), drug loading and relative humidity (RH) storage conditions.<sup>60</sup>

### 1.5.3.3 Solid-state nuclear magnetic resonance (ss-NMR)

ss-NMR has been applied in several studies to investigate a number of aspects of ASDs, including molecular mobility, inter-molecular interactions and quantification of crystallinity.<sup>61–64</sup> <sup>19</sup>F ss-NMR was employed to determine the mobility of ASDs of flufenamic acid in PVP and HPMC.<sup>63</sup> The molecular mobility was found to be higher in the HPMC dispersion compared to the PVP dispersion. Due to the lower molecular mobility, the PVP dispersion was found to be more stable to crystallisation compared to the HPMC dispersion. <sup>19</sup>F ss-NMR has also been used to detect crystallinity in amorphous systems, with a detection limit of approximately 3%.<sup>64</sup>

#### 1.5.3.4 Differential scanning calorimetry (DSC)

One of the most common applications of DSC is the determination of the  $T_g$ . As discussed earlier, the  $T_g$  is of particular importance as the re-crystallisation of amorphous materials is known to be faster above the  $T_g$  than below the  $T_g$ .<sup>41</sup> Another application of DSC is the determination of crystallisation during heating. Yoshihashi et al. have investigated the induction times for the crystallisation of flurbiprofen and tolbutamide dispersions with PVP.<sup>65</sup> They observed that the induction time increased with an increasing amount of PVP, and that PVP was more effective at increasing the induction time for tolbutamide compared to flurbiprofen. DSC can also be used to estimate the presence of crystalline material arising from processing or storage through the determination of a melt endotherm.<sup>66</sup> This can be done by comparing the melt endotherm of the partially crystallised solid dispersion with the melt endotherm of the pure crystalline drug, with the ratio giving the amount of re-crystallised material.

#### 1.5.3.5 Raman and infrared (IR) spectroscopy

Both Raman and IR spectroscopy are methods widely used to characterise ASDs in terms of crystallisation rates and drug-polymer inter-molecular interactions. The main advantage of Raman is that it is able to readily discriminate between amorphous and crystalline forms. Raman spectra of crystalline materials are characterised by sharp peaks, while those from amorphous materials by broader bands. In addition, drugs typically have a stronger Raman spectrum than the excipients, which is important for the determination of low levels of crystallinity in multi-component systems. For example, Raman has been employed to detect the presence of less than 0.05% weight of crystallinity in ASDs of ibipinabant and PVP.<sup>67</sup> Another key advantage of Raman is that it can be coupled with a microscope to obtain highly spatially-resolved chemical images. Raman mapping was used,

for example, to discriminate between amorphous and crystalline domains in troglitazone-PVP ASDs.<sup>68</sup>

IR is a very useful technique to evaluate the drug-polymer miscibility and inter-molecular interactions. It has been employed to determine the interactions of ASDs of felodipine with PVP, HPMC and HPMCAS.<sup>49</sup> PVP was shown to form the strongest hydrogen bonds with felodipine. In another study, IR was employed to characterise the interactions in ASDs of indomethacin and PVP.<sup>69</sup> It was observed that the hydrogen bonds between the carboxylic acid functional group of indomethacin and the carbonyl acceptor of PVP (drug-polymer interactions) led to the disruption of the carboxylic acid dimers formed in the pure amorphous drug (drug-drug interactions).

#### 1.5.4 Physical stability during storage

The re-crystallisation event during storage depends on a number of factors such as the temperature,<sup>70</sup> water content,<sup>57</sup> and type and amount of polymer used.<sup>57,71</sup> As previously indicated, polymers have a key role in stabilising ASDs and preventing the drug re-crystallisation, and this is achieved by simply keeping the drug molecules apart via steric hindrance, reducing the molecular mobility of the drug and forming specific drug:polymer chemical interactions (e.g. hydrogen bonding).<sup>36,69,72-74</sup>

Polymers used for preparing ASDs typically have a  $T_g$  greater than 100 °C. When a higher  $T_g$  polymer is combined with a drug with lower  $T_g$ , the resultant dispersion will have a decreased molecular mobility and re-crystallisation tendency compared to the pure amorphous material (anti-plasticisation effect). Increasing the polymer molecular weight (MW) will increase the  $T_g$ , and this will result in a greater crystallisation inhibitory effect. It has been shown that the crystallisation inhibition of PVP for a model compound MK-059 increased with the polymer MW.<sup>73</sup>

The formation of chemical interactions between the drug and the polymer and the disruption of drug-drug interactions are also important for stabilising ASDs. Indomethacin and PVP have been shown by Raman and IR spectroscopy to form inter-molecular hydrogen bonding interactions in the solid dispersion.<sup>69</sup> The drug-polymer hydrogen bonds prevented the self-association of indomethacin dimers which characterises the crystal. In another work, it has been observed that ASDs of acetaminophen and PAA were stable for longer time compared to ASDs of acetaminophen in PVP.<sup>70</sup> This was attributed to the stronger chemical interactions between the carboxylic acid group of PAA and the hydroxyl group of acetaminophen compared to the carbonyl group of PVP.

The amount of polymer in ASDs can greatly affect the crystallisation tendency. It has been shown that ASDs of indomethacin and PVP containing only 5% w/w of polymer were stable up to a period of six months.<sup>75</sup> Increasing the amount of polymer to 30% w/w prevented nucleation and crystal growth for over two years.

Temperature significantly affects the physical stability of ASDs. Storing an ASD at elevated temperatures above the  $T_g$  will increase the molecular mobility, enhancing phase separation and/or re-crystallisation potential. A recommendation is to keep the storage temperature at  $T_g - 50$  °C, so that the molecular mobility can be practically neglected due to the high viscosity of the system.<sup>36,76</sup>

Another important consideration is that when an ASD is exposed to elevated RH conditions, the material will absorb the water vapour with consequent effects on the bulk properties of the solid such as the  $T_g$  and the molecular mobility.<sup>77</sup> The water molecules act as an excellent plasticiser, significantly reducing the  $T_g$  of amorphous solids and therefore increasing the re-crystallisation tendency.<sup>78</sup> Figure 1.5 shows the water vapour absorption for PVP, HPMC and HPMCAS at room temperature. PVP was shown to be the most hygroscopic polymer with 26% w/w of water vapour

absorption at 75% RH, while the water uptake of HPMC and HPMCAS were found to be 10% w/w and 7% w/w respectively.<sup>79</sup>

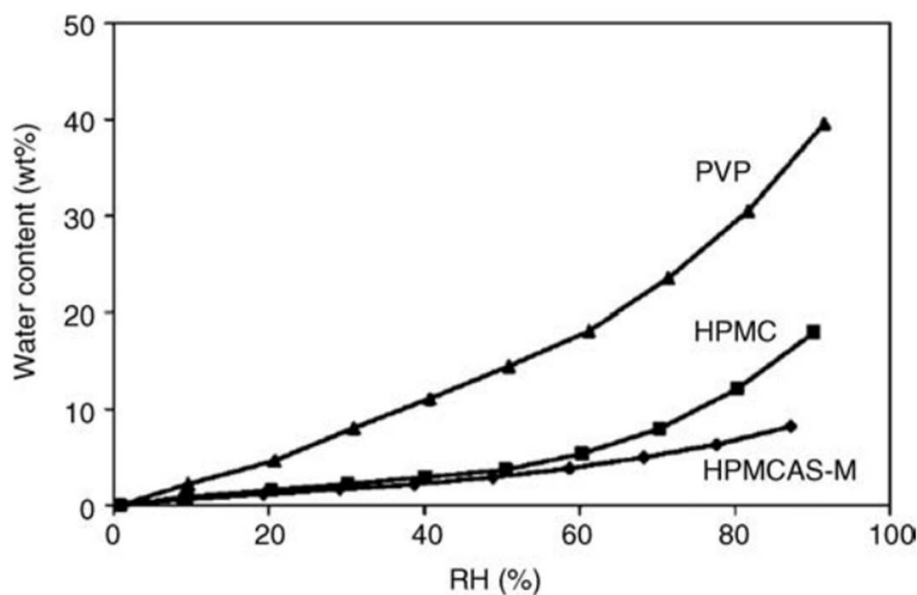


FIGURE 1.5: Water vapour absorption for PVP, HPMC and HPMCAS at room temperature.<sup>79</sup>

Although ASDs represent a very promising platform for increasing the dissolution properties of poorly soluble drugs, to date only a limited number of products have been brought to market (Table 1.1).<sup>80</sup> The main concern is the possibility of drug re-crystallisation during manufacturing, storage and dissolution which can lead to unpredictable performance in the patient with potentially harmful consequences.

Product	Compound	Polymer	Process	Approval
Sporanox	Itraconazole	HPMC	Fluid bed bead layering	1992
Prograf	Tacrolimus	HPMC	Spray drying	1994
Kaletra	Lopinavir/ritonavir	Copovidone	HME	2007
Intelence	Etravirine	HPMC	Spray drying	2008
Zortress	Everolimus	HPMC	Spray drying	2010
Onmel	Itraconazole	HPMC	HME	2010
Norvir	Ritonavir	Copovidone	HME	2010
Incivek	Telaprevir	HPMCAS	Spray drying	2011
Zelboraf	Vemurafenib	HPMCAS	Solvent/antisolvent precipitation	2011
Kalydeco	Ivacaftor	HPMCAS	Spray drying	2012

TABLE 1.1: Solid dispersion products in the market.<sup>80</sup>

### 1.5.5 Dissolution performance in aqueous media

The main advantages of using ASDs are the increased dissolution and improved bioavailability compared to the crystalline form. A drug in an ASD, when immersed in an aqueous dissolution medium, will rapidly dissolve and reach some level of supersaturation. However, the amorphous drug molecules due to their physical instability are likely to crystallise over time, thus depleting the solution of dissolved drug and reducing the bioavailability.

There are two potential re-crystallisation routes in aqueous media: direct solid-solid and solution-mediated crystallisation.<sup>6</sup> In aqueous media the water penetration into the amorphous material increases the molecular mobility due to plasticisation effect (same as during storage), thus facilitating the direct solid-solid transformation within the material. However, the most important crystallisation process in aqueous media is the solution-mediated crystallisation. The drug in the crystalline form dissolves until the thermodynamic solubility of the drug is reached, after which the concentration of the drug remains constant. On the other hand, the amorphous drug dissolves more rapidly than the crystalline form and reaches higher concentrations. However, the solution is supersaturated with respect to the crystalline state and therefore it is thermodynamically viable for the drug to precipitate into the crystalline form until the concentration equals the solubility of the crystalline drug. The generation and stabilisation of a metastable supersaturated state can be described using the “spring and parachute” model (Figure 1.6).<sup>81</sup> The amorphous form can be associated to the “spring”. The lack of three-dimensional long-range order results in an increased dissolution rate, but there is a thermodynamic driving force for crystallisation due to the saturation solubility of the crystalline form being exceeded. The higher the level of supersaturation is achieved, the higher the rates of nucleation and crystal growth are.<sup>82</sup> Polymers or other additives that act as crystallisation inhibitors are described as “parachutes”.

They maintain the supersaturation for a longer time period, increasing the absorption and bioavailability.

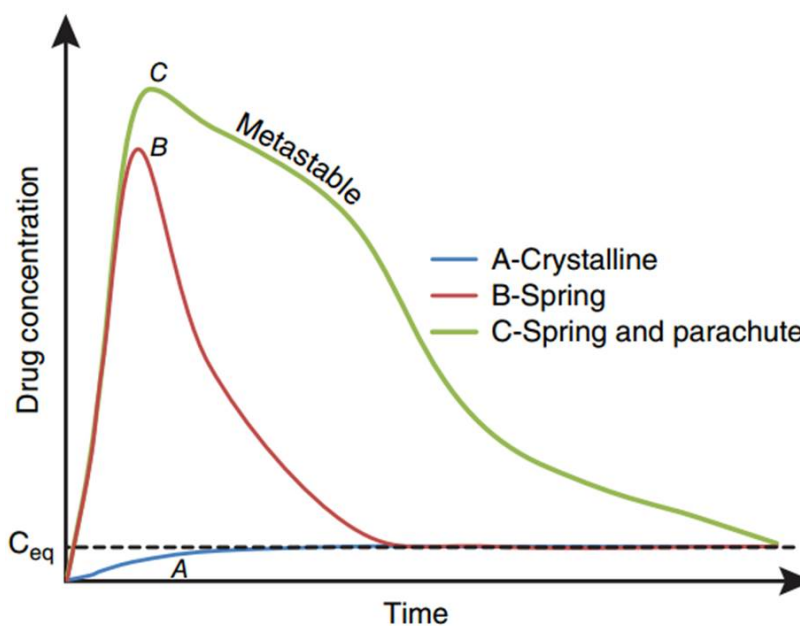


FIGURE 1.6: Schematic illustration of the “spring and parachute” model.<sup>81</sup>

The parachute effect of the polymer is due to a combination of mechanisms. Polymers can form complexes with the drug molecules in solution, via electrostatic bonds, van der Waals forces and hydrogen bonding, thus inhibiting nucleation and crystal growth.<sup>83</sup> In addition, the viscosity of the polymer can also have an effect on nucleation and crystal growth.<sup>84</sup> The impact on crystal nucleation of various polymers has been evaluated for a number of drugs.<sup>85</sup> For example, the induction time for crystallisation of celecoxib was about 20 min in presence of the polymer, compared to less than 5 min in absence of the polymer. HPMC was also found to reduce the nucleation rate of felodipine by a factor of 1000.<sup>86</sup>

The dissolution performance of ASDs depends on a number of factors such as the physicochemical properties of the drug and the polymer, and the drug:polymer ratio. Craig classified the drug release from ASDs as drug-controlled or polymer-controlled.<sup>87</sup> For a carrier-controlled release, the rate-limiting step for drug dissolution is the release of the polymer itself.<sup>88</sup> The drug is released into solution at a rate dictated by the carrier. For a

drug-controlled release, the dissolution will depend on the physicochemical properties of the drug. The drug is released into the dissolution medium at a rate proportional to its aqueous solubility.<sup>89</sup> In this case, the low aqueous solubility can induce physical instability and drug re-crystallisation.

## 1.6 Dissolution measurements

By far the most common method of investigating the drug release from ASDs and other oral dosage forms is the use of US pharmacopeia (USP) apparatuses (types I, II and IV).<sup>90</sup> These solution-based tests consist in dissolving the material in water or in other physiologically relevant fluids which are kept in motion at a constant speed, and measuring the drug content in solution as a function of time using ultraviolet-visible (UV-Vis) spectroscopy or high performance liquid chromatography (HPLC). These *in vitro* dissolution testing methods are robust, easy to operate and widely available, and can be used to determine the key factors that influence the performance of products. However the mechanism of dissolution is inferred indirectly, with no data being collected directly from the dosage form. In addition, they can not provide any direct spatially-resolved information on potential changes occurring to the solid form (e.g. amorphous to crystalline, polymorphs or solvation-related transformations), which can be extremely important for better understanding the dissolution performance of ASDs.

Due to the outlined limitations of the USP tests, solution-based and solid-based techniques have been developed and employed to characterise the drug release from pharmaceutical products.

## 1.6.1 Solution-based methods

### 1.6.1.1 Quantitative suppressed-water $^1\text{H}$ nuclear magnetic resonance

Quantitative suppressed-water  $^1\text{H}$  NMR is an example of solution-based technique that has been recently employed to obtain additional information on the drug release of pharmaceutical products.<sup>91</sup> For chemical species lacking a UV chromophore (e.g. soluble fillers), or medicines containing more than one active ingredient, quantification can be challenging using UV absorbance data.  $^1\text{H}$  NMR offers high chemical selectivity and therefore is capable of resolving signals from components through differences in their chemical shifts. The increased resolution of NMR reduces the chance of overlapping signals compared to UV. In addition, as  $^1\text{H}$  NMR spectra obtained from a dissolution test can be referenced against a spectrum of a solution with known concentration, quantification is possible.<sup>92,93</sup> An important consideration with  $^1\text{H}$  NMR is that signals from protonated solvents can interfere with the samples. However, high quality spectra can be now easily obtained using water suppression and gradient shimming  $^1\text{H}$  NMR experiments.<sup>91</sup>

## 1.6.2 Solid-based methods

Solid-based techniques have been also developed with strong focus on obtaining in real time and *in situ* spatially-resolved and chemically-detailed information. Methods have included UV imaging,<sup>94-96</sup> IR<sup>97-105</sup> and Raman spectroscopy,<sup>106-112</sup> and also magnetic resonance imaging (MRI).<sup>113-116</sup>

### 1.6.2.1 Ultraviolet imaging

In a UV imaging set-up, the dissolution medium is pumped into a flow-through cell that is equipped with a light source and a charge-coupled device

(CCD) camera chip. UV imaging can provide spatially- and temporally-resolved information, and in addition enables real time dissolution rates to be obtained. In a UV imaging experiment, the intensity of the light passing through a quartz cell is measured as a function of position and time, and therefore absorbance and concentration maps can be generated. Hulse et al. have compared the dissolution rates obtained by UV imaging for  $\alpha$  and  $\gamma$  indomethacin, theophylline anhydrate and hydrate, and ibuprofen free acid and its sodium salt.<sup>94</sup> The ratio in dissolution rate between the  $\alpha$  form over the  $\gamma$  form of indomethacin was found to be approximately 1.7, while that for the anhydrate form over the hydrate form of theophylline was 2.1. A 46.5 fold increase in dissolution rate was observed for the sodium salt of ibuprofen over the free acid form. UV imaging was used in another study to monitor the dissolution behaviour of amlodipine besylate in three different solid forms: amorphous, dihydrate and free base.<sup>95</sup> UV imaging combined with Raman spectroscopy indicated the re-crystallisation of the amorphous form into the monohydrate form. UV imaging has been also employed to study the dissolution of the amorphous both sodium salt and free acid of furosemide compared to the corresponding crystalline forms.<sup>96</sup> The salts were shown to have a higher dissolution rate compared to the free acids. Raman spectroscopy indicated the transformation of amorphous acid into crystalline acid, while the salt forms of furosemide were shown by PLM to convert into a trihydrate form during dissolution.

### 1.6.2.2 Infrared and Raman spectroscopy

IR and Raman spectroscopy used in combination with multivariate data analysis approaches (e.g. multivariate curve resolution (MCR) and principal component analysis (PCA)) can be very useful for mechanistic studies of drug dissolution. Both techniques present high chemical specificity and therefore they can be used to monitor solvent-mediated phase transformations that occur during the dissolution.

Fourier transform (FT) IR has been employed to investigate the drug release mechanisms of testosterone-poly(ethylene oxide) dispersions.<sup>97</sup> Two different types of drug release were observed depending on the drug loading. At low drug loading the dissolution was polymer-controlled, while at higher drug loading the dissolution of the drug was the controlling factor. Kazarian and Chan employed attenuated total reflection (ATR) FT-IR to image the crystallisation of ibuprofen molecularly dispersed in PEG during the dissolution in water.<sup>98</sup> Combining ATR spectroscopy with FT-IR resulted in a method with high both chemical specificity and spatial resolution. They have also built a combined compaction and flow-through cell to study the dissolution of a tablet composed of caffeine and HPMC.<sup>99</sup> The main advantages of this special cell were the good contact between the ATR surface and the sample for improving the quality of the images, and a more controlled water penetration into the compact. In another work by the same group, the combined compaction and flow-through cell was linked to a UV detector to quantify, similarly to the conventional dissolution tests, the amount of niacinamide released from HPMC tablets.<sup>100</sup> Later, ATR FT-IR and UV were employed to evaluate the drug precipitation in buffers at different pH conditions from tablets containing diclofenac sodium and HPMC.<sup>104</sup> In another work, ATR FT-IR and visible macro-photography were employed to evaluate the water ingress fronts into a tablet containing buflomedil pyridoxal phosphate and HPMC.<sup>101</sup> The correct assignment of these fronts was shown to be important for understanding the drug release mechanisms. In a recent work by Keles et al., ATR FT-IR imaging has been used to monitor during dissolution in deuterated water the release of growth hormone (hGH) from poly(lactide-co-glycolide) (PLGA)/polylactic acid (PLA) microparticles and Poloxamer 407 excipient, and to study the effects of  $\gamma$ -radiation on the release kinetics of such system.<sup>102</sup> The  $\gamma$ -radiation was shown to increase the number of oxygenated components in the Poloxamer 407, thus increasing the rate of hydration and leading to a faster and more pronounced initial burst release of hGH. One of the main limitations of IR for investigating the dissolution is that its radiation

is strongly absorbed by the water molecules. However, this can be worked around by integrating only bands for each component which appear distant from the absorption of water, as Kazarian et al. have shown in a number of reports.<sup>103–105</sup>

Raman spectroscopy, unlike IR, is relatively insensitive to water,<sup>117</sup> which is clearly an advantage for testing the dissolution in aqueous environments. One of the key advantages of Raman spectroscopy is the access to the low-wavenumber region that has been demonstrated to be extremely sensitive to differences between amorphous and crystalline forms and among different polymorphic forms.<sup>118–120</sup> The ability to differentiate between amorphous and crystalline forms is particularly relevant as it is known that the physical form of the drug substance can change during the course of the dissolution test, and this can limit the performance.<sup>103,113,121</sup> Aaltonen et al. studied the solvent-mediated phase transformations of theophylline and nitrofurantoin using *in situ* Raman spectroscopy.<sup>106</sup> It was shown that both theophylline and nitrofurantoin anhydrides underwent to a transformation to the corresponding monohydrates, with a decrease in dissolution rate for theophylline. In another work, *in situ* Raman spectroscopy was used to monitor the solid-phase transitions during the dissolution of indomethacin.<sup>107</sup> The decrease in dissolution rate for amorphous indomethacin was shown to be related to the drug re-crystallisation into the  $\alpha$  form. Raman spectroscopy has been also employed to investigate during dissolution the different component distribution and structural changes of extrudates containing theophylline anhydrate, tripalmitin and PEG.<sup>108</sup> It was observed that the lipid structure remained intact, while the water-soluble polymer rapidly dissolved from the matrix, leaving pores that facilitated the water ingress, thus accelerating the drug release. Choi et al. have used Raman spectroscopy to evaluate the distribution and movement of a model drug (tamsulosin HCl dihydrate) during the swelling of three-layer tablets.<sup>109</sup> In another report, *in situ* Raman spectroscopy was used to study the precipitation of dipyrindamole during transfer from a simulated gastric medium into a simulated

intestinal medium.<sup>110</sup> Due to the higher pH of the latter, dipyrindamole precipitated from solution and it was possible to build based on the Raman data a theoretical model of drug nucleation and crystal growth during transfer tests.

Coherent anti-Stokes Raman scattering (CARS) spectroscopy has been also employed to monitor the solid-state changes during the dissolution of pharmaceutical formulations. In CARS, compared to spontaneous Raman spectroscopy, two pulsed lasers are focused on the sample to generate a coherent anti-Stokes signal. CARS requires very specialised equipment, while conventional Raman requires only one laser and is therefore much more readily accessible. Kang et al. have used CARS to characterise the spatial organisation during dissolution of paclitaxel, PEG and PLGA in spray-coated blend films.<sup>111</sup> It was observed that PEG accelerated the burst release of paclitaxel through dissolution of PEG and paclitaxel at the film surface. The release of the drug inside the film was retarded due to the presence of PLGA. In a more recent work, *in situ* CARS combined with UV absorption spectroscopy was used to monitor the solid-state changes in oral dosage forms containing theophylline anhydrate.<sup>112</sup> The CARS results indicated that theophylline anhydrate converted into theophylline monohydrate, resulting in a decrease of the dissolution rate.

### 1.6.2.3 Magnetic resonance imaging

MRI offers relatively low chemical selectivity, measuring the concentration of a particular nucleus, typically hydrogen. However, it is the only technique of those described that can provide three-dimensional information on molecular mobility. In a work by Langham et al.,<sup>113</sup> MRI was used to monitor the physical processes occurring during the dissolution of various compositions of felodipine and copovidone ASDs compacts inside a flow-through cell installed in the MRI magnet. The temporal changes in longer and shorter dimensions of the compacts in one-dimensional cross-sectioned

images were measured to obtain information on the erosion and swelling processes. It was observed that the dissolution of the 5% and 15% drug loadings followed a linear erosion of both the short and long dimensions, indicating a polymer-controlled drug release. In contrast, for the 30% and 50% drug loadings swelling due to hydration was apparent. The residue of the 50% drug loading was recovered after 52 h and shown by XRPD to contain crystalline felodipine, pointing to the drug re-crystallisation. In another work, MRI has been employed to identify morphological details in hydrating HPMC tablets during dissolution.<sup>114</sup> Five different regions were identified, i.e. dry glassy, hydrated solid like, two interface layers and gel layer. These regions were found to be separated by four evolving fronts, i.e. penetration, full hydration, total gelification and apparent erosion.

## 1.7 Motivation and aims of the work

Although ASDs represent a very promising formulation platform for improving the dissolution properties of poorly water-soluble drugs, often this approach fails to achieve the required bioavailability due to the drug re-crystallising during manufacturing, storage as well as dissolution in the GI fluids. The dissolution performance of ASDs is of particular importance as it underpins the *in vivo* efficacy. Gaps in the current knowledge of ASDs include a lack of understanding of the dissolution mechanisms due to a number of processes being involved. The drug re-crystallisation from a supersaturated state in solution or in the solid-state, the formation of nano or microparticles, and also the dissolution behaviour of the carrier itself, contribute to the complexity of the dissolution performance.

Three solid dispersions were employed in this thesis as model systems, which include felodipine, bicalutamide and indomethacin, all poorly soluble drugs, dispersed in a copovidone matrix. Felodipine, bicalutamide and indomethacin all belong to class 2 of the BCS as they are characterised

by low aqueous solubility and high intestinal permeability. Copovidone is a water-soluble polymer which was used in this work in an attempt to improve the dissolution properties of felodipine, bicalutamide and indomethacin. However, as mentioned, the dissolution of these systems can be complicated. In particular, previous studies have shown that the drug-to-polymer ratio strongly affects the dissolution behaviour of ASDs.<sup>87,113</sup> The dissolution performance of all the solid dispersion models was therefore tested as a function of the drug loading. Two drug loadings were prepared for felodipine (5% and 50% w/w), three for bicalutamide (5%, 30% and 50% w/w), and the full range of drug loadings was manufactured for indomethacin (5%, 15%, 30%, 50%, 70% and 90% w/w). In addition, as indomethacin presents a pH-variable solubility and dissolution rate due to its weakly acidic nature ( $pK_a$  of 4.5), the dissolution performance of this drug was also tested as a function of the pH of the dissolution medium (pH 2 and 6.8).

The research detailed in this thesis aims to fill the gaps related to the understanding of the dissolution mechanisms of ASDs and the outlined limitations of the conventional USP apparatuses for testing the dissolution. This was attempted by using Raman spectroscopy as primary analytical technique. Raman spectroscopy provides a number of advantages: i) speed (millisecond acquisition); ii) lack of sensitivity to water; iii) spatial (sub-micron) and spectral resolution; iv) strong chemical specificity; v) ability to readily differentiate between crystalline and amorphous forms. The novelty of this method for testing the dissolution derives from collecting Raman data in real time and *in situ* during the course of the dissolution experiment using a flow-through cell, as will be shown in the study of felodipine (Chapter 3). Raman data were analysed using a novel mathematical approach which derives from the use of concatenated maps to explicitly probe the changes as a function of time as well as space (Chapter 3). The dissolution medium pumped through the flow-through cell can be easily switched to another, for example in the study of indomethacin the dissolution medium

was switched from pH 2 to 6.8 to mimic the stomach and small intestine conditions (Chapter 6). In that study Raman spectroscopy integrated with in-line UV-Vis spectroscopy was also employed to directly relate changes in dissolution behaviour to physicochemical changes that occur to the ASD during the dissolution test. In the studies of bicalutamide the use of a combined suite of state-of-the-art analytical techniques was explored, including an integrated MRI UV-Vis flow cell system and a novel quantitative suppressed-water  $^1\text{H}$  NMR method to complement the Raman data (Chapters 4 and 5). In Chapters 3, 4 and 6 the rotating disk dissolution rate (RDDR) test (a modified version of the conventional intrinsic dissolution rate (IDR) test) was employed for the first time to gain information on the dissolution rates of both the drug and the polymer.

The new knowledge on the drug release mechanisms obtained from Raman spectroscopy and the other complementary techniques could be used to recognise potential risks or benefits of ASDs during dissolution, and enables formulators to design more effective and reliable formulation systems.

# Chapter 2

## Materials and experimental techniques

The aim of this chapter is to provide an overview of the materials and the main experimental techniques employed in this thesis to produce and analyse the ASDs under investigation. In this chapter the theory behind the techniques as well as the reasons for their use will be briefly discussed. Full experimental details will not be discussed in this chapter, but in the “Materials and methods” sections of Chapters 3, 4, 5 and 6.

### 2.1 Materials

#### 2.1.1 Copovidone

Copovidone (Figure 2.1) is a highly water-soluble polymer (solubility higher than  $100 \mu\text{g} \cdot \text{mL}^{-1}$ ),<sup>122</sup> commonly used in the tableting process as a granulating and film forming agent. Copovidone is recognised as a chemical analogue of PVP, which has been employed in several studies to both inhibit the re-crystallisation and improve the dissolution performance of poorly



### 2.1.3 Bicalutamide

Bicalutamide (Figure 2.1) is an important front-line treatment for prostate cancer. It is a non-steroidal anti-androgen that has a low aqueous solubility (lower than  $5 \mu\text{g}\cdot\text{mL}^{-1}$ ) and belongs to class II of the BCS. ASDs of bicalutamide with PVP or PEO have shown significantly enhanced dissolution properties compared to the crystalline material.<sup>52,127</sup> Bicalutamide exists in two known crystalline phases (polymorphs I and II). Form I is currently marketed, form II is metastable and therefore can convert into form I in appropriate conditions (e.g. mechanical treatment, high temperatures).<sup>128</sup> The polymorphic forms of bicalutamide have been thoroughly characterised by Vega et al.<sup>129</sup> They have reported single crystal X-ray structures and shown that low energy form I relates monotropically to metastable form II, i.e. under standard conditions form I is more stable than form II at all temperatures. Due to the different crystal structures, forms I and II have different physicochemical properties. The melting points have been found by Vega et al. to be  $192^\circ\text{C}$  for form I and  $189^\circ\text{C}$  for form II, and form II has been demonstrated to be 2.4 times more water-soluble than form I at room temperature. They have also characterised forms I and II using Raman spectroscopy. They observed several differences between the two polymorphic forms in the fingerprint region because the two polymorphs contain different conformations of bicalutamide. The existence of at least three bicalutamide solid forms with different physicochemical properties, i.e. amorphous, form I and form II, made this compound an interesting poorly soluble drug model for monitoring solid-phase changes during dissolution, as will be detailed in Chapters 4 and 5.

### 2.1.4 Indomethacin

Indomethacin (Figure 2.1) is a NSAID drug widely used for pain relief. It is poorly water-soluble and belongs to class 2 of the BCS.<sup>130</sup> Indomethacin formulated as pure amorphous material or as ASD has shown significantly

improved dissolution properties compared to the crystalline form.<sup>20,55,131–133</sup> Due to its weakly acidic nature ( $\text{pK}_a$  of 4.5), indomethacin presents a pH-dependent solubility and dissolution rate.<sup>55,132,134–136</sup> The aqueous solubility of indomethacin has been reported to increase from  $1.5 \mu\text{g} \cdot \text{mL}^{-1}$  at pH 1.2 to  $105.2 \mu\text{g} \cdot \text{mL}^{-1}$  at pH 7.4.<sup>137</sup> Due to the significant change in aqueous solubility between acidic to neutral/alkaline pH conditions, indomethacin represents an ideal model compound for studying the effects of the environmental pH on the dissolution performance, as will be discussed further in Chapter 6.

## 2.2 Experimental techniques

### 2.2.1 Hot melt extrusion

HME, as previously described, is a fusion method employed to manufacture ASDs. An extruder consists of three sections: the feed zone, the compression zone and the metering zone (Figure 2.2).<sup>6,45</sup> After the feeding stage, the material is moved through the extruder via one or two rotating screws which are located inside a cylindrical barrel. At this stage, the material is melted, homogenised and compressed. In the metering zone the thickness of the product can be controlled by stabilisation of the flow of the extrudate. In most of extruders the sections in the barrel are interchangeable to allow different configurations to be used and therefore more flexibility during manufacturing. The molten material is then passed through the die plate and, following the exit from the die, it is cooled and subject to further down-stream processing (e.g. milling). The shape of the final product is determined by the design of the die plate. HME has been used to prepare ASDs in a number of previous studies, several of which used felodipine, bicalutamide and indomethacin as drug models.<sup>6,45,52,126,127,133</sup>

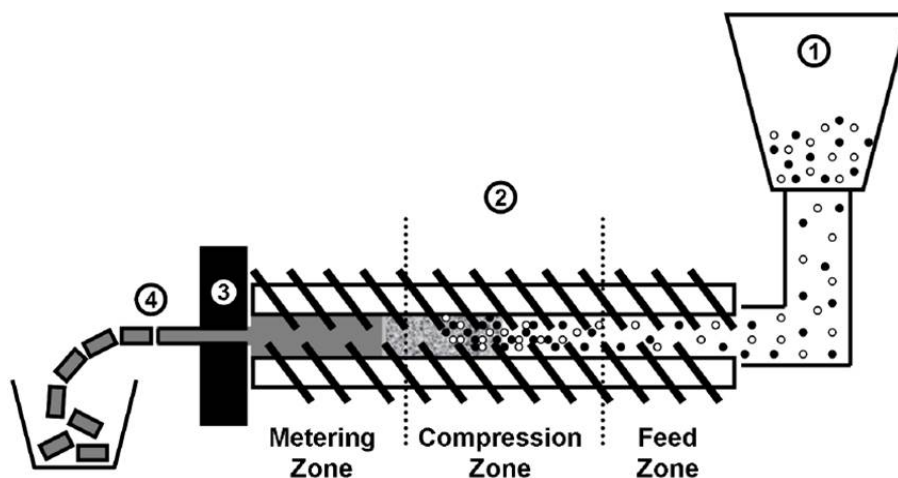


FIGURE 2.2: Schematic representation of a common hot melt extruder.

### 2.2.2 X-ray powder diffraction

XRPD is a powerful technique for determining the crystal packing of materials and the level of crystallinity in ASDs. The wavelength of X-rays is of the same magnitude as the interatomic spacings of molecules and therefore X-ray diffraction is possible. However, for diffracted X-rays to be intense enough for detection, a constructive interference according to the Bragg's law must occur.<sup>138</sup> W. L. Bragg considered the X-rays diffraction from a set of different crystal planes characterised by different positions ( $h, k, l$ ). For a constructive interference to occur, the path difference between the beams must differ by an integer number of wavelengths. In other words, the Bragg's law (Equation 2.1) needs to be satisfied:

$$n\lambda = 2d_{hkl}\sin\theta \quad (2.1)$$

where  $n$  is an integer,  $\lambda$  is the wavelength of the incident light,  $d$  is the distance between the planes and  $\theta$  is the incident angle with respect to the crystal planes. Based on this, the diffractograms of a crystalline material are characterised by a number of peaks which are unique to its crystal structure. In contrast, amorphous materials can not fulfil the Bragg condition

as they do not possess the regular repeating structures which are present in the crystalline materials. As a result, the diffractograms of amorphous materials do not contain the Bragg peaks, but they are characterised by a broad halo.

## 2.2.3 Raman spectroscopy

### 2.2.3.1 Principles of Raman spectroscopy

The Raman effect was first reported in 1928 by Raman and Krishnan and can be described as the inelastic scattering of light from a sample.<sup>139</sup> In inelastic scattering the frequency and energy of photons in monochromatic light change upon interaction with a sample. As shown in Figure 2.3, when a sample is irradiated, molecules are promoted to a virtual state. When molecules relax, they return to the ground state emitting light with the same frequency as the excitation source (Rayleigh scattering) or with a different frequency (Raman scattering). Raman scattering can be either Stokes (i.e. molecules are initially in the ground state) or anti-Stokes (i.e. molecules are initially in the excited state) scattering. In Stokes scattering part of the energy of the photon is transferred to the molecular vibration and the resulting frequency of the scattered light is reduced. In anti-Stokes scattering the excess of energy of the excited molecular vibration is released and as a consequence the frequency of the scattered light is increased. Rayleigh scattering is the more probable event (scattered intensity is approximately  $10^{-3}$  less than that of the original incident radiation) compared to Raman scattering (intensity is approximately  $10^{-6}$  less than that of the incident light for strong Raman scattering). In terms of Raman scattering, the intensity ratio between Stokes and anti-Stokes scattering depends on the absolute temperature of the sample. Since most molecules exist in the ground state at ambient temperature (Boltzmann equation),<sup>140</sup> Stokes scattering is a much stronger effect compared to anti-Stokes scattering.

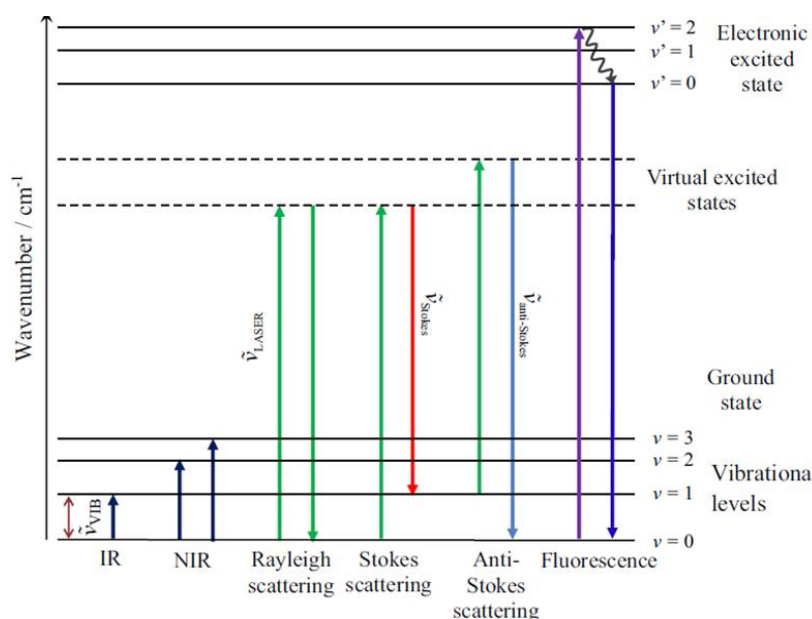


FIGURE 2.3: Scheme of the energy levels changes in IR, near-IR, Rayleigh scattering, Raman scattering and fluorescence.<sup>139</sup>

Raman spectroscopy therefore measures the vibrational energies of the molecules in a sample, which in turn are related to the type of chemical bonds. IR spectroscopy probes the same range of energies as Raman, however it is based on absorption rather than scattering. The frequencies of the molecular vibrations in IR and Raman spectra depend on the masses of the atoms and the strength of their chemical bonds. In addition, the selection rules for IR transitions differ from Raman. A vibration is IR active when there is a change in dipole moment, and is Raman active when there is a change in polarisability. The difference in selection rules means that strong IR vibrations are not necessarily intense in Raman spectra and *vice versa*. For example, water has a strong dipole moment, thus its IR spectrum is intense, whilst the electrons are not easily polarised and as a consequence the Raman scattering is weak. Another important consideration is that most APIs contain  $\pi$ -electrons which are easily polarised, and therefore they show strong Raman scattering. In contrast, excipients are primarily  $\sigma$ -bonded molecules with weak Raman scattering. This can become important, for example, when detecting low levels of drug crystallinity in multi-component pharmaceutical products.<sup>67</sup>

### 2.2.3.2 Raman microscopy

Raman microscopy refers to the combination of Raman spectroscopy and optical microscopy. As schematically reported in Figure 2.4, the excitation laser beam is directed onto the sample through the objective lens, and the scattered light is collected using the same objective (180° back-scattered configuration). The Raman light is then directed into a spectrograph and diffracted across a CCD detector. The use of pinhole apertures situated between the objective and the detector in a confocal microscope allows depth of field to be controlled, by removing unwanted signal from outside the focal point (Figure 2.5). Using a confocal approach may also help to reduce the fluorescence emission.

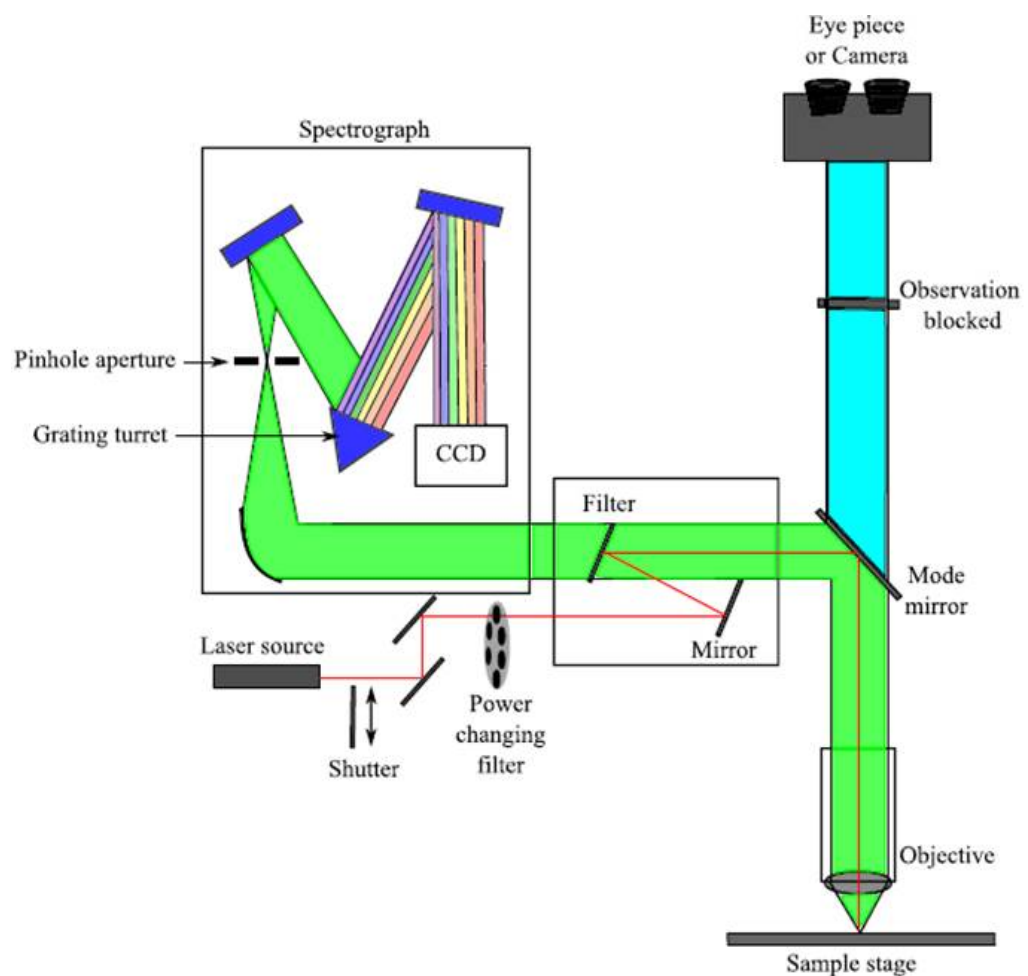


FIGURE 2.4: Diagram of a CCD-based Raman microscope.<sup>139</sup>

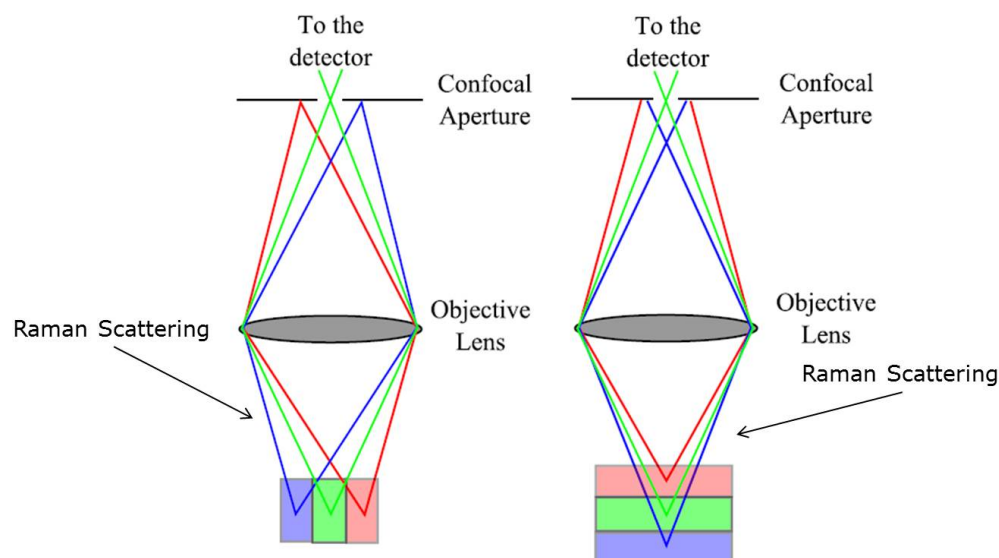


FIGURE 2.5: Scheme showing the effect of the confocal aperture on the Raman scattering.<sup>139</sup>

The laser choice is very important and can have a major impact on the spatial resolution and fluorescence. The diameter of the laser spot can be described using the Abbe equation (Equation 2.2):

$$d = \frac{\lambda}{2\text{NA}} \quad (2.2)$$

in which  $d$  is the laser spot diameter,  $\lambda$  is the laser wavelength and NA is the numerical aperture of the objective. Therefore, using a laser with a longer wavelength will generate a larger spot diameter. The use of a longer wavelength laser (e.g. near-IR) will also reduce fluorescence, by preventing excitation to the higher electronic energy state.

### 2.2.3.3 Raman mapping

Raman mapping involves collecting Raman spectra from a section of a surface. A Raman spectrum is collected from a specific point in coordinate space, then the sample is moved and another spectrum is acquired. This

method is called point-by-point mapping (Figure 2.6a).<sup>139,141</sup> The experiment can be made faster by using an irradiating line rather than a point (line-scanning, Figure 2.6b). This can be achieved using cylindrical optics or moving mirrors.

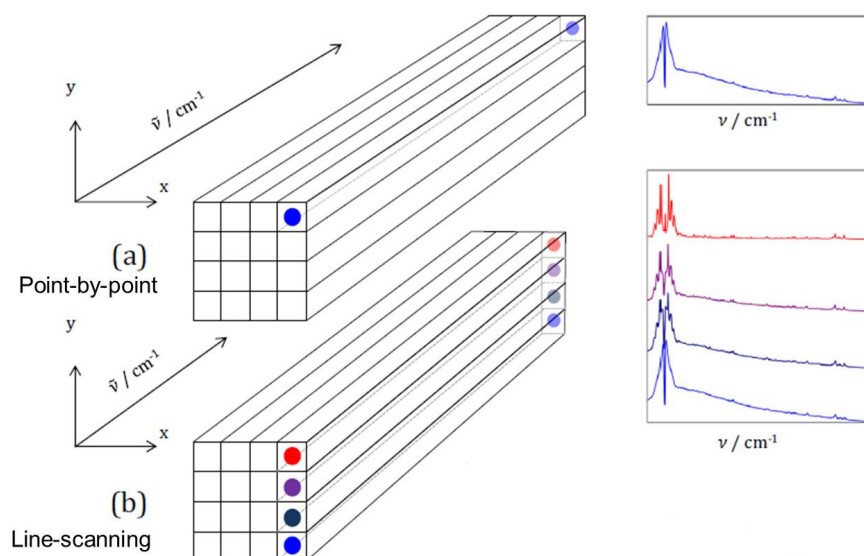


FIGURE 2.6: Point-by-point (a) and line-scanning (b) Raman mapping.<sup>139</sup>

#### 2.2.3.4 Data analysis

The amount of data generated using Raman spectroscopy/microscopy can be rather large (tens/hundreds of thousands of spectra), thus it is necessary to use appropriate statistical analyses to obtain unambiguous and meaningful outputs. Data analysis can be divided into two main stages: data pre-processing and processing.

**Pre-processing** Data pre-processing consists of reducing interference effects from, for instance, sample focus or detector artefacts. This step is of particular importance for multivariate data analysis techniques. A multivariate analysis without adequate pre-processing will likely result in models containing differences associated to the experimental set-up (e.g. sample focus) rather than changes in chemical composition. Variance-scaling the

data is a simple way to reduce the effect of variations in Raman scattering efficiency.<sup>117</sup> The CCD detectors are able to detect subatomic particles which can give a far more intense signal than Raman scattering (cosmic events). These signals appear as sharp and very narrow spikes that can be automatically removed using most commercial software.

**Data processing** Data processing can be done using univariate or multivariate methods. Univariate methods consist in selecting a band of the chemical of interest in the spectral region which is not masked by other component spectral features to determine the spatial distribution of that chemical entity.<sup>142–145</sup> The band width/position can be used, for example, to follow the potential drug re-crystallisation during manufacturing or storage.<sup>142,146</sup> The ratio between two different bands, i.e. bivariate analysis, can also be used to give an insight into how the relative amount of two chemicals changes across the surface of the same sample.<sup>147–149</sup> A major drawback of the univariate approach is that selecting a specific band in multi-component systems can be challenging due to overlapping. In addition, prior knowledge on the chemical composition of the formulation is required. Finally, as most of the data are not used, important information can be lost.

The main advantage of multivariate analysis is that the false-colour images produced are based on the entire spectrum and not on one single band. PCA<sup>119,120,150–152</sup> and MCR-ALS (alternating least-squares)<sup>152–154</sup> are established multivariate analysis techniques to deconvolute Raman data from pharmaceutical samples. PCA operates through rotation of a large number of data onto a smaller number of orthogonal variables, known as principal components (PCs).<sup>151</sup> The first of these components, i.e. PC1, accounts for the greatest amount of variance between datasets, and the subsequent PCs correspond to increasingly smaller amount of variance. Each PC is characterised by a single value known as score and a loading which comprises as many values as in the original spectrum. PCA does not require a

definition of the number of components, however the loadings can be both positive or negative and therefore the spectral interpretation may result difficult. The MCR-ALS method attempts to deconvolute the data into the individual spectral components and their concentration. This can be achieved through an initial estimation of the spectral and concentration matrices followed by an iterative optimisation using the ALS algorithm.<sup>155,156</sup> Constraints such as non-negativity, unimodality and closure are commonly employed to reduce the ambiguity linked to the MCR results and thus to generate meaningful solutions. Non-negativity forces concentration or response profiles to be positive (e.g. UV absorption, mass spectra). Unimodality allows profiles to have a single maximum (e.g. chromatographic peaks). Finally, closure or mass balance forces concentration profiles to add up to a certain constant value. MCR-ALS is the main statistical method employed in this work to analyse Raman data as it provides more readily interpretable spectral traces compared to PCA.

#### **2.2.4 Quantitative suppressed-water $^1\text{H}$ nuclear magnetic resonance spectroscopy**

NMR is an analytical technique commonly employed to elucidate the structure of small and macro molecules. NMR can be also employed for quantitative analysis in in-line processes such as reaction monitoring.<sup>93</sup> *In situ* reaction monitoring by NMR consists of following the reaction progress with the ultimate goal to optimise such process in terms of predictability and reliability. The most important feature of quantitative NMR is that the peak area in the NMR spectrum is directly proportional to the number of nuclei responsible for that particular resonance.<sup>92</sup> Quantitative analysis requires a reference compound for measuring the concentration of the analyte. This can be done using internal or external standards. An internal standard is a compound with known concentration or weight that is dissolved in a known volume of analyte solution. The main challenges of internal standards are

the potential insufficient solubility in a particular solvent, peak overlapping and chemical interactions with the analyte. External standards can be a valid alternative to internal standards as they are not added to the solution. External standards provide a clear advantage for monitoring in-line processes as it is possible to quantify samples generated from a process (e.g. chemical reaction, dissolution) against a sample of known concentration.<sup>91</sup> Another important consideration for quantitative NMR is that the solvents in most in-line processes are not deuterated, therefore the signals of the solvents can obscure the spectral features of the analyte, compromising the analysis. Solvent-suppression techniques can be employed to preserve the signals of the analyte. Solvent-suppression can be done by perturbing the solvent magnetisation (e.g. by pre-saturation) or using selective excitation techniques such as WET (water suppression by  $T_1$  effect) or WATERGATE (water suppression by gradient tailored excitation).<sup>93</sup>

### 2.2.5 Magnetic resonance imaging

MRI is a technique commonly employed in clinical diagnosis due to its ability to differentiate between soft tissues. However, in the last two decades there has been a growing body of work describing the use of MRI to study the dissolution of pharmaceutical formulations.<sup>116,157,158</sup> The magnetisation of the nuclei after excitation by a radio-frequency pulse returns to an equilibrium state via relaxation. The relaxation event is characterised by two relaxation times: the spin lattice relaxation time ( $T_1$ ) and the spin-spin relaxation time ( $T_2$ ).  $T_1$  describes the exponential recovery of the equilibrium, while  $T_2$  describes the exponential decay of the NMR signal.  $T_2$  strongly depends on the molecular mobility. As shown in Figure 2.7, protons in a solid environment have a faster  $T_2$  relaxation time and therefore the solid materials appear dark in the images. In contrast, protons in solution have a significantly slower  $T_2$  relaxation time and thereby they generate

a bright image. Protons in a hydrating layer give an intermediate brightness. MRI has been used to assess and quantify the dimensional properties (e.g. thickness, area, volume) of the water movement and its effects on the polymeric matrix (e.g. gelation, swelling, erosion).<sup>113,115,116,157</sup>

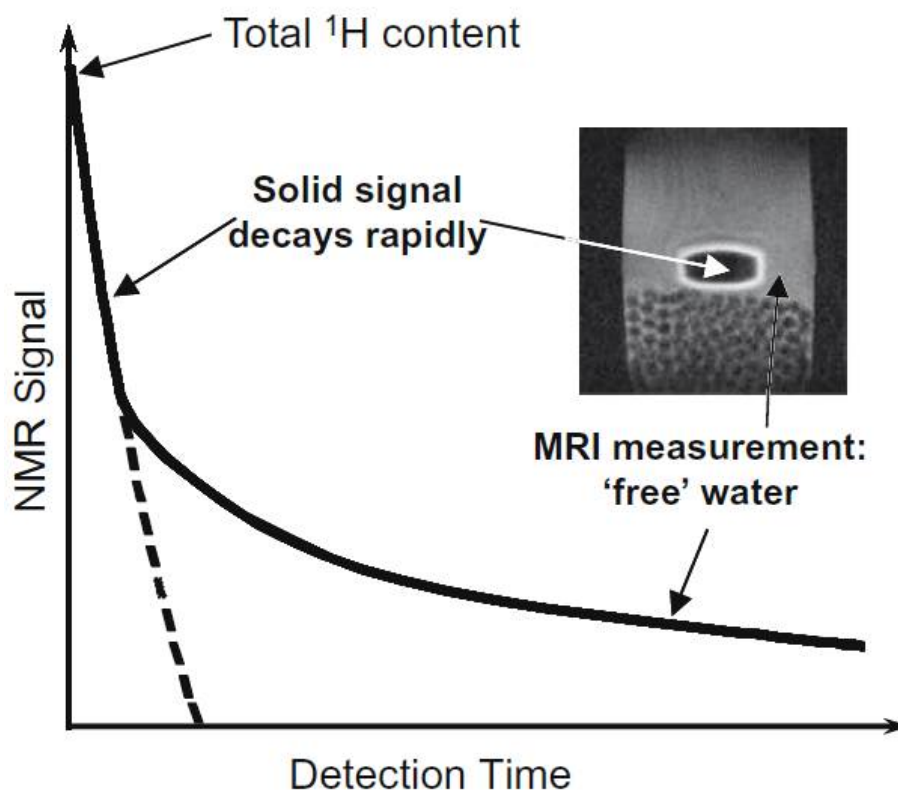


FIGURE 2.7: Scheme showing the decay of the NMR signal after excitation by a radio-frequency pulse.<sup>158</sup>

## 2.2.6 Rotating disk dissolution rate test

The intrinsic dissolution rate (IDR) test is an important screening tool which has been widely used in biopharmaceutics for measuring the dissolution rate of pure active ingredients.<sup>159–161</sup>

The IDR test requires far less material than a traditional USP dissolution test. The IDR is defined as the dissolution rate of a pure active substance, where the conditions of surface area, temperature, agitation, medium pH and ionic strength are all constant.<sup>90,162</sup> The IDR is commonly measured using the rotating disk system, also known as “Wood’s apparatus”. The

system includes a punch and a matrix (die) with a cavity of known surface area for placing the drug. The system is immersed in the dissolution medium in a conventional USP dissolution bath and rotated at a constant rate (Figure 2.8). IDR measurements yield a dissolution rate normalised to the exposed surface area of the material. Formally, IDR applies only to pure drug substances. In this thesis, the IDR concept has been extended to formulations. By analogy with the disk IDR, a “rotating disk dissolution rate” (RDDR) was defined. By simply coupling an IDR apparatus to a HPLC system, the partial RDDR of both the drug substance and the excipients (in the present case copovidone) can be simultaneously measured and compared for different formulations. The dissolution profile of the polymeric carrier can provide valuable information in the case of binary systems such as ASDs, as the carrier has been shown to significantly affect the dissolution performance of poorly soluble active ingredients.<sup>20,87,88,163</sup>



FIGURE 2.8: Rotating disk system in the dissolution equipment.

# Chapter 3

## Raman mapping to understand the dissolution performance of amorphous felodipine extrudates

### 3.1 Introduction

As discussed in Chapter 1, despite the large number of works in literature reporting the dissolution enhancements of ASDs compared to the free drugs, the dissolution mechanisms are still not fully understood. Obtaining a good dissolution profile is extremely important as it directly influences the amount of drug available for absorption, i.e. oral bioavailability.

In this chapter, felodipine and copovidone ASDs were used as a model system to investigate the dissolution mechanisms using Raman spectroscopy. Previous studies have shown that the dissolution properties of poorly water-soluble felodipine can be enhanced by using ASDs.<sup>50,60,113,123-126</sup> In one of these studies,<sup>113</sup> a combined MRI UV-Vis flow-through cell system was employed to test the dissolution performance of felodipine:copovidone ASDs

prepared in different compositions (5%, 15%, 30% and 50% w/w) using spray drying. Erosion and dissolution were observed for the low drug-loaded compacts (5% and 15%), pointing to a polymer-controlled dissolution process. In contrast, for the high drug-loaded compacts (30% and 50%) the water ingress was much slower and the physical behaviour was characterised by swelling rather than erosion, pointing to a dissolution performance dependent on the low water solubility of felodipine. The 50% drug-loaded compact remained essentially intact at the end of the test and the residue was shown by XRPD to contain crystalline felodipine.

The dissolution performance of felodipine-copovidone ASDs was investigated as a function of the drug loading (5% and 50%), with the aim of studying the effects of increasing the amount of active ingredient on the dissolution mechanisms. Real time *in situ* Raman mapping was employed as primary technique in an attempt to gain additional spatially-detailed chemical information during dissolution. The RDDR test was also used to simultaneously track the dissolution trend of both the drug and the polymer from the ASD.

## **3.2 Materials and methods**

### **3.2.1 Materials**

Crystalline felodipine was provided by AstraZeneca (Macclesfield, United Kingdom). Copovidone was supplied by BASF (Ludwigshafen, Germany). Both materials were used as received, without any further purification.

### 3.2.2 Preparation of the amorphous form of felodipine and the extrudates

The amorphous form of felodipine was obtained by heating the drug as received in the oven to 160 °C and, after melting, cooling back to room temperature. Raman spectroscopy confirmed the formation of the amorphous form and the absence of crystalline material, as will be shown in Section 3.3.3.1. 5% and 50% drug-loaded extrudates of felodipine in copovidone were prepared using a co-rotating twin-screw extruder (Thermo Scientific HAAKE MiniLab II). Felodipine and copovidone were pre-mixed for 20 min in a Turbula T2F mixer (Willy A. Bachofen AG Mashinefabrik). The extruder was manually fed with the blends. The screw speed was set to 150 rpm and the temperature to 160 °C. The extrudates with *spaghetti* shape were then collected, cooled to room temperature and manually milled with a T&G CrushGrind mill to fine powder. XRPD confirmed the formation of the amorphous form within the extrudates and the absence of crystalline material (Figure A.1 of the Appendix A).

### 3.2.3 Analytical methods

#### 3.2.3.1 X-ray powder diffraction

XRPD patterns were obtained using a PANalytical CubiX PRO diffractometer. Samples were spun at 30 rpm and exposed to a Cu-K $\alpha$  radiation at a voltage of 45 kV and a current of 40 mA. After being smeared onto the holder, samples were scanned from 2° to 40° 2 $\theta$ , with a 25 s exposure per 0.02° 2 $\theta$  increment.

#### 3.2.3.2 Rotating disk dissolution rate test

RDDR testing was carried on using the “Wood’s apparatus”. The die cavity has a diameter of 8 mm with subsequent exposed sample surface area

of approximately  $0.5 \text{ cm}^2$ . About 250 mg of extrudate powder was compressed under a compression force of *ca.* 20 kN using a manual IR press (Specac). The experiment was performed in a Sotax AT7 semi-automated dissolution bath equipped with an automated sample collector. Compressed disks were immersed in 500 mL of deionised water at  $37 \text{ }^\circ\text{C}$  ( $\pm 0.5$ ), at 100 rpm rotational speed. The automated sample collector removed aliquots of sample from the dissolution medium at regular time intervals over 120 min. The samples were then analysed by HPLC. Both the experiments for the 5% and 50% extrudates were performed in triplicate. Analysis was carried out using an Agilent 1100 HPLC with UV detection at 210 nm, equipped with an Agilent PLRP-S 300 Å  $3 \mu\text{m}$  50 mm column (polystyrene/divinylbenzene stationary phase). The flow rate was set to  $1 \text{ mL}\cdot\text{min}^{-1}$  and the temperature of the column was kept at  $40 \text{ }^\circ\text{C}$ . A linear gradient elution was used starting at 40% acetonitrile/60% deionised water and ending at 90% acetonitrile/10% deionised water after 3.5 min, with chromatograms collected up to 5 min. A series of standard solutions of felodipine and copovidone were prepared to generate a calibration curve covering the concentration range of the dissolved sample. The partial RDDR of both the drug and the polymer was calculated applying linear regression analysis using the first 20 min time period, where the trend is linear, in accordance with Pharmacopoeia procedures.<sup>90,162</sup> The partial RDDR of the material tested was determined from the slope of the regression line.

### 3.2.3.3 Raman spectroscopy

The dissolution performance of compressed extrudate powder was investigated. Circular compacts with a diameter of 5 mm and a weight of approximately 50 mg were prepared with a manual IR press (Specac) using a compression force of *ca.* 20 kN. The dissolution test was performed in a flow cell, which is illustrated in Figure 3.1.

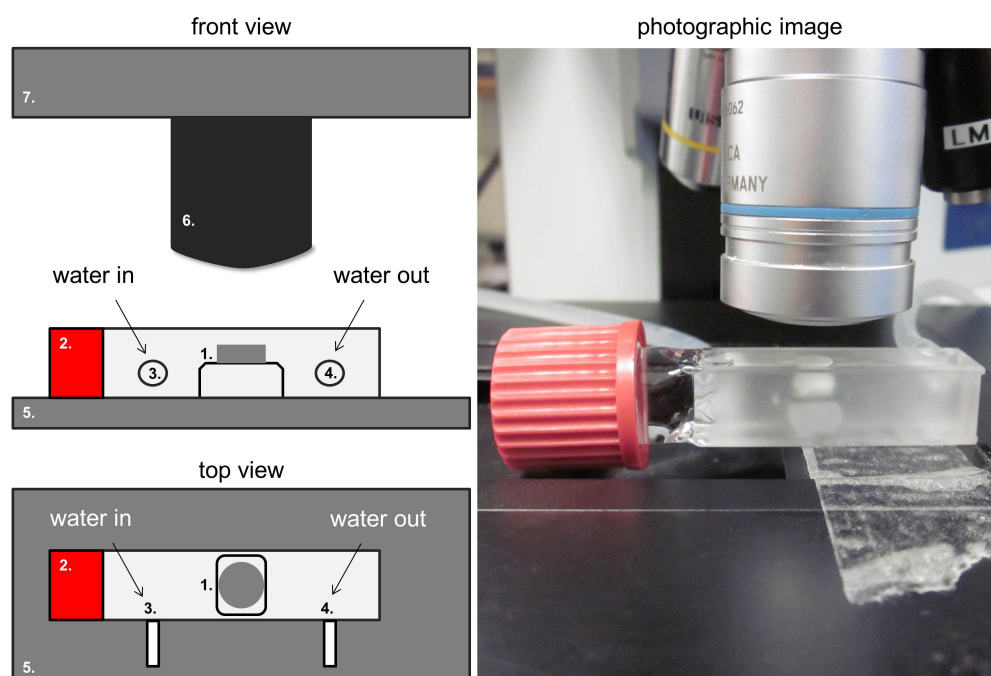


FIGURE 3.1: Schematic diagram and photographic image of the flow cell employed in the Raman and optical imaging experiments. The compact (1) can be placed in the flow cell due to the presence of a removable sealing cap (2). Two small apertures (3 and 4) allow a continuous flow of the dissolution medium. The flow cell is placed on the automated xyz stage (5) under the objective (6) of the Raman microscope (7).

Deionised water was used as dissolution medium and the flow rate was set to  $10 \text{ mL} \cdot \text{min}^{-1}$ . The flow cell was placed under the objective of the Raman microscope and data were collected as a function of time using a Horiba LabRAM HR confocal microscope/spectrometer. The system has an automated xyz stage (Märzhäuser) for mapping. In all the experiments, a near-IR laser (785 nm) of 250 mW power was employed. Spectra were acquired using a  $50\times$  objective and a  $300 \mu\text{m}$  confocal hole. A 600 lines/mm rotatable diffraction grating along a path length of 800 mm was used to simultaneously scan a range of Raman shifts. Raman spectra were collected using a SYNAPSE CCD detector (1024 pixels). During the dissolution experiment, before each map being acquired, the z-axis position of the sample was adjusted to maximise the Raman signal. For both extrudates (5% and 50% felodipine), spectra were obtained mapping an area of  $500 \times 500 \mu\text{m}$  with a grid spacing of  $50 \mu\text{m}$  along both x-axis and y-axis, a total of

121 spectra per map. As each individual spectrum was collected for 1 s, repeated once in order to automatically remove the spikes due to cosmic rays, the whole map required only 5 min. For the 5% extrudate compact, eight maps were acquired across a 70 min time frame in the spectral range from 1100 to 1750  $\text{cm}^{-1}$  (fingerprint region). For the 50% extrudate compact, eight maps were acquired over 1705 min (28 h 25 min) in the phonon-mode (40–400  $\text{cm}^{-1}$ ) and fingerprint (1100–1750  $\text{cm}^{-1}$ ) regions using a fixed grating to allow relatively rapid mapping. In the latter case, the phonon-mode range was also scanned because it is extremely sensitive to the different solid forms (amorphous, crystalline, *etc.*) and therefore the potential drug re-crystallisation can be readily detected.<sup>119,120</sup> All the spectra from each map were integrated to produce a single averaged spectrum corresponding to each time point. In this way, it was possible to determine any spectral changes occurring during the dissolution test.

To obtain spatially-resolved information from the 50% extrudate, the dissolution experiment was repeated increasing significantly the spatial resolution. Seven maps were acquired over 1705 min (28 h 25 min) in the spectral range between 1100 and 1750  $\text{cm}^{-1}$ , across a  $500 \times 1000 \mu\text{m}$  area at a grid spacing of 15  $\mu\text{m}$  along the x-axis, and 30  $\mu\text{m}$  along the y-axis, a total of 1156 spectra per map. As the data acquisition time was 2 s for each spectrum, repeated once, each map required 1.5 h for acquisition. False colour maps were generated using MCR. A single data matrix, comprising all the spectra collected across the entire dissolution experiment (8092 spectra), was produced in order to probe changes as a function of both xy-position and time. Numerical codes for statistical analyses were written in the “R” language, which is open-source and freely available.<sup>164</sup> Data were scaled prior to analysis and plotting using variance-scaling standard methods, as per standard practice to reduce the effect of variability in Raman scattering efficiency.<sup>117</sup> For MCR analysis, the “ALS-MCR” module was employed, while hierarchical agglomerative clustering (HAC) is part of the standard package in R. All numerical routines along with the raw data have

been published.<sup>165</sup>

#### 3.2.3.4 Optical imaging

Photographic images of the compact during the dissolution test were taken at regular time intervals using a CoolSNAP-Pro CF camera (Media Cybernetics) equipped with a Nikon AF Micro NIKKOR 60 mm lens. The same experimental set-up described in Section 3.2.3.3 was used, with the flow cell placed under the camera instead of the Raman microscope. For the dissolution test of the 50% extrudate, the “imgThreshold” function part of the “biOps” package in R was employed to count the number of pixels above a pre-defined colour threshold of the images collected during the dissolution experiment.<sup>164</sup> In this way, it was possible to focus only on the pixels of the compact and build a trend which shows how the surface area of the compact changes as a function of time.

### 3.3 Results and discussion

#### 3.3.1 Optical imaging

Before commencing a full discussion of the RDDR and Raman data, it is important to observe the optical images taken through the dissolution experiment for the 5% and 50% drug-loaded extrudates (Figure 3.2). Prior to the dissolution test, both extrudates appear similar, being yellowish materials. It is important to notice the different experimental time-scale used for the two extrudates.

The 5% extrudate dissolution experiment was carried out for 80 min after which time the images show that the compact is completely dissolved. For the 50% drug-loaded extrudate, the time-scale was significantly longer.

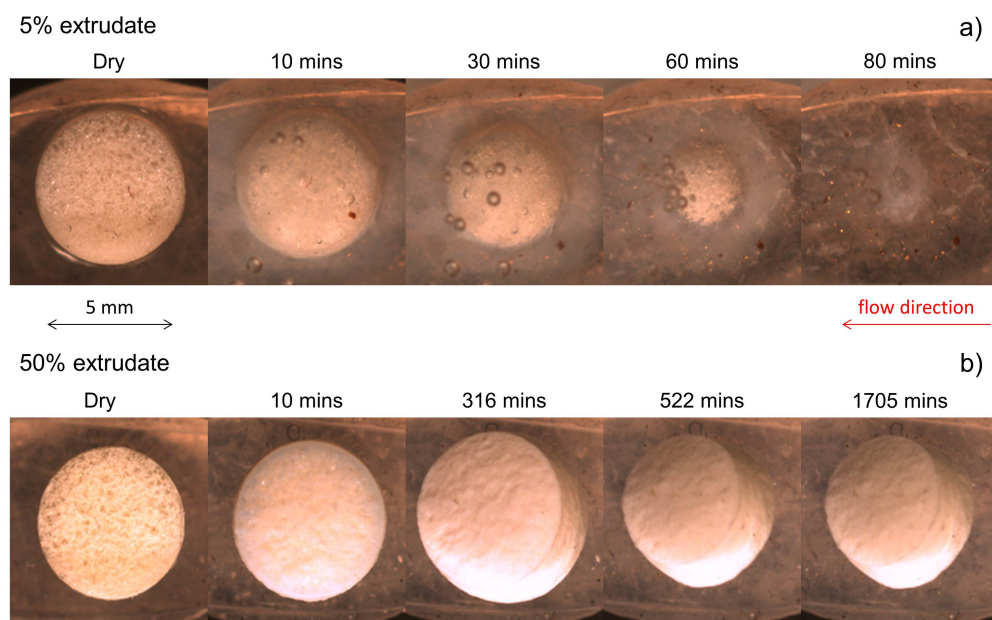


FIGURE 3.2: Optical images taken through the dissolution experiment of the 5% extrudate (a) and 50% extrudate (b).

In total, the compact was observed in the flow cell for 1705 min, remaining intact even after the end of this period. An in depth observation of the images from the 50% extrudate shows that the compact swells and increases in size during the first 316 min, then slightly reduces and remains intact until the end of the experiment. This suggests that the initial hydration leads to swelling of the compact rather than to dissolution/erosion, due to the high content of poorly water-soluble felodipine in the extrudate (images until 316 min). This behaviour was previously described by Langham et al.<sup>113</sup> In Figure 7 of their paper, they reported MRI sequences showing that the 50% felodipine-loaded spray-dried material swells as a result of water ingress from the dissolution medium. The visual observation of the optical images of the 50% extrudate is confirmed by the trend generated by measuring the surface area of the compact during the dissolution test (Figure 3.3). The trend is characterised by an increase in surface area until 316 min, which corresponds to the observed increase in the compact size. Following this, the surface area decreases with the rate of decrease falling to near-zero between 1093 and 1705 min, confirming that the size of the

compact reduces after an initial swelling. The reduction of the compact size after an initial swelling was not previously seen in the MRI images reported by Langham et al.<sup>113</sup> This change in behaviour may be related to the different conditions during preparation via HME compared to spray drying (e.g. high temperatures, absence of solvents) which may affect the final physicochemical properties of the ASDs and thus their performance in aqueous media.

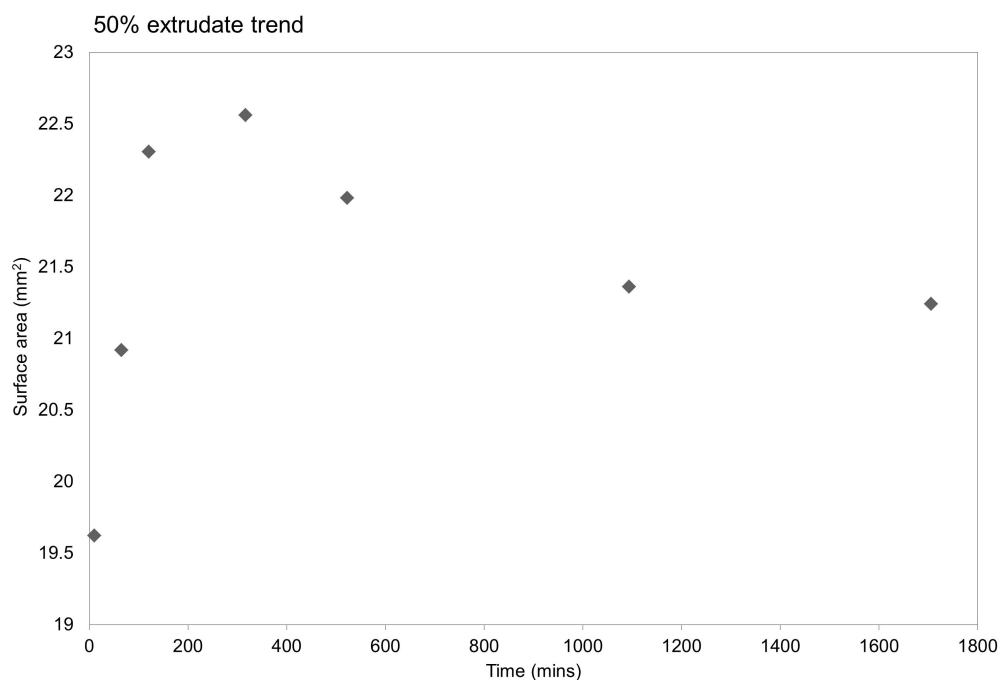


FIGURE 3.3: Trend obtained by plotting the surface area of the 50% extrudate compact in water *vs.* time.

### 3.3.2 Rotating disk dissolution rate test

The dissolution rate values for the 5% and 50% drug-loaded extrudates are summarised in Table 3.1, while the dissolution profiles are presented in Figure 3.4.

Looking at the formulation with 5% drug loading, the partial RDDR value for felodipine is  $0.17 \text{ mg}/(\text{min} \cdot \text{cm}^2)$ , while the partial RDDR for copovidone is  $3.10 \text{ mg}/(\text{min} \cdot \text{cm}^2)$ .

	RDDR, mg/(min · cm <sup>2</sup> )			Index of performance
	Felodipine	Copovidone	Total	
5% extrudate	0.17 (±0.02)	3.10 (±0.43)	3.26 (±0.43)	1.03 (±0.18)
50% extrudate	0.01 (±0.01)	0.25 (±0.01)	0.26 (±0.01)	0.07 (±0.08)

TABLE 3.1: Partial RDDR values of felodipine and copovidone for the 5% and 50% extrudates, along with the index of performance.

The IDR value of pure crystalline felodipine has been previously found to be 0.00064 mg/(min · cm<sup>2</sup>) in pH 6.5 FaSSIF medium, so in comparison the 5% extrudate exhibits approximately a 265 fold increase in dissolution rate.<sup>161</sup> The significant improvement in dissolution is concurrent with literature on felodipine ASDs.<sup>126</sup>

The dissolution rate of the drug and the polymer allows an index of dissolution performance to be readily calculated. This essentially shows how the two components of the extrudate behave during the dissolution process. The index of performance was obtained dividing the partial RDDR value of felodipine by the total RDDR value of the extrudate (felodipine plus copovidone) and then normalising by the felodipine mass fraction (Equation 3.1):

$$\text{Index of performance} = \frac{\text{Partial RDDR drug} / \text{Total RDDR}}{\text{drug mass fraction}} \quad (3.1)$$

The index of performance for the low drug-loaded extrudate results in a value of approximately 1, indicating that felodipine and copovidone have the same dissolution trend and thus they effectively dissolve as a single entity, the molecular dispersion of felodipine in copovidone. Given the very low aqueous solubility of felodipine, the release of the 5% extrudate is clearly dependent on high water-soluble copovidone.

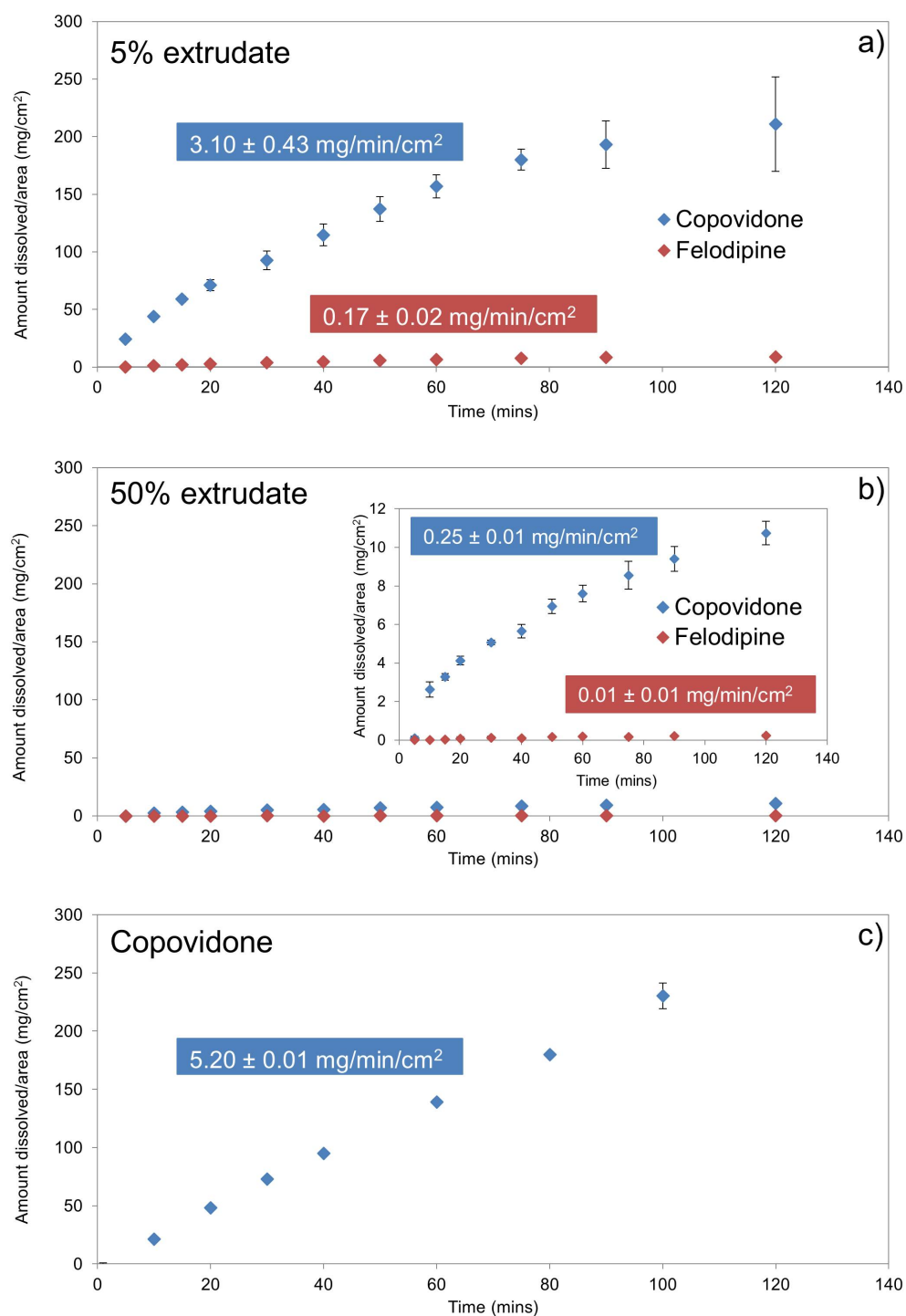


FIGURE 3.4: Dissolution profiles of the 5% extrudate in water (a), 50% extrudate in water (b) and pure copovidone in pH 6.8 blank FaSSIF medium (c).

Turning now to the extrudate with high drug loading, it is immediately evident that both felodipine and copovidone have partial RDDR values significantly lower when compared to those calculated for the 5% extrudate (Table 3.1). The index of performance is also very low (0.07), indicating that the dissolution rates of felodipine and copovidone are in this case very different, suggesting that the drug and the polymer are not behaving as a single entity but as two separate components. Compared to the IDR value of pure extruded copovidone ( $5.20 \text{ mg}/(\text{min} \cdot \text{cm}^2)$  in pH 6.8 blank FaSSIF medium, Figure 3.4c), copovidone present in the 50% extrudate shows approximately a 21 fold decrease in dissolution rate. RDDR data suggest that the drug release is felodipine-dependent, where the low solubility in water and high hydrophobicity of the drug contribute to decrease the wettability and to slow the water uptake in the material.

Summarising, the 5% drug-loaded extrudate showed a polymer-dependent dissolution behaviour with felodipine dissolving simultaneously with copovidone. For the 50% extrudate, the rate of felodipine released is considerably lower than that observed for the 5% drug-loaded extrudate. Although the RDDR test gives a comprehensive explanation on the dissolution trend observed for the low drug-loaded formulation, it does not clearly explain why felodipine shows a very low dissolution rate for the 50% extrudate. To obtain a better understanding of the chemical changes that occur during the dissolution of the extrudates, Raman spectroscopic mapping was used to test the samples.

### 3.3.3 Raman spectroscopy results

#### 3.3.3.1 Dry raw materials spectra: visual observation

The Raman spectra of the raw materials are shown in Figure 3.5a (1100–1750  $\text{cm}^{-1}$  fingerprint region) and 3.5b (40–400  $\text{cm}^{-1}$  phonon-mode region).

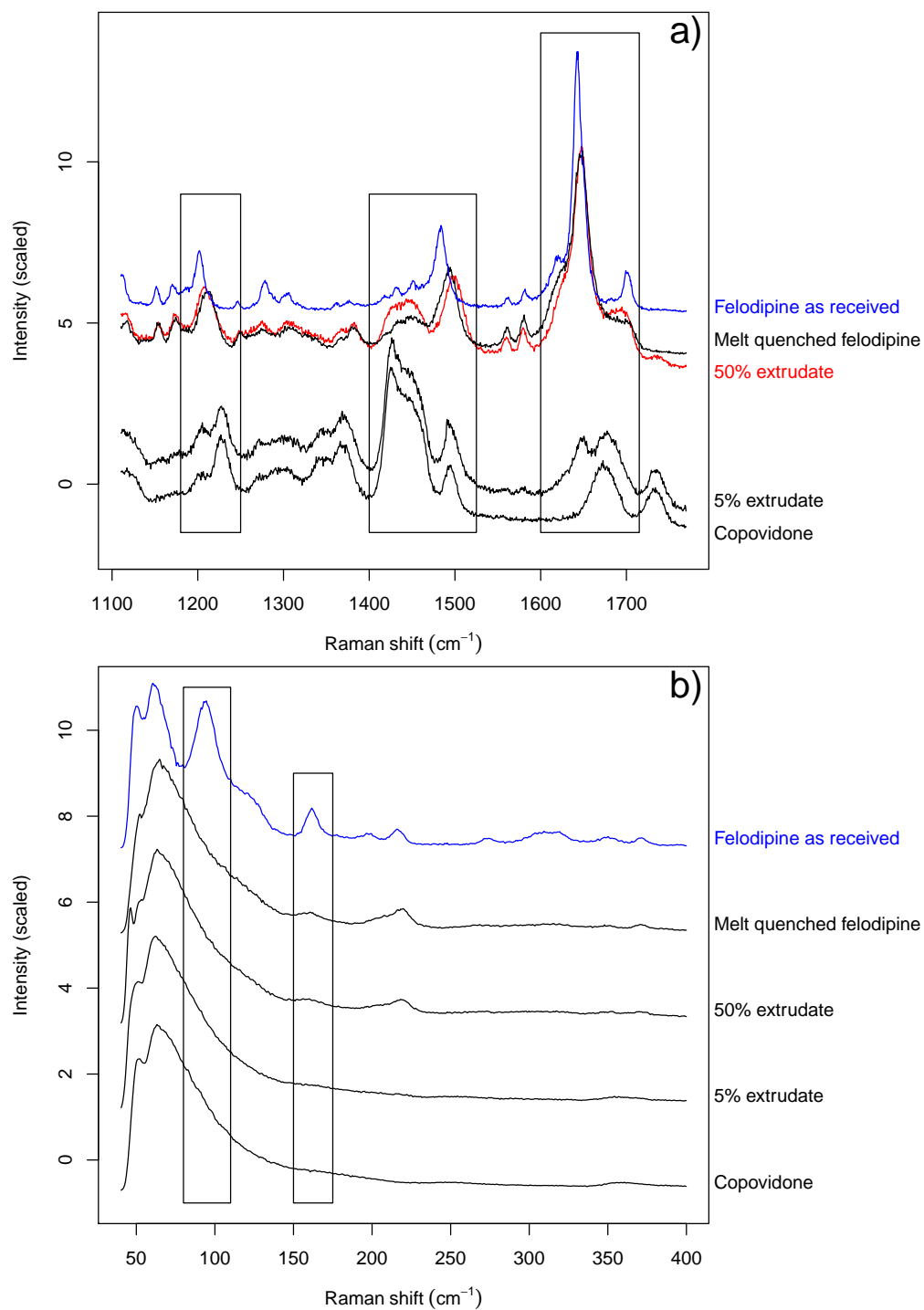


FIGURE 3.5: 1100–1750  $\text{cm}^{-1}$  fingerprint (a) and 40–400  $\text{cm}^{-1}$  (b) regions of raw materials spectra with reference spectra in red. Y-axis offsets were employed for presentational purposes and differ between panels.

Starting with the pure components, it is evident that the spectrum of felodipine is characterised by sharp bands and a good signal/noise ratio, whereas the spectrum of copovidone shows less-defined bands. At first approximation, the extrudate spectra appear as a linear combination of melt quenched felodipine (amorphous reference form) and copovidone. In the 5% extrudate spectrum, copovidone bands are predominant, while in the 50% extrudate bands related to felodipine prevail. In the latter case two slight shifts appear when comparing to the spectrum of melt quenched felodipine: the band at  $1209\text{ cm}^{-1}$  moves to a lower wavenumber, while the band at  $1497\text{ cm}^{-1}$  appears at higher wavenumber. These changes can be ascribed to the formation of a hydrogen bond between the dihydropyridine N-H group (proton donor) of felodipine and the carbonyl group of copovidone (proton acceptor), coupled with minor conformational changes, as has been previously reported for ASDs of felodipine and PVP.<sup>49,53</sup>

Turning now to the felodipine spectra, it is possible to see significant differences between the amorphous (melt quenched felodipine) and the crystalline (felodipine as received) solid forms. Firstly, the bands of the crystalline form appear sharper than those of the amorphous form, due to the disorganised molecular environment of the amorphous solid state. Furthermore, a detailed observation highlights that the intra-molecular vibration bands at  $1213$ ,  $1492$  and  $1645\text{ cm}^{-1}$  of the amorphous form slightly shift to higher wavenumber. This has been shown to be due to the presence of different intra-molecular hydrogen bonds within the amorphous solid compared to the crystalline form.<sup>49</sup> In the phonon-mode region, which results from the inter-molecular vibrations, the two felodipine solid forms have different spectra. The amorphous form spectrum is characterised by broad bands and a continuous distribution of inter-molecular vibrations. In the crystalline form, sharp bands are present at  $94$  and  $168\text{ cm}^{-1}$ , due to the quantised nature of the inter-molecular vibrations in the crystalline material. Thus, as reported in literature,<sup>119,120</sup> the phonon-mode region represents an area of the Raman spectrum where it is possible to rapidly

distinguish between different solid forms.

### 3.3.3.2 Dissolution experiments

**Averaged spectra: visual observation** Averaged Raman spectra of the 5% extrudate dissolution are presented in Figure 3.6. Examination of the data does not reveal significant changes in the spectra across the entire period covered by these data (0-70 min), beyond a reduction in spectral intensity as the compact dissolves (as seen in the optical images, Figure 3.2a). The ratio between the band of felodipine at  $1650\text{ cm}^{-1}$  (ring stretching mode) and that of copovidone at  $1426\text{ cm}^{-1}$  (bending modes of methylene functional groups) is preserved throughout the whole dissolution test. The Raman data essentially show that felodipine and copovidone dissolve as a single entity rather than as two separate components. This is in accordance with the RDDR data, which illustrated that felodipine and copovidone dissolve with the same rate. Therefore, it seems reasonable to suggest that the dissolution occurs from the molecular dispersion, with the overall behaviour being dependent on the highly water-soluble polymer (Figure 3.6).

Raman data of the 50% extrudate dissolution are shown in Figure 3.7a (1100–1750  $\text{cm}^{-1}$  fingerprint region) and 3.7b (40–400  $\text{cm}^{-1}$  phonon-mode region). Raman data show that the spectrum does not change after 10 min (Figure 3.7a, 10 mins). Bands of felodipine ( $1497\text{ cm}^{-1}$ ) and copovidone ( $1426\text{ cm}^{-1}$ ) preserve the same ratio as in the spectrum of the compact “Dry”. Proceeding with the analysis, after 65 min the intensity of the copovidone band at  $1426\text{ cm}^{-1}$  appears to decrease in relation to that of felodipine at  $1497\text{ cm}^{-1}$ . A comparison with the “50% extrudate” reference spectrum reveals that the band at  $1209\text{ cm}^{-1}$  moves to slightly higher wavenumber and that at  $1497\text{ cm}^{-1}$  shifts to lower wavenumber. Spectra collected between 65 and 316 min show a strong correlation with the melt quenched (amorphous) felodipine spectrum.

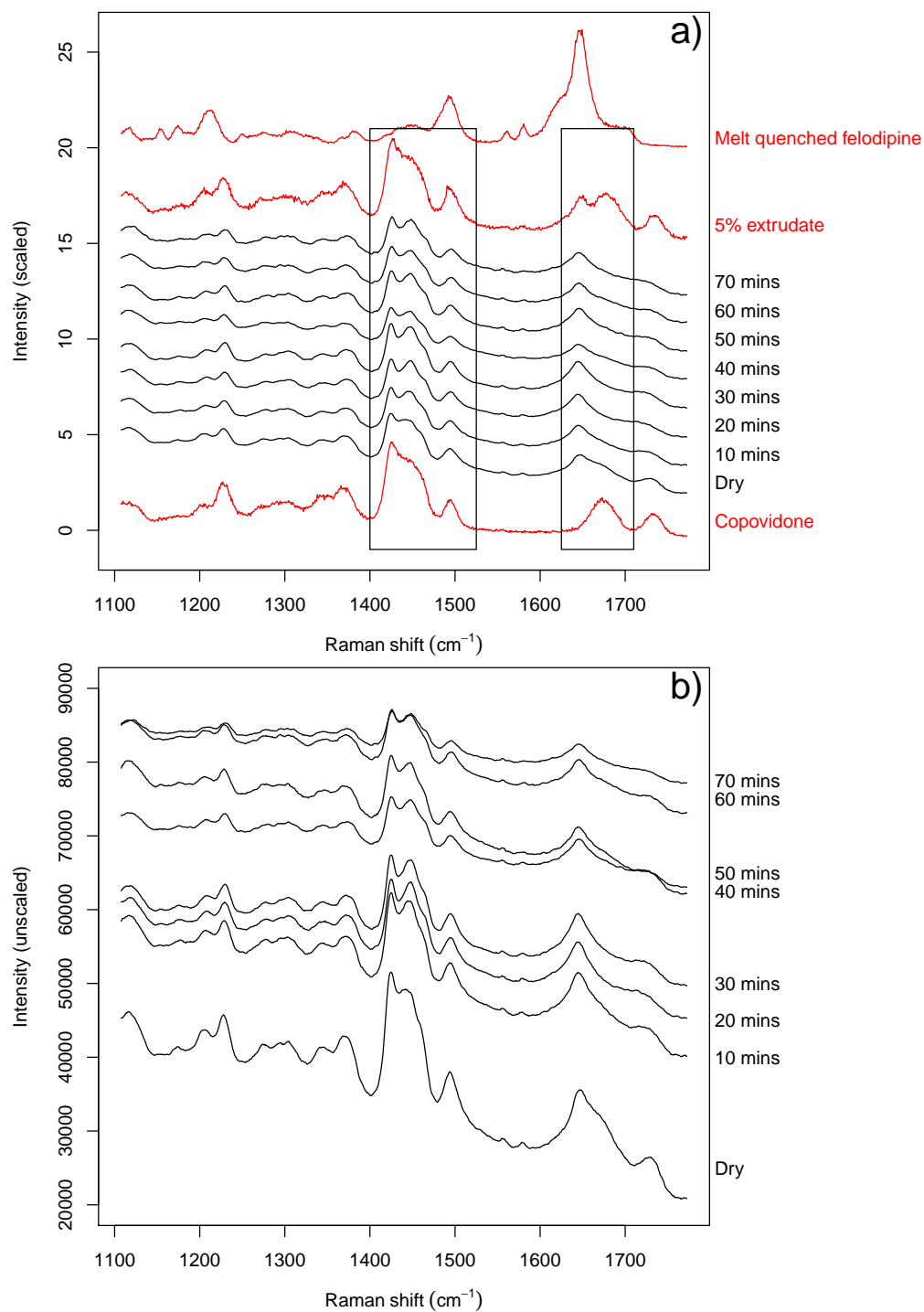


FIGURE 3.6: Scaled (a) and unscaled (b) averaged Raman spectra (1100–1750 cm<sup>-1</sup>) of the dissolution of the 5% extrudate, with raw materials spectra in red. Y-axis offsets were applied for presentational purposes.

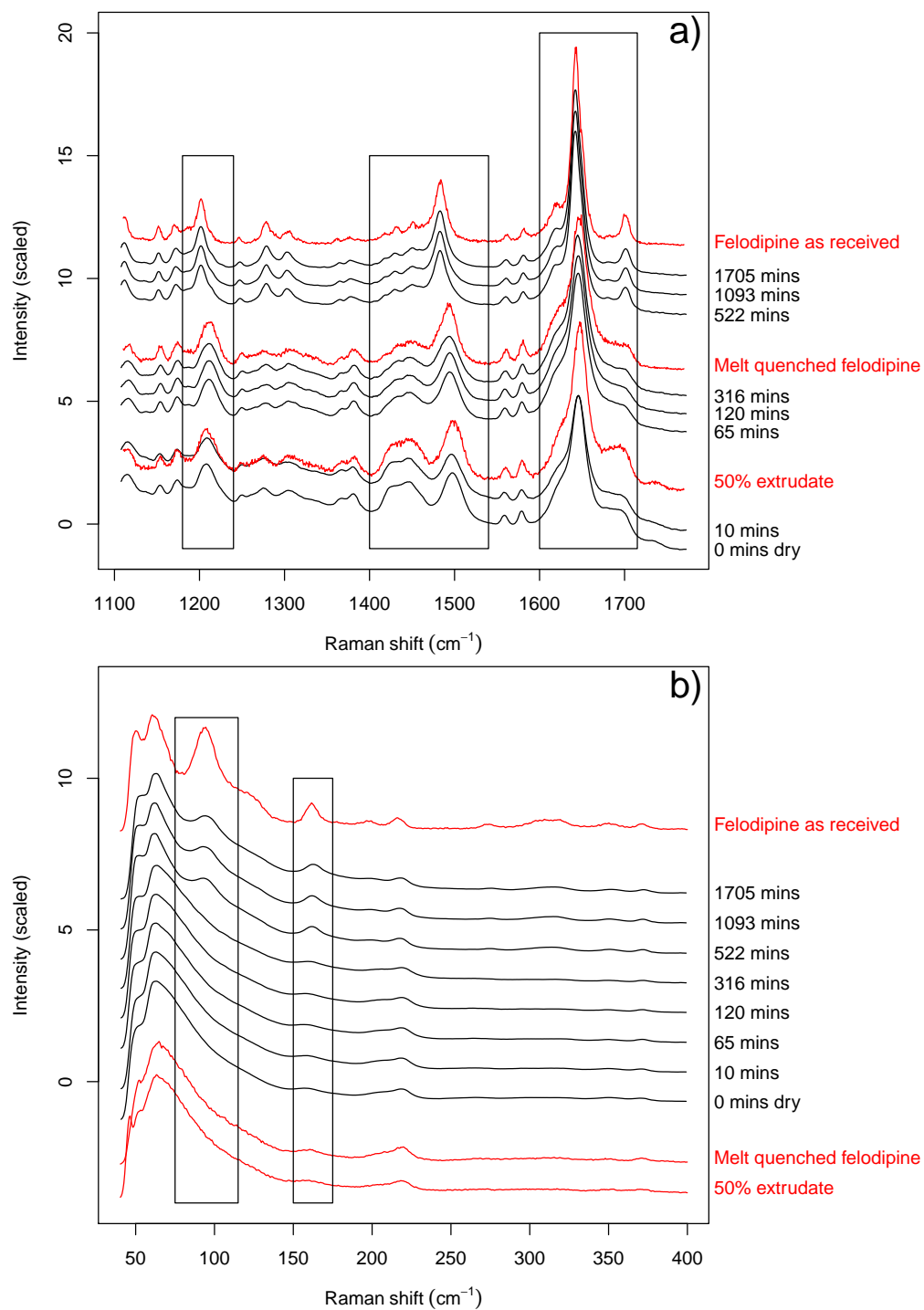


FIGURE 3.7: 1100–1750  $\text{cm}^{-1}$  fingerprint (a) and 40–400  $\text{cm}^{-1}$  (b) regions of the averaged Raman spectra collected during the dissolution of the 50% extrudate, with raw materials spectra in red. Y-axis offsets have been applied for presentational purposes and differ between panels.

It is likely that the faster dissolution of copovidone with respect to felodipine from the extrudate leads to a build-up of felodipine-rich amorphous material on the surface of the compact. The second important change occurs at 522 min. It is immediately apparent that the averaged spectrum, after 522 min, corresponds to the crystalline form of felodipine. When compared to melt quenched felodipine, intra-molecular bands at 1202, 1484 and 1642  $\text{cm}^{-1}$  shift to lower wavenumber as well as become sharper. These spectral changes were previously seen in Figure 3.5a, revealing the formation of crystalline felodipine. In the phonon-mode region (Figure 3.7b), well-defined bands appear at 94 and 168  $\text{cm}^{-1}$  after 522 min, essentially confirming that amorphous felodipine begins to re-crystallise after this time-point.

**Averaged spectra: hierarchical agglomerative clustering** In this section the use of an objective statistical analysis method to validate the subjective interpretation of the Raman data is described. HAC is an automated method of cluster analysis which calculates a distance, also called “degree of dissimilarity”, between datasets,<sup>166</sup> including Raman spectra.<sup>120</sup> The dendrogram obtained applying HAC to the 21 datasets is shown in Figure 3.8. It is immediately evident that the overall structure of the dendrogram is governed by two branches: spectra of the dissolution of the 5% extrudate with the 5% extrudate and copovidone reference spectra, and spectra of the dissolution of the 50% extrudate with the remaining reference spectra (“50% extrudate”, “Melt quenched felodipine” and “Felodipine as received”). Starting with the branch of the 5% extrudate (LHS of plot), it is clear that all the spectra of the dissolution can be classified by only one cluster, as they are characterised by a high degree of similarity. This trend is in a good agreement with the visual inspection of the data. As noted earlier (Figure 3.6), significant changes were not observed in the spectra collected during the dissolution of the 5% extrudate compact. Turning now to the other portion of the dendrogram, that of the high drug-loaded

extrudate (RHS of plot), the presence of three main clusters is immediately apparent.

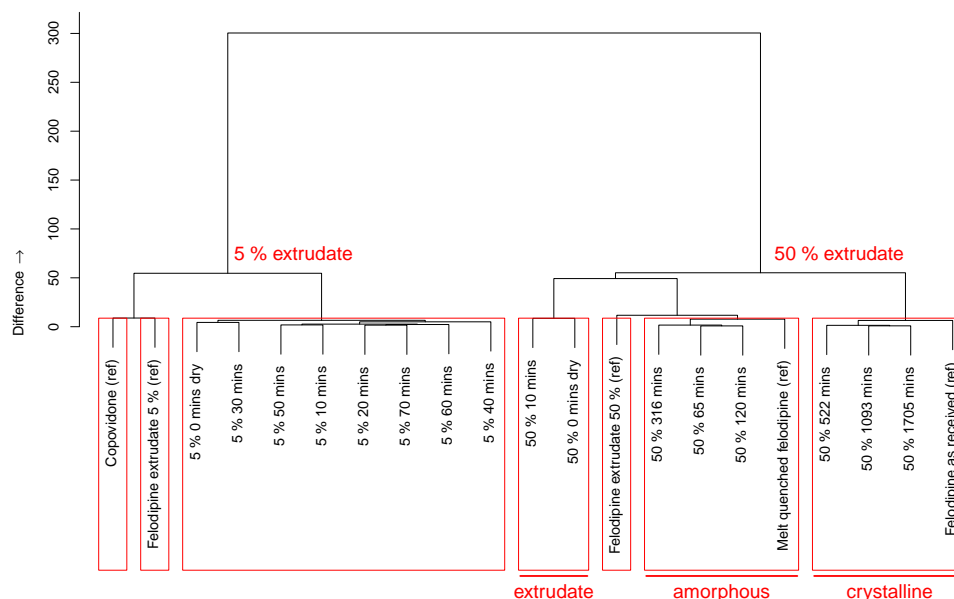


FIGURE 3.8: Similarity dendrogram with clusters indicated by red boxes. Raw data were variance-scaled before performing HAC. The Euclidean distance measure was employed to define clusters.

The first includes “50% extrudate dry” and “50% extrudate 10 mins” spectra. The second cluster includes spectra collected between 65 and 361 min, with the reference spectrum of melt quenched (amorphous) felodipine. The last cluster includes spectra collected from 522 min until the end of the experiment along with the reference crystalline form of felodipine. Again, HAC confirms the visual inspection of the data, further demonstrating that two transformations occur during the dissolution of the high drug-loaded extrudate. The first involves the conversion, via dissolution of copovidone, of mixed extrudate into a felodipine-rich amorphous material on the surface of the compact, indeed spectra collected between 65 and 361 min showed high similarity for the melt quenched reference form. The other is the re-crystallisation of amorphous felodipine after 522 min. The first transformation clearly explains the extremely low partial RDDR values observed during the dissolution of the 50% extrudate. Copovidone

can not drive the dissolution of felodipine due to an insufficient polymer to drug ratio, resulting in formation of felodipine-rich amorphous areas on the compact surface. The disruption of the drug-polymer molecular dispersion system through loss of copovidone then induces the drug re-crystallisation.

In conclusion, HAC widely validated all the subjective observations of the Raman data, adding to them an objective and impartial component.

**Multivariate curve resolution analysis** In this section temporally- and spatially-resolved maps of the crystallisation event observed for felodipine present in the high drug-loaded extrudate are presented (Figure 3.9). The MCR model was employed to spatially and spectrally deconvolute the changes in the patterns. MCR is a very well-established component analysis method, and has been used to resolve ToF-SIMS, IR and Raman data from pharmaceutical samples.<sup>167–170</sup> MCR requires input of a body of spectral data in a matrix format, each spectrum being tagged with a set of labels (e.g. x, y position), which is resolved by the MCR method into a number of components. The only user input is the requested number of components, i.e. MCR is a model-free method. Outputs from MCR include loadings (which in the present case correspond to Raman spectra of the resolved components) and scores (which provide the spectral weighting of a given component for the relevant unique set of labels). Labels typically comprise x and y position, but there is no reason why they can not include more information. To include time in the analysis, all xy spectral maps were simply concatenated together and a time label included for each input spectrum, in addition to the usual x and y labels. The MCR results are reproducible for multiple runs, despite a different randomly generated set of numbers being employed as a starting model for each run. This provides confidence that the results are robust, which is important in the context of the well-known rotational ambiguities present in the MCR methodology.<sup>155,156</sup>

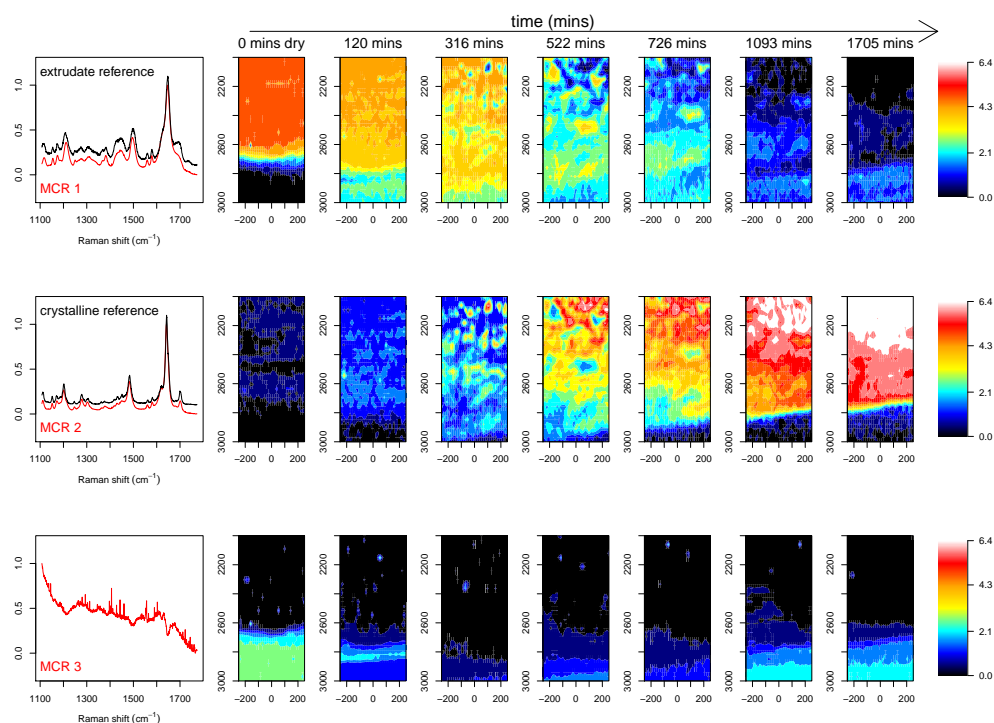


FIGURE 3.9: Raman maps of the 50% extrudate compact as a function of time, generated by MCR analysis.

Three components were required to deconvolute the mapped data. Comparison with the reference spectra unambiguously indicates that the first component, MCR1, can be associated with the extrudate and the second, MCR2, with the crystalline form of felodipine. The excellent peak to peak correlation between loadings and reference spectra confirms the utility of MCR as statistical method to analyse spatial-temporal Raman data. MCR3 mostly picked up the background noise which characterises areas where no compact is present. The scores plots show that the extrudate (MCR1) is homogeneously distributed throughout the mapped compact surface before immersion in water. Corresponding MCR2 scores plot indicated no traces of crystalline material in the mapped area of the dry compact. Then, after 316 min the amount of crystalline felodipine (MCR2) rapidly increases at the expense of the extrudate (MCR1), and this is reflected by the recrystallisation kinetic shown in Figure 3.10. It is interesting to notice the complementarity of MCR1 and MCR2 scores plots at 316 and 522 min, which denotes the coexistence of the extrudate and crystalline felodipine.

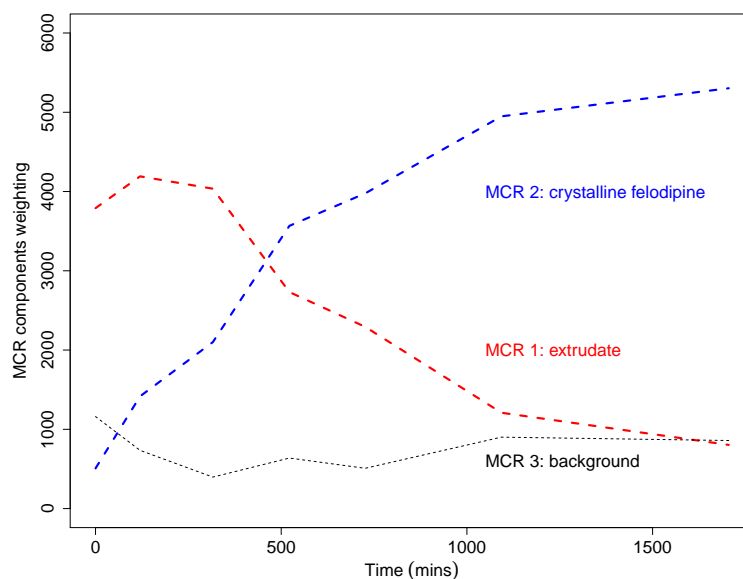


FIGURE 3.10: Crystallisation kinetic generated by plotting the MCR components weighting in each map as a function of time.

Regions where the extrudate (MCR1) is present to its maximum are indicated by yellow colour, while the corresponding crystalline regions (MCR2) are characterised by blue colour, and *vice versa*. The crystallisation process is likely linked with loss of copovidone from the extrudate. It is well known that the polymeric carrier in ASDs has not only the function to improve the dissolution properties of poorly soluble drugs, but also inhibits crystal growth of the amorphous form, via antiplasticisation effect or hydrogen-bonding interactions between the drug and the polymer.<sup>69</sup> It is therefore likely that the loss of copovidone during the first 316 min, previously observed in the averaged Raman spectra (Figure 3.7), promotes the crystallisation of felodipine-rich amorphous material in the compact surface.

At the end of the experiment, after 1705 min, the residue of the compact was recovered and analysed using Raman and XRPD. MCR maps of the core (after breaking the compact into two parts) and surface are presented in Figure 3.11. Two components were required in this case to deconvolute the data, with the first component (MCR1) corresponding to amorphous felodipine and the second (MCR2) corresponding to crystalline felodipine. The scores plots show that felodipine is predominantly amorphous in the

core, whereas in the surface is crystalline. Raman data suggest that the crystallisation begins from the compact surface exposed to water and propagates towards the core, where only a little amount of crystalline drug was found. The XRPD pattern of the compact after grinding it into powder can be seen in Figure 3.12. The pattern appears as a combination of sharp bands, typical of the crystalline materials, and a broad halo which characterises the amorphous materials. XRPD therefore indicates that felodipine sampled from the entire compact after the dissolution experiment is a mixture of crystalline and amorphous. This is in full agreement with the Raman results, which indicated a crystalline outer section and an amorphous inner section of the compact.

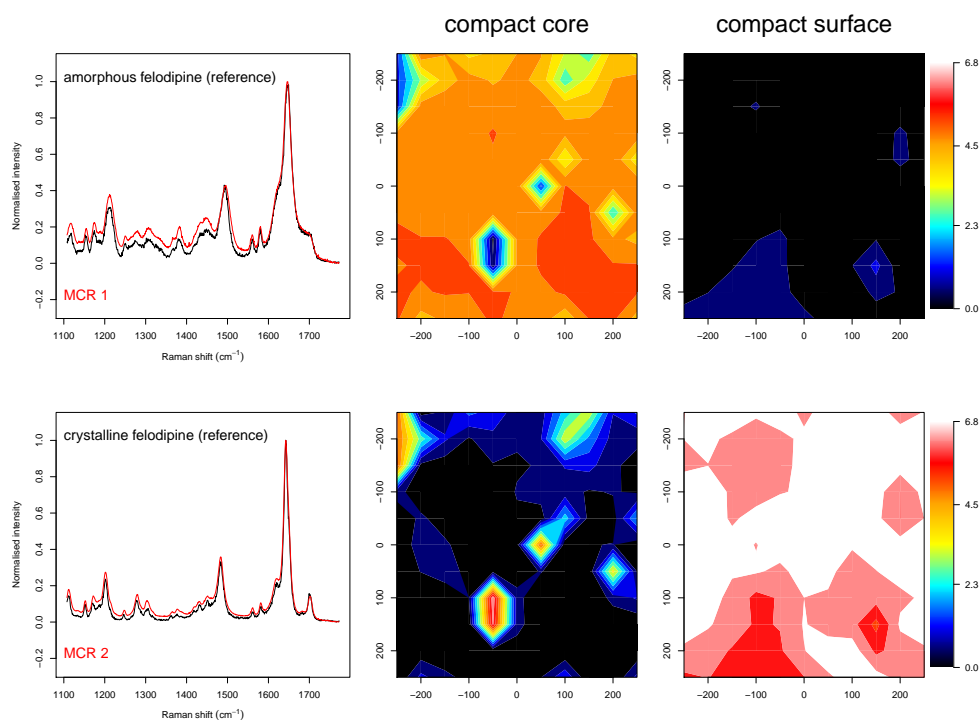


FIGURE 3.11: MCR loadings and scores plots of the 50% extrudate compact core and surface after the dissolution test.

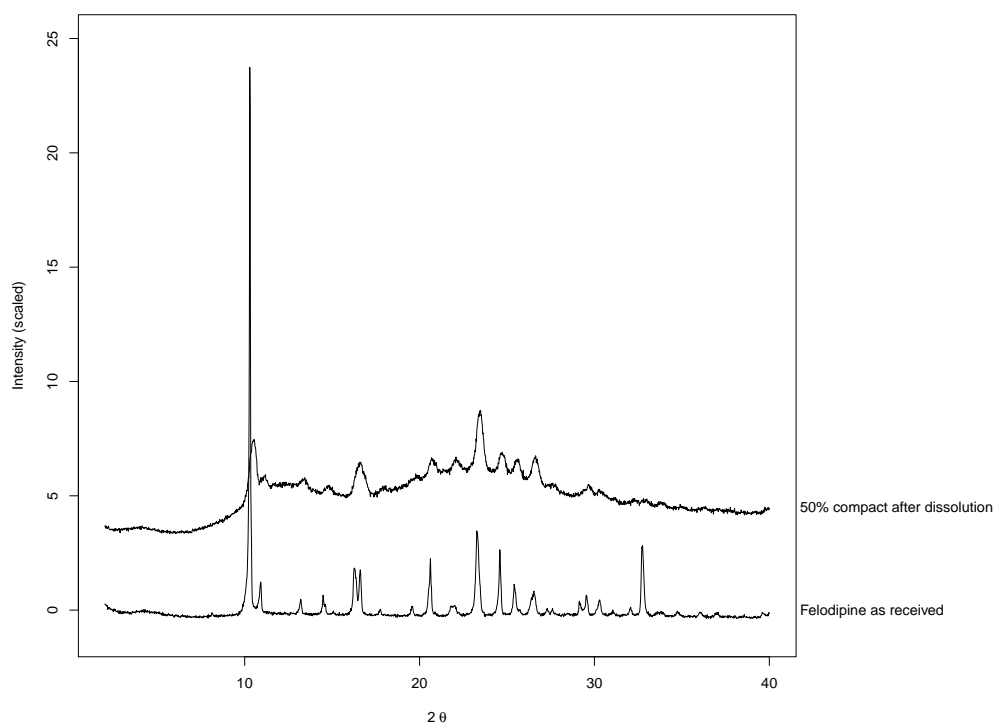


FIGURE 3.12: XRPD patterns of the crystalline reference form (“Felodipine as received”) and the 50% extrudate residue recovered after the dissolution experiment.

### 3.4 Conclusions

This chapter showed that real time *in situ* Raman mapping is ideal for providing additional spatially-resolved chemical information on changes occurring to the ASD, which suggested dissolution mechanisms. In addition, the RDDR methodology was successfully employed to simultaneously track the dissolution profiles of both the drug and the polymer, and ultimately measure the dissolution performance in multi-component systems. The dissolution performance of the low drug-loaded extrudate (5% w/w) was dependent on the high water solubility of copovidone. Felodipine and copovidone were shown to dissolve with the same rate from the dispersion, and Raman data did not show any significant changes in all the spectra collected during the course of the dissolution test. In contrast, the dissolution performance of the high drug-loaded extrudate (50% w/w) was strongly dependent on the physicochemical properties of the drug, e.g. low water solubility and

high hydrophobicity. Raman data indicated the formation of an amorphous drug-rich shell in the early time-points of the experiment, followed by the drug re-crystallisation. The MCR model applied to the concatenated Raman maps was demonstrated to be a robust method to analyse temporally- and spatially-resolved Raman data. The re-crystallisation of felodipine led to large variations in the Raman spectra and thus it was readily detectable. In particular in the phonon-mode region, the spectrum of the crystalline form was characterised by clear and sharp bands, while that of the amorphous form by a broad halo. The crystallisation process proceeded from the surface towards the core and was likely linked to loss of copovidone from the extrudate.

# Chapter 4

## Monitoring the dissolution mechanisms of bicalutamide extrudates via Raman mapping

### 4.1 Introduction

The overall aim of this thesis, as outlined in Chapter 1, was to obtain additional information on the dissolution mechanisms of ASDs by using Raman spectroscopy as primary characterisation technique. In Chapter 3 it was found that the dissolution performance of felodipine and copovidone ASDs is strongly dependent on the drug loading. Raman and RDDR data indicated that felodipine and copovidone in the 5% extrudate dissolved with the same rate, pointing to a polymer-controlled drug release. In contrast, the dissolution rates of both the drug and the polymer in the 50% extrudate were significantly slower compared to the 5% extrudate, and this was shown by Raman spectroscopy to be due to a build-up of a drug-rich amorphous material followed by the drug re-crystallisation. Raman spectroscopy was

demonstrated to be a very useful technique for gaining temporally- and spatially-resolved information on the drug release.

The same combination of analytical techniques employed in Chapter 3, i.e. optical imaging, RDDR and Raman spectroscopy, was used to investigate the dissolution performance of another solid dispersion model which consists of poorly soluble bicalutamide with copovidone. The dissolution behaviour was tested as a function of the drug loading (5% and 50% w/w), which has been shown in Chapter 3 to be a key factor in determining the dissolution mechanisms. The aim of this chapter is to gain additional chemical information on the drug release of amorphous bicalutamide solid dispersions, and potentially correlate the dissolution mechanisms with those hypothesised from the felodipine study.

## **4.2 Materials and methods**

### **4.2.1 Materials**

Crystalline bicalutamide form I was provided by AstraZeneca (Macclesfield, United Kingdom) and used as received, without any further purification. The polymorphic purity of form I was verified by XRPD (Figure B.1 of the Appendix B). Details for copovidone can be seen in Chapter 3, Section 3.2.1.

### **4.2.2 Samples preparation**

#### **4.2.2.1 Preparation of the amorphous form and crystalline bicalutamide form II**

Amorphous bicalutamide was obtained by heating form I to 200 °C, removing the melt from the oven and leaving it in the bench to cool at room

temperature. XRPD confirmed the formation of the amorphous form and the absence of crystalline material (Figure B.1 of the Appendix B). Crystalline bicalutamide form II was produced according to patent, by heating the amorphous form to 175 °C.<sup>171</sup> XRPD confirmed the formation of polymorphic form II (Figure B.1 of the Appendix B).

#### **4.2.2.2 Preparation of the bicalutamide-copovidone extrudates**

5% and 50% w/w drug-loaded bicalutamide-copovidone extrudates were prepared according to the method reported in Chapter 3, Section 3.2.2. The temperature was set to 170 °C. XRPD confirmed the formation of the amorphous form and the absence of crystalline material (Figure B.1 of the Appendix B).

### **4.2.3 Analytical methods**

#### **4.2.3.1 X-ray powder diffraction**

The XRPD method is reported in Chapter 3, Section 3.2.3.1.

#### **4.2.3.2 Rotating disk dissolution rate test**

The RDDR test was conducted as previously described in Chapter 3, Section 3.2.3.2. For the HPLC, a linear gradient elution was used starting at 40% acetonitrile/60% deionised water and ending at 70% acetonitrile/30% deionised water after 2 min, with chromatograms collected for 3.5 min. The partial RDDR of both drug and polymer was calculated using linear regression analysis. The partial RDDR of the materials was obtained from the slope of the regression line. For the 5% extrudate, the RDDR was calculated using the first 20 min time period, where the trend is linear. For the 50% extrudate, the RDDR was obtained using the time interval between

40 and 120 min, where the trend of both bicalutamide and copovidone is linear, in accordance with Pharmacopoeia procedures.<sup>90,162</sup>

### 4.2.3.3 Raman spectroscopy

The same Raman system and dissolution set-up previously described in Chapter 3, Section 3.2.3.3 was employed. Deionised water was used as dissolution medium with the flow rate set to  $5 \text{ mL} \cdot \text{min}^{-1}$ . The time frames, dimensions of the mapped areas and acquisition times for the 5% and 50% extrudate experiments are depicted in Table 4.1.

	5% extrudate	50% extrudate
Time frame (min)	80	2946
Total number of maps	7	14
Total number of spectra per map	121	1156
Acquisition time per spectrum (s)	2	2
Acquisition time per map (min)	8	90
Mapped area ( $\mu\text{m}$ )	$500 \times 500$	$500 \times 1000$
Grid spacing x-axis ( $\mu\text{m}$ )	50	15
Grid spacing y-axis ( $\mu\text{m}$ )	50	30

TABLE 4.1: Experimental details of the Raman map acquisition during the dissolution experiments of the 5% and 50% extrudates.

For Raman data analysis, to obtain spatial information for the 50% extrudate dissolution experiment, false colour maps were generated using MCR. In order to monitor changes as function of both time and xy-position, a single data matrix was generated which includes all the spectra collected across the entire dissolution experiment time scale (16184 spectra). All the raw data and the numerical routines written in the R language have been published.<sup>172</sup>

### 4.2.3.4 Optical imaging

The optical imaging method has been previously described in Chapter 3, Section 3.2.3.4.

## 4.3 Results and discussion

### 4.3.1 Optical imaging and rotating disk dissolution rate

Before commencing a full discussion of the results, a key point needs to be made. Extrinsic factors such as hydrodynamics (e.g. disk rotation speed and fluid flow) and test conditions (e.g. temperature and pH of the medium) certainly differ between the RDDR test and Raman/optical imaging experiments. The primary aim of the present work is simply to investigate whether or not the combination of these techniques can provide a full and clear understanding of the bicalutamide release from the extrudates.

Figure 4.1 shows the optical images observed during the dissolution of the 5% and 50% drug-loaded extrudates. It is important to note the different time-scales between the two experiments which is due to the difference in dissolution rates. The 5% extrudate is completely dissolved after approximately 85 min, whereas the 50% drug-loaded extrudate remains intact after 3000 min. The optical imaging experiment clearly shows that the two different drug loadings behave very differently in aqueous media. The 5% extrudate compact undergoes erosion and is completely dissolved by 85 min from the beginning of the experiment. The 50% extrudate compact swells during the first 600 min of the dissolution experiment and remains intact even after 3000 min. The initial swelling is confirmed by the trend generated by plotting the surface area of the compact *vs* time (Figure 4.2). The dissolution/erosion of the 5% extrudate and the swelling of the 50% extrudate are consistent with the behaviours previously observed for ASDs of felodipine and copovidone (Chapter 3, Section 3.3.1).

RDDR measurements were then carried out in order to determine the amount of drug and polymer released into solution as a function of time.

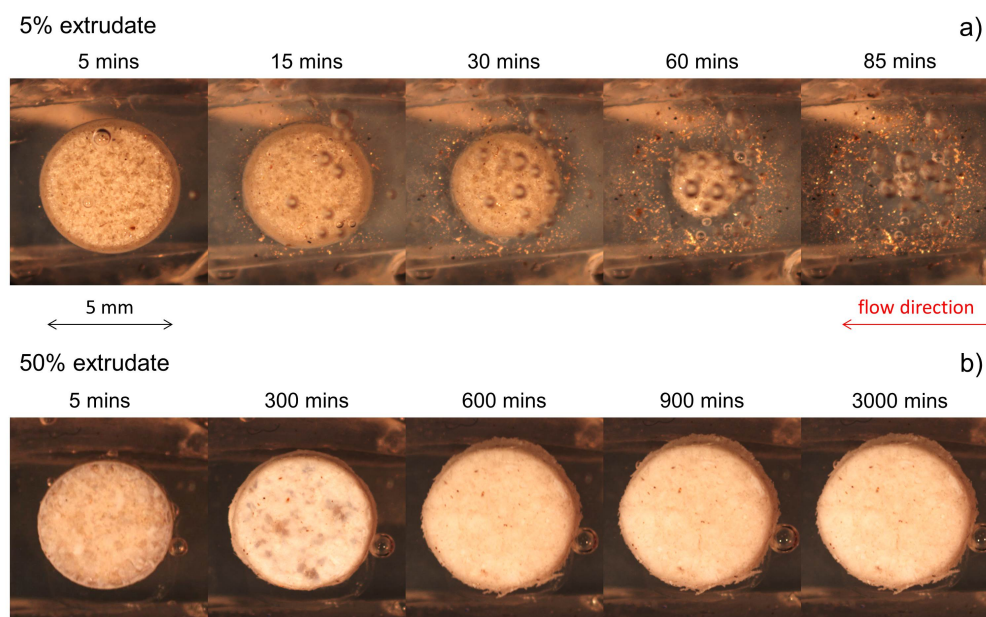


FIGURE 4.1: Optical images collected through the dissolution experiment for the 5% (a) and 50% (b) extrudates.

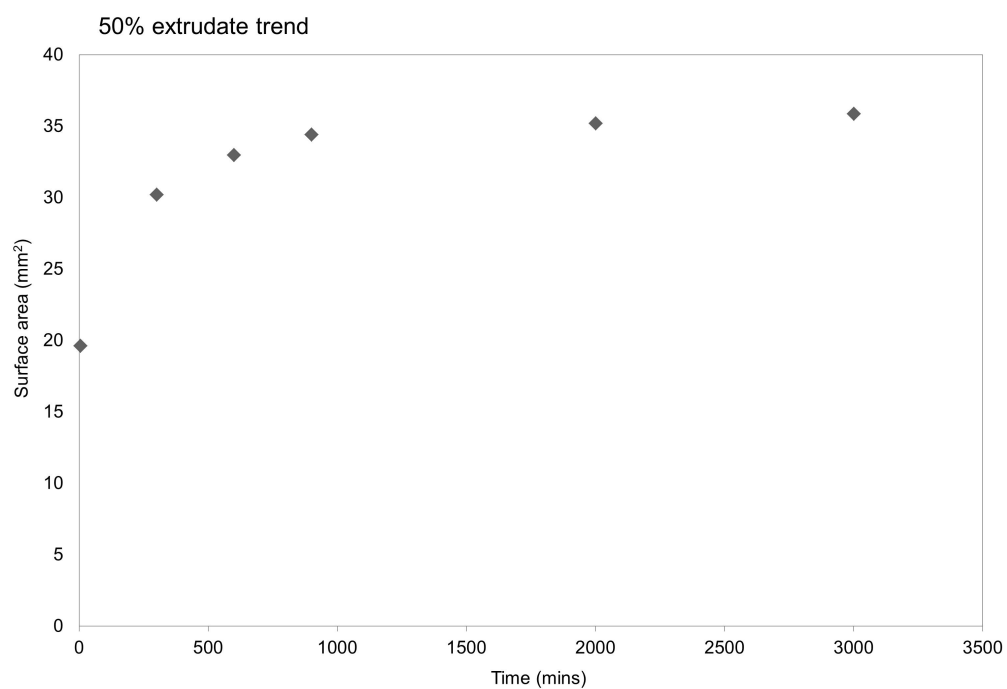


FIGURE 4.2: Trend showing the variation in the surface area of the 50% extrudate compact in water (Figure 4.1b) as a function of time.

The RDDR values for both the 5% and 50% extrudates are shown in Table 4.2, while the dissolution profiles are presented in Figure 4.3.

RDDR, mg/(min · cm <sup>2</sup> )				
Drug loading	Bicalutamide	Copovidone	Total	Index of performance
5%	0.24 (±0.005)	4.85 (±0.127)	5.09 (±0.127)	0.94 (±0.030)
50%	0.008 (±0.001)	0.025 (±0.001)	0.033 (±0.001)	0.48 (±0.064)

TABLE 4.2: Partial RDDR values along with the index of performance for the 5% and 50% extrudates.

For the 5% extrudate, the partial RDDR value for bicalutamide is 0.24 mg/(min · cm<sup>2</sup>) and that for copovidone is 4.85 mg/(min · cm<sup>2</sup>). Compared to the IDR of pure crystalline bicalutamide (0.003 mg/(min · cm<sup>2</sup>), Figure 4.3), bicalutamide present in the 5% extrudate shows a 80 fold increase in dissolution rate. The index of performance results in a value close to unity, indicating that the two components have a very similar dissolution trend and thus they dissolve simultaneously from the molecular dispersion. An index of performance close to unity has been obtained also for the 5% extrudate of felodipine and copovidone (Chapter 3, Section 3.3.2). In accordance with previous works,<sup>87,113</sup> the overall behaviour of the 5% bicalutamide-loaded extrudate is clearly dominated by water-soluble copovidone. Considering the 50% extrudate, it is immediately apparent that the partial RDDR values of both bicalutamide and copovidone are much lower than those observed for the 5% extrudate. The partial RDDR of bicalutamide (0.008 mg/(min · cm<sup>2</sup>)) is comparable with the IDR of pure crystalline bicalutamide (0.003 mg/(min · cm<sup>2</sup>)). Optical images and RDDR data therefore suggest that the dissolution behaviour of the 50% extrudate is dominated by the physicochemical properties of bicalutamide, and this is consistent with the behaviour previously observed for high drug-loaded extrudates of felodipine and copovidone (Chapter 3, Section 3.3.2). The low water solubility and high hydrophobicity of the drug prevent the wetting and water uptake of the compact due to an insufficient ratio of copovidone to bicalutamide at the diffusion layer. As a result, the dissolution of both bicalutamide and copovidone is very limited.

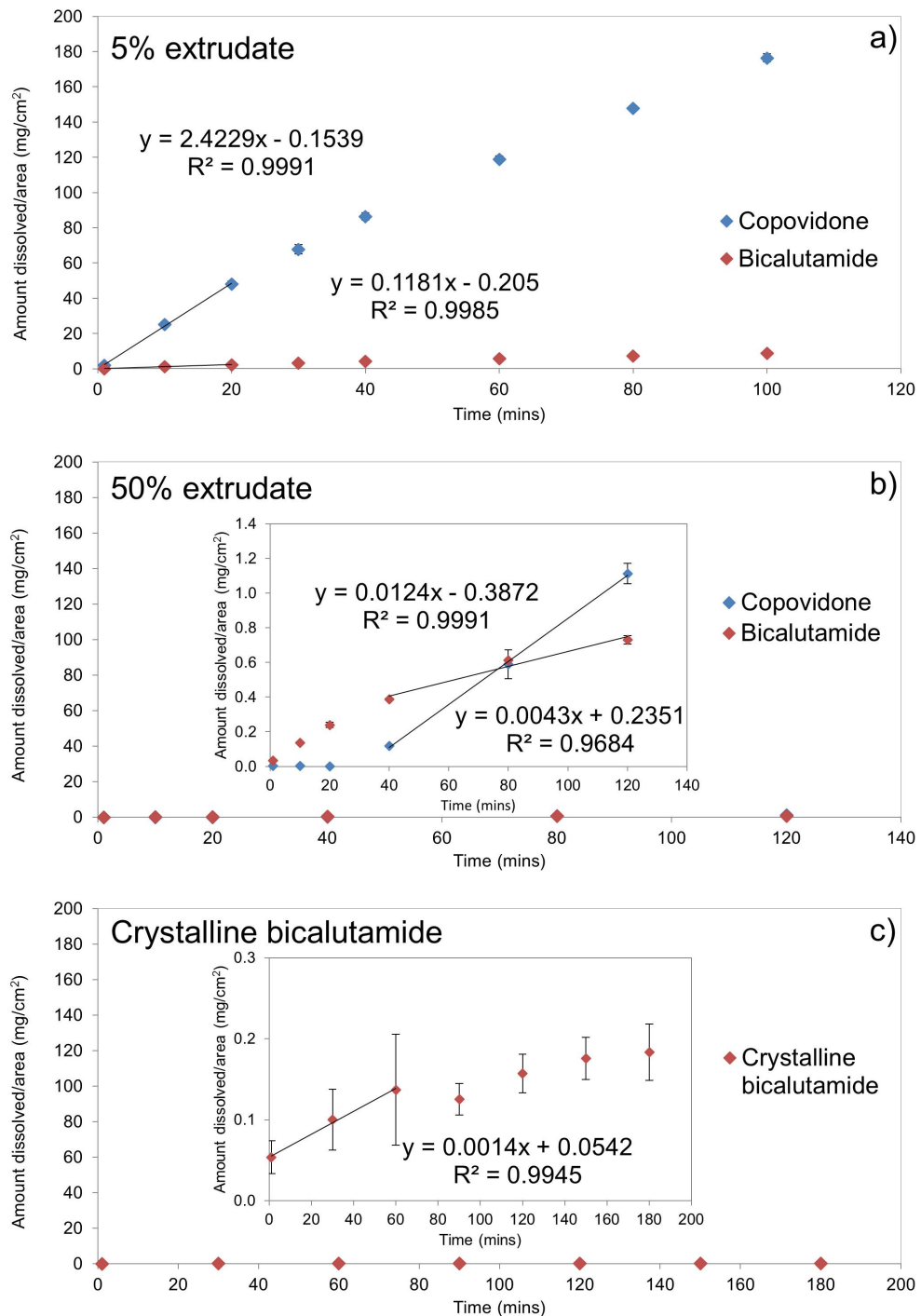


FIGURE 4.3: RDDR trends for the 5% (a) and 50% extrudates (b). The IDR trend of pure crystalline bicalutamide is presented in (c).

Summarising, the dissolution performance of the amorphous bicalutamide solid dispersions was found to be very similar to that previously observed for the amorphous felodipine solid dispersions, being strongly dependent on the drug:polymer ratio. The drug release of the 5% drug-loaded extrudate is clearly polymer-dependent, with bicalutamide dissolving simultaneously with the hydrophilic polymer. For the 50% extrudate, optical images and RDDR measurements indicated that its behaviour in water is dependent on the physicochemical properties of the hydrophobic bicalutamide. However, this does not clearly explain which processes occur during the course of the dissolution test, as data are not being collected directly from the dosage form, nor do the RDDR data provide any direct chemical explanation of the differences in dissolution rates between the 5% and 50% extrudates. For this reason, real time *in situ* Raman spectroscopic mapping along with off-line XRPD were used to investigate the samples.

## 4.3.2 Raman spectroscopy results

### 4.3.2.1 Raman spectra of “dry” raw materials

Raman spectra of the dry raw materials are available in Figure 4.4. The three solid forms of bicalutamide present spectra with clear and obvious differences. Considering the region between 1055 and 1724  $\text{cm}^{-1}$  (Figure 4.4a), the differences between the crystalline forms are reasonable, given that they are known to be conformational polymorphs. The band deriving from the stretching mode of the carbonyl group moves to higher wavenumber in form II (1709  $\text{cm}^{-1}$ ) compared to form I (1686  $\text{cm}^{-1}$ ). Due to the different conformation of forms I and II, the oxygen of the carbonyl group is involved in different intra-molecular hydrogen bond interactions, which lead to the observed peak shift. Atoms are also involved in inter-molecular interactions. The hydrogen bonding between the N–H of the amide group and one of the oxygen atoms of the sulfonyl group determines the formation of a dimer in the molecules of form II.

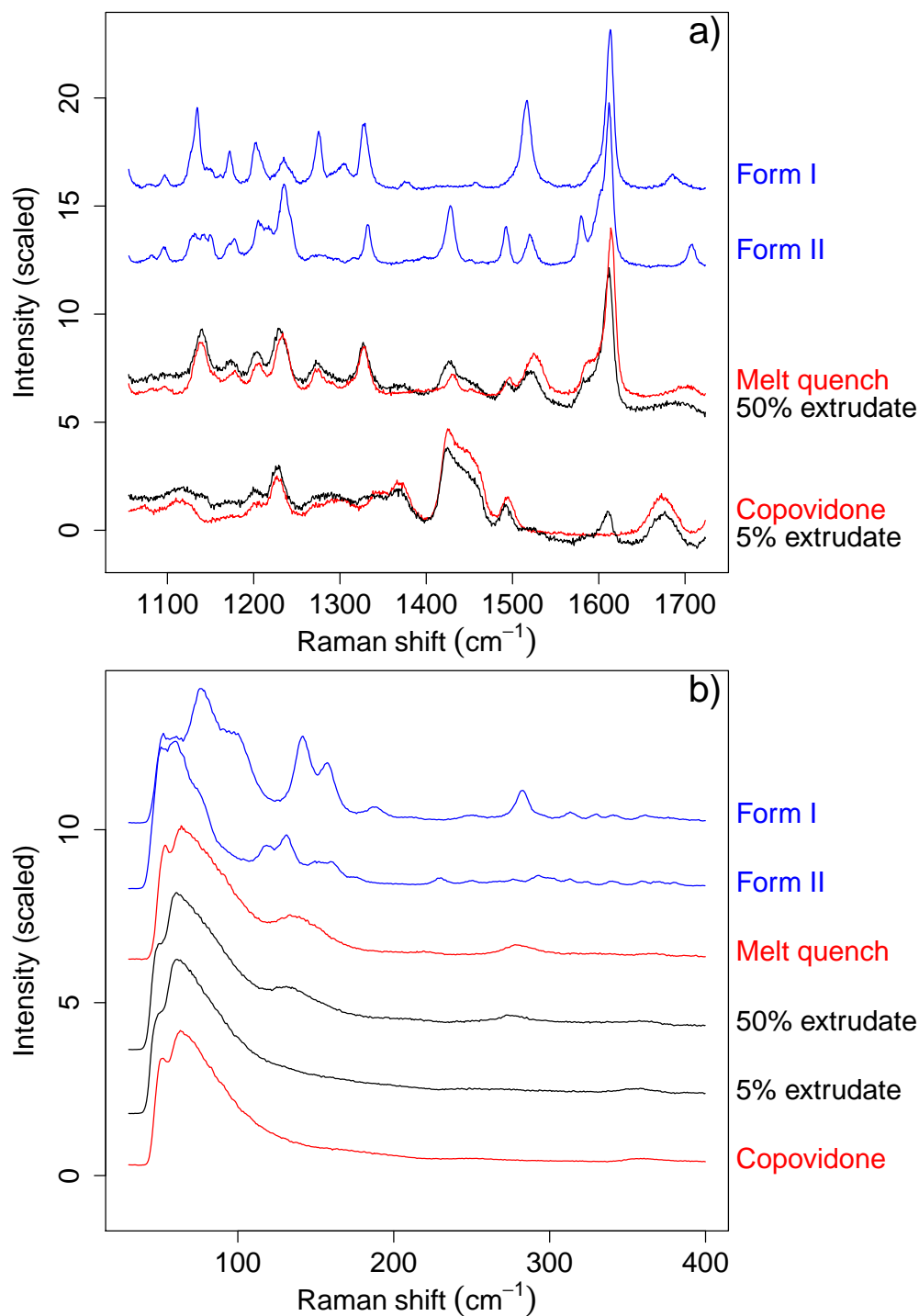


FIGURE 4.4: 1055–1724  $\text{cm}^{-1}$  (a) and 40–400  $\text{cm}^{-1}$  (b) regions of the Raman spectra of “dry” raw materials. Data were variance-scaled before plotting. Y-axis offsets have been applied for presentation purpose and differ between the two panels.

This interaction would explain why an intense single band at  $1517\text{ cm}^{-1}$  corresponding to the N–H bending and C–N stretching modes of the amide group is replaced by three peaks with inferior intensity appearing at 1428, 1493 and  $1520\text{ cm}^{-1}$  in form II. In addition, the particular conformation of form II enables  $\pi$ – $\pi$  stacking interactions between the two rings. Due to this extra interaction form II presents a small peak at  $1579\text{ cm}^{-1}$  (ring stretching mode) which is not present in the spectrum of form I. The schematic representation of the structural conformations of forms I and II is shown in Figure 4.5. Raman spectra from form I, II and the amorphous form of bicalutamide are consistent with those previously reported by other workers.<sup>52,127–129</sup>

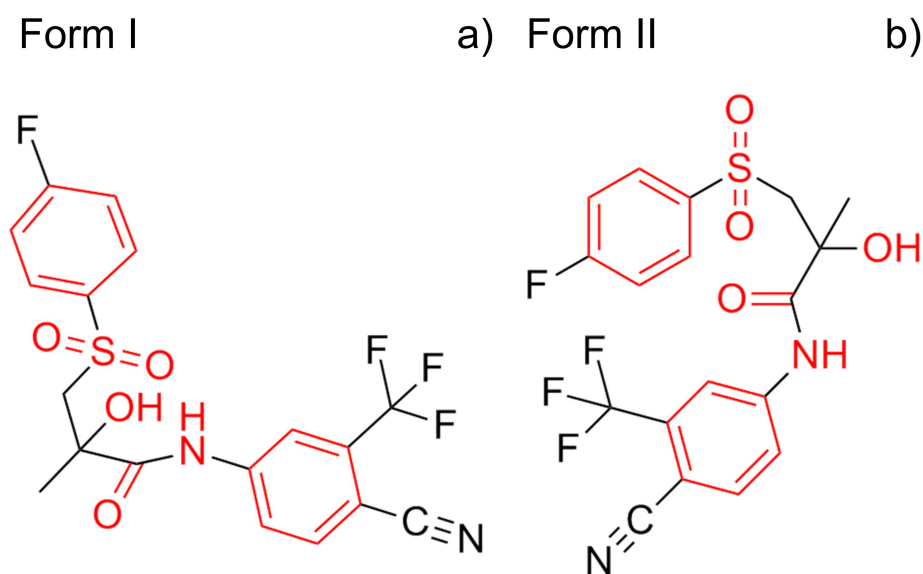


FIGURE 4.5: Scheme of the structural conformations of form I (a) and form II (b), with the functional groups involved in chemical interactions shown in red.

The amorphous (melt quench) form presents a spectrum more similar to that of crystalline form II than form I (e.g. bands at  $1428$  and  $1493\text{ cm}^{-1}$  are present in the amorphous spectrum and the form II spectrum but not in the form I spectrum). This spectral similarity with form II suggests that the molecular conformation of the amorphous form is more similar

to that of the metastable form II than that of highly stable form I. The amorphous form also exhibits greater peak widths when compared to the crystalline forms I and II, which is expected due to the molecular disorder inherent in the amorphous form but not present in the two crystalline forms. The spectra for the two extrudates are at first approximation simply a linear combination of the spectra for the amorphous drug and the polymer. A detailed inspection reveals some subtle differences, including a shift of the bands of the N–H bending mode at 1490 and 1516  $\text{cm}^{-1}$  for the 50% extrudate, and at 1490  $\text{cm}^{-1}$  for the 5% extrudate. These likely arise from the inter-molecular hydrogen bonding interactions between the amide of bicalutamide (N–H, proton donor) and the oxygen atoms of the carbonyl groups of copovidone (proton acceptor).<sup>52</sup>

In the low-wavenumber region between 40 and 400  $\text{cm}^{-1}$  (Figure 4.4b) the two crystalline forms of bicalutamide present clear, well-resolved bands, and the spectra are easily distinguishable from each other. This is wholly consistent with previous work by other workers on low-wavenumber Raman spectroscopy applied to polymorphs.<sup>118,119</sup> The melt-quenched bicalutamide, the two extrudates and the pure polymer exhibit the typical broad halo at low wavenumber expected for amorphous materials,<sup>118,119</sup> with the differences between these amorphous forms being subtle in this spectral region.

In summary, the various pure forms of bicalutamide and the extrudates can be distinguished using the reference Raman spectra, especially the region from 1055 to 1724  $\text{cm}^{-1}$ . The low-wavenumber data (40–400  $\text{cm}^{-1}$ ) allow the crystalline forms to be distinguished both from each other and from the various amorphous forms. Bicalutamide form II and the amorphous form present similar spectra in the region between 1055 and 1724  $\text{cm}^{-1}$  and all amorphous forms (pure bicalutamide and the extrudates) exhibit similar spectra at low wavenumber.

### 4.3.2.2 Raman spectroscopic mapping

In order to gain chemical and spatial detail on the dissolution processes in the extrudates, Raman mapping was undertaken as a function of time in the region between 1055 and 1724  $\text{cm}^{-1}$ . The data for the 5% extrudate are presented in Figure 4.6. No changes were observed during the dissolution beyond a reduction in the overall Raman intensity, which may result from the presence of the medium, loss of focus and the surface changing from flat and even to relatively rounded and uneven as the dissolution proceeds. These factors reduce the amount of sample in the Raman confocal plane and lead to a reduction in signal. These data, similarly to those obtained from the low drug-loaded amorphous felodipine solid dispersions (Chapter 3, Section 3.3.3.2), indicate that bicalutamide and copovidone dissolve with the same rate from the molecular dispersion, with the overall dissolution performance being dependent on the high water solubility of copovidone.

For the 50% extrudate, averaging the spectra from each map indicated that some changes occurred as the dissolution progressed (Figure B.2 in the Appendix B). However, averaged spectra are difficult to interpret in this case due to the similarity in the bicalutamide spectra already noted between forms II and the amorphous form, as well as due to the multi-component nature of the formulation. Therefore, MCR was used to spatially and spectrally deconvolute the changes in the patterns for the 50% extrudate. In the analysis, trial runs indicated that a suitable choice for number of components was three, and intensity thresholding was employed so that only the spectra from the compact were included in the analysis, i.e. the surrounding solution was excluded. The results of the MCR analysis are presented graphically in Figure 4.7. Note that half the maps are shown for reasons of space, i.e. every second one starting at 9 min, however the analysis included all maps and the remaining time-point maps can be found in the Appendix B (Figure B.3).

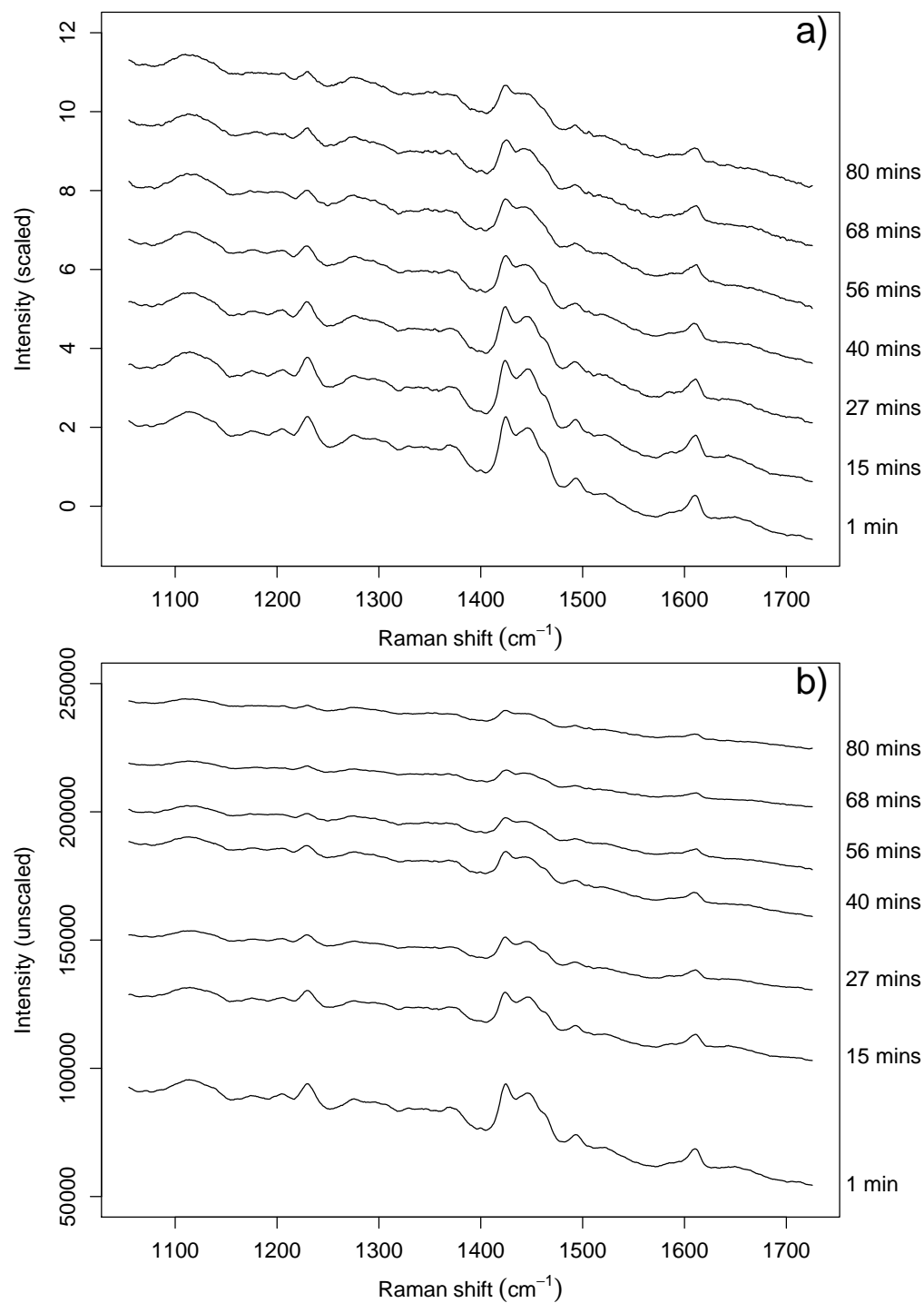


FIGURE 4.6: Averaged Raman spectra (1055–1724 cm<sup>-1</sup>) collected during the dissolution of the 5% extrudate. Presented in (a) are the variance-scaled Raman spectra and in (b) are the un-scaled Raman spectra. Y-axis offsets have been applied and differ between the two panels.

Comparison of the MCR loadings with reference spectra clearly indicates that the data have been resolved into components which correspond remarkably well with crystalline bicalutamide forms I and II, and the bicalutamide:copovidone extrudate. The variation in the scores as a function of space (within each map) and time (between maps, vertically descending) indicates that the starting material, the extrudate, decreases in weighting as time passes. In the early stages of the experiment crystalline form II appears and grows in weighting, while after approximately the 592-min time-point the weighting of form I increases. Form I continues to increase in weighting at the expense of both the extrudate and form II, with the latter reducing in weighting after 889 min. The crystallisation of amorphous bicalutamide into form II has been previously reported,<sup>128,129</sup> and the hypothetical sequence amorphous  $\rightarrow$  metastable form II  $\rightarrow$  stable form I is in accord with the long-standing Ostwald's rule of stages. However, from the results presented so far it is not possible to distinguish between the linear pathway amorphous  $\rightarrow$  form II  $\rightarrow$  form I, and an alternative parallel pathway whereby amorphous  $\rightarrow$  form II and amorphous  $\rightarrow$  form I occur independently, with the crystallisation to form I having a longer induction period than the crystallisation to form II.

At the end of the experiment the remaining compact was removed from the flow cell, cut through the centre and analysed by Raman spectroscopy and visually. Data are presented in Figure 4.8. The re-crystallisation of the drug to a mixture of forms I (dominant at the end of the experiment) and II occurs from the outside of the compact, with the interior being unchanged bicalutamide/copovidone extrudate. XRPD data from the entire compact recovered after the dissolution experiment (Figure 4.9) are in full accord with these *ex situ* Raman data, showing that bicalutamide is predominantly a mixture of crystalline form I and amorphous.

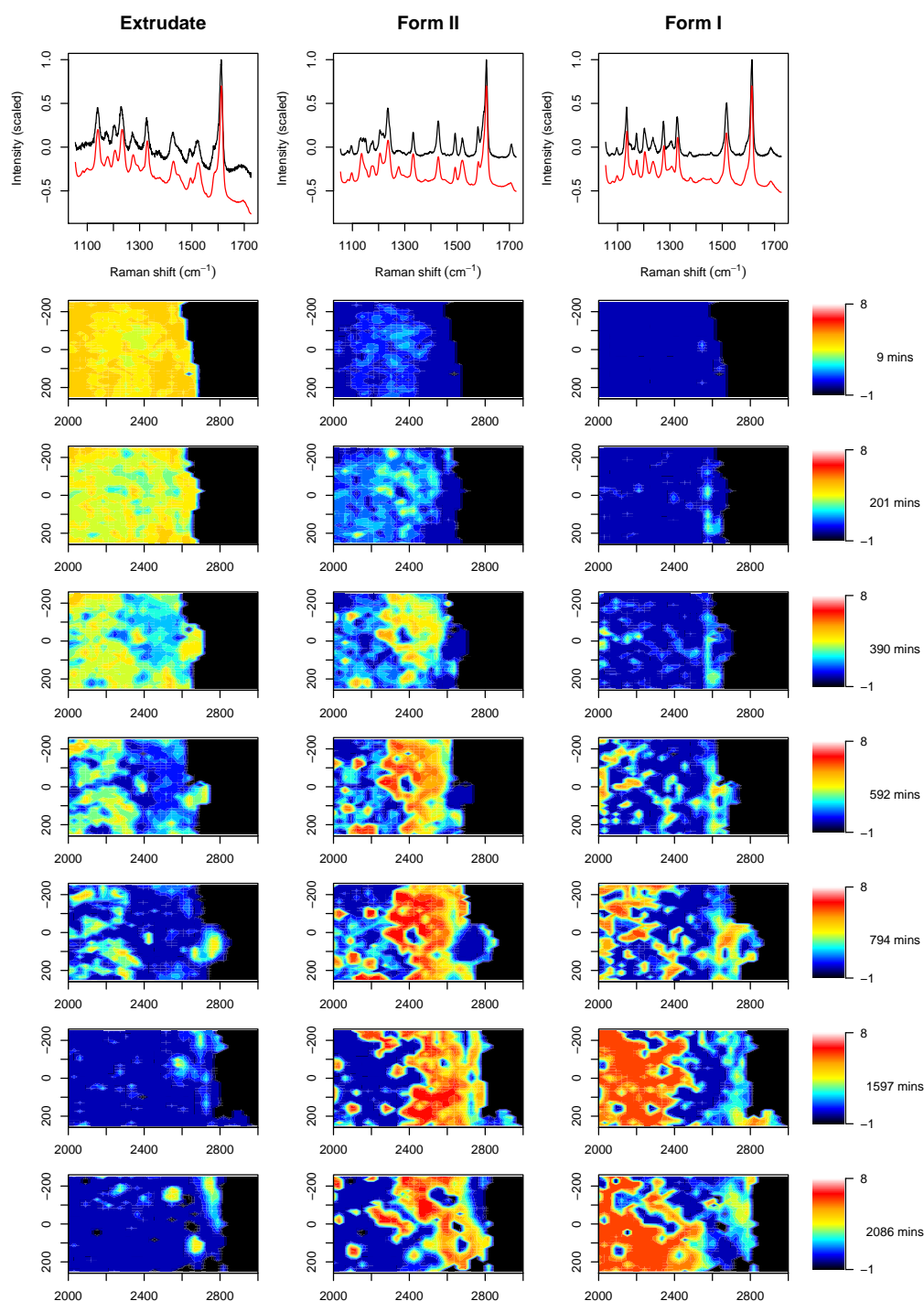


FIGURE 4.7: MCR Raman maps collected as a function of time through the dissolution experiment for the 50% extrudate. Here presented are the loadings (with reference spectra in black) and the scores plots for the first three MCR components. White/red colours indicate areas where a phase is present to its maximum, while black/blue colours represent areas where it is present at its minimum. Areas with variable weighting of that phase are indicated by a continuum of white-red-orange-yellow-cyan-blue-black colours. Raw data were variance-scaled before performing MCR analysis.

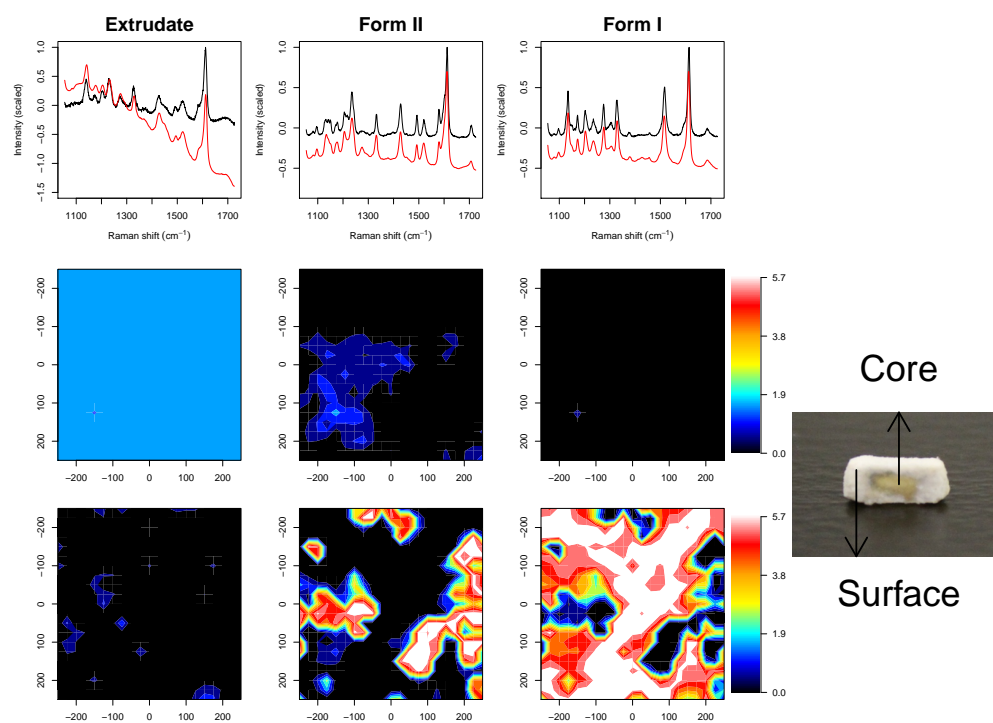


FIGURE 4.8: MCR Raman maps of the inner and outer sections of the compact. Here presented are the loadings (with reference spectra in black) and the scores plots of the first three MCR components, with data being variance-scaled prior to plotting.

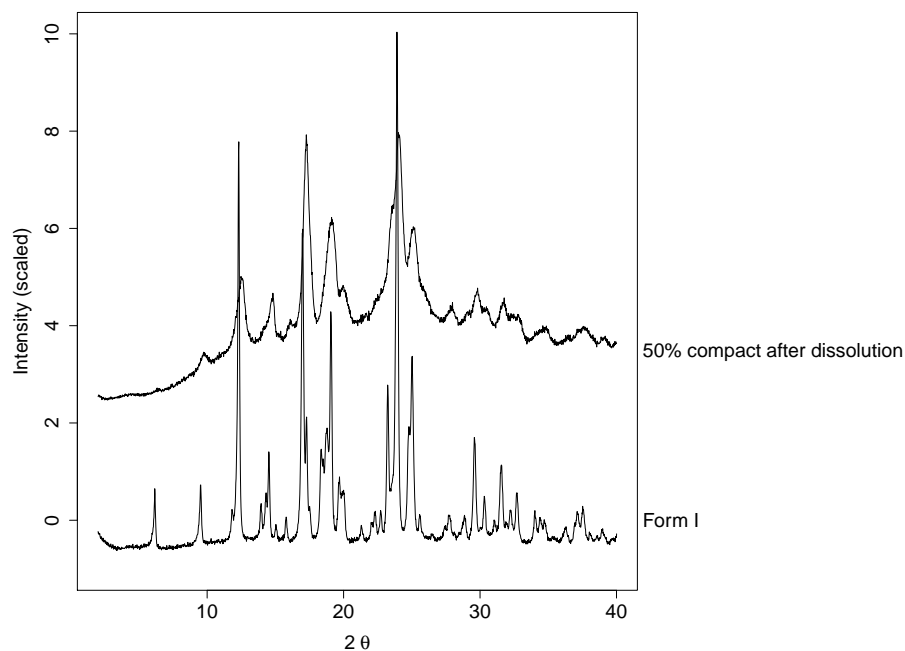


FIGURE 4.9: XRPD patterns of crystalline bicalutamide form I (reference) and the 50% extrudate residue recovered after the dissolution experiment.

The Raman mapping results, for the 50% extrudate, considered alongside the RDDR analysis and the previous data on high-drug loaded amorphous felodipine solid dispersions (Chapter 3, Section 3.3.3.2), suggest that the hydrophilic polymer preferentially dissolves from the exterior of the compact. This leaves a drug-rich (therefore hydrophobic) shell on the outside of the compact, which is initially amorphous. The decrease in polymer concentration and increase in (amorphous) drug naturally leads to the crystallisation of the drug. To address directly the question of the crystallisation mechanism, a kinetic analysis of the crystallisation processes was undertaken, as outlined below.

While the MCR results are very useful for gaining a qualitative understanding of the spectral changes occurring, they are less useful for a quantitative analysis as the proportion of the spectral weighting cannot be related to the actual concentration without suitable standards. Therefore, a simple three-level classification procedure was undertaken and each spectrum at every x-y-time point was assigned to extrudate, form I or form II, based upon the calculated correlations between the three reference spectra and the relevant experimental spectrum with its unique x-y-time labels. To remove the effect of the compact expanding/moving, the results are reported as percentages. Only the area corresponding to the compact was included in this analysis.

Results for the kinetic analysis are presented in Figure 4.10 for both the classification (i.e. experimental data) and for the kinetic model. The kinetic model included first-order rate constants for the processes  $A \rightarrow II$ ,  $A \rightarrow I$  and  $II \rightarrow I$ , which were adjusted according to the least-squares method until an optimised model was arrived at. To summarise, the rates of conversion  $A \rightarrow II$  and  $A \rightarrow I$  are similar, both being around  $10^{-3} \text{ min}^{-1}$ . The rate of conversion  $II \rightarrow I$  is found to be approximately an order of magnitude lower and therefore the analysis distinctly points towards a mixed crystallisation mechanism. The appearance of form I directly from the amorphous form is favoured compared to the conversion  $II \rightarrow I$ . The robustness of the analysis

was cross-checked by constraining the rate constant for  $A \rightarrow I$  to be  $0 \text{ min}^{-1}$ , and the resulting model (Figure B.4 of Appendix B) is clearly far inferior to the unconstrained model in which the rate constant for  $A \rightarrow I$  is found to be of order  $10^{-3} \text{ min}^{-1}$ . Therefore, it can be concluded that the parallel crystallisation mechanism is dominant compared to the serial one in terms of kinetics.

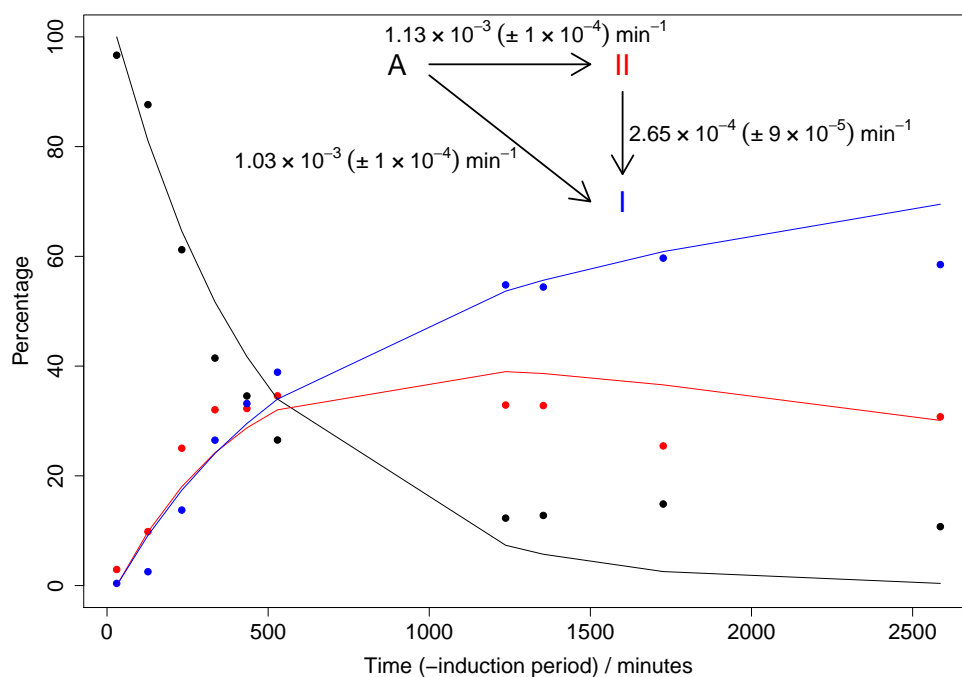


FIGURE 4.10: Experimental (dotted plots) and fitted (line plots) data of the three-step kinetic model. The induction period represents the first 360 min of the experiment. Estimated uncertainties are shown in parentheses.

To summarise, kinetic modelling of the classification data pointed towards the predominance of a non-Ostwald “parallel” crystallisation mechanism, in which crystalline form I bicalutamide nucleates directly from the amorphous form rather than from form II. Given that the amount of form II decreases after 889 min the pathway  $II \rightarrow I$  clearly has some importance, but the main route for formation of form I appears to be direct random nucleation from the amorphous form.

## 4.4 Conclusions

This chapter showed that the drug-to-polymer ratio is a key factor for determining the dissolution mechanisms of the amorphous bicalutamide solid dispersions, and this is consistent with the previous work on felodipine reported in Chapter 3. The 5% sample dissolution mechanism involved the hydrophilic polymer and the hydrophobic drug dissolving at the same rate and the compact was completely dissolved after 85 min. The same behaviour was observed for the low drug-loaded amorphous felodipine solid dispersions (Chapter 3). In contrast, the 50% sample remained intact even after 3000 min. It was hypothesised, based on the previous findings on the high drug-loaded felodipine ASDs, that the preferential dissolution of the hydrophilic polymer led to a shell of amorphous hydrophobic drug around the exterior of the compact. Highly chemically- and spatially-detailed Raman maps indicated that this shell transformed firstly to metastable crystalline form II, then to stable form I. The combination of Raman spectroscopy and MCR analysis was demonstrated to be very useful for discriminating between the different solid forms of bicalutamide, i.e. amorphous, form II and form I. By fitting a kinetic model to the data extracted from the Raman maps it was possible to understand the re-crystallisation mechanisms by which the low energy form I appeared. Form I was shown to crystallise preferentially from the amorphous form in a random nucleation mechanism, rather than from the crystalline form II. The interior of the compact was protected from water ingress by the shell of hydrophobic drug and remained a copovidone/bicalutamide molecular dispersion even after *ca.* 50 h of immersion in flowing water.

## Chapter 5

# Magnetic resonance imaging and $^1\text{H}$ nuclear magnetic resonance for studying the dissolution of bicalutamide extrudates

### 5.1 Introduction

In Chapter 4 Raman spectroscopy along with the RDDR test and the optical observation were employed to gain additional chemical information on the dissolution performance of the bicalutamide extrudates. The dissolution performance, similarly to the felodipine ASDs, was shown to be strongly affected by the drug loading. In the 5% drug loading, bicalutamide and copovidone dissolved with the same rate from the molecular dispersion, pointing to a polymer-controlled drug release mechanism. In contrast, for the 50% extrudate the dissolution rates of both bicalutamide and copovidone were found to be extremely low due to the formation of an amorphous

drug-rich shell followed by the drug re-crystallisation, pointing to a drug release dependent on the low aqueous solubility and high hydrophobicity of bicalutamide.

In this chapter the dissolution mechanisms of the bicalutamide:copovidone ASDs were further explored using a combined suite of analytical techniques, in an attempt to complement the Raman data shown in Chapter 4. The dissolution of the 5% extrudate (low drug loading) and this time the 30% extrudate (intermediate drug loading) was tested, with the aim of obtaining additional information on how the drug amount affects the dissolution performance and mechanisms. A combined MRI/UV-Vis flow cell system was used, allowing changes in dissolution profile to be related to physical changes occurring in the solid material. Off-line quantitative suppressed-water  $^1\text{H}$  NMR was also employed to, similarly to the RDDR test, simultaneously measure the dissolution profiles and rates of both the drug and the polymer from the molecular dispersion.

## 5.2 Materials and methods

### 5.2.1 Materials

Details of bicalutamide were discussed in Chapter 4, Section 4.2.1, while information on copovidone in Chapter 3, Section 3.2.1.

### 5.2.2 Samples preparation

The details for the preparation of the extrudates (5% and 30% drug loading) were discussed in Chapter 4, Section 4.2.2. The XRPD pattern and Raman spectrum of the 5% extrudate were shown in Figures B.1 and 4.4 respectively, while those of the 30% extrudate are presented in Figures C.1 and C.2 of the Appendix C.

## 5.2.3 Analytical methods

### 5.2.3.1 X-ray powder diffraction

The XRPD method is reported in Chapter 3, Section 3.2.3.1.

### 5.2.3.2 Raman spectroscopy

The same Raman system previously described in Chapter 3, Section 3.2.3.3 was employed.

### 5.2.3.3 Magnetic resonance imaging ultraviolet-visible flow cell system

The dissolution performance of circular compacts with a diameter of 10 mm and a weight of approximately 290 mg was investigated. Powders were compressed using a Specac manual hydraulic press using a compression force of *ca.* 50 kN. The difference in compression force compared to the Raman studies derives from the use of different dies (10 mm *vs* 5 mm) which allow different maximum compression forces to be used, i.e. *ca.* 50 kN for the 10 mm die and *ca.* 20 kN for the 5 mm die. The dissolution tests were performed in a USP IV-type flow cell previously described by Langham et al.<sup>113</sup> 1 L of pH 6.5 phosphate buffer dissolution medium maintained at a temperature of 37 °C using a temperature-controlled water bath was circulated continuously at a flow rate of 15 mL·min<sup>-1</sup>.

The dissolution profile of bicalutamide was obtained by recording the absorbance of the unfiltered dissolution medium at 275 nm (wavelength maxima of bicalutamide) and 350 nm (no observed absorbance, for correction for any suspended particles) at regular time intervals using a Agilent 8453 UV-Vis spectrophotometer with a 10 mm quartz flow cell (Starna Scientific). The dissolution data were calibrated against the absorbance of a series of standard solutions of bicalutamide in water-acetonitrile 75/25 (v/v).

The flow cell was sited in the probe of a 400 MHz Bruker Avance NMR spectrometer fitted with a Micro2.5 imaging accessory fitted with a 25 mm O.D. RF coil. The images were collected as a function of time using a FLASH protocol to generate  $16 \times 1 \text{ mm}^2$  concatenated axial slices with a field of view of 25 mm. The echo time was 3.0 ms and the repetition time was 500 ms giving a scan time of 1 min 4 s for each 16 slice experiment. A data matrix size of  $128 \times 128$  pixels was recorded giving a resolution of 0.0195 cm/pixel in the read direction. Data were processed using ParaVision™ software v4.0. Changes in the size of the compacts were followed by measuring the dimensions of a single slice as a function of time.

#### 5.2.3.4 $^1\text{H}$ nuclear magnetic resonance

All NMR measurements were performed on a Bruker Avance III 500 MHz NMR spectrometer fitted with a 5 mm QCI cryoprobe. The spectra from the dissolution samples and the reference solutions were acquired at 300.0 K with a spectral width of 10 kHz, with 64k data points in the time domain. A recycle delay of 4 s was used and the peak due to water was suppressed using a 1D NOESY pulse program with presaturation and spoil gradients (noesygprr1d) and with irradiation at the water frequency during the recycle and mixing time delays. The receiver gain was set to 128 and kept the same for each experiment. Data were processed using the Bruker Topspin 3.0 software. Interactive zero order phase correction was applied to all the spectra and the “Use lastscale for calibration” functionality was employed to directly compare integrals across multiple spectra.

## 5.3 Results and discussion

### 5.3.1 Solution-state assays

#### 5.3.1.1 Ultraviolet-visible flow cell experiments

The UV-Vis dissolution profiles of the 5% and 30% extrudates are presented in Figure 5.1. The experiments were repeated twice for each drug loading to obtain an indication of the reproducibility in dissolution performance. A good reproducibility was observed of the two experiments of the 5% extrudate. Both profiles are characterised by two regions which correspond to the dissolving bicalutamide followed by the drug precipitation. In contrast, the two dissolution profiles of the 30% extrudate appear highly non-reproducible, i.e. they are characterised by a different number of regions, but both show two pronounced “turning points” at 350 and 700 min (first experiment) and 250 and 500 min (second experiment) where the rate of drug dissolution increases. Overall, the UV-Vis data indicate a lack of controlled release for the 30% extrudate compared to the 5% extrudate.

These data indicate that there is a significant difference in dissolution behaviour between the two drug loadings. In the first experiment the 5% extrudate reaches a maximum concentration of  $8.5 \mu\text{g}\cdot\text{mL}^{-1}$  (which corresponds to approximately 59% of cumulative drug amount in solution) at 95 min, with an initial dissolution rate of  $0.12 \mu\text{g}\cdot\text{mL}^{-1}\cdot\text{min}^{-1}$ . The 30% extrudate achieves a maximum concentration in solution of  $14.1 \mu\text{g}\cdot\text{mL}^{-1}$  ( $\approx 16\%$  of cumulative drug amount in solution) at 1179 min and an initial dissolution rate of  $0.01 \mu\text{g}\cdot\text{mL}^{-1}\cdot\text{min}^{-1}$ . For both drug loadings, the concentration of bicalutamide in solution declines after reaching the maximum concentration. The final measured concentration at 1319 min is  $4.1 \mu\text{g}\cdot\text{mL}^{-1}$  ( $\approx 28\%$  of cumulative drug amount in solution) and  $13.6 \mu\text{g}\cdot\text{mL}^{-1}$  ( $\approx 15\%$  of cumulative drug amount in solution) for the 5% extrudate and 30% extrudate respectively.

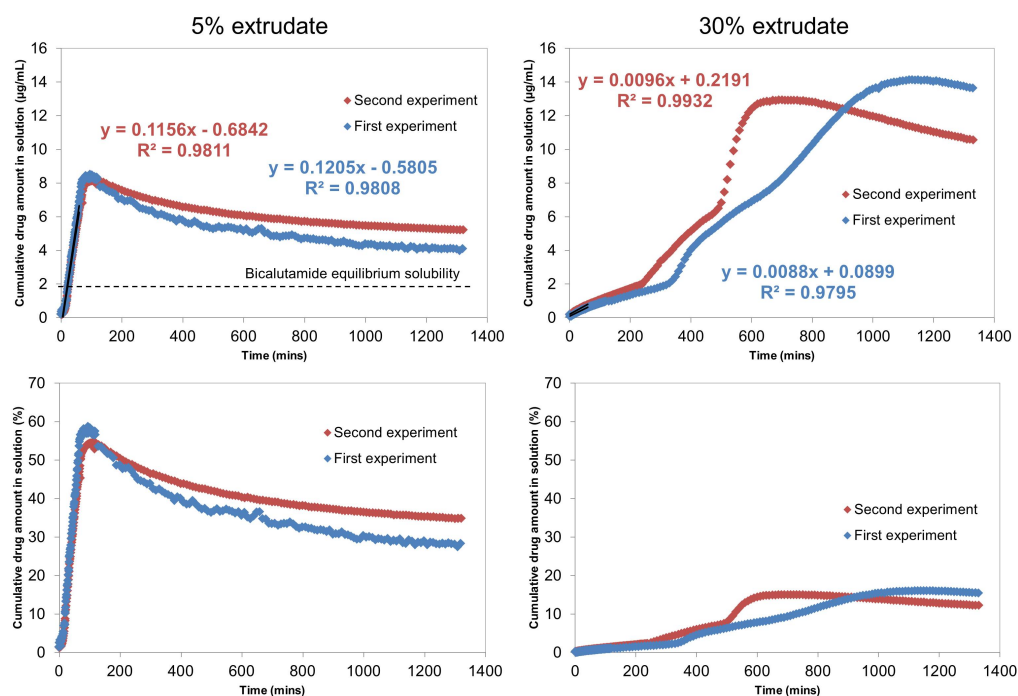


FIGURE 5.1: UV-Vis dissolution profiles of bicalutamide released from the 5% and 30% extrudates. The dissolution rates of the initial time-points were calculated using linear regression analysis. Linear best fits for the 5% and 30% dissolution experiments are included.

In accordance with the previous data on felodipine (Chapter 3, Section 3.3.2) and bicalutamide (Chapter 4, Section 4.3.1), the dissolution behaviour of the bicalutamide extrudates is clearly dependent on the drug loading. At low drug loading (i.e. 5% extrudate), the performance is dependent on the high aqueous solubility of the polymer. The drug is quickly released and the maximum concentration corresponding to approximately 59% of cumulative drug amount in solution is reached within 95 min. For the extrudate containing a higher proportion of bicalutamide (i.e. 30% extrudate), the dissolution performance is dominated by the physicochemical properties of the drug (e.g. low aqueous solubility and high hydrophobicity). As a result, the initial dissolution rate is approximately one order of magnitude lower ( $0.01 \mu\text{g}\cdot\text{mL}^{-1}\cdot\text{min}^{-1}$  vs  $0.12 \mu\text{g}\cdot\text{mL}^{-1}\cdot\text{min}^{-1}$ ) and the maximum concentration corresponding to 16% of cumulative drug amount in solution is achieved only after 1179 min.

The UV-Vis data also show that the bicalutamide content in solution for both the 5% and 30% extrudates decreases after achieving the maximum concentration at 95 and 1179 min respectively, indicating that the drug supersaturation in solution is not maintained by the presence of copovidone across the entire dissolution test. In addition, in both experiments this reduction is accompanied by an increase of the absorbance at 350 nm (Figure 5.2), which is related to the scattering as well as absorption contributions of insoluble particles.<sup>173</sup> The formation of these particles, which cause the subsequent reduction in solution concentration, has been previously observed also for amorphous spray-dried solid dispersions of felodipine and copovidone.<sup>113</sup>

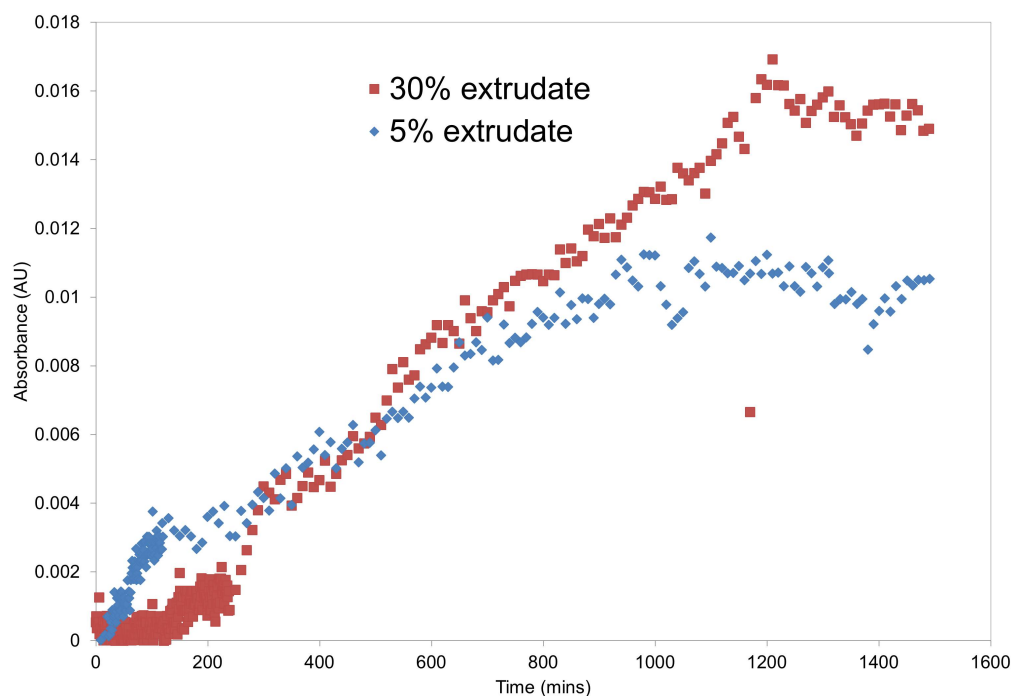


FIGURE 5.2: Absorbance UV-Vis values at 350 nm acquired during the dissolution of the 5% and 30% extrudates.

It is also important to note that the 30% bicalutamide extrudate exhibited a markedly superior dissolution profile compared to the corresponding drug loading of amorphous spray-dried solid dispersions of felodipine and copovidone.<sup>113</sup> This can be ascribed to the higher dissolution rate of bicalutamide over felodipine,<sup>161</sup> although the manufacturing route (hot melt extrusion *vs* spray drying) may also be a factor.

### 5.3.1.2 $^1\text{H}$ nuclear magnetic resonance

In this section  $^1\text{H}$  NMR is employed to complement the UV-Vis data for understanding the dissolution performance of the bicalutamide extrudates. With respect to standard UV-Vis measurements, by  $^1\text{H}$  NMR it is possible to simultaneously determine the amount of drug and polymer in solution. As the dissolution performance of poorly soluble drugs can be largely dependent on that of the polymeric carrier, quantitative measurements of the latter provide valuable information.<sup>20,163</sup> In addition, similarly to the previously employed RDDR methodology, the dissolution rate of the drug and the polymer can be used to determine an index of dissolution performance of the extrudate (Chapter 3, Section 3.3.2, Equation 3.1). The temporal evolution of NMR spectra for the 5% and 30% extrudates are presented in Figure 5.3, while the spectra from the reference solutions are shown in Figure C.3 of the Appendix C. For each spectrum, two integrals from bicalutamide and copovidone were generated and then scaled to integrals obtained from the reference solutions of known concentration. The spectra from the reference solutions were obtained using identical experimental conditions. The release profiles of the individual species are shown in Figure 5.4.

For the 5% extrudate (e.g. first experiment), bicalutamide exhibits an initial dissolution rate of  $0.16 \mu\text{g} \cdot \text{mL}^{-1} \cdot \text{min}^{-1}$  and that of copovidone is  $3.84 \mu\text{g} \cdot \text{mL}^{-1} \cdot \text{min}^{-1}$ . The index of performance resulted in a value of 0.8, indicating that the drug and polymer dissolve approximately with the same rate from the dispersion. The index of performance obtained from the  $^1\text{H}$  NMR system is similar to that previously obtained from the RDDR test (value of 0.94, Chapter 4, Section 4.3.1, Table 4.2).

For the 30% extrudate, the dissolution rates of both bicalutamide and copovidone are lower with values of 0.009 and  $0.18 \mu\text{g} \cdot \text{mL}^{-1} \cdot \text{min}^{-1}$  respectively.

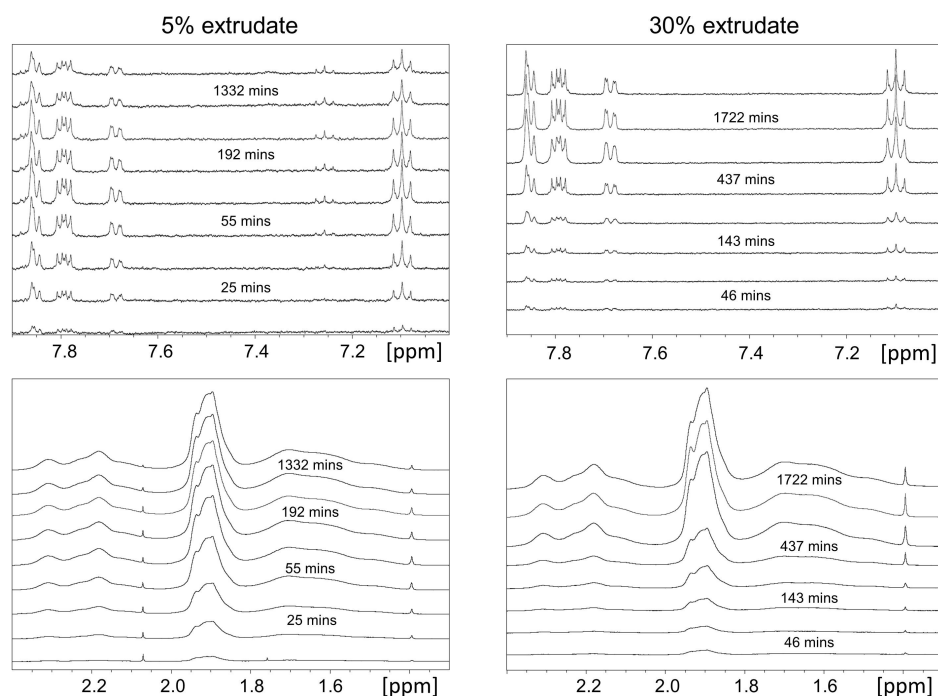


FIGURE 5.3: Portions of the  $^1\text{H}$  NMR spectra acquired during the dissolution of the 5% and 30% extrudates. Bicalutamide and copovidone data were obtained from single integrals at 7.06–7.14 ppm (two aromatic protons of fluorobenzene) and 1.2–2.6 ppm (protons of pyrrolidone ring and methylene chains) respectively.

In agreement with these data, the dissolution rates of bicalutamide and copovidone from the 50% extrudate were also found extremely low using the RDDR test (Chapter 4, Section 4.3.1, Table 4.2). The index of performance of the 30% extrudate is also far inferior (0.15) compared to that of the 5% extrudate, indicating that for this drug loading the higher content of bicalutamide limits the dissolution performance of both bicalutamide and copovidone.

The dissolution rates of bicalutamide obtained from the  $^1\text{H}$  NMR experiments ( $0.16 \text{ mL}^{-1} \cdot \text{min}^{-1}$  for the 5% extrudate and  $0.009 \text{ mL}^{-1} \cdot \text{min}^{-1}$  for the 30% extrudate) are in good agreement with those obtained from the UV-Vis ( $0.12 \text{ mL}^{-1} \cdot \text{min}^{-1}$  for the 5% extrudate and  $0.009 \text{ mL}^{-1} \cdot \text{min}^{-1}$  for the 30% extrudate).

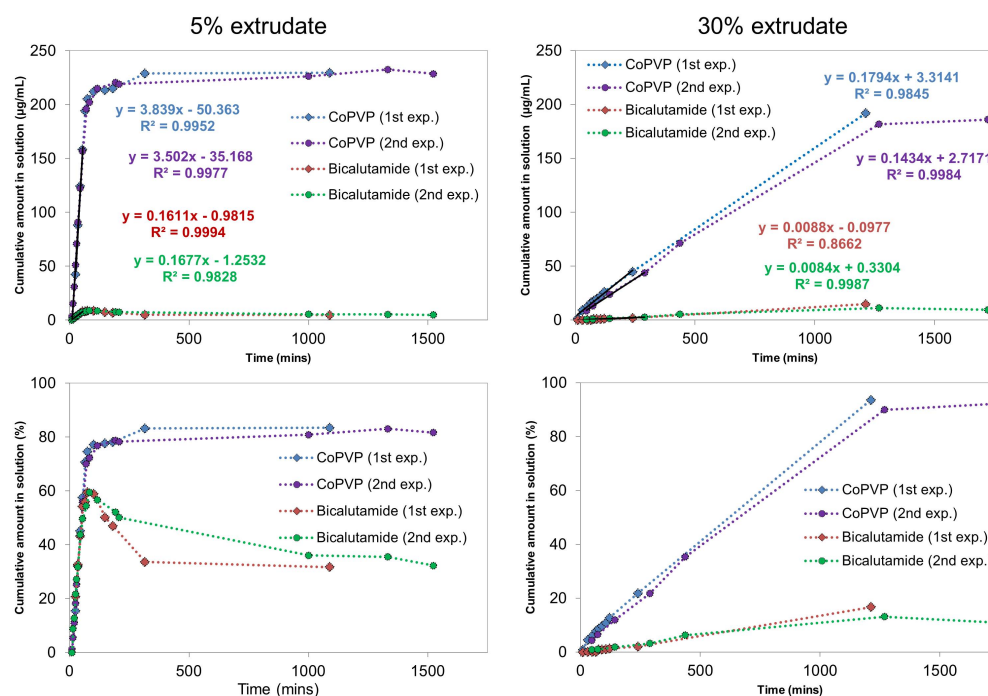


FIGURE 5.4: Release profiles obtained from the  $^1\text{H}$  NMR spectra of bicalutamide and copovidone from the 5% and 30% extrudates. Data were scaled using the reference standard solutions. Linear best fits for the dissolution profiles of the 5% and 30% extrudates are included.

Figure 5.4 also shows that for both the 5% and 30% extrudates, whilst copovidone achieves a dissolution release plateau, the bicalutamide concentration declines after reaching a maximum. In addition, for the 5% extrudate the bicalutamide precipitation begins before the copovidone dissolution is complete. This, in agreement with the previous UV-Vis data, clearly indicates that the supersaturation of the drug is not maintained by the polymer across the entire dissolution test.

## 5.3.2 Solid-state analysis

### 5.3.2.1 Magnetic resonance imaging flow cell experiments

The solution-state measurements obtained from the UV-Vis and  $^1\text{H}$  NMR data were then complemented with the solid-state measurements, i.e. MRI. The magnetic resonance images showing the temporal changes in one cross

sectional slice of the 5% and 30% extrudates during the dissolution test are shown in Figure 5.5 (first experiment) and Figure C.4 of the Appendix C (second experiment). In this MRI experiment the image contrast is due to differences in molecular mobility. As a result, protons in a solid environment have a faster  $T_2$  relaxation time and therefore the solid materials appear dark in the images. Protons in solution have a significantly slower  $T_2$  relaxation time and thereby they generate a bright image, while, for example, protons in a hydrating gel give an intermediate brightness.<sup>113</sup>

The images presented in Figure 5.5 show significantly different dissolution behaviours for the 5% extrudate (Figure 5.5a) and 30% extrudate (Figure 5.5b). The 5% extrudate undergoes erosion and it is almost entirely dissolved over a period of 56 min, while the 30% extrudate swells and remains intact after 265 min (it is then no longer attached to the support due to its swelling and expansion and as a consequence it is out of the instrumental field of view).

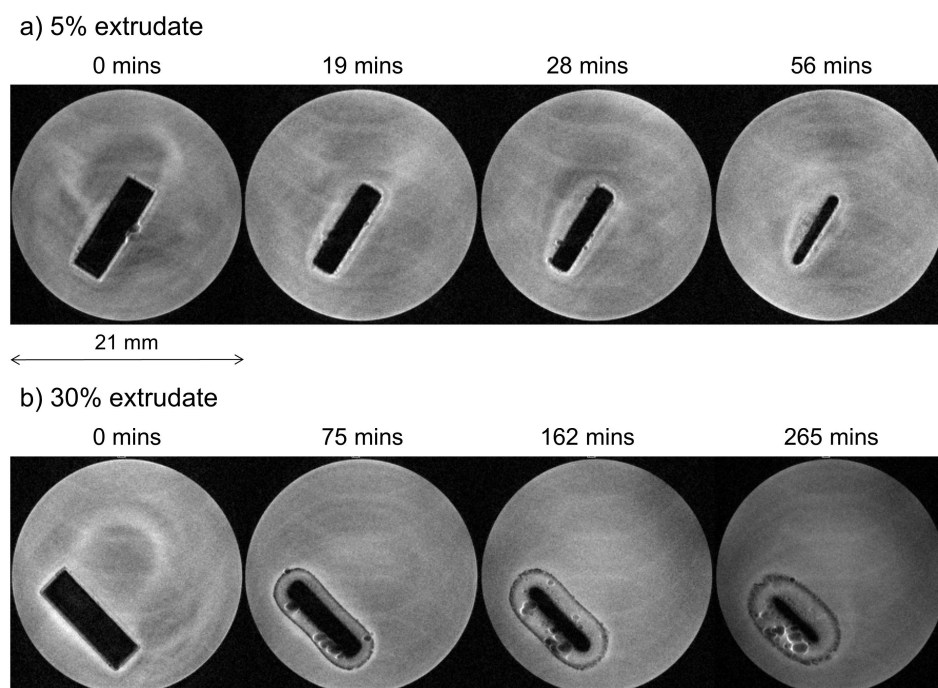


FIGURE 5.5: Magnetic resonance images (first experiment) showing the changes as a function of time in one cross sectional slice of the extrudates containing 5% (a) and 30% (b) of bicalutamide.

Throughout the experiments, the 30% extrudate exhibits a well-defined region of intermediate MRI contrast, which is either not present, or hardly present, in the 5% extrudate (Figure 5.6). This region is due to water ingress into the compact. It is clear that for the 5% sample the rates of water ingress and dissolution are similar, which prevents the formation of the intermediate contrast region, whereas for the 30% compact dissolution is markedly slower than water ingress.

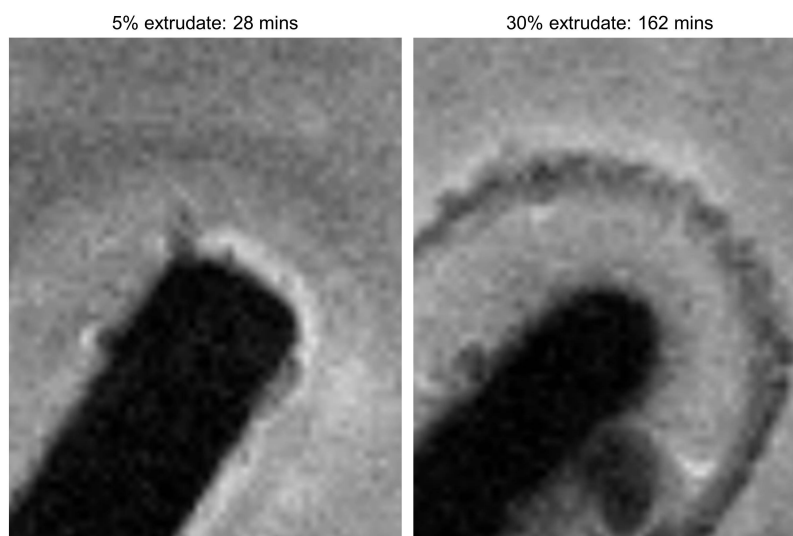


FIGURE 5.6: Zoom of the images collected for the 5% extrudate (28 min) and 30% extrudate (162 min) to highlight the well-defined region of intermediate MRI contrast present in the 30% extrudate.

Previous Raman data on a 50% sample indicated that the preferential dissolution of copovidone led to formation of an amorphous drug-rich shell which crystallised and appeared to strongly inhibit further erosion and dissolution of the compact (Chapter 3, Section 3.3.3.2 and Chapter 4, Section 4.3.2.2). Therefore, it is reasonable to suggest that this region of intermediate contrast in the magnetic resonance images of the 30% sample is due to water partially diffused in the copovidone matrix, which does not lead to dissolution and drug release due to a drug-rich shell which prevents further water ingress, and thus greatly reduces the dissolution rate of the compact. The formation of an amorphous drug-rich shell and the drug re-crystallisation are likely to be the main factors which determine lack of controlled release observed in the UV-Vis profiles for the 30% drug loading.

The difference in dissolution performance between the two drug loadings is reflected in Figure 5.7. The 5% extrudate quickly erodes with a linear erosion rate of  $1.1 \text{ mm}^2 \cdot \text{min}^{-1}$ , while the erosion rate for the 30% extrudate is slower and not linear due to the presence of the hydrating layer.

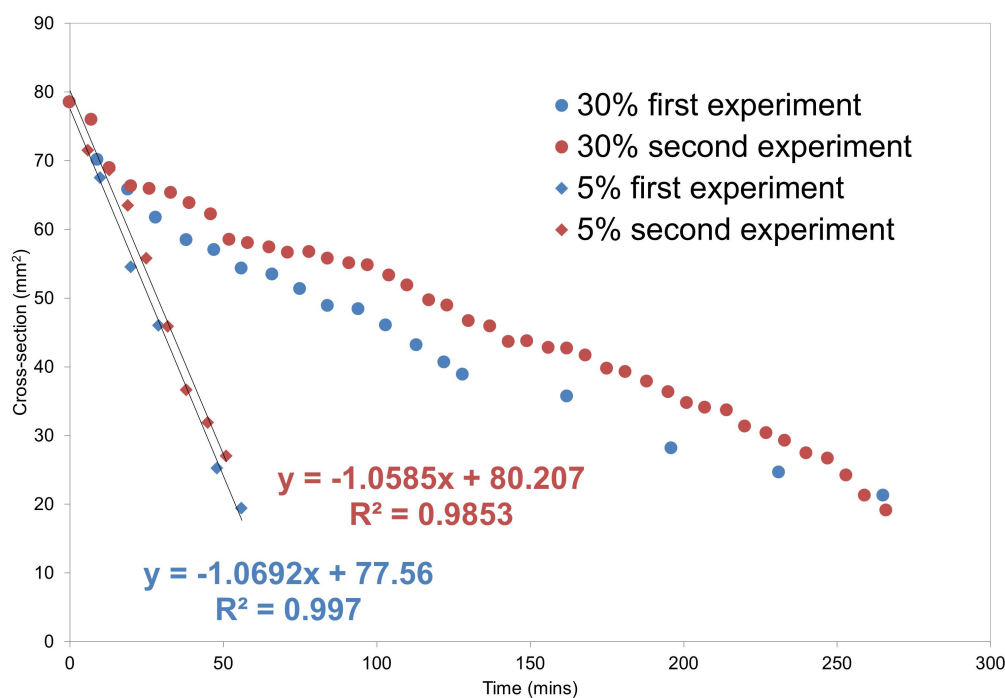


FIGURE 5.7: Evolution of the compact dimensions as a function of time for the 5% extrudate and 30% extrudate. Linear best fit to the data for the 5% extrudate is included. For the 30% extrudate, the dimensions of the compact core (solid material) were measured without considering those of the hydrated layer, to facilitate the comparison with the 5% extrudate. Data were collected only up to approximately 300 min due to the compact falling off from the support and being out of the instrumental field of view after this time-point.

At the end of the dissolution test of the 30% extrudate (approximately after 1700 min), a significant amount of undissolved material was present in the flow cell. This residue was removed from the flow cell and showed by Raman spectroscopy to contain crystalline bicalutamide form I (Figure 5.8), pointing to the drug re-crystallisation. The drug re-crystallisation was also observed during the dissolution experiment of the 50% drug-loaded extrudate (Chapter 4, Section 4.3.2.2).

The MRI images are in agreement the UV-Vis and  $^1\text{H}$  NMR data, indicating that for the 5% extrudate the release of bicalutamide is a polymer-controlled process whereby the dissolution is governed by the fast hydration of the highly water-soluble copovidone. For the 30% extrudate, the dissolution is dependent on the physicochemical properties of bicalutamide.

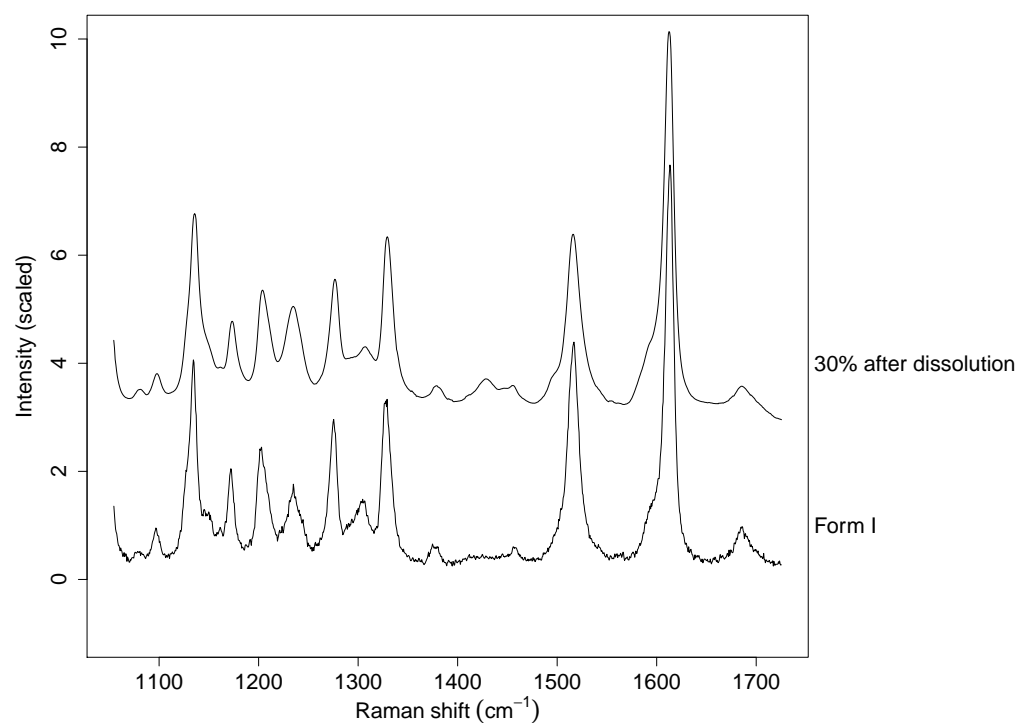


FIGURE 5.8: Raman spectra of crystalline bicalutamide form I (reference) and the 30% extrudate residue recovered after the dissolution experiment.

The low aqueous solubility and high hydrophobicity of the drug contribute to a slower water uptake into the compact which corresponds to a slower dissolution rate of both bicalutamide and copovidone.

## 5.4 Conclusions

In this chapter a combination of solution-state and solid-state analytical techniques was employed to complement the Raman data previously shown in Chapter 4 on amorphous bicalutamide solid dispersions. The MRI data

indicated that the 5% extrudate eroded linearly, which can be linked to the Raman data showing bicalutamide and copovidone dissolving with the same rate from the molecular dispersion (Chapter 4). In contrast, for the 30% extrudate the water ingress was significantly slower and this is thought to be due to the formation of an amorphous drug-rich shell (as shown by Raman in Chapters 3 and 4) which prevented further water ingress and thus greatly reduced the dissolution.  $^1\text{H}$  NMR has been proved to be a valid alternative to the previously employed RDDR methodology for tracking the dissolution profiles of different materials in multi-component systems. Quantitative  $^1\text{H}$  NMR data showed that for the 5% extrudate, bicalutamide and copovidone dissolved with approximately the same rate pointing to a matrix-controlled release, while for the 30% drug loading they dissolved at a significantly lower rate. For the 30% extrudate the dissolution performance, as previously seen in Chapter 4, was dominated by the physicochemical properties of the drug. It is important to compare the two solid-state analytical techniques used in this work, i.e. MRI and Raman spectroscopy. MRI can provide useful physical information on the dissolution processes (e.g. gel formation, matrix erosion, polymer swelling), by directly measuring the molecular mobility of water. However, the main limitation of MRI is the relatively low chemical selectivity. In contrast, Raman spectroscopy is able to readily discriminate between different chemical species (e.g. drug *vs* excipients) and solid forms (e.g. amorphous *vs* crystalline, polymorphic forms). However, compared to MRI, Raman spectroscopy can not provide any direct physical information on water ingress and hydrating polymeric matrices. Overall, only the chemical and physical data generated by the combination of these two advanced analytical techniques can provide a clear understanding of the drug release mechanisms from ASD formulations.

# Chapter 6

## Indomethacin-copovidone extrudates: a mechanistic study of pH-dependent controlled release

### 6.1 Introduction

As discussed in Chapters 3, 4 and 5 the dissolution performance of both felodipine and bicalutamide ASDs is strongly dependent on the drug loading. Raman spectroscopy along with a combination of other analytical techniques were successfully employed to identify the solid-state and solution-state changes and therefore draw potential mechanisms by which the dissolution occurred. For both APIs, at low drug loading the drug and the polymer dissolved with the same rate, with the overall behaviour being dependent on the high aqueous solubility of the polymer. In contrast, both amorphous felodipine and bicalutamide in the high drug-loaded extrudates re-crystallised, and the drug re-crystallisation was shown to follow the formation of an amorphous drug-rich shell.

In this chapter the dissolution behaviour of another ASD model which consists of poorly soluble indomethacin and copovidone was investigated. The aqueous solubility of indomethacin has been reported to increase from  $1.5 \mu\text{g}\cdot\text{mL}^{-1}$  at pH 1.2 to  $105.2 \mu\text{g}\cdot\text{mL}^{-1}$  at pH 7.4.<sup>137</sup> Previous dissolution studies on this drug have typically used a single constant pH,<sup>39,42,86,174,175</sup> which is un-representative of the *in vivo* situation, in which the pH typically differs between GI compartments, being 1.7-3.3 (median of 2.5) in the stomach and 5.6-7.0 (median of 6.3) in the duodenum (Figure 6.1).<sup>176</sup> In a recent work, however, ASDs of indomethacin and a range of polymers were tested in two independent experiments at pH 1.2 and 7.4 using the USP II apparatus.<sup>137</sup> In this chapter, the dissolution tests was performed in the flow-through cell previously described in Chapter 3. The flow-through cell is ideal for changing the dissolution medium during the test and this can be easily accomplished by directing the input from a different source. The materials were tested in pH 2 HCl dissolution medium to mimic the stomach conditions followed by a switch during the test to pH 6.8 phosphate buffer to simulate the post-stomach conditions, with the aim of probing the interactions between environmental pH and extrudate components. The dissolution behaviour of the indomethacin:copovidone extrudates was also studied as a function of the drug loading (from 5% to 90%). A Raman UV-Vis flow cell system along with optical observation and the RDDR test were used. The flow cell system includes an in-line UV-Vis spectrophotometer which enables changes in the amount of drug in solution (monitored by UV-Vis) to be directly related to physicochemical changes that occur in the solid-state to the extrudate (monitored by Raman).

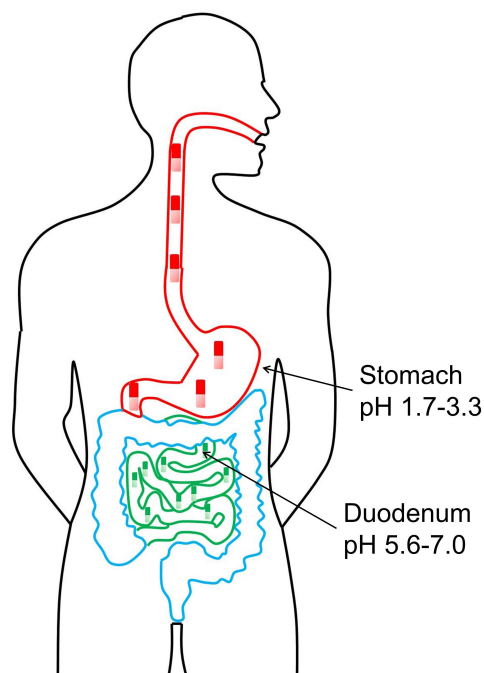


FIGURE 6.1: Scheme of the body showing the pH values in the stomach and in the duodenum.

## 6.2 Materials and methods

### 6.2.1 Materials

Indomethacin ( $\geq 99\%$  purity) was purchased from Sigma-Aldrich (St. Louis, USA) and found by XRPD and Raman spectroscopy to be the  $\gamma$  polymorph (Figures D.1 and D.2 of the Appendix D). Indomethacin was used as received and without any further purification. Details of copovidone were provided in Chapter 3, Section 3.2.1.

### 6.2.2 Samples preparation

#### 6.2.2.1 Preparation of the amorphous and $\alpha$ forms of indomethacin

The amorphous form of indomethacin was prepared by heating the  $\gamma$  form to  $170\text{ }^{\circ}\text{C}$  and cooling the melt to room temperature. The formation of the

amorphous form was confirmed by XRPD and Raman spectroscopy (Figures D.3 and D.4 of the Appendix D). The  $\alpha$  form was prepared according to literature by the addition of deionised water to a saturated solution of  $\gamma$  indomethacin in ethanol at 80 °C.<sup>177</sup> The precipitated crystals were removed by filtration and dried under vacuum at room temperature. XRPD and Raman spectroscopy confirmed the formation of the  $\alpha$  form (Figures D.1 and D.2 of the Appendix D).<sup>47,69</sup>

### **6.2.2.2 Preparation of the indomethacin-copovidone extrudates**

The extrudates of indomethacin and copovidone at a different drug-to-polymer ratio (5% w/w, 15% w/w, 30% w/w, 50% w/w, 70% w/w and 90% w/w indomethacin) were prepared using the method reported in Chapter 3, Section 3.2.2. The temperature was set to 170 °C. XRPD and Raman spectroscopy confirmed the formation of the amorphous form and the absence of the  $\gamma$  form (Figures D.3 and D.4 of the Appendix D).

## **6.2.3 Analytical methods**

### **6.2.3.1 X-ray powder diffraction**

The XRPD method is reported in Chapter 3, Section 3.2.3.1.

### **6.2.3.2 Rotating disk dissolution rate test**

The RDDR test was conducted as previously described in Chapter 3, Section 3.2.3.2. The dissolution experiments were performed in a relevant dissolution medium (pH 2 HCl and pH 6.8 phosphate buffer) at a temperature of 25 °C ( $\pm 0.5$ ). All the experiments were carried out in duplicate. For the HPLC, acetonitrile/deionised water containing 0.025% of ammonia water was selected as the optimal mobile phase. A linear gradient elution

was used starting at 5% acetonitrile/95% deionised water and ending at 90% acetonitrile/10% deionised water after 3.5 min, with chromatograms collected up to 5 min. Standard solutions of indomethacin and copovidone were prepared to generate a calibration curve covering the concentration range of the dissolved samples and analysed alongside the RDDR samples. The partial RDDR of indomethacin and copovidone from all materials was calculated using linear regression analysis of the first 20 min, where the trend is linear, in accordance with Pharmacopoeia procedures.<sup>90,162</sup>

### 6.2.3.3 Raman ultraviolet-visible flow cell system

**Raman spectroscopy** The same Raman system and dissolution set-up previously described in Chapter 3, Section 3.2.3.3 was employed. All experiments were performed in 500 mL of pH 2 HCl water solution which was replaced after 120 min by 500 mL of pH 6.8 phosphate buffer. The flow rate was set to 5 mL·min<sup>-1</sup>.

Raman spectra of the reference materials were acquired from 40 to 3500 cm<sup>-1</sup>. During the dissolution experiments, spectra were collected between 1055 and 1725 cm<sup>-1</sup> as a function of time across an area of 500 × 500 μm with a grid spacing of 50 μm along both the x and y axes, a total of 121 spectra per map. As each individual spectrum was collected for 3 s, repeated once in order to automatically remove the spikes due to cosmic rays, the whole map required approximately 15 min.

For Raman data analysis, spectra from each time-point map were integrated to generate a single averaged spectrum. Averaging facilitated the determination of any spectral changes occurring to the solid form during the dissolution test.

**Ultraviolet-visible** UV-Vis data were collected using a combined miniature light source-flow cell-spectrometer system. A Z-shaped flow cell (FIA-Z-SMA, Ocean Optics, USA) with a 10 mm pathlength was simultaneously

connected through optical fibers to a deuterium light source (DT-MINI-2, Ocean Optics, USA) and a CCD spectrometer (USB2000+, Ocean Optics, USA). The dissolution profiles of indomethacin were obtained by measuring the absorbance at 318 nm every 1 min. The scheme of the Raman UV-Vis flow cell system is shown in Figure 6.2. A peristaltic pump (IPS, ISMATEC, Switzerland) pumped the relevant dissolution medium through the Z-shaped UV-Vis flow cell and the Raman flow cell in a closed loop flow.

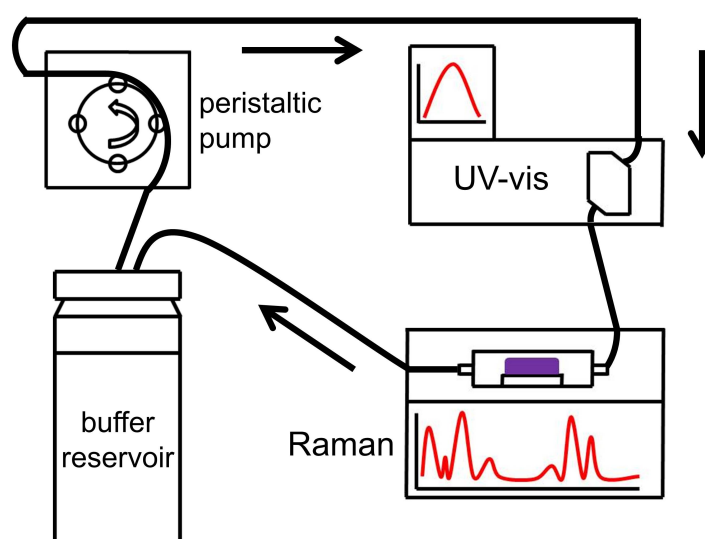


FIGURE 6.2: Scheme of the experimental configuration employed to monitor in real time the dissolution of the extrudates by UV-Vis spectrophotometry and Raman spectroscopy. The arrows indicate the direction of the flow of the buffer solution.

#### 6.2.3.4 Optical imaging

The optical imaging method has been previously described in Chapter 3, Section 3.2.3.4.

## 6.3 Results and discussion

### 6.3.1 Optical imaging

Optical images from the dissolution experiment of the indomethacin and copovidone extrudates, 100% copovidone and both the 100% amorphous and 100%  $\gamma$  forms of indomethacin are presented in Figures 6.3 and 6.4. Firstly, it is important to notice the different time-scales between dissolution of 100% copovidone and the 5% extrudate (Figure 6.3), and the other indomethacin-copovidone extrudates (from 15% to 90% drug loading), the 100% amorphous and 100%  $\gamma$  forms of indomethacin (Figure 6.4). The former were observed in pH 2 HCl buffer for 90 min, after which the images show that both compacts are completely dissolved. Photographs of the latter were taken after 120 min in pH 2 HCl buffer, followed by switching to pH 6.8 phosphate buffer for the rest of the test with images being collected for another 380 min.

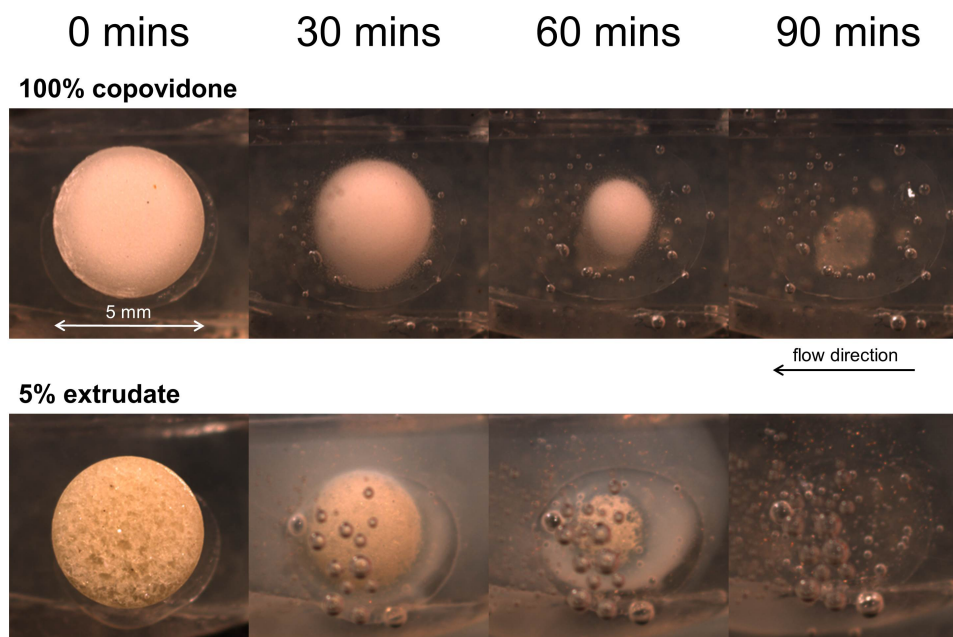


FIGURE 6.3: Photographs taken through the dissolution experiment in pH 2 HCl buffer of 100% copovidone and the 5% extrudate.

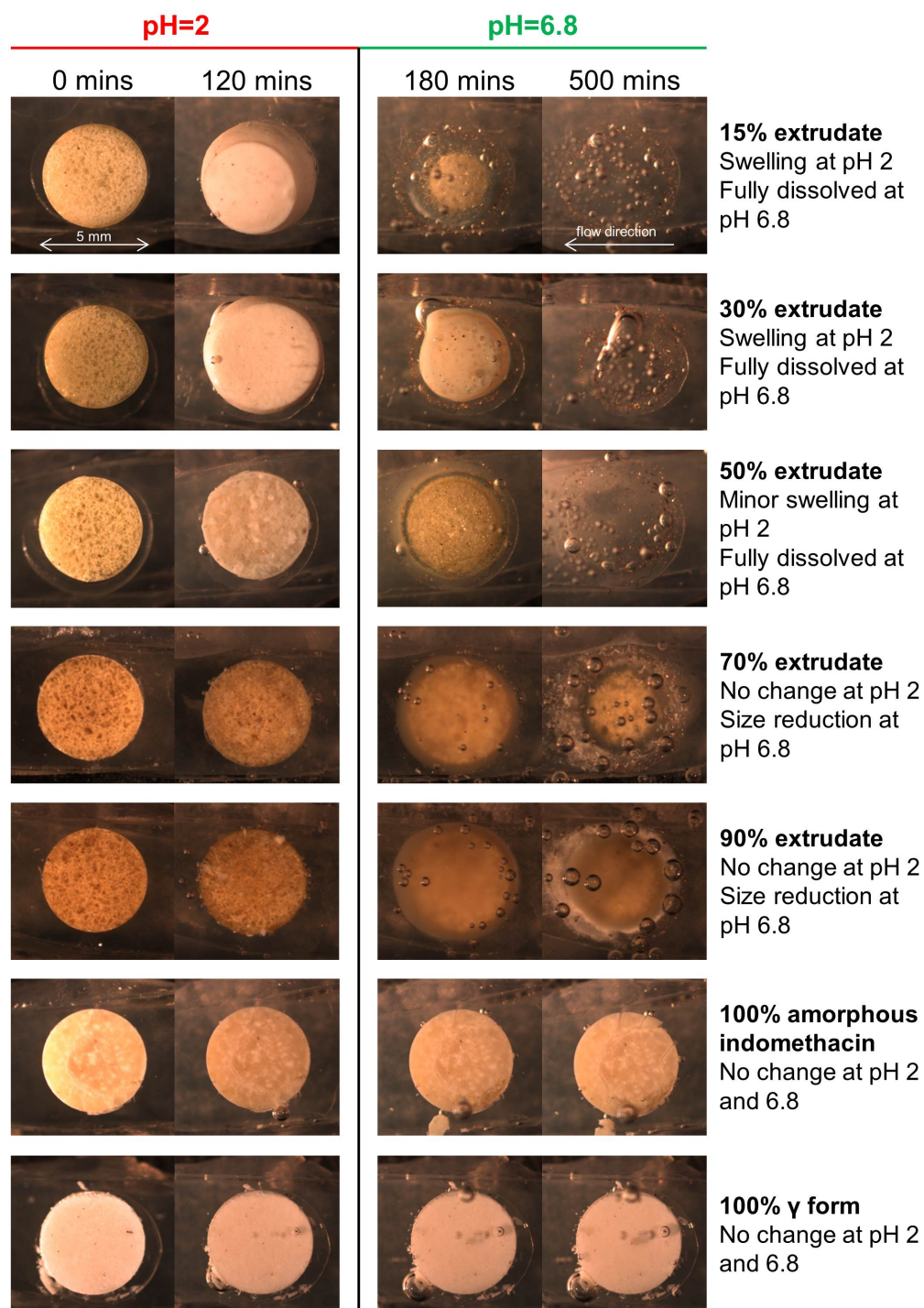


FIGURE 6.4: Images collected during the dissolution experiment of the indomethacin-copovidone extrudates (from 15% to 90% drug loading), and the 100% amorphous and 100%  $\gamma$  forms of indomethacin.

From the images it is clear that the extrudates containing  $\geq 15\%$  indomethacin and the 100% amorphous and 100%  $\gamma$  forms of indomethacin do not appreciably erode when the buffer is pH 2 HCl. Further analysis of the images reveals that the 15%, 30% and 50% extrudates exhibit signs of swelling as confirmed by plotting the surface area of the compacts as a function of time (Figure 6.5). It is apparent that the surface area of the 15% and 30% extrudates show a similar increase after 120 min. It is also possible to observe an increase in the surface area of the 50% extrudate, however the onset of swelling begins later and is of a lesser extent compared to that of the 15% and 30% extrudates.

The images in Figure 6.4 also show that all the extrudates begin to dissolve when the pH 2 HCl medium is switched to pH 6.8 phosphate buffer. The 15%, 30% and 50% extrudates are entirely dissolved by 500 min, whereas residues from the 70% and 90% extrudates remain at this time-point.

Images of the 100% amorphous and 100%  $\gamma$  forms of indomethacin illustrate that these compacts do not significantly dissolve at a pH both below and above the indomethacin  $pK_a$  of 4.5, pointing to the important role of copovidone of improving the dissolution performance of indomethacin.

The optical imaging experiments revealed that only 100% copovidone and the 5% extrudate are entirely dissolved when the medium is pH 2 HCl buffer. The situation with the other compacts is different because none of them show clear evidence of erosion at a pH below the indomethacin  $pK_a$  of 4.5. In contrast, the images indicated swelling only of the 15%, 30% and 50% extrudates suggesting water ingress into these compacts, attributed to the higher amount of water-soluble copovidone in the extrudate which promotes the water absorption. When the medium is switched to pH 6.8 phosphate buffer, all the extrudates begin to dissolve with a different rate.

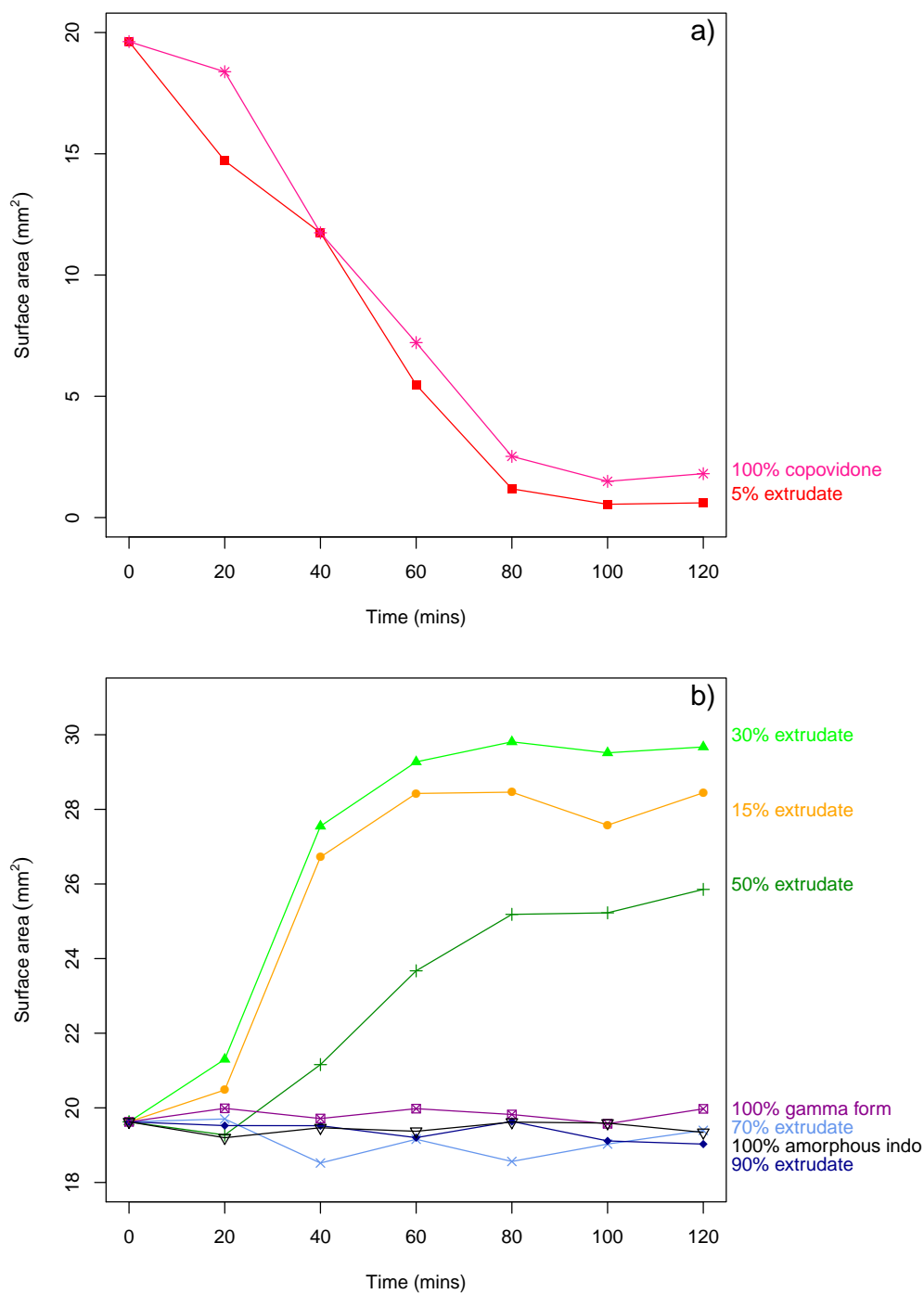


FIGURE 6.5: Trends showing how the compact surface changes as a function of time in pH 2 HCl dissolution medium. Trends of 100% copovidone and the 5% extrudate are shown in (a), while those from the other indomethacin-copovidone extrudates (from 15% to 90% drug loading), the 100% amorphous and 100%  $\gamma$  forms are illustrated in (b).

### 6.3.2 Rotating disk dissolution rate test

The RDDR test was performed at pH 2 and 6.8 to determine the effect of pH on the dissolution rate of poorly soluble indomethacin formulated as extrudate. The partial RDDR values determined at pH 2 and 6.8 along with the index of performance of all indomethacin-copovidone extrudates are reported in Table 6.1. The IDR values of 100% copovidone and the 100%  $\gamma$  form of indomethacin experimentally determined at pH 2 and 6.8 are also shown in Table 6.1 for comparison with the partial RDDR values of the extrudates. The dissolution profiles of all materials can be seen in Figures 6.6 (pH 2) and 6.7 (pH 6.8).

Material	Dissolution rate (n = 2) (mg/(min · cm <sup>2</sup> ))					
	pH 2			pH 6.8		
	Indomethacin	Copovidone	Index of performance	Indomethacin	Copovidone	Index of performance
100% copovidone		3.66 (±0.50)			3.05 (±0.16)	
5% extrudate	0.12 (±0.01)	4.12 (±0.40)	0.55 (±0.07)	0.18 (±0.01)	3.17 (±0.21)	1.06 (±0.09)
15% extrudate	approx. 0	0.30 (±0.07)	n/a	0.35 (±0.03)	2.02 (±0.16)	0.99 (±0.10)
30% extrudate	approx. 0	0.36 (±0.04)	n/a	0.63 (±0.04)	1.42 (±0.08)	1.02 (±0.07)
50% extrudate	approx. 0	approx. 0	n/a	1.16 (±0.04)	1.02 (±0.02)	1.06 (±0.04)
70% extrudate	approx. 0	approx. 0	n/a	0.80 (±0.05)	0.38 (±0.04)	0.97 (±0.09)
90% extrudate	approx. 0	approx. 0	n/a	0.67 (±0.04)	0.16 (±0.06)	0.90 (±0.01)
100% $\gamma$ form	approx. 0			0.04 (±0.01)		

TABLE 6.1: Partial RDDR values at pH 2 and 6.8 of indomethacin and copovidone formulated as extrudates along with the index of performance. The IDR values at pH 2 and 6.8 of the 100% indomethacin  $\gamma$  form and 100% copovidone are also reported.

Starting with the experiments conducted in pH 2 HCl buffer (LHS of Table 6.1), it is possible to see that the partial RDDR values of indomethacin and copovidone from the 5% extrudate are 0.12 and 4.12 mg/(min · cm<sup>2</sup>) respectively and the resulting index of performance is 0.55. The amount of indomethacin released from the rest of the extrudates (from 15% to 90% drug loading) at this pH was undetectable using the present experimental set-up, while copovidone is released only from the 15% and 30% extrudates with a partial RDDR of 0.30 and 0.36 mg/(min · cm<sup>2</sup>) respectively. The IDR value of 100% copovidone was found to be 3.66 mg/(min · cm<sup>2</sup>), while the IDR of the 100% indomethacin  $\gamma$  form was undetectable at a pH below the pK<sub>a</sub> of 4.5.

Turning to the experiments performed in pH 6.8 phosphate buffer (RHS of Table 6.1), the partial RDDR of indomethacin increases linearly with the drug loading up to 50% (Figure 6.8), and then reduces for the 70% and 90% extrudates. The partial RDDR of copovidone decreases as a function of the drug loading, and the resulting index of performance values are close to unity for all the extrudates, essentially indicating that the drug release at pH 6.8 is non-dependent on the drug loading and this is due to the drastic increase of the indomethacin aqueous solubility in neutral/alkaline pH conditions compared to acidic conditions.

From the RDDR data and also from the photos it is clear that the indomethacin extrudates show a pH-dependent dissolution behaviour. Indomethacin is released from the 5% extrudate at both pH 2 and 6.8 with a dissolution rate and resulting index of performance higher at pH 6.8 compared to pH 2, which is consistent with the higher indomethacin aqueous solubility at neutral/alkaline pH compared to acidic conditions. For the higher drug-loaded extrudates ( $\geq 15\%$  w/w) the amount of drug released at a pH below the indomethacin  $pK_a$  of 4.5 was undetectable under the current experimental set-up, while a detectable amount of copovidone is only released from the 15% and 30% extrudates at pH 2. At pH 6.8, all the extrudates behave similarly with the best performance from the 50% extrudate, which exhibits a 29 fold increase in dissolution rate compared to the 100% indomethacin  $\gamma$  form. It is also interesting to notice that the 90% extrudate shows approximately a 17 fold increase in dissolution rate compared to the 100% indomethacin  $\gamma$  form, indicating that even a small amount of copovidone in the ASD significantly enhances the dissolution performance.

The dramatic difference in dissolution behaviour of the indomethacin extrudates at pH 2 and 6.8 is entirely reasonable as the aqueous solubility of indomethacin is known to significantly increase from acidic to neutral pH (from  $1.5 \mu\text{g}\cdot\text{mL}^{-1}$  at pH 1.2 to  $105.2 \mu\text{g}\cdot\text{mL}^{-1}$  at pH 7.4).<sup>137</sup>

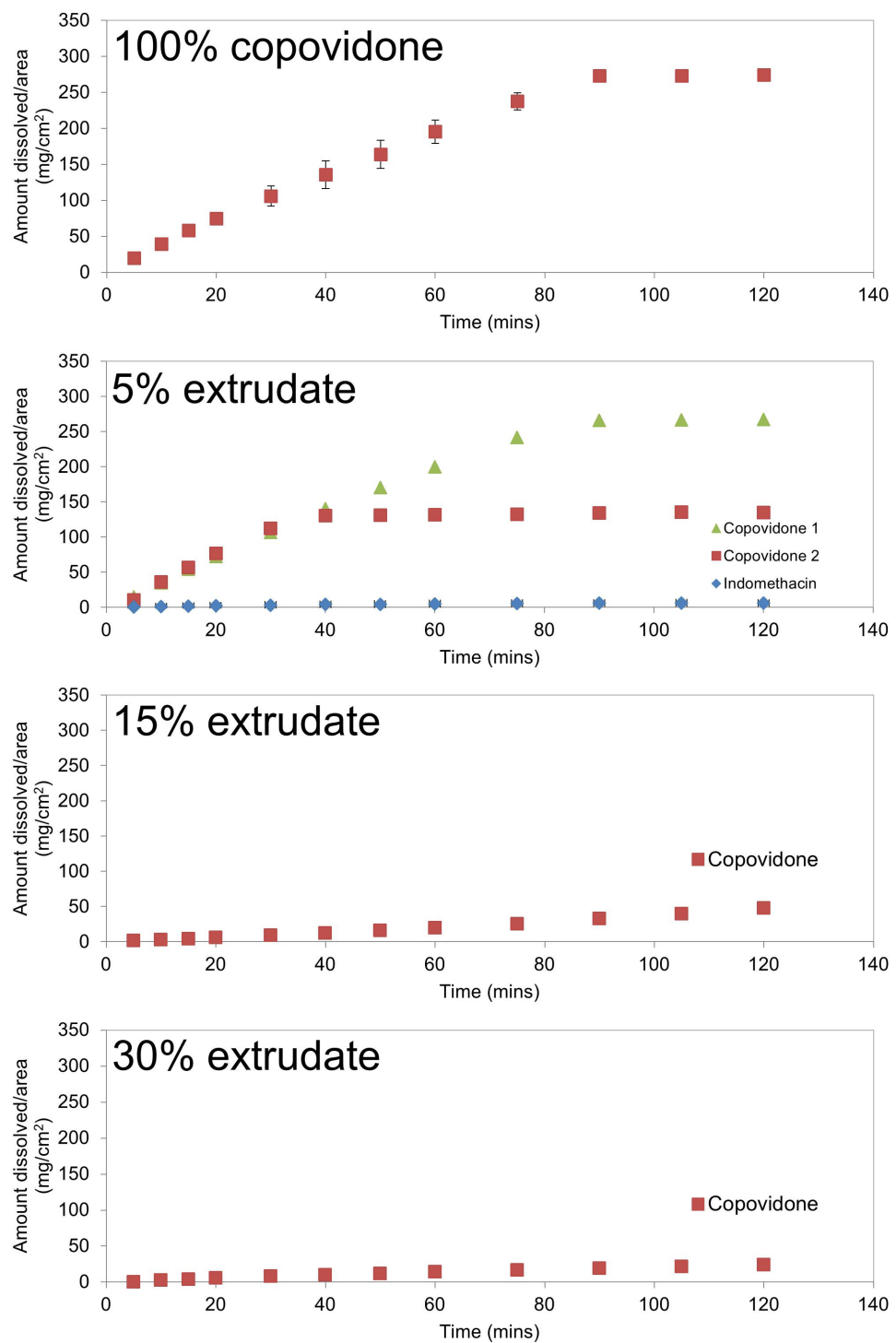


FIGURE 6.6: Dissolution profiles obtained from the RDDR and IDR experiments conducted in pH 2 HCl buffer. For copovidone in the 5% extrudate, trends of both experiments rather than the average are shown due to the significant difference in behaviour. The amount of indomethacin released from the 15% and 30% extrudates was undetectable in the present experimental set-up.

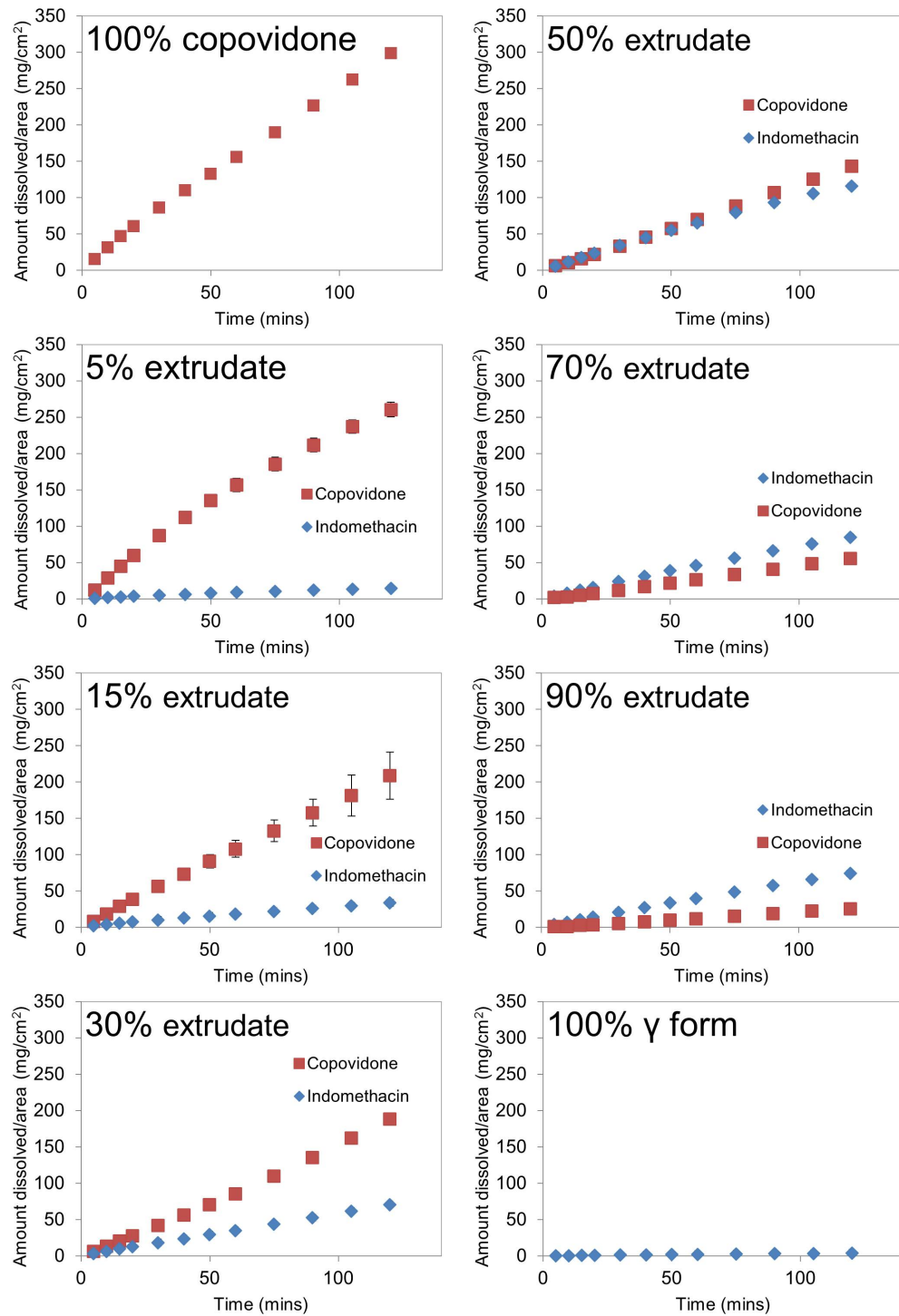


FIGURE 6.7: Dissolution trends of all materials obtained from the RDDR and IDR experiments conducted at pH 6.8.

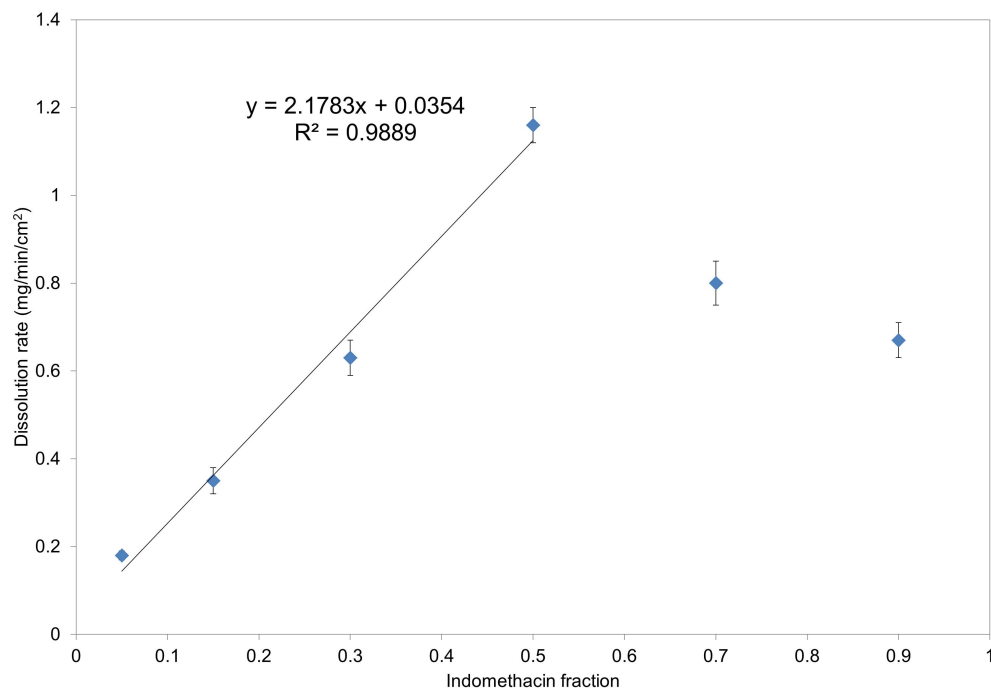


FIGURE 6.8: Partial RDDR of indomethacin at pH 6.8 as a function of the indomethacin weight fraction for all the extrudates (from 5% to 90% drug loading).

At pH 6.8 the drug is released from all the drug loadings, while at pH 2 the drug is released only from the 5% extrudate due to the high amount of highly water-soluble copovidone in the formulation, i.e. polymer-controlled drug release.<sup>87</sup>

Although the RDDR test clearly indicates that the indomethacin-copovidone extrudates behave very differently at a pH below and above the  $pK_a$  of 4.5, it does not provide a physicochemical explanation of the poor dissolution performance at low pH. Therefore, Raman spectroscopy and in-line UV-Vis were employed to study the system.

### 6.3.3 Raman ultraviolet-visible flow cell experiments

#### 6.3.3.1 Ultraviolet-visible

The dissolution profiles of indomethacin released from the extrudates and both the 100% amorphous and 100%  $\gamma$  forms of indomethacin obtained from the flow cell experiments are presented in Figure 6.9. These data are in good agreement with the RDDR test, although the shear forces generated in the two techniques are clearly different, and indicate that the dissolution performance of the extrudates is intrinsic to the formulation rather than the technique employed to measure it.

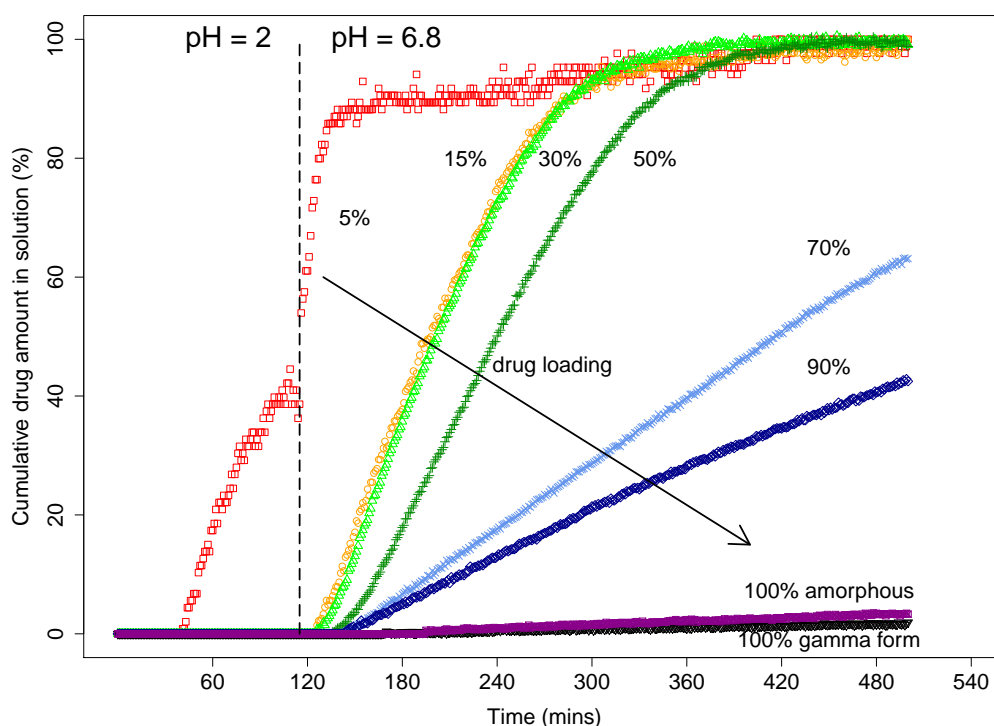


FIGURE 6.9: Dissolution profiles of indomethacin released from the extrudates and profiles of the pure materials (100% amorphous and 100%  $\gamma$  forms of indomethacin).

5% extrudate is the only formulation that gives increasing solution concentration of indomethacin (up to approximately 40% of cumulative drug amount in solution) when the pH is 2. 100% of cumulative drug amount in solution is reached within a few minutes after the dissolution medium is switched to pH 6.8 phosphate buffer.

The other extrudates (from 15% to 90% drug loading) along with the 100% amorphous and 100%  $\gamma$  forms of indomethacin do not show any detectable (within the limits of detection of the present experimental set-up) drug release at pH 2.

These extrudates and the pure materials begin to release indomethacin only after the medium is changed to pH 6.8 phosphate buffer. The 15% and 30% extrudates reach the maximum indomethacin solution concentration at about 400 min. The release of the 50% extrudate is slightly slower giving increasing solution concentrations up to a maximum at about 440 min. Both the 70% and 90% extrudates do not reach the maximum indomethacin solution concentration within 500 min, with the first releasing 60% and the second 40% at this time-point. The 100% amorphous and 100%  $\gamma$  forms of indomethacin show very similar dissolution profiles, with a cumulative drug amount in solution still increasing at the end of the experimental time-frame, having reached a value of 3% and 2% respectively at 500 min.

The UV-Vis data are in agreement with the images and the RDDR data, and showed that only the 5% extrudate exhibits a detectable dissolution rate at a pH below the  $pK_a$  of indomethacin. The other drug loadings and the pure materials do not release any detectable (in the current experimental set-up) indomethacin when the dissolution medium is pH 2 HCl. The buffer switch then promotes the drug release given that the aqueous solubility of indomethacin greatly increases (approximately two orders of magnitude higher at pH 7.4 compared to pH 1.2)<sup>137</sup> at a pH above the indomethacin  $pK_a$  of 4.5. The 15% and 30% extrudates begin to release the drug approximately at the same time and this can be linked to the similar swelling and therefore water ingress observed at pH 2. For the 50% extrudate, the release of the drug begins later and this is consistent with a minor and retarded swelling at pH 2 as seen in Figure 6.5.

### 6.3.3.2 Raman spectroscopy

Raman spectroscopy was used to monitor the physicochemical changes that occurred during the dissolution of the indomethacin-copovidone extrudates under similar conditions to those outlined above.

**Reference spectra** Before commencing a full discussion of the data, it is useful to notice the differences between Raman spectra of the raw materials. Raman spectra of the extrudates, the 100% amorphous form of indomethacin, and the 100% ‘dry’ and ‘wet’ copovidone are presented in Figure 6.10. The spectrum of the 100% ‘wet’ copovidone was collected immediately after immersing compressed powder of copovidone in water. Raman spectra of the extrudates approximate to a linear combination of amorphous indomethacin and dry copovidone in the region between 1100 and 1750  $\text{cm}^{-1}$  (Figure 6.10). The peak from dry copovidone at 1425  $\text{cm}^{-1}$  is clearly evident in the spectra of the 5%, 15% and 30% extrudates, while it is greatly reduced in the spectrum of the 50% extrudate, and falls below the limit of detection in the spectra of the 70% and 90% extrudates. This is reasonable as copovidone is known to be a weaker Raman scatterer than indomethacin.<sup>6</sup>

It is also important to notice that Raman spectra of ‘dry’ and ‘wet’ copovidone are different. The bands deriving from the carbonyl stretching mode of the vinylpyrrolidone and vinylacetate blocks move to a lower Raman shift in the spectrum of ‘wet’ copovidone (1651 and 1717  $\text{cm}^{-1}$ ) compared to that of ‘dry’ copovidone (1673 and 1734  $\text{cm}^{-1}$ ). These shifts likely arise from the inter-molecular hydrogen bonding interactions between copovidone and the water molecules. In addition, it is possible to note differences in the spectral region deriving from the bending modes of the methylene functional groups. The band at 1425  $\text{cm}^{-1}$  is sharper in the spectrum of 100% wet copovidone compared to that of 100% dry copovidone.

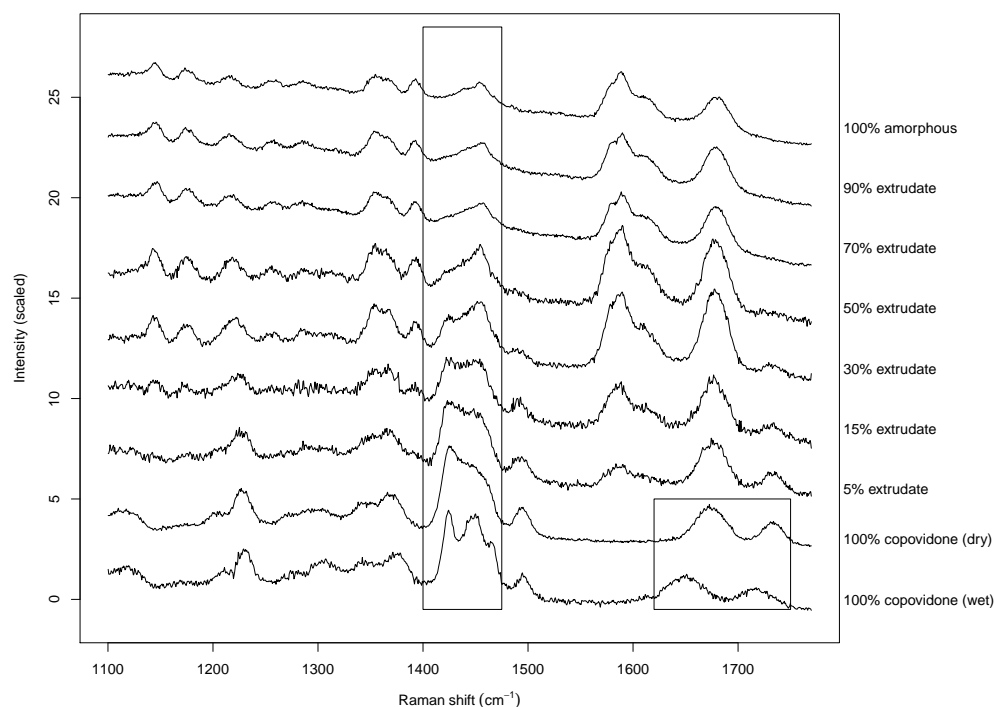


FIGURE 6.10: Raman spectra of raw materials (1100–1750  $\text{cm}^{-1}$  region). Spectra were variance-scaled before plotting.

Moreover, a peak at  $1450 \text{ cm}^{-1}$  appears clearly in the spectrum of 100% wet copovidone that is not present in 100% dry copovidone. These spectral differences can be ascribed to conformational changes that occur when dry copovidone is immersed in water.

In the low-wavenumber region ( $40\text{--}400 \text{ cm}^{-1}$ , Figure D.4 of the Appendix D), spectra of all materials show the typical broad distribution expected for amorphous solids.<sup>118–120</sup> Raman spectra of the  $\gamma$  and  $\alpha$  indomethacin polymorphs are shown in Figure D.2 of the Appendix D. The  $\gamma$  polymorph is the thermodynamically stable form and the  $\alpha$  polymorph is the most commonly observed metastable form.<sup>178</sup> Due to the different conformations of indomethacin, Raman spectra of the  $\gamma$  and  $\alpha$  polymorphs significantly differ both in the  $1100\text{--}1750 \text{ cm}^{-1}$  (Figure D.2a) and  $40\text{--}400 \text{ cm}^{-1}$  (Figure D.2b) regions. Raman spectra of the two indomethacin polymorphs are consistent with those previously reported by others.<sup>69,178</sup>

**Dissolution: time-resolved spectra** The variation in the averaged spectra collected during the dissolution of the extrudates is now discussed (Figure 6.11). Starting with 100% copovidone and the 5% extrudate (Figure 6.11a and b), it is apparent that no evidence of form change occurs during the entire dissolution test conducted at pH 2. All the spectra present two clear bands at 1425 and 1450  $\text{cm}^{-1}$  which are typical of wet copovidone, indicating that the compacts are fully hydrated during the entire dissolution experiment at pH 2.

Turning to the 15% extrudate (Figure 6.11c), it is possible to see that at pH 2 the band due to copovidone at 1425  $\text{cm}^{-1}$  decreases in intensity as a function of time. Comparison of the averaged spectrum collected at 93 min with the reference spectra indicates a strong correlation with the 100% amorphous indomethacin reference form. When the pH is switched to 6.8, i.e. above the indomethacin  $\text{pK}_a$  of 4.5, the two distinctive bands of wet copovidone at 1425 and 1450  $\text{cm}^{-1}$  appear (averaged spectra collected after 168 min). The situation with the 30% extrudate (Figure 6.11d) is largely identical to that of the 15% extrudate. Spectra collected at pH 2 between 7 and 112 min become more similar to that of the 100% amorphous reference form of indomethacin, and spectra collected at pH 6.8 between 174 and 318 min present the characteristic bands of wet copovidone at 1425 and 1450  $\text{cm}^{-1}$ . At pH 2, Raman data indicate that for the extrudates with 15% or higher drug loading hydrophilic copovidone preferentially dissolves from the exterior of the compact leaving an amorphous drug-rich and hydrophobic shell, which acting as an *in situ* formed enteric coating inhibits the drug release. The depletion of copovidone at low pH from the 15% and 30% extrudates is confirmed by the RDDR test. The pH switch from below to above the  $\text{pK}_a$  increases the aqueous solubility of indomethacin which in turn removes the shell and enables the drug release. The dissolution model described here is schematically reported in Figure 6.12.

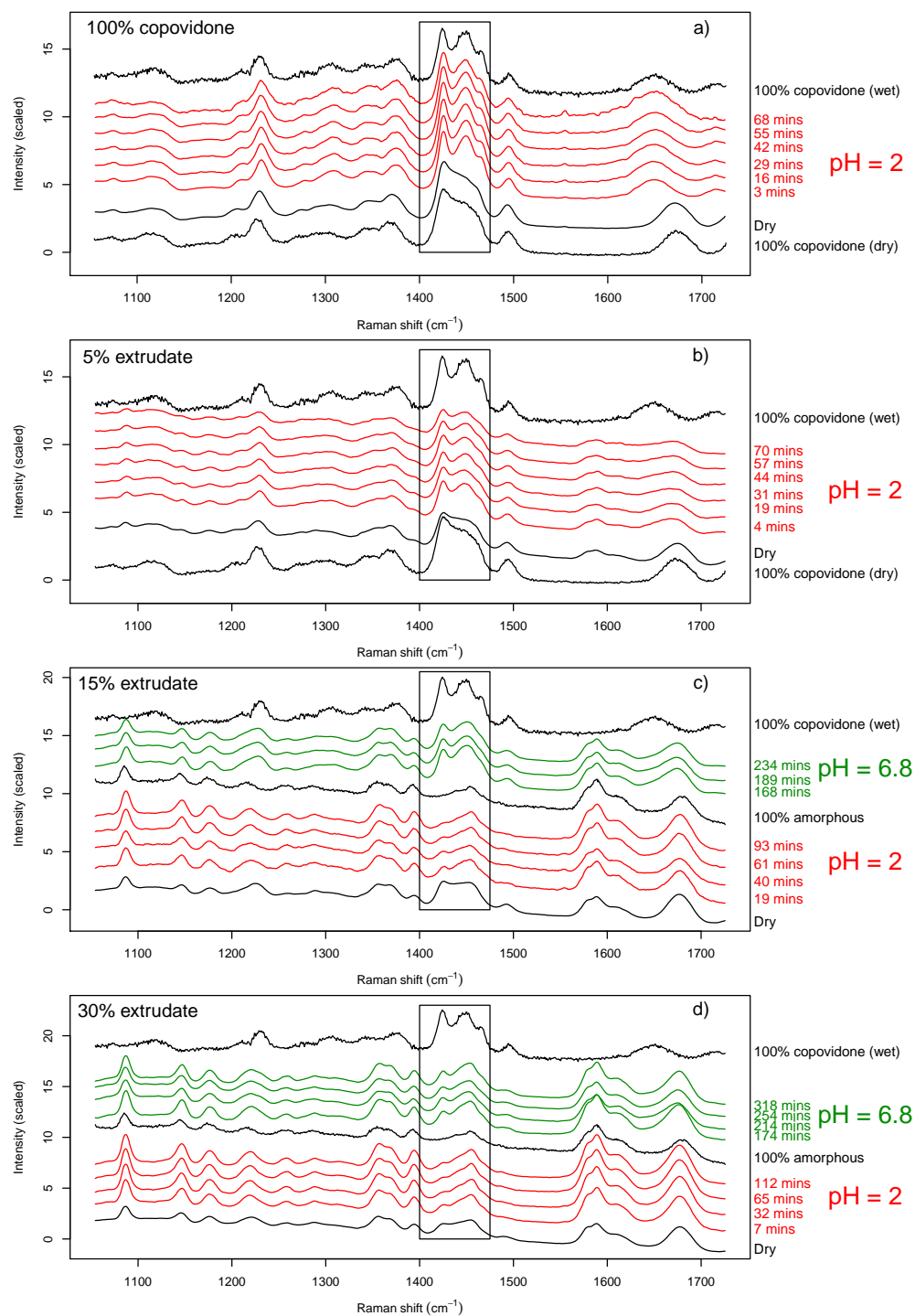


FIGURE 6.11: Spatially-averaged Raman spectra of the dissolution experiment of (a) 5%, (b) 15%, (c) 30% and (d) 50% extrudates. Data were variance-scaled before plotting. Y-axis offsets have been applied for presentational purpose and vary between panels.

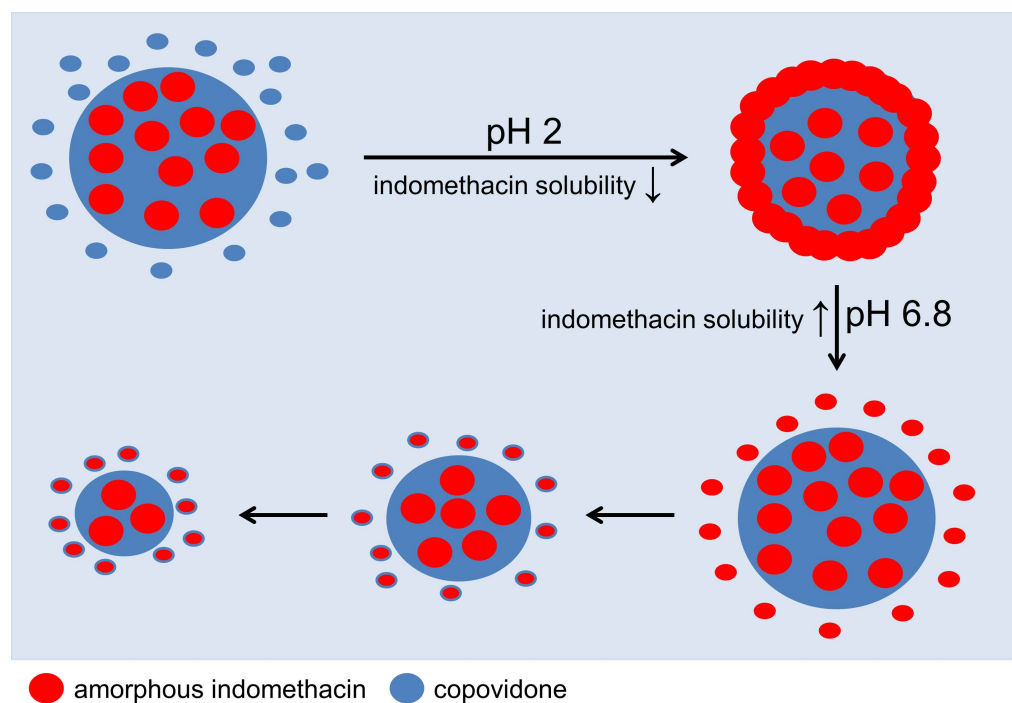


FIGURE 6.12: Schematic model depicting the dissolution mechanism of the indomethacin-copovidone extrudates in pH 2 HCl and pH 6.8 phosphate buffer.

The dissolution for 100% copovidone and the 5% extrudate at pH 2 (Figures 6.11a and b), and the 15% and 30% extrudates at pH 6.8 (Figures 6.11c and d) is clearly associated with the appearance of hydrated copovidone after water ingress. This is clear by observing the characteristic bands of wet copovidone at 1425 and 1450  $\text{cm}^{-1}$ . The dissolution process observed here, i.e. dry  $\rightarrow$  hydration  $\rightarrow$  dissolution, is consistent with dissolution-controlled release mechanisms from medium-soluble carriers.<sup>137</sup> The build-up of an amorphous drug-rich shell seen for the 15% and 30% extrudates at pH 2 has been previously observed also for ASDs of indomethacin and PEG.<sup>174</sup> It was proposed that, based on ATR-FTIR spectroscopic imaging experiments, the initial rapid dissolution of PEG led to the accumulation of amorphous indomethacin which re-crystallised into the  $\gamma$  form due to an increase in molecular mobility.

For the 50% (Figure 6.13a), 70% (Figure 6.13b) and 90% (Figure 6.13c) extrudates, the amount of copovidone in the extrudate is too low to generate well-resolved bands and therefore Raman spectra of these materials can not

be differentiated from the spectrum of the 100% amorphous reference form of indomethacin. For the 70% and 90% extrudates it is possible to observe a peak shift after approximately 280 min from 1676 to 1670  $\text{cm}^{-1}$  along with a change in peak shape (Figures 6.13b and 6.13c). The sharp band at 1670  $\text{cm}^{-1}$  corresponds to a crystalline form that has been previously observed by Greco et al. during the dissolution of amorphous indomethacin.<sup>175</sup> Using PLM they demonstrated that needles of this crystalline form of indomethacin were present at the end of the dissolution test. The presence of sharp bands in the low-wavenumber region (Figure 6.14) confirms the drug re-crystallisation. The data indicate that for the 70% and 90% extrudates a lower ratio of copovidone to indomethacin at the surface in contact with water induces the drug re-crystallisation and as a result the drug release is reduced. Averaged spectra of the dissolution experiment of the 100% amorphous form of indomethacin are presented in Figure 6.13d. The real time data acquisition was in this case extremely difficult due to the high fluorescence emission of this material. The remaining compact was therefore removed from the flow cell after 4440 min of immersion in dissolution medium and analysed by Raman and XRPD. Both Raman spectrum (Figure 6.13d) and XRPD pattern (Figure 6.15) show high similarity with those of the  $\alpha$  reference form of indomethacin, pointing to the re-crystallisation of the amorphous material. The re-crystallisation of amorphous indomethacin into the metastable  $\alpha$  polymorph in aqueous environments has been previously reported and is in agreement with the Ostwald's rule of stages which states that the least stable polymorph tends to crystallise first, in this case the  $\alpha$  form.<sup>175,178</sup>

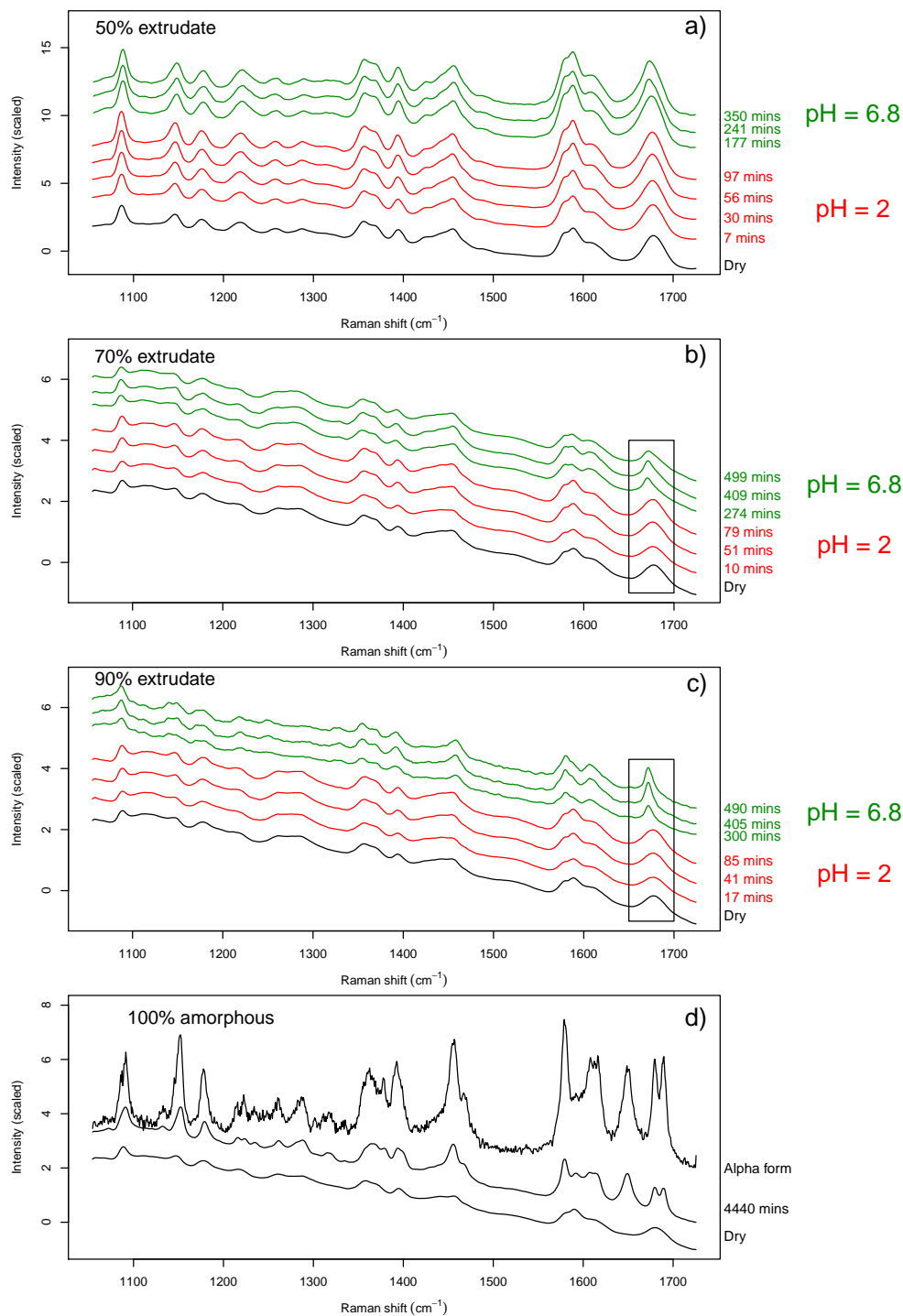


FIGURE 6.13: Spatially-averaged Raman spectra of the dissolution experiment of (a) 50% extrudate, (b) 70% extrudate, (c) 90% extrudate and (d) 100% amorphous indomethacin, with data being variance-scaled before plotting. Y-axis offset has been applied for presentational effect.

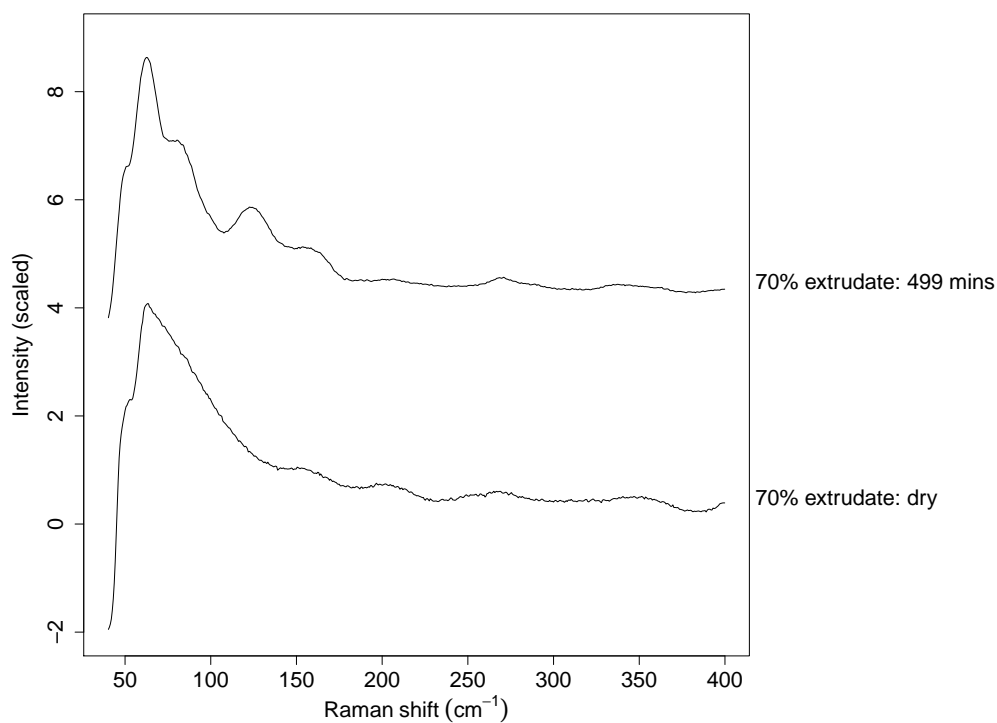


FIGURE 6.14: Phonon-mode Raman region of the 70% extrudate compact collected under dry conditions and after 499 min of immersion in dissolution medium.

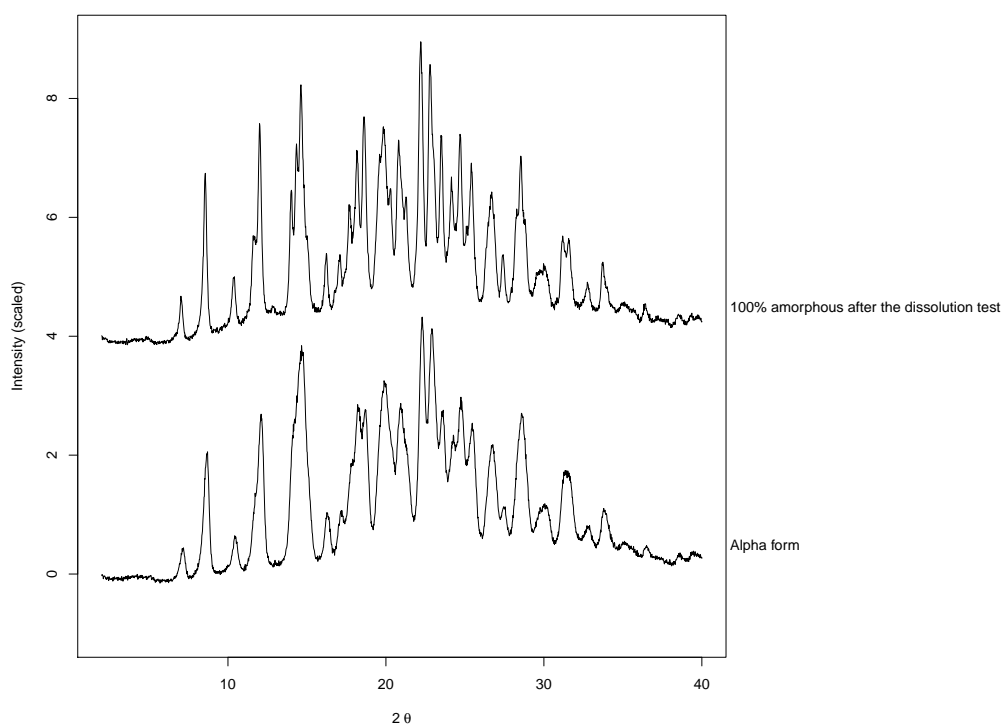


FIGURE 6.15: XRPD patterns of the  $\alpha$  reference form and the 100% amorphous residue recovered after the dissolution experiment.

## 6.4 Conclusions

In this chapter the dissolution performance of the indomethacin-copovidone extrudates was tested as a function of both the drug loading and the pH of the dissolution medium. Raman spectroscopy along with in-line UV-vis were employed to directly relate changes in the amount of drug in solution to physicochemical changes that occur to the solid form during the test. The RDDR test was also used to simultaneously measure the dissolution rate of both indomethacin and copovidone from the molecular dispersion. The experiments were performed at pH 2 to mimic the stomach conditions and pH 6.8 to simulate the post-stomach conditions. Only the 5% extrudate exhibited a detectable dissolution rate at pH 2, pointing to a drug release mechanism dependent on the highly water-soluble copovidone. Raman data showed that the 5% extrudate remained hydrated across the entire experiment at pH 2, and this behaviour is consistent with those previously observed for low drug-loaded ASDs of felodipine (Chapter 3) and bicalutamide (Chapter 4). For the rest of drug loadings (15% or higher), the poor dissolution performance at pH 2 is related to the *in situ* formation of an amorphous and hydrophobic enteric coating of drug which further limits drug release from the interior of the compact. The formation of an amorphous drug-rich shell has been also observed during the dissolution of high drug-loaded extrudates of felodipine (Chapter 3) and bicalutamide (Chapters 4 and 5). The pH switch from below to above the indomethacin  $pK_a$  of 4.5 dissolved this coating and enabled the dissolution of the extrudates.

# Chapter 7

## Conclusions and future work

The aim of the work in this thesis was to investigate the use of Raman spectroscopy as primary technique to obtain additional information on the dissolution performance of ASDs. Gaps in the current knowledge of ASDs include a lack of understanding of the dissolution performance due to the complexity of the mechanisms by which the drug is released and the outlined limitations of the conventional dissolution testing. The novelty of using Raman arises from obtaining in real time and *in situ* highly spatially-resolved chemical images of the solid form changes during the dissolution process. This was done by using point-by-point Raman mapping and a flow cell system placed below the Raman microscope. The Raman information were also complemented by data obtained from a number of other techniques/methodologies, including optical imaging, the RDDR test, quantitative suppressed-water  $^1\text{H}$  NMR spectroscopy and MRI.

The dissolution performance of three ASD model systems (manufactured by hot HME) including felodipine, bicalutamide and indomethacin, all poorly soluble drugs, with copovidone was explored. The complexity of the model systems was being built-up through the chapters, starting with a well-documented poorly soluble drug model, i.e. felodipine (Chapter 3), then investigating bicalutamide which is known to exist in at least two polymorphic forms (form I and form II) with different physicochemical

properties (Chapters 4 and 5), and finally testing the dissolution of indomethacin whose aqueous solubility significantly changes between acidic and neutral/alkaline conditions (Chapter 6).

In Chapter 3 the dissolution behaviour of amorphous felodipine solid dispersions was tested as a function of the drug loading (5% *vs* 50% w/w). Optical imaging and for the first time the RDDR test were used to complement the Raman data. The RDDR test uses HPLC to separate and quantify both the drug and the polymer and ultimately enables an index of performance to be obtained. For the 5% extrudate, felodipine and copovidone were shown to erode with approximately the same rate from the molecular dispersion and real time Raman data did not show any significant changes across the entire dissolution experiment. This indicated a dissolution mechanism strongly dependent on the high water solubility of copovidone, with the drug release rate being dictated by the dissolution of the polymer. In contrast, the 50% extrudate compact was shown to swell rather than erode/dissolve. In agreement with the optical images, the partial RDDRs of both felodipine and copovidone were found to be extremely low, pointing to a dissolution mechanism dependent on the low aqueous solubility and high hydrophobicity of felodipine. Raman data indicated that felodipine within the 50% extrudate re-crystallised and that the re-crystallisation followed the formation of an amorphous drug-rich shell around the compact via copovidone dissolution in the initial part of the test. These two transformations, i.e. the formation of an amorphous drug-rich shell and the drug re-crystallisation, were determined to be responsible for the limited dissolution performance observed for the 50% extrudate. Raman maps of the re-crystallisation event were generated using the MCR model. The novelty of this mathematical approach derives from the use of concatenated Raman maps to explicitly probe the changes as a function of time as well as space.

In Chapter 4 the same combination of analytical techniques used in Chapter 3, i.e. Raman spectroscopy, the RDDR test and optical imaging, was

employed to explore the dissolution behaviour of another ASD model system which includes poorly soluble bicalutamide and highly water-soluble copovidone. The dissolution performance of the bicalutamide-copovidone ASD was tested as a function of the drug loading (5% *vs* 50% w/w). Bicalutamide and copovidone in the 5% drug loading, similarly to the low drug-loaded felodipine ASD, were shown to erode/dissolve with the same rate, pointing to a polymer-dependent dissolution performance. In contrast, the drug and the polymer in the 50% extrudate dissolved with significantly lower dissolution rates, pointing to a dissolution dependent on the physicochemical properties of the drug, i.e. low solubility and high hydrophobicity. This limited dissolution performance, similar to that observed for the high drug-loaded felodipine ASDs, was due to the build-up of bicalutamide-rich amorphous material on the compact surface followed by the drug re-crystallisation. Highly spatially-resolved chemical Raman maps generated by the MCR model indicated that amorphous bicalutamide crystallised first into metastable polymorphic form II and then into stable polymorphic form I. Raman spectroscopy, due to the high chemical specificity, was able to discriminate between the three different solid forms of bicalutamide, i.e. amorphous, form II and form I. In addition, by fitting a kinetic model to the data extracted from the Raman maps it was possible to understand the re-crystallisation mechanisms by which the low energy form I appeared. Form I was shown to crystallise preferentially from the amorphous form in a random nucleation mechanism, rather than from the crystalline form II.

In Chapter 5 the dissolution performance as a function of the drug loading (5% and 30% w/w) of the bicalutamide-copovidone extrudates was further investigated using a suite of state-of-the-art analytical techniques, including a combined MRI/UV-Vis flow cell system to allow changes in dissolution profile to be related to physical changes occurring in the solid material, and for the first time quantitative suppressed-water  $^1\text{H}$  NMR spectroscopy was applied to ASD formulations.  $^1\text{H}$  NMR, due to the high chemical

selectivity, allowed the dissolution profiles and rates of both the drug and the polymer from the molecular dispersion to be simultaneously obtained. In agreement with the Raman and RDDR data showed in Chapter 4, the 5% compact was shown to erode linearly (MRI images) with bicalutamide and copovidone being released at similar rate (UV-Vis and  $^1\text{H}$  NMR data), pointing to a polymer-controlled drug release. In contrast, the dissolution rates of both bicalutamide and copovidone were found to be significantly lower in the 30% extrudate due to a slower water ingress into the compact, pointing to a drug-controlled dissolution mechanism. The lower and slower water ingress was thought to be due to the formation of an amorphous drug-rich shell which has been previously observed and hypothesised for the dissolution of high drug-loaded extrudates of felodipine (Chapter 3) and bicalutamide (Chapter 4).

In Chapter 6 the behaviour during dissolution of another ASD model system which includes indomethacin and copovidone was explored. Indomethacin presents a pH-dependent solubility and dissolution rate, so in addition to the drug loading (from 5% to 90%), the dissolution performance was tested also as a function of the dissolution medium pH. This was done by switching the dissolution medium from pH 2 HCl (to mimic the stomach conditions) to pH 6.8 phosphate buffer (to mimic the post-stomach conditions) during the dissolution test. In addition, an in-line UV-Vis spectrophotometer was connected to the Raman flow cell system to enable changes in dissolution trend (monitored by UV-Vis) to be directly related to physicochemical changes that occur to the extrudate (monitored by Raman). The 5% extrudate was shown to be the only drug loading to exhibit a detectable dissolution rate at pH 2, and this was found by Raman to be due to the compact remaining hydrated across the entire experiment at pH 2. For the rest of drug loadings (15% or higher), the poor dissolution performance observed at pH 2 was related to the *in situ* formation of an amorphous and hydrophobic enteric coating due to the low aqueous solubility of indomethacin at this pH. Raman data indicated that the dissolution medium switch to

pH 6.8 phosphate buffer removed the shell and enabled drug release due to the significant increase of the aqueous solubility of indomethacin in neutral/alkaline pH conditions. Raman spectroscopy for this particular study was able to discriminate between water ingress/not water ingress and ultimately to provide a mechanistic explanation on the dissolution performance as a function of pH conditions and drug loading.

In summary, a number of methodologies were discussed in this thesis to provide additional and complementary information on the drug release mechanisms from ASDs of felodipine, bicalutamide and indomethacin. From the data generated it was possible to make a number of potential explanations regarding the effects of drug loading and environmental pH on the dissolution performance of ASDs.

The first potential continuation of the work presented in this thesis is to complement the Raman data on the indomethacin-copovidone model system by using the MRI method. MRI could provide very useful physical information on the rate of water ingress at pH 2 and 6.8 which could be linked to the chemical transformations observed by Raman. In addition, the composition of the indomethacin dispersions could be changed and the dissolution performance investigated. For example, adding a water-soluble compound such as caffeine to the indomethacin-copovidone dispersion could help to elucidate the formation of the hydrophobic enteric coating. The quick dissolution at pH 2 of the water-soluble molecule from the surface and the resulting formation of the amorphous drug-rich shell should be readily detected by both Raman and UV-Vis. Then, a second polymer such as Eudragit EPO could be added to the indomethacin-copovidone dispersion. Eudragit EPO is a cationic polymer soluble in gastric fluid up to pH 5, which could potentially facilitate to maintain the material hydrated in acidic conditions.

A very interesting correlation and consistency in performance has been observed between the different ASD model systems. A future work is to apply

the RDDR test to other binary model solid dispersions. The dissolution rate of both the drug and the polymer could be tested as a function of well-selected factors such as the number of hydrogen bonds between the drug and the polymer in the dispersion. This will enable a correlation between those properties and the dissolution behaviour of the drug and the polymer to be built. The ultimate aim is to generate information that allow formulators to specifically select a certain polymer or composition for a drug in development and therefore to obtain a formulation strategy with the desired controlled drug release.

Another important consideration is that a number of different techniques including solution-based and solid-based methods have been combined in-line and off-line to provide complementary information on the drug release. This paradigm could be further exploited in future works, and other techniques for providing more information could be implemented, with the ultimate aim to assure the quality of performance of formulations. For example, to study the dissolution from ASD formulations, an ideal dissolution set-up may include Raman spectroscopy and MRI to obtain chemical and physical information directly from the dosage form, UV-Vis and  $^1\text{H}$  NMR to quantify the amount of drug and polymer in solution, and a particle size analyser (e.g. dynamic light scattering and image analysis) to determine the drug precipitation. The latter is of particular importance for ASD formulations as it is well known that the amorphous form due to its thermodynamic instability tends to precipitate into the crystalline form. Overall, the combination of a number of complementary analytical techniques will allow several information and therefore a clearer understanding of the drug release mechanisms to be obtained from a single dissolution experiment.

# Appendix A

## Supplementary information part-I

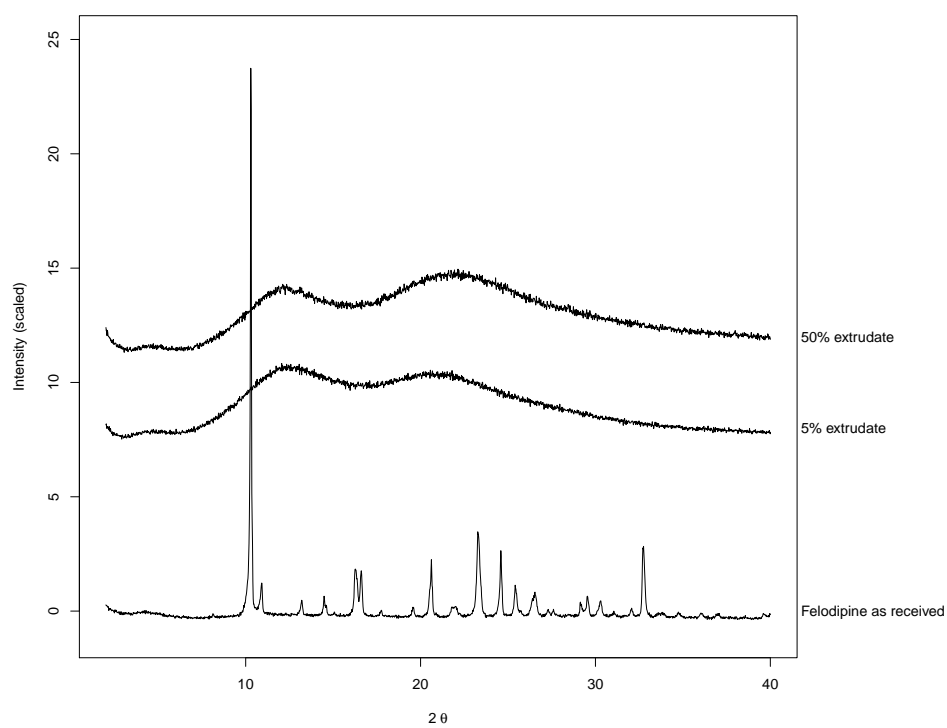


FIGURE A.1: XRPD patterns of the extrudates and the crystalline reference form (“Felodipine as received”).

# Appendix B

## Supplementary information part-II

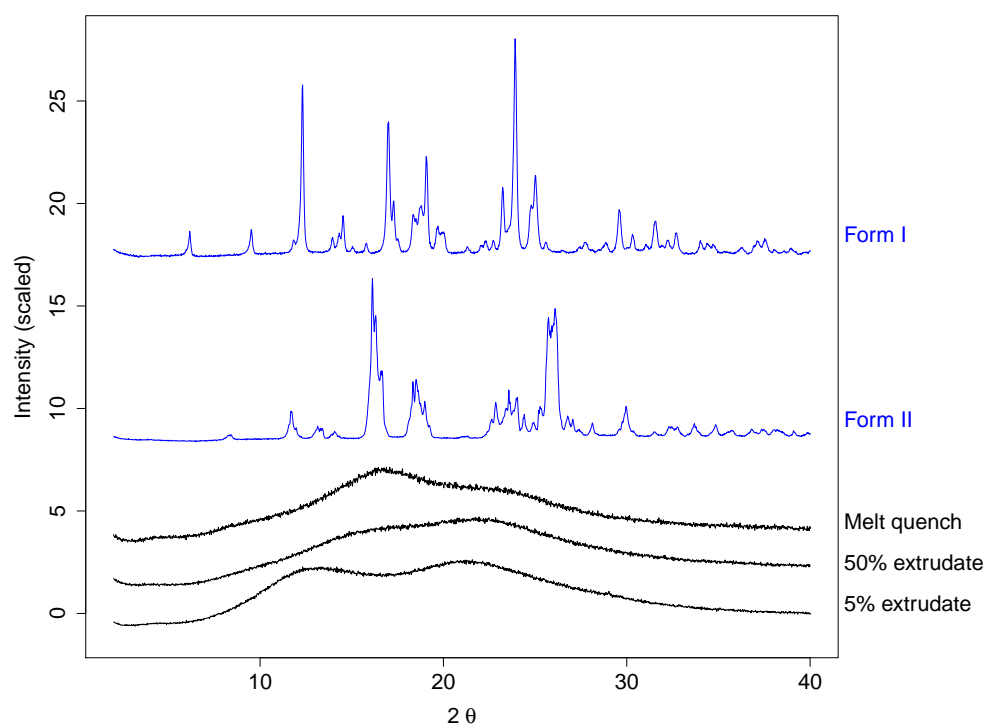


FIGURE B.1: XRPD patterns of the raw materials. Raw data were variance-scaled before plotting.

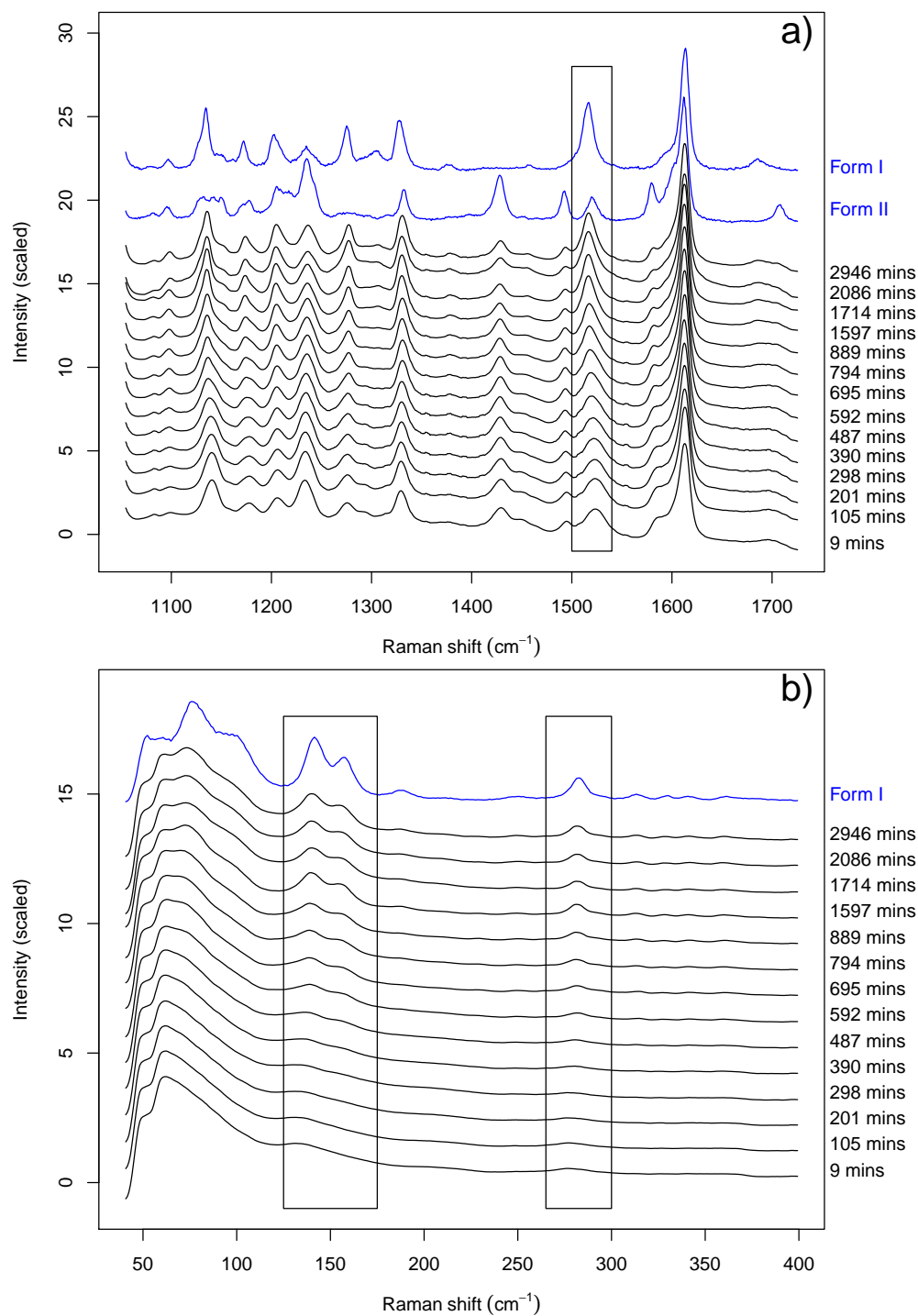


FIGURE B.2: Fingerprint (a) and phonon-mode (b) regions of the averaged Raman spectra collected during the dissolution of the 50% extrudate, with raw materials spectra in blue. Y-axis offsets have been applied for presentational purposes and differ between panels.

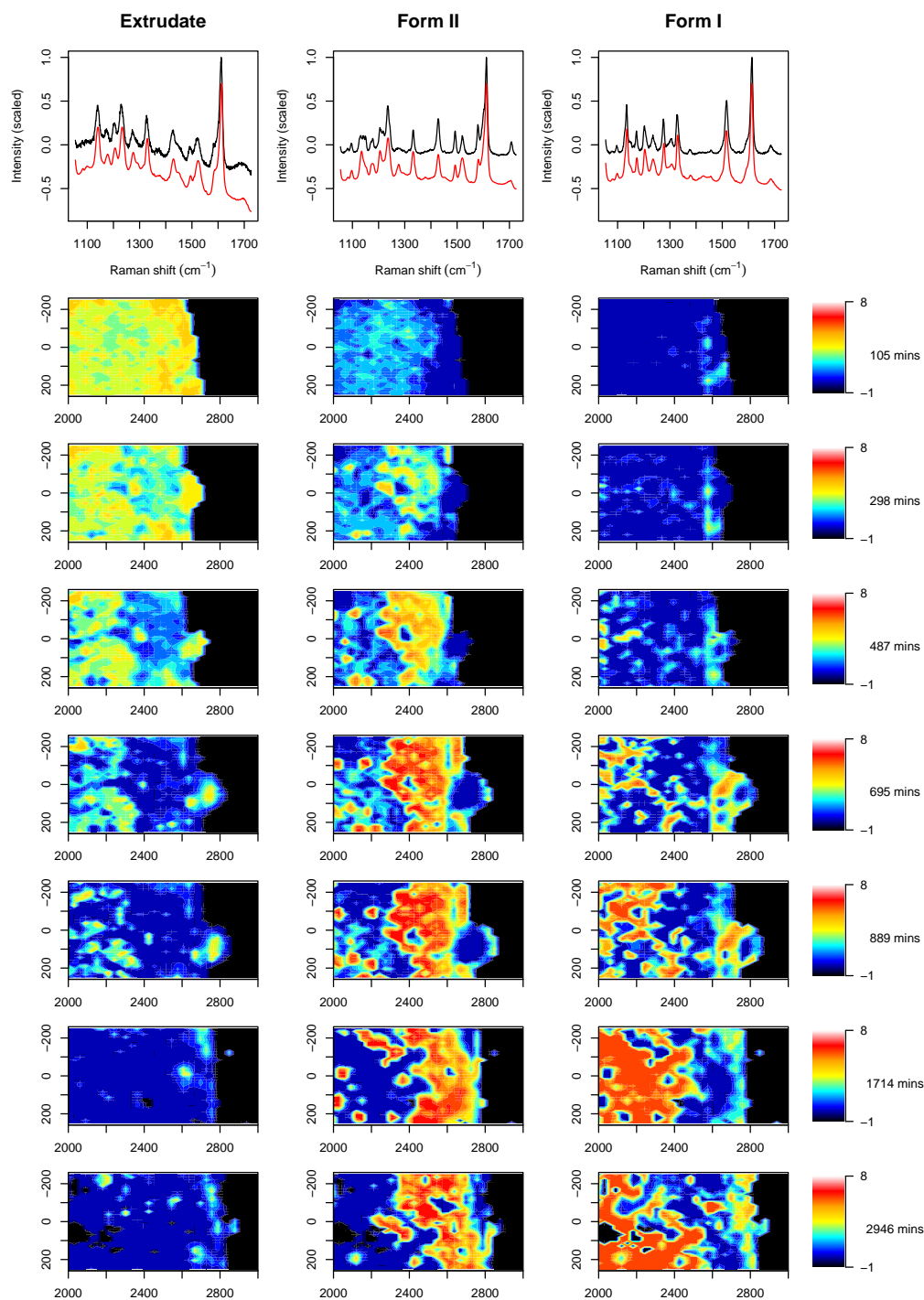


FIGURE B.3: Remaining time-point maps collected through the dissolution experiment of the 50% extrudate.

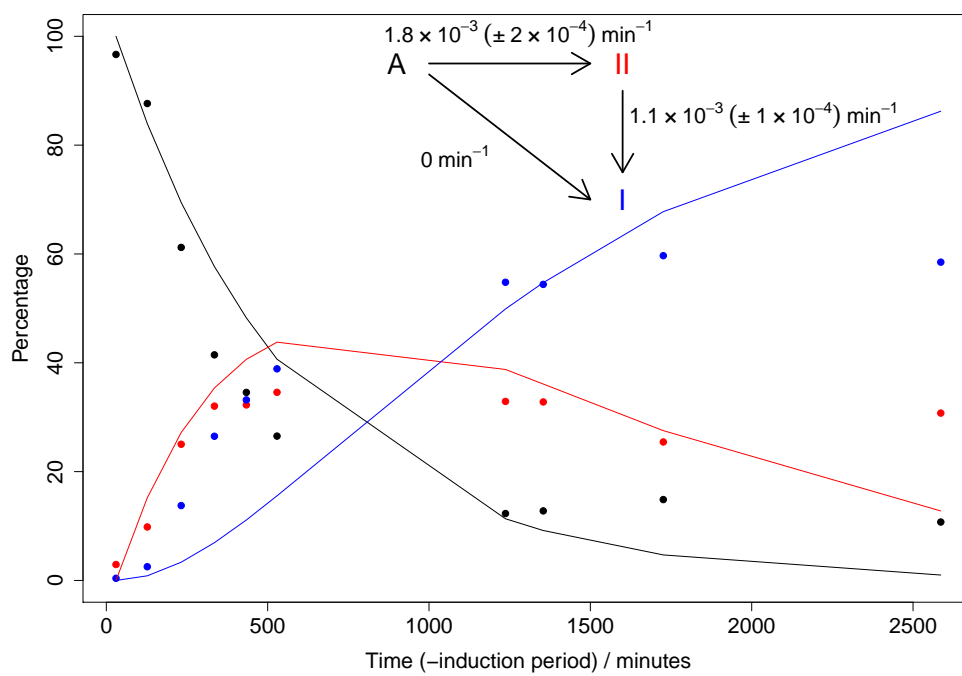


FIGURE B.4: Fit (line plots) to the experimental data (dotted plots) obtained by constraining the rate constant  $A \rightarrow I$  to be  $0 \text{ min}^{-1}$ . Estimated uncertainties are shown in parentheses.

# Appendix C

## Supplementary information part-III

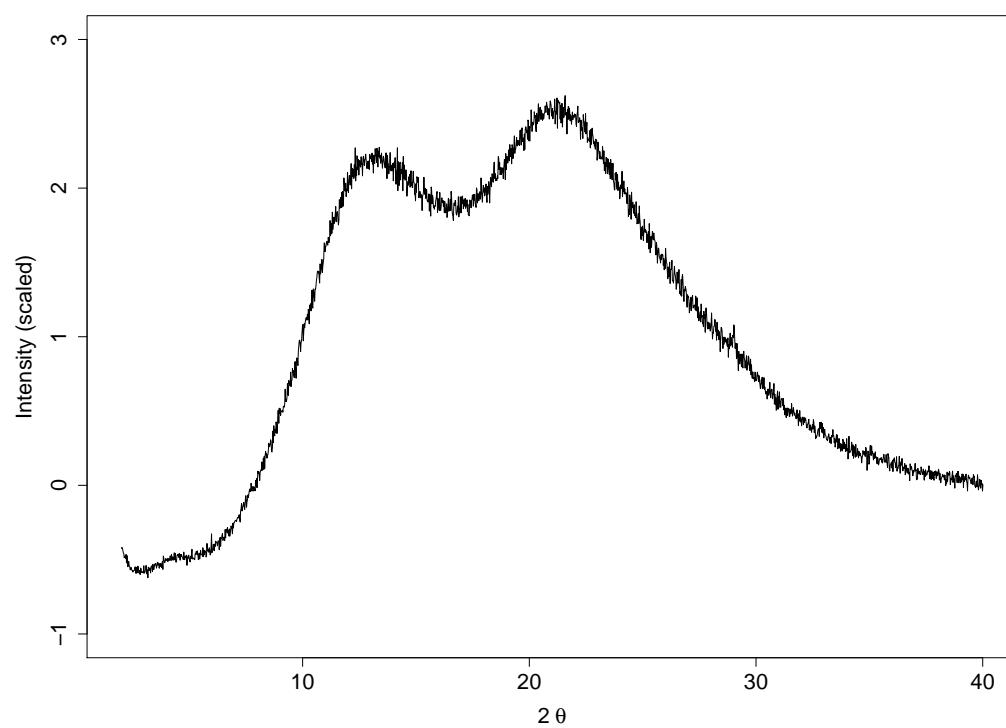


FIGURE C.1: Variance-scaled XRPD pattern of the 30% extrudate.

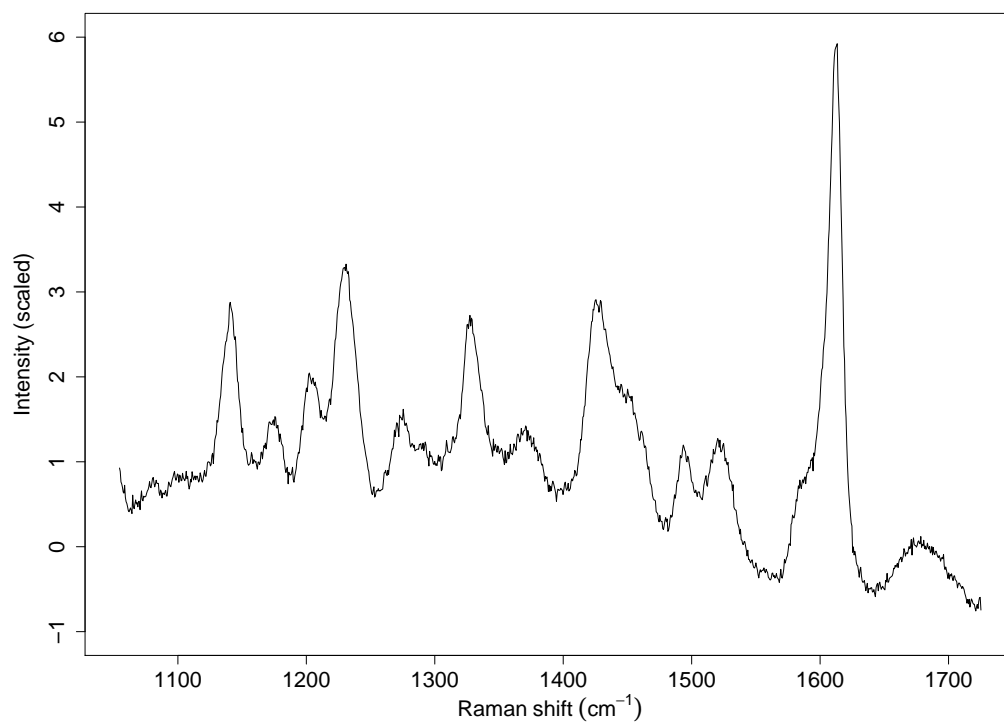
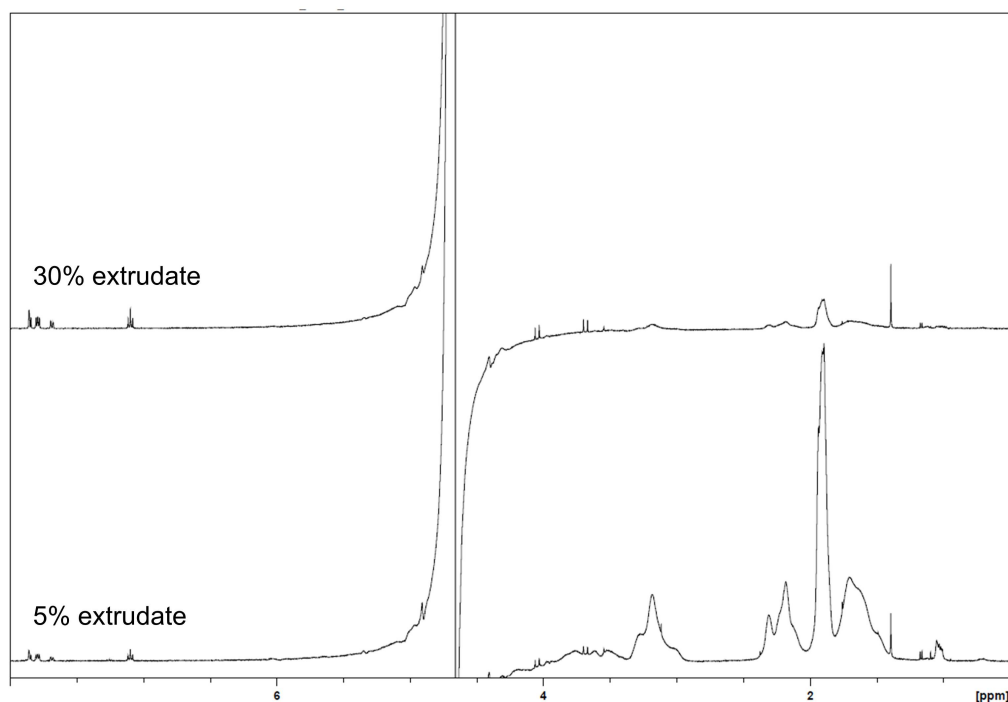


FIGURE C.2: Variance-scaled Raman spectrum of the 30% extrudate.

FIGURE C.3: <sup>1</sup>H NMR spectra of reference solutions of 5% and 30% extrudates.

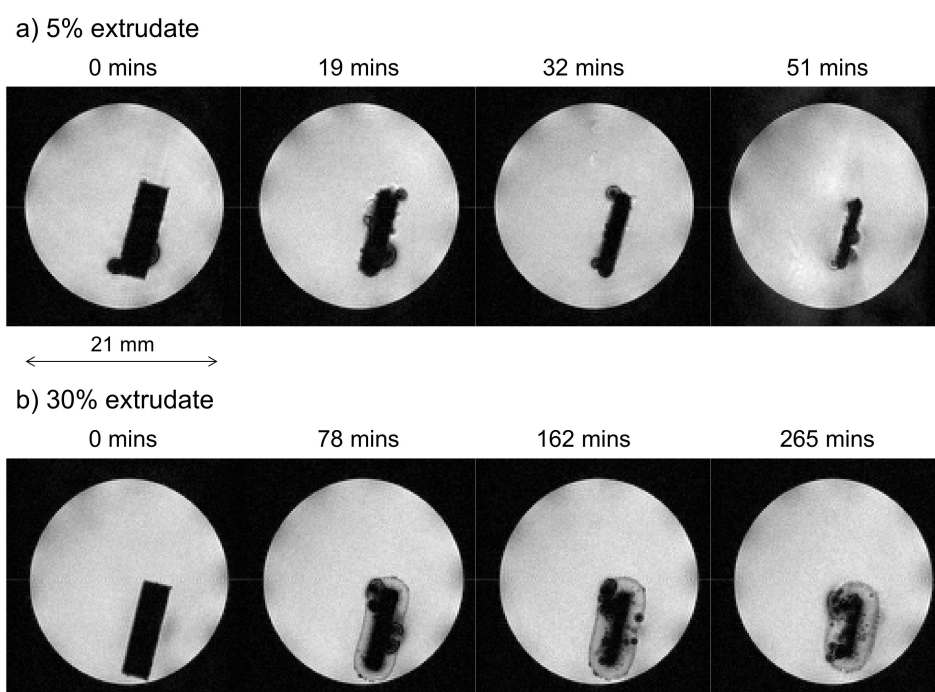


FIGURE C.4: Magnetic resonance images (second experiment) showing the changes as a function of time in one cross sectional slice of the extrudates containing 5% (a) and 30% (b) of bicalutamide.

# Appendix D

## Supplementary information

### Part-IV

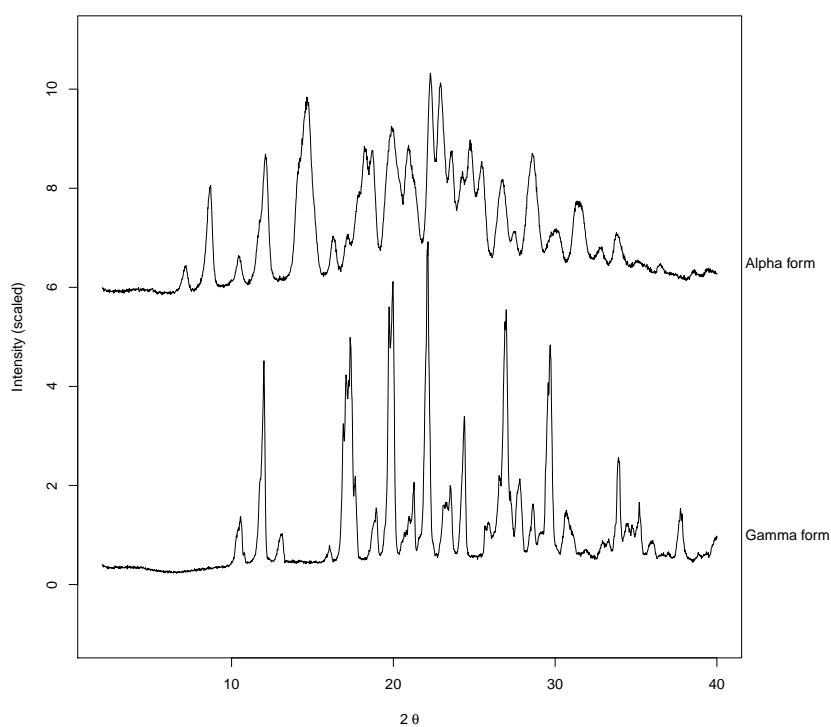


FIGURE D.1: Variance-scaled XRPD data of the  $\gamma$  and  $\alpha$  indomethacin reference forms.

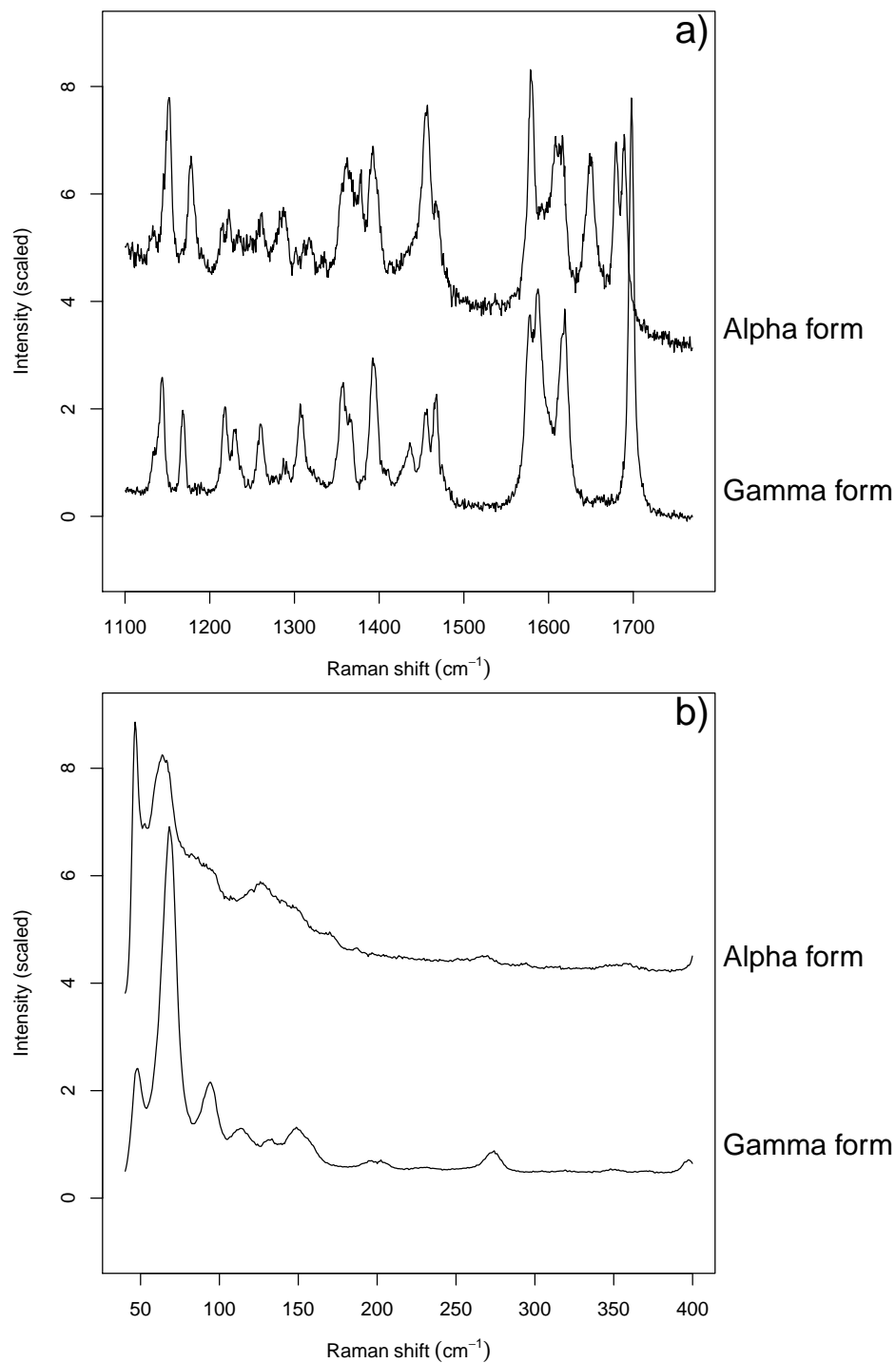


FIGURE D.2: 1100–1770 cm<sup>-1</sup> (a) and 40–400 cm<sup>-1</sup> (b) Raman regions of  $\gamma$  and  $\alpha$  crystalline indomethacin forms. Data have been variance-scaled before plotting. Y-axis offsets were applied for presentational purpose.

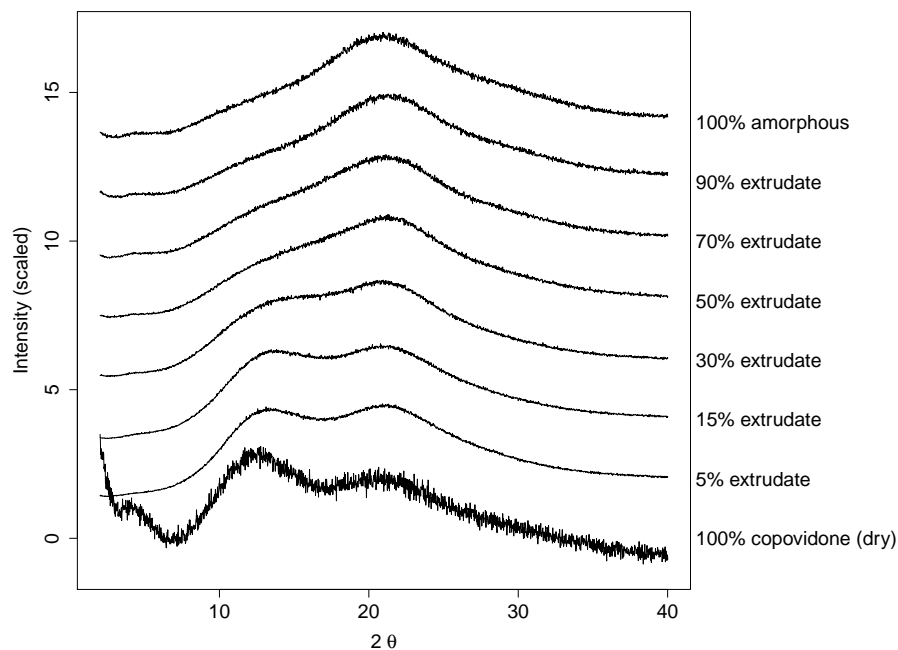


FIGURE D.3: XRPD patterns of the dry indomethacin:copovidone extrudates, 100% copovidone and the 100% amorphous form of indomethacin. Data were variance-scaled before plotting.

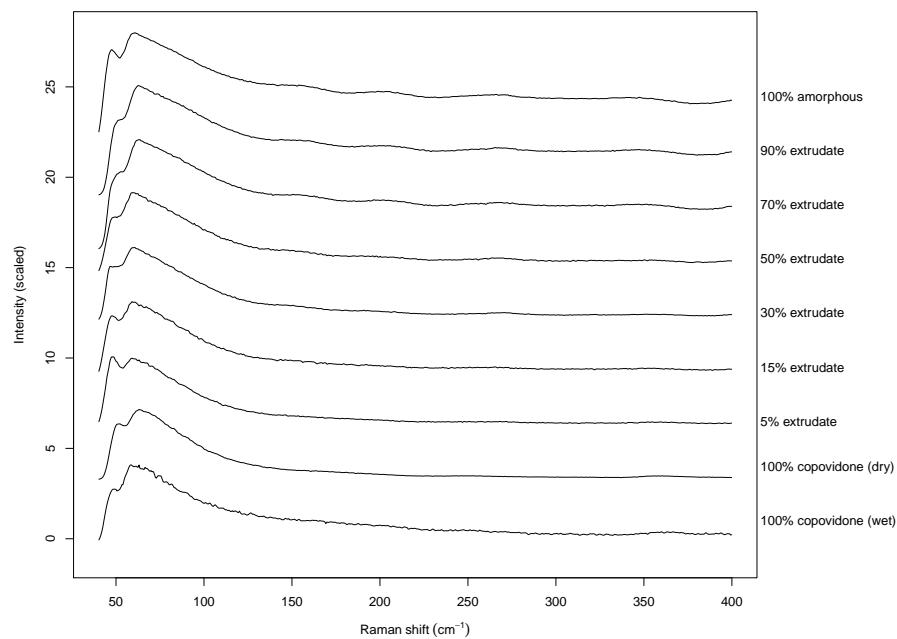


FIGURE D.4: Raman phonon-mode region ( $40\text{--}400\text{ cm}^{-1}$ ) of raw materials. Spectra were variance-scaled before plotting.

# Bibliography

- [1] Florence, A. T.; Attwood, D. *Physicochemical Principles of Pharmacy*, 4th ed.; Pharmaceutical Press: London, 2006.
- [2] Williams III, R. O.; Watts, A. B.; Miller, D. A. *Formulating Poorly Water Soluble Drugs*; Springer: New York, 2012.
- [3] Leuner, C.; Dressman, J. Improving drug solubility for oral delivery using solid dispersions. *Eur. J. Pharm. Biopharm.* **2000**, *50*, 47–60.
- [4] Amidon, G. L.; Lennernäs, H.; Shah, V. P.; Crison, J. R. A Theoretical Basis for a Biopharmaceutic Drug Classification: The Correlation of in Vitro Drug Product Dissolution and in Vivo Bioavailability. *Pharm. Res.* **1995**, *12*, 413–420.
- [5] Takagi, T.; Ramachandran, C.; Bermejo, M.; Yamashita, S.; Yu, L. X.; Amidon, G. L. A Provisional Biopharmaceutical Classification of the Top 200 Oral Drug Products in the United States, Great Britain, Spain, and Japan. *Mol. Pharmaceutics* **2006**, *3*, 631–643.
- [6] Newman, A. *Pharmaceutical Amorphous Solid Dispersions*; Wiley: Hoboken, New Jersey, 2015.
- [7] Butler, J. M.; Dressman, J. B. The developability classification system: Application of biopharmaceutics concepts to formulation development. *J. Pharm. Sci.* **2010**, *99*, 4940–4954.
- [8] Takano, R.; Sugano, K.; Higashida, A.; Hayashi, Y.; Machida, M.; Aso, Y.; Yamashita, S. Oral Absorption of Poorly Water-Soluble Drugs: Computer Simulation of Fraction Absorbed in Humans from a Miniscale Dissolution Test. *Pharm. Res.* **2006**, *23*, 1144–1156.
- [9] Ogunbona, F. A.; Smith, I. F.; Olawoye, O. S. Fat contents of meals and bioavailability of griseofulvin in man. *J. Pharm. Pharmacol.* **1985**, *37*, 283–284.

- [10] Crouse, R. G. Human Pharmacology of Griseofulvin: The Effect of Fat Intake on Gastrointestinal Absorption. *J Invest. Dermatol.* **1961**, *37*, 529–533.
- [11] Schäfer-Korting, M.; Korting, H.; Mutschler, E. Human plasma and skin blister fluid levels of griseofulvin after its repeated administration. *Eur. J. Clin. Pharmacol.* **1985**, *29*, 351–354.
- [12] Winiwarter, S.; Bonham, N. M.; Ax, F.; Hallberg, A.; Lennernäs, H.; Karlén, A. Correlation of Human Jejunal Permeability (in Vivo) of Drugs with Experimentally and Theoretically Derived Parameters. A Multivariate Data Analysis Approach. *J. Med. Chem.* **1998**, *41*, 4939–4949.
- [13] Noyes, A. A.; Whitney, W. R. The rate of solution of solid substances in their own solutions. *J. Am. Chem. Soc.* **1897**, *19*, 930–934.
- [14] Stella, V. J.; Nti-Addae, K. W. Prodrug strategies to overcome poor water solubility. *Adv. Drug Deliv. Rev.* **2007**, *59*, 677–694.
- [15] Wu, K. A New Classification of Prodrugs: Regulatory Perspectives. *Pharmaceuticals* **2009**, *2*, 77–81.
- [16] Serajuddin, A. T. Salt formation to improve drug solubility. *Adv. Drug Deliv. Rev.* **2007**, *59*, 603–616.
- [17] Nelson, E. Solution rate of theophylline salts and effects from oral administration. *J. Am. Pharm. Assoc.* **1957**, *46*, 607–614.
- [18] Nelson, E. Comparative dissolution rates of weak acids and their sodium salts. *J. Am. Pharm. Assoc.* **1958**, *47*, 297–299.
- [19] Atkinson, R. M.; Bedford, C.; Child, K. J.; Tomich, E. G. Effect of Particle Size on Blood Griseofulvin-Levels in Man. *Nature* **1962**, *193*, 588–589.
- [20] Hancock, B. C.; Parks, M. What is the True Solubility Advantage for Amorphous Pharmaceuticals? *Pharm. Res.* **2000**, *17*, 397–404.
- [21] Law, D.; Krill, S. L.; Schmitt, E. A.; Fort, J. J.; Qiu, Y.; Wang, W.; Porter, W. R. Physicochemical considerations in the preparation of amorphous ritonavir–poly(ethylene glycol) 8000 solid dispersions. *J. Pharm. Sci.* **2001**, *90*, 1015–1025.

- [22] Hilfiker, R. *Polymorphism: in the Pharmaceutical Industry*; Wiley-VCH: Weinheim, 2006.
- [23] Kobayashi, Y.; Ito, S.; Itai, S.; Yamamoto, K. Physicochemical properties and bioavailability of carbamazepine polymorphs and dihydrate. *Int. J. Pharm.* **2000**, *193*, 137–146.
- [24] Blagden, N.; de Matas, M.; Gavan, P.; York, P. Crystal engineering of active pharmaceutical ingredients to improve solubility and dissolution rates. *Adv. Drug Deliv. Rev.* **2007**, *59*, 617–630.
- [25] Aakeröy, C. B. Crystal Engineering: Strategies and Architectures. *Acta Crystallogr., B* **1997**, *53*, 569–586.
- [26] Desiraju, G. R. Crystal and co-crystal. *CrystEngComm* **2003**, *5*, 466–467.
- [27] Dunitz, J. D. Crystal and co-crystal: a second opinion. *CrystEngComm* **2003**, *5*, 506–506.
- [28] McNamara, D. P.; Childs, S. L.; Giordano, J.; Iarriccio, A.; Cassidy, J.; Shet, M. S.; Mannion, R.; O'Donnell, E.; Park, A. Use of a Glutaric Acid Cocrystal to Improve Oral Bioavailability of a Low Solubility API. *Pharm. Res.* **2006**, *23*, 1888–1897.
- [29] Aulton, M. E. *Pharmaceutics: The Science of Dosage Form Design*; Churchill Livingstone, 2002.
- [30] Narang, A. S.; Delmarre, D.; Gao, D. Stable drug encapsulation in micelles and microemulsions. *Int. J. Pharm.* **2007**, *345*, 9–25.
- [31] Trull, A. K.; Tan, K. K.; Tan, L.; Alexander, G. J.; Jamieson, N. V. Absorption of cyclosporin from conventional and new microemulsion oral formulations in liver transplant recipients with external biliary diversion. *Br. J. Clin. Pharmacol.* **1995**, *39*, 627–631.
- [32] Loftsson, T.; Brewster, M. E. Pharmaceutical applications of cyclodextrins. 1. Drug solubilization and stabilization. *J. Pharm. Sci.* **1996**, *85*, 1017–1025.
- [33] Stella, V. J.; He, Q. Cyclodextrins. *Toxicol. Pathol.* **2008**, *36*, 30–42.
- [34] Debenedetti, P. G.; Stillinger, F. H. Supercooled liquids and the glass transition. *Nature* **2001**, *410*, 259–267.

- [35] Aso, Y.; Yoshioka, S.; Kojima, S. Relationship between the crystallization rates of amorphous nifedipine, phenobarbital, and flopropione, and their molecular mobility as measured by their enthalpy relaxation and  $^1\text{H}$  NMR relaxation times. *J. Pharm. Sci.* **2000**, *89*, 408–416.
- [36] Hancock, B. C.; Shamblin, S. L. Molecular mobility of amorphous pharmaceuticals determined using differential scanning calorimetry. *Thermochim. Acta* **2001**, *380*, 95–107.
- [37] Marsac, P.; Konno, H.; Taylor, L. A Comparison of the Physical Stability of Amorphous Felodipine and Nifedipine Systems. *Pharm. Res.* **2006**, *23*, 2306–2316.
- [38] Hancock, B. C.; Zografi, G. The Relationship Between the Glass Transition Temperature and the Water Content of Amorphous Pharmaceutical Solids. *Pharm. Res.* **1994**, *11*, 471–477.
- [39] Karmwar, P.; Graeser, K.; Gordon, K. C.; Strachan, C. J.; Rades, T. Investigation of properties and recrystallisation behaviour of amorphous indomethacin samples prepared by different methods. *Int. J. Pharm.* **2011**, *417*, 94–100.
- [40] Kestur, U. S.; Ivanovic, I.; Alonzo, D. E.; Taylor, L. S. Influence of particle size on the crystallization kinetics of amorphous felodipine powders. *Powder Technol.* **2013**, *236*, 197–204.
- [41] Andronis, V.; Zografi, G. Crystal nucleation and growth of indomethacin polymorphs from the amorphous state. *J. Non Cryst. Solids* **2000**, *271*, 236–248.
- [42] Alonzo, D. E.; Gao, Y.; Zhou, D.; Mo, H.; Zhang, G. G.; Taylor, L. S. Dissolution and precipitation behavior of amorphous solid dispersions. *J. Pharm. Sci.* **2011**, *100*, 3316–3331.
- [43] Newman, A.; Knipp, G.; Zografi, G. Assessing the performance of amorphous solid dispersions. *J. Pharm. Sci.* **2012**, *101*, 1355–1377.
- [44] Serajuddin, A. T. M. Solid dispersion of poorly water-soluble drugs: Early promises, subsequent problems, and recent breakthroughs. *J. Pharm. Sci.* **1999**, *88*, 1058–1066.

- [45] Crowley, M. M.; Zhang, F.; Repka, M. A.; Thumma, S.; Upadhye, S. B.; Kumar Battu, S.; McGinity, J. W.; Martin, C. Pharmaceutical Applications of Hot-Melt Extrusion: Part I. *Drug Dev. Ind. Pharm.* **2007**, *33*, 909–926.
- [46] Paudel, A.; Worku, Z. A.; Meeus, J.; Guns, S.; den Mooter, G. V. Manufacturing of solid dispersions of poorly water soluble drugs by spray drying: Formulation and process considerations. *Int. J. Pharm.* **2013**, *453*, 253–284.
- [47] Rumondor, A. C. F.; Marsac, P. J.; Stanford, L. A.; Taylor, L. S. Phase Behavior of Poly(vinylpyrrolidone) Containing Amorphous Solid Dispersions in the Presence of Moisture. *Mol. Pharmaceutics* **2009**, *6*, 1492–1505.
- [48] Ivanisevic, I. Physical stability studies of miscible amorphous solid dispersions. *J. Pharm. Sci.* **2010**, *99*, 4005–4012.
- [49] Konno, H.; Taylor, L. S. Influence of different polymers on the crystallization tendency of molecularly dispersed amorphous felodipine. *J. Pharm. Sci.* **2006**, *95*, 2692–2705.
- [50] Rumondor, A. C. F.; Ivanisevic, I.; Bates, S.; Alonzo, D. E.; Taylor, L. S. Evaluation of Drug-Polymer Miscibility in Amorphous Solid Dispersion Systems. *Pharm. Res.* **2009**, *26*, 2523–2534.
- [51] Six, K.; Murphy, J.; Weuts, I.; Craig, D. Q.; Verreck, G.; Peeters, J.; Brewster, M.; Van den Mooter, G. Identification of Phase Separation in Solid Dispersions of Itraconazole and Eudragit® E100 Using Microthermal Analysis. *Pharm. Res.* **2003**, *20*, 135–138.
- [52] Andrews, G. P.; AbuDiak, O. A.; Jones, D. S. Physicochemical characterization of hot melt extruded bicalutamide–polyvinylpyrrolidone solid dispersions. *J. Pharm. Sci.* **2010**, *99*, 1322–1335.
- [53] Karavas, E.; Ktistis, G.; Xenakis, A.; Georgarakis, E. Effect of hydrogen bonding interactions on the release mechanism of felodipine from nanodispersions with polyvinylpyrrolidone. *Eur. J. Pharm. Biopharm.* **2006**, *63*, 103–114.
- [54] Ilevbare, G. A.; Liu, H.; Edgar, K. J.; Taylor, L. S. Inhibition of solution crystal growth of ritonavir by cellulose polymers - factors influencing polymer effectiveness. *CrystEngComm* **2012**, *14*, 6503–6514.

- [55] De Filippis, P.; Boscolo, M.; Gibellini, M.; Rupena, P.; Rubessa, F. The Release Rate of Indomethacin from Solid Dispersions with Eudragit E. *Drug. Dev. Ind. Pharm.* **1991**, *17*, 2017–2028.
- [56] Van Eerdenbrugh, B.; Taylor, L. S. Small Scale Screening To Determine the Ability of Different Polymers To Inhibit Drug Crystallization upon Rapid Solvent Evaporation. *Mol. Pharmaceutics* **2010**, *7*, 1328–1337.
- [57] Konno, H.; Taylor, L. Ability of Different Polymers to Inhibit the Crystallization of Amorphous Felodipine in the Presence of Moisture. *Pharm. Res.* **2008**, *25*, 969–978.
- [58] Rumondor, A. C.; Taylor, L. S. Application of Partial Least-Squares (PLS) modeling in quantifying drug crystallinity in amorphous solid dispersions. *Int. J. Pharm.* **2010**, *398*, 155–160.
- [59] Nunes, C.; Mahendrasingam, A.; Suryanarayanan, R. Quantification of Crystallinity in Substantially Amorphous Materials by Synchrotron X-ray Powder Diffractometry. *Pharm. Res.* **2005**, *22*, 1942–1953.
- [60] Rumondor, A. C.; Stanford, L. A.; Taylor, L. S. Effects of Polymer Type and Storage Relative Humidity on the Kinetics of Felodipine Crystallization from Amorphous Solid Dispersions. *Pharm. Res.* **2009**, *26*, 2599–2606.
- [61] Aso, Y.; Yoshioka, S. Molecular mobility of nifedipine–PVP and phenobarbital–PVP solid dispersions as measured by  $^{13}\text{C}$ -NMR spin-lattice relaxation time. *J. Pharm. Sci.* **2006**, *95*, 318–325.
- [62] Tatton, A. S.; Pham, T. N.; Vogt, F. G.; Iuga, D.; Edwards, A. J.; Brown, S. P. Probing Hydrogen Bonding in Cocrystals and Amorphous Dispersions Using  $^{14}\text{N}$ – $^1\text{H}$  HMQC Solid-State NMR. *Mol. Pharmaceutics* **2013**, *10*, 999–1007.
- [63] Aso, Y.; Yoshioka, S.; Miyazaki, T.; Kawanishi, T. Feasibility of  $^{19}\text{F}$ -NMR for Assessing the Molecular Mobility of Flufenamic Acid in Solid Dispersions. *Chem. Pharm. Bull.* **2009**, *57*, 61–64.
- [64] Calahan, J. L.; Zanon, R. L.; Alvarez-Nunez, F.; Munson, E. J. Isothermal Microcalorimetry To Investigate the Phase Separation for Amorphous Solid Dispersions of AMG 517 with HPMC-AS. *Mol. Pharmaceutics* **2013**, *10*, 1949–1957.

- [65] Yoshihashi, Y.; Iijima, H.; Yonemochi, E.; Terada, K. Estimation of physical stability of amorphous solid dispersion using differential scanning calorimetry. *J. Therm. Anal. Calorim.* **2006**, *85*, 689–692.
- [66] Yang, J.; Grey, K.; Doney, J. An improved kinetics approach to describe the physical stability of amorphous solid dispersions. *Int. J. Pharm.* **2010**, *384*, 24–31.
- [67] Sinclair, W.; Leane, M.; Clarke, G.; Dennis, A.; Tobyn, M.; Timmins, P. Physical stability and recrystallization kinetics of amorphous ibipinabant drug product by fourier transform raman spectroscopy. *J. Pharm. Sci.* **2011**, *100*, 4687–4699.
- [68] Furuyama, N.; Hasegawa, S.; Hamaura, T.; Yada, S.; Nakagami, H.; Yonemochi, E.; Katsuhide, Evaluation of solid dispersions on a molecular level by the Raman mapping technique. *Int. J. Pharm.* **2008**, *361*, 12–18.
- [69] Taylor, L. S.; Zografi, G. Spectroscopic Characterization of Interactions Between PVP and Indomethacin in Amorphous Molecular Dispersions. *Pharm. Res.* **1997**, *14*, 1691–1698.
- [70] Miyazaki, T.; Yoshioka, S.; Aso, Y.; Kojima, S. Ability of polyvinylpyrrolidone and polyacrylic acid to inhibit the crystallization of amorphous acetaminophen. *J. Pharm. Sci.* **2004**, *93*, 2710–2717.
- [71] Yoshioka, M.; Hancock, B. C.; Zografi, G. Inhibition of indomethacin crystallization in poly(vinylpyrrolidone) coprecipitates. *J. Pharm. Sci.* **1995**, *84*, 983–986.
- [72] Crowley, K. J.; Zografi, G. The use of thermal methods for predicting glass-former fragility. *Thermochim. Acta* **2001**, *380*, 79–93.
- [73] Khougaz, K.; Clas, S. D. Crystallization inhibition in solid dispersions of MK-0591 and poly(vinylpyrrolidone) polymers. *J. Pharm. Sci.* **2000**, *89*, 1325–1334.
- [74] Tantishaiyakul, V.; Kaewnopparat, N.; Ingkatawornwong, S. Properties of solid dispersions of piroxicam in polyvinylpyrrolidone. *Int. J. Pharm.* **1999**, *181*, 143–151.
- [75] Matsumoto, T.; Zografi, G. Physical Properties of Solid Molecular Dispersions of Indomethacin with Poly(vinylpyrrolidone) and

- Poly(vinylpyrrolidone-co-vinyl-acetate) in Relation to Indomethacin Crystallization. *Pharm. Res.* **1999**, *16*, 1722–1728.
- [76] Qian, F.; Huang, J.; Hussain, M. A. Drug–polymer solubility and miscibility: Stability consideration and practical challenges in amorphous solid dispersion development. *J. Pharm. Sci.* **2010**, *99*, 2941–2947.
- [77] Andronis, V.; Zografi, G. The Molecular Mobility of Supercooled Amorphous Indomethacin as a Function of Temperature and Relative Humidity. *Pharm. Res.* **1998**, *15*, 835–842.
- [78] Miller, D. P.; Lechuga-Ballesteros, D. Rapid Assessment of the Structural Relaxation Behavior of Amorphous Pharmaceutical Solids: Effect of Residual Water on Molecular Mobility. *Pharm. Res.* **2006**, *23*, 2291–2305.
- [79] Friesen, D. T.; Shanker, R.; Crew, M.; Smithey, D. T.; Curatolo, W. J.; Nightingale, J. A. S. Hydroxypropyl Methylcellulose Acetate Succinate-Based Spray-Dried Dispersions: An Overview. *Mol. Pharmaceutics* **2008**, *5*, 1003–1019.
- [80] Kawabata, Y.; Wada, K.; Nakatani, M.; Yamada, S.; Onoue, S. Formulation design for poorly water-soluble drugs based on biopharmaceutics classification system: Basic approaches and practical applications. *Int. J. Pharm.* **2011**, *420*, 1–10.
- [81] Guzmán, H. R.; Tawa, M.; Zhang, Z.; Ratanabanangkoon, P.; Shaw, P.; Gardner, C. R.; Chen, H.; Moreau, J. P.; Almarsson, O.; Remenar, J. F. Combined use of crystalline salt forms and precipitation inhibitors to improve oral absorption of celecoxib from solid oral formulations. *J. Pharm. Sci.* **2007**, *96*, 2686–2702.
- [82] Six, K.; Verreck, G.; Peeters, J.; Brewster, M.; Van den Mooter, G. Increased physical stability and improved dissolution properties of itraconazole, a class II drug, by solid dispersions that combine fast- and slow-dissolving polymers. *J. Pharm. Sci.* **2004**, *93*, 124–131.
- [83] Loftsson, T.; Fridriksdóttir, H.; Gudmundsdóttir, T. K. The effect of water-soluble polymers on aqueous solubility of drugs. *Int. J. Pharm.* **1996**, *127*, 293–296.
- [84] Warren, D. B.; Benameur, H.; Porter, C. J.; Pouton, C. W. Using polymeric precipitation inhibitors to improve the absorption of poorly

- water-soluble drugs: A mechanistic basis for utility. *J. Drug. Target.* **2010**, *18*, 704–731.
- [85] Ilevbare, G. A.; Liu, H.; Edgar, K. J.; Taylor, L. S. Maintaining Supersaturation in Aqueous Drug Solutions: Impact of Different Polymers on Induction Times. *Cryst. Growth Des.* **2013**, *13*, 740–751.
- [86] Alonzo, D. E.; Raina, S.; Zhou, D.; Gao, Y.; Zhang, G. G. Z.; Taylor, L. S. Characterizing the Impact of Hydroxypropylmethyl Cellulose on the Growth and Nucleation Kinetics of Felodipine from Supersaturated Solutions. *Cryst. Growth Des.* **2012**, *12*, 1538–1547.
- [87] Craig, D. Q. M. The mechanisms of drug release from solid dispersions in water-soluble polymers. *Int. J. Pharm.* **2002**, *231*, 131–144.
- [88] Craig, D.; Newton, J. The dissolution of nortriptyline HCl from polyethylene glycol solid dispersions. *Int. J. Pharm.* **1992**, *78*, 175–182.
- [89] Saers, E. S.; Craig, D. Q. M. An investigation into the mechanisms of dissolution of alkyl p-aminobenzoates from polyethylene glycol solid dispersions. *Int. J. Pharm.* **1992**, *83*, 211–219.
- [90] *United States Pharmacopoeia 31 and National Formulary 26*; The United States Pharmacopeial Convention, Inc.: Rockville, Md, 2008.
- [91] Coombes, S. R.; Hughes, L. P.; Phillips, A. R.; Wren, S. A. C. Proton NMR: A New Tool for Understanding Dissolution. *Anal. Chem.* **2014**, *86*, 2474–2480.
- [92] Bharti, S. K.; Roy, R. Quantitative  $^1\text{H}$  NMR spectroscopy. *Trends Anal. Chem.* **2012**, *35*, 5–26.
- [93] Dalitz, F.; Cudaj, M.; Maiwald, M.; Guthausen, G. Process and reaction monitoring by low-field NMR spectroscopy. *Prog. Nucl. Magn. Reson. Spectrosc.* **2012**, *60*, 52–70.
- [94] Hulse, W. L.; Gray, J.; Forbes, R. T. A discriminatory intrinsic dissolution study using UV area imaging analysis to gain additional insights into the dissolution behaviour of active pharmaceutical ingredients. *Int. J. Pharm.* **2012**, *434*, 133–139.
- [95] Boetker, J. P.; Savolainen, M.; Koradia, V.; Tian, F.; Rades, T.; Müllertz, A.; Cornett, C.; Rantanen, J.; Østergaard, J. Insights into

- the Early Dissolution Events of Amlodipine Using UV Imaging and Raman Spectroscopy. *Mol. Pharmaceutics* **2011**, *8*, 1372–1380.
- [96] Nielsen, L. H.; Gordon, S.; Pajander, J. P.; Østergaard, J.; Rades, T.; Müllertz, A. Biorelevant characterisation of amorphous furosemide salt exhibits conversion to a furosemide hydrate during dissolution. *Int. J. Pharm.* **2013**, *457*, 14–24.
- [97] Coutts-Lendon, C. A.; Wright, N. A.; Mieso, E. V.; Koenig, J. L. The use of FT-IR imaging as an analytical tool for the characterization of drug delivery systems. *J. Control. Release* **2003**, *93*, 223–248.
- [98] Kazarian, S. G.; Chan, K. L. A. “Chemical Photography” of Drug Release. *Macromolecules* **2003**, *36*, 9866–9872.
- [99] van der Weerd, J.; Chan, K. A.; Kazarian, S. G. An innovative design of compaction cell for in situ FT-IR imaging of tablet dissolution. *Vib. Spectrosc.* **2004**, *35*, 9–13.
- [100] van der Weerd, J.; Kazarian, S. G. Combined approach of FTIR imaging and conventional dissolution tests applied to drug release. *J. Control. Release* **2004**, *98*, 295–305.
- [101] Kazarian, S. G.; van der Weerd, J. Simultaneous FTIR Spectroscopic Imaging and Visible Photography to Monitor Tablet Dissolution and Drug Release. *Pharm. Res.* **2008**, *25*, 853–860.
- [102] Keles, H.; Naylor, A.; Clegg, F.; Sammon, C. Studying the release of hGH from gamma-irradiated PLGA microparticles using ATR-FTIR imaging. *Vib. Spectrosc.* **2014**, *71*, 76–84.
- [103] Wray, P. S.; Clarke, G. S.; Kazarian, S. G. Dissolution of tablet-in-tablet formulations studied with ATR-FTIR spectroscopic imaging. *Eur. J. Pharm. Sci.* **2013**, *48*, 748–757.
- [104] van der Weerd, J.; Kazarian, S. G. Release of poorly soluble drugs from HPMC tablets studied by FTIR imaging and flow-through dissolution tests. *J. Pharm. Sci.* **2005**, *94*, 2096–2109.
- [105] Chan, K. L. A.; Kazarian, S. G. FTIR Spectroscopic Imaging of Dissolution of a Solid Dispersion of Nifedipine in Poly(ethylene glycol). *Mol. Pharmaceutics* **2004**, *1*, 331–335.

- [106] Aaltonen, J.; Heinänen, P.; Peltonen, L.; Kortejärvi, H.; Tanninen, V. P.; Christiansen, L.; Hirvonen, J.; Yliruusi, J.; Rantanen, J. In situ measurement of solvent-mediated phase transformations during dissolution testing. *J. Pharm. Sci.* **2006**, *95*, 2730–2737.
- [107] Savolainen, M.; Kogermann, K.; Heinz, A.; Aaltonen, J.; Peltonen, L.; Strachan, C.; Yliruusi, J. Better understanding of dissolution behaviour of amorphous drugs by in situ solid-state analysis using Raman spectroscopy. *Eur. J. Pharm. Biopharm.* **2009**, *71*, 71–79.
- [108] Windbergs, M.; Haaser, M.; McGoverin, C. M.; Gordon, K. C.; Kleinebudde, P.; Strachan, C. J. Investigating the relationship between drug distribution in solid lipid matrices and dissolution behaviour using Raman spectroscopy and mapping. *J. Pharm. Sci.* **2010**, *99*, 1464–1475.
- [109] Choi, D. H.; Kim, K. H.; Park, J. S.; Jeong, S. H.; Park, K. Evaluation of drug delivery profiles in geometric three-layered tablets with various mechanical properties, in vitro–in vivo drug release, and Raman imaging. *J. Control. Release* **2013**, *172*, 763–772.
- [110] Arnold, Y. E.; Imanidis, G.; Kuentz, M. T. Advancing in-vitro drug precipitation testing: new process monitoring tools and a kinetic nucleation and growth model. *J. Pharm. Pharmacol.* **2011**, *63*, 333–341.
- [111] Kang, E.; Robinson, J.; Park, K.; Cheng, J.-X. Paclitaxel distribution in poly(ethylene glycol)/poly(lactide-co-glycolic acid) blends and its release visualized by coherent anti-Stokes Raman scattering microscopy. *J. Control. Release* **2007**, *122*, 261–268.
- [112] Fussell, A.; Garbacik, E.; Offerhaus, H.; Kleinebudde, P.; Strachan, C. In situ dissolution analysis using coherent anti-Stokes Raman scattering (CARS) and hyperspectral CARS microscopy. *Eur. J. Pharm. Biopharm.* **2013**, *85*, 1141–1147.
- [113] Langham, Z. A.; Booth, J.; Hughes, L. P.; Reynolds, G. K.; Wren, S. A. C. Mechanistic insights into the dissolution of spray-dried amorphous solid dispersions. *J. Pharm. Sci.* **2012**, *101*, 2798–2810.
- [114] Kulinowski, P.; Młynarczyk, A.; Dorożyński, P.; Jasiński, K.; Gruwel, M. L. H.; Tomanek, B.; Weglarz, W. P. Magnetic Resonance Microscopy for Assessment of Morphological Changes in Hydrating

- Hydroxypropylmethyl Cellulose Matrix Tablets In Situ. *Pharm. Res.* **2012**, *29*, 3420–3433.
- [115] Chen, Y. Y.; Hughes, L. P.; Gladden, L. F.; Mantle, M. D. Quantitative ultra-fast MRI of HPMC swelling and dissolution. *J. Pharm. Sci.* **2010**, *99*, 3462–3472.
- [116] Richardson, J. C.; Bowtell, R. W.; Mäder, K.; Melia, C. D. Pharmaceutical applications of magnetic resonance imaging (MRI). *Adv. Drug Deliv. Rev.* **2005**, *57*, 1191–1209.
- [117] Šašić, S. *Pharmaceutical Applications of Raman Spectroscopy*; Wiley-Interscience: Hoboken, New Jersey, 2007.
- [118] Brillante, A.; Bilotti, I.; Della Valle, R. G.; Venuti, E.; Girlando, A. Probing polymorphs of organic semiconductors by lattice phonon Raman microscopy. *CrystEngComm* **2008**, *10*, 937–946.
- [119] Al-Dulaimi, S.; Aina, A.; Burley, J. C. Rapid polymorph screening on milligram quantities of pharmaceutical material using phonon-mode Raman spectroscopy. *CrystEngComm* **2010**, *12*, 1038–1040.
- [120] Alkhalil, A.; Babu, J. N.; Burley, J. C. Analysis of phase transitions in molecular solids: quantitative assessment of phonon-mode vs intramolecular spectral data. *RSC Adv.* **2012**, *2*, 209–216.
- [121] Alonzo, D. E.; Zhang, G. G. Z.; Zhou, D.; Gao, Y.; Taylor, L. S. Understanding the Behavior of Amorphous Pharmaceutical Systems during Dissolution. *Pharm. Res.* **2010**, *27*, 608–618.
- [122] Bühler, V. *Kollidon® Polyvinylpyrrolidone excipients for the pharmaceutical industry*, 9th ed.; BASF: Ludwigshafen, Germany, 2008.
- [123] Karavas, E.; Georgarakis, E.; Sigalas, M. P.; Avgoustakis, K.; Bikiaris, D. Investigation of the release mechanism of a sparingly water-soluble drug from solid dispersions in hydrophilic carriers based on physical state of drug, particle size distribution and drug–polymer interactions. *Eur. J. Pharm. Biopharm.* **2007**, *66*, 334–347.
- [124] Marsac, P. J.; Konno, H.; Rumondor, A. C. F.; Taylor, L. S. Recrystallization of Nifedipine and Felodipine from Amorphous Molecular Level Solid Dispersions Containing Poly(vinylpyrrolidone) and Sorbed Water. *Pharm. Res.* **2008**, *25*, 647–656.

- [125] Sarode, A. L.; Wang, P.; Obara, S.; Worthen, D. R. Supersaturation, nucleation, and crystal growth during single- and biphasic dissolution of amorphous solid dispersions: Polymer effects and implications for oral bioavailability enhancement of poorly water soluble drugs. *Eur. J. Pharm. Biopharm.* **2014**, *86*, 351–360.
- [126] Song, Y.; Wang, L.; Yang, P.; Wenslow, R. M.; Tan, B.; Zhang, H.; Deng, Z. Physicochemical characterization of felodipine-kollidon VA64 amorphous solid dispersions prepared by hot-melt extrusion. *J. Pharm. Sci.* **2013**, *102*, 1915–1923.
- [127] Abu-Diak, O. A.; Jones, D. S.; Andrews, G. P. Understanding the performance of melt-extruded poly(ethylene oxide)–bicalutamide solid dispersions: Characterisation of microstructural properties using thermal, spectroscopic and drug release methods. *J. Pharm. Sci.* **2012**, *101*, 200–213.
- [128] Németh, Z.; Sztatisz, J.; Demeter, A. Polymorph transitions of bicalutamide: A remarkable example of mechanical activation. *J. Pharm. Sci.* **2008**, *97*, 3222–3232.
- [129] Vega, D. R.; Polla, G.; Martinez, A.; Mendioroz, E.; Reinoso, M. Conformational polymorphism in bicalutamide. *Int. J. Pharm.* **2007**, *328*, 112–118.
- [130] Löbmann, K.; Laitinen, R.; Grohgan, H.; Gordon, K. C.; Strachan, C.; Rades, T. Coamorphous Drug Systems: Enhanced Physical Stability and Dissolution Rate of Indomethacin and Naproxen. *Mol. Pharmaceutics* **2011**, *8*, 1919–1928.
- [131] Karmwar, P.; Graeser, K.; Gordon, K. C.; Strachan, C. J.; Rades, T. Effect of different preparation methods on the dissolution behaviour of amorphous indomethacin. *Eur. J. Pharm. Biopharm.* **2012**, *80*, 459–464.
- [132] Oth, M.; Moës, A. Enhanced in vitro release of indomethacin from non-aqueous suspensions using indomethacin-polyvinylpyrrolidone coprecipitate. *Int. J. Pharm.* **1985**, *24*, 275–286.
- [133] Sarode, A. L.; Sandhu, H.; Shah, N.; Malick, W.; Zia, H. Hot Melt Extrusion for Amorphous Solid Dispersions: Temperature and Moisture Activated Drug–Polymer Interactions for Enhanced Stability. *Mol. Pharmaceutics* **2013**, *10*, 3665–3675.

- [134] Aunins, J. G.; Southard, M. Z.; Myers, R. A.; Himmelstein, K. J.; Stella, V. J. Dissolution of carboxylic acids III: The effect of polyionizable buffers. *J. Pharm. Sci.* **1985**, *74*, 1305–1316.
- [135] Tirkkonen, S.; Urtti, A.; Paronen, P. Buffer controlled release of indomethacin from ethylcellulose microcapsules. *Int. J. Pharm.* **1995**, *124*, 219–229.
- [136] Alhalaweh, A.; Roy, L.; Rodríguez-Hornedo, N.; Velaga, S. P. pH-Dependent Solubility of Indomethacin–Saccharin and Carbamazepine–Saccharin Cocrystals in Aqueous Media. *Mol. Pharmaceutics* **2012**, *9*, 2605–2612.
- [137] Sun, D. D.; Lee, P. I. Probing the mechanisms of drug release from amorphous solid dispersions in medium-soluble and medium-insoluble carriers. *J. Control. Release* **2015**, *211*, 85 – 93.
- [138] Smart, L. E.; Moore, E. A. *Solid State Chemistry: An Introduction*, 4th ed.; CRC Press: London, 2012.
- [139] Smith, G. P.; McGoverin, C. M.; Fraser, S. J.; Gordon, K. C. Raman imaging of drug delivery systems. *Adv. Drug Deliv. Rev.* **2015**, *89*, 21–41.
- [140] Larkin, P. J. *Infrared and Raman Spectroscopy; Principles and Spectral Interpretation*, 1st ed.; Elsevier: Waltham, 2011.
- [141] Gordon, K. C.; McGoverin, C. M. Raman mapping of pharmaceuticals. *Int. J. Pharm.* **2011**, *417*, 151–162.
- [142] Balss, K.; Llanos, G.; Papandreou, G.; Maryanoff, C. Quantitative spatial distribution of sirolimus and polymers in drug-eluting stents using confocal Raman microscopy. *J. Biomed. Mater. Res. A* **2008**, *85A*, 258–270.
- [143] Franzen, L.; Windbergs, M. Accessing Raman spectral variability in human stratum corneum for quantitative in vitro depth profiling. *J. Raman. Spectrosc.* **2014**, *45*, 82–88.
- [144] van Apeldoorn, A. A.; van Manen, H.-J.; Bezemer, J. M.; de Bruijn, J. D.; van Blitterswijk, C. A.; Otto, C. Raman Imaging of PLGA Microsphere Degradation Inside Macrophages. *J. Am. Chem. Soc.* **2004**, *126*, 13226–13227.

- [145] Rizi, K.; Green, R. J.; Khutoryanskaya, O.; Donaldson, M.; Williams, A. C. Mechanisms of burst release from pH-responsive polymeric microparticles. *J. Pharm. Pharmacol.* **2011**, *63*, 1141–1155.
- [146] Vervaeck, A.; Saerens, L.; Geest, B. D.; Beer, T. D.; Carleer, R.; Adriaensens, P.; Remon, J.; Vervaet, C. Prilling of fatty acids as a continuous process for the development of controlled release multiparticulate dosage forms. *Eur. J. Pharm. Biopharm.* **2013**, *85*, 587–596.
- [147] Karavas, E.; Georgarakis, M.; Docoslis, A.; Bikiaris, D. Combining SEM, TEM, and micro-Raman techniques to differentiate between the amorphous molecular level dispersions and nanodispersions of a poorly water-soluble drug within a polymer matrix. *Int. J. Pharm.* **2007**, *340*, 76–83.
- [148] Breitenbach, J.; Schrof, W.; Neumann, J. Confocal Raman Spectroscopy: Analytical Approach to Solid Dispersions and Mapping of Drugs. *Pharm. Res.* **1999**, *16*, 1109–1113.
- [149] Zhang, G.; Flach, C. R.; Mendelsohn, R. Tracking the dephosphorylation of resveratrol triphosphate in skin by confocal Raman microscopy. *J. Control. Release* **2007**, *123*, 141–147.
- [150] Alkhalil, A.; Nanubolu, J. B.; Roberts, C. J.; Aylott, J. W.; Burley, J. C. Confocal Raman Microscope Mapping of a Kofler Melt. *Cryst. Growth Des.* **2011**, *11*, 422–430.
- [151] Burley, J. C.; Alkhalil, A.; Bloomfield, M.; Matousek, P. Transmission Raman spectroscopy for quality control in model cocrystal tablets. *Analyst* **2012**, *137*, 3052–3057.
- [152] Nanubolu, J. B.; Burley, J. C. Investigating the Recrystallization Behavior of Amorphous Paracetamol by Variable Temperature Raman Studies and Surface Raman Mapping. *Mol. Pharmaceutics* **2012**, *9*, 1544–1558.
- [153] Krier, F.; Mantanus, J.; Sacré, P. Y.; Chavez, P. F.; Thiry, J.; Pestieau, A.; Eric, PAT tools for the control of co-extrusion implants manufacturing process. *Int. J. Pharm.* **2013**, *458*, 15–24.
- [154] Vajna, B.; Pataki, H.; Nagy, Z.; Farkas, I.; Marosi, G. Characterization of melt extruded and conventional Isoptin formulations using Raman chemical imaging and chemometrics. *Int. J. Pharm.* **2011**, *419*, 107–113.

- [155] Rutan, S.; de Juan, A.; Tauler, R. *Comprehensive Chemometrics*; Elsevier: Oxford, 2009; Vol. 2; Chapter 2.15 - Introduction to Multivariate Curve Resolution, pp 249–259.
- [156] de Juan, A.; Rutan, S.; Tauler, R. *Comprehensive Chemometrics*; Elsevier: Oxford, 2009; Vol. 2; Chapter 2.19 - Two-Way Data Analysis: Multivariate Curve Resolution – Iterative Resolution Methods, pp 325–344.
- [157] Melia, C. D.; Rajabi-Siahboomi, A. R.; Bowtell, R. W. Magnetic resonance imaging of controlled release pharmaceutical dosage forms. *Pharma. Sci. Technol. Today* **1998**, *1*, 32–39.
- [158] Nott, K. P. Magnetic resonance imaging of tablet dissolution. *Eur. J. Pharm. Biopharm.* **2010**, *74*, 78–83.
- [159] Yu, L. X.; Carlin, A. S.; Amidon, G. L.; Hussain, A. S. Feasibility studies of utilizing disk intrinsic dissolution rate to classify drugs. *Int. J. Pharm.* **2004**, *270*, 221–227.
- [160] Zakeri-Milani, P.; Barzegar-Jalali, M.; Azimi, M.; Valizadeh, H. Biopharmaceutical classification of drugs using intrinsic dissolution rate (IDR) and rat intestinal permeability. *Eur. J. Pharm. Biopharm.* **2009**, *73*, 102–106.
- [161] Fagerberg, J. H.; Tsinman, O.; Sun, N.; Tsinman, K.; Avdeef, A.; Bergström, C. A. S. Dissolution Rate and Apparent Solubility of Poorly Soluble Drugs in Biorelevant Dissolution Media. *Mol. Pharmaceutics* **2010**, *7*, 1419–1430.
- [162] *European Pharmacopoeia*, 6th ed.; Directorate for the Quality of Medicines and Healthcare of the Council of Europe: Strasbourg, France, 2008.
- [163] Hancock, B. C.; Zografi, G. Characteristics and significance of the amorphous state in pharmaceutical systems. *J. Pharm. Sci.* **1997**, *86*, 1–12.
- [164] R Development Core Team, *R: A language and environment for statistical computing*; R Foundation for Statistical Computing: Vienna, Austria, 2011.
- [165] Tres, F.; Treacher, K.; Booth, J.; Hughes, L. P.; Wren, S. A. C.; Aylott, J. W.; Burley, J. C. Real time Raman imaging to understand

- dissolution performance of amorphous solid dispersions. *J. Control. Release* **2014**, *188*, 53–60.
- [166] Murtagh, F. A Survey of Recent Advances in Hierarchical Clustering Algorithms. *Comput. J.* **1983**, *26*, 354–359.
- [167] Gendrin, C.; Roggo, Y.; Collet, C. Pharmaceutical applications of vibrational chemical imaging and chemometrics: A review. *J. Pharm. Biomed. Anal.* **2008**, *48*, 533–553.
- [168] Gallagher, N. B.; Shaver, J. M.; Martin, E. B.; Morris, J.; Wise, B. M.; Windig, W. Curve resolution for multivariate images with applications to TOF-SIMS and Raman. *Chemometr. Intell. Lab. Syst.* **2004**, *73*, 105–117.
- [169] Duponchel, L.; Elmi-Rayaleh, W.; Ruckebusch, C.; Huvenne, J. P. Multivariate Curve Resolution Methods in Imaging Spectroscopy: Influence of Extraction Methods and Instrumental Perturbations. *J. Chem. Inf. Comput. Sci.* **2003**, *43*, 2057–2067.
- [170] Awa, K.; Okumura, T.; Shinzawa, H.; Otsuka, M.; Ozaki, Y. Self-modeling curve resolution (SMCR) analysis of near-infrared (NIR) imaging data of pharmaceutical tablets. *Anal. Chim. Acta* **2008**, *619*, 81–86.
- [171] Westheim, R. Bicalutamide forms. US 20040063782, 2004.
- [172] Tres, F.; Patient, J. D.; Williams, P. M.; Treacher, K.; Booth, J.; Hughes, L. P.; Wren, S. A. C.; Aylott, J. W.; Burley, J. C. Monitoring the Dissolution Mechanisms of Amorphous Bicalutamide Solid Dispersions via Real-Time Raman Mapping. *Mol. Pharmaceutics* **2015**, *12*, 1512–1522.
- [173] Van Eerdenbrugh, B.; Alonzo, D. E.; Taylor, L. S. Influence of Particle Size on the Ultraviolet Spectrum of Particulate-Containing Solutions: Implications for In-Situ Concentration Monitoring Using UV/Vis Fiber-Optic Probes. *Pharm. Res.* **2011**, *28*, 1643–1652.
- [174] Ewing, A. V.; Clarke, G. S.; Kazarian, S. G. Stability of indomethacin with relevance to the release from amorphous solid dispersions studied with ATR-FTIR spectroscopic imaging. *Eur. J. Pharm. Sci.* **2014**, *60*, 64–71.

- [175] Greco, K.; Bogner, R. Crystallization of Amorphous Indomethacin during Dissolution: Effect of Processing and Annealing. *Mol. Pharmaceutics* **2010**, *7*, 1406–1418.
- [176] Bergström, C. A. S.; Holm, R.; Jørgensen, S. A.; Andersson, S. B. E.; Artursson, P.; Beato, S.; Borde, A.; Box, K.; Brewster, M.; Dressman, J.; Feng, K.-I.; Halbert, G.; Kostewicz, E.; McAllister, M.; Muenster, U.; Thinnes, J.; Taylor, R.; Mullertz, A. Early pharmaceutical profiling to predict oral drug absorption: Current status and unmet needs. *Eur. J. Pharm. Sci.* **2014**, *57*, 173–199.
- [177] Kaneniwa, N.; Otsuka, M.; Hayashi, T. Physicochemical Characterization of Indomethacin Polymorphs and the Transformation Kinetics in Ethanol. *Chem. Pharm. Bull.* **1985**, *33*, 3447–3455.
- [178] Surwase, S. A.; Boetker, J. P.; Saville, D.; Boyd, B. J.; Gordon, K. C.; Peltonen, L.; Strachan, C. J. Indomethacin: New Polymorphs of an Old Drug. *Mol. Pharmaceutics* **2013**, *10*, 4472–4480.



## Real time Raman imaging to understand dissolution performance of amorphous solid dispersions



Francesco Tres<sup>a</sup>, Kevin Treacher<sup>b</sup>, Jonathan Booth<sup>b</sup>, Les P. Hughes<sup>b</sup>, Stephen A.C. Wren<sup>b</sup>, Jonathan W. Aylott<sup>a</sup>, Jonathan C. Burley<sup>a,\*</sup>

<sup>a</sup> School of Pharmacy, Boots Science Building, University of Nottingham, Nottingham NG7 2RD, United Kingdom

<sup>b</sup> Pharmaceutical Development, AstraZeneca, Macclesfield, SK10 2NA, United Kingdom

### ARTICLE INFO

#### Article history:

Received 28 March 2014

Accepted 30 May 2014

Available online 5 June 2014

#### Keywords:

Poorly soluble drugs

Amorphous solid dispersions

Solid-state transformations

Raman imaging

Intrinsic dissolution rate

Multi-variate curve resolution (MCR)

### ABSTRACT

We have employed for the first time Raman spectroscopic imaging along with multi-variate curve resolution (MCR) analysis to investigate in real time and *in-situ* the dissolution mechanisms that underpin amorphous solid dispersions, with data being collected directly from the dosage form itself. We have also employed a novel rotating disk dissolution rate (RDDR) methodology to track, through the use of high-performance liquid chromatography (HPLC), the dissolution trends of both drug and polymer simultaneously in multi-component systems. Two formulations of poorly water-soluble felodipine in a polymeric matrix of copovidone VA64 which have different drug loadings of 5% and 50% w/w were used as models with the aim of studying the effects of increasing the amount of active ingredient on the dissolution performance. It was found that felodipine and copovidone in the 5% dispersion dissolve with the same dissolution rate and that no Raman spectral changes accompanied the dissolution, indicating that the two components dissolve as single entity, whose behaviour is dominated by water-soluble copovidone. For the 50% drug-loaded dispersion, partial RDDR values of both felodipine and copovidone were found to be extremely low. MCR Raman maps along with classical Raman/X-ray powder diffraction (XRPD) characterisation revealed that after an initial loss of copovidone from the extrudate the drug re-crystallises, pointing to a release dynamics dependent on the low water solubility and high hydrophobicity of felodipine. Raman imaging revealed different rates of transition from amorphous to crystalline felodipine at different locations within the dosage form.

© 2015 The Authors. Published by Elsevier Inc. This is an open access article under the CC BY license (<http://creativecommons.org/licenses/by/4.0/>).

### 1. Introduction

A high number of new chemical entities emerging from the drug development process show pharmacological activity, but at the same time are characterised by poor dissolution and solubility profiles [1]. As a result, there is a strong push to develop innovative formulations for the delivery of such compounds so that the desired oral bioavailability and pharmacological effects are achieved. An increasingly popular class of formulation is represented by amorphous solid dispersions, which are prepared by co-processing the drug and a water-soluble or water-swelling polymeric carrier, commonly *via* spray drying or hot melt extrusion [2,3]. The resultant dispersion, as widely demonstrated for several poorly soluble compounds, has an improved dissolution profile and consequently bioavailability compared to the pure drug [4]. This is attributed to the fact that the drug within the dispersion exists in the amorphous form, which gives a higher dissolution rate than

the corresponding crystalline form, and also due to the presence of the water-soluble polymer [5,6].

One of the key challenges for deploying amorphous solid dispersions in real-world formulations is the understanding of the dissolution performance. Although this is very relevant, due to the fact that the dissolution performance limits the *in vivo* efficacy, relatively few studies have been conducted to investigate the dissolution mechanisms that underpin these systems. As reported by Craig, [7] the dissolution mechanism of amorphous solid dispersions is characterised by a number of critical processes, which primarily depend on the chemical nature of the components and on the drug-to-polymer ratio. In relation to these parameters, Craig classified the drug release from amorphous solid dispersions as polymer-controlled or drug-controlled. It has been demonstrated that the re-crystallisation of the drug either in the solid state or after precipitation in solution, [8,9] the formation of nano- and micro-particles during the dissolution [10] and also the behaviour of the polymer itself, [11] strongly contribute to the final dissolution performance. Amorphous solid dispersion dissolution mechanisms are extremely difficult to de-convolute due to several processes occurring simultaneously.

\* Corresponding author.

E-mail address: [jonathan.burley@nottingham.ac.uk](mailto:jonathan.burley@nottingham.ac.uk) (J.C. Burley).

Classical methods of investigating drug release such as the use of USP dissolution apparatuses [12] do not offer any chemical or spatially-resolved information on potential changes of the solid form (e.g. from amorphous to crystalline, polymorphic transformations or formation of hydrate states) during the dissolution, since the data are collected from the solution, rather than directly from the solid dosage form itself. Given the limitations of the conventional dissolution apparatuses, innovative methods have been developed in an attempt to provide a more complete picture of the drug release. Such methods have included mid-IR, [13,14] near-IR [15,16] and magnetic resonance imaging (MRI) [8,17]. Mid-IR and near-IR provide chemical information, but also have a significant drawback; they are very sensitive to water which clearly limits the use of these techniques in aqueous environments. MRI is attractive as it can offer three-dimensional information, however it provides little chemical specificity.

Raman spectroscopy, theoretically, offers advantages/complementarities compared to these techniques. It provides chemically detailed and two-dimensional spatial information ('hyper-spectral data', one spectrum per pixel) and is able to readily differentiate between amorphous and crystalline solid forms [18,19]. These properties are significant since the chemical and physical forms of the drug can change during the course of the dissolution test [8,9,14]. Moreover, with respect to mid-IR and near-IR, Raman spectroscopy is relatively insensitive to water [20]. Raman spectroscopy is therefore an appropriate technique to investigate how the solid state properties of the drug affect its release and for this reason was employed in this work to understand the performance of amorphous solid dispersions during dissolution in aqueous media.

An amorphous solid dispersion of felodipine, the active ingredient, in a polymeric matrix of copovidone VA64, was used as model formulation. Felodipine is an antihypertensive drug, characterised by high permeability and low water solubility (lower than 0.5 mg/Lt) [21]. Copovidone VA64 is a highly water-soluble polymer (solubility higher than 100 mg/Lt), [22] recognised as a chemical analogue of polyvinylpyrrolidone (PVP). In previous studies, PVP and copovidone VA64 have been successfully used to prepare one-phase amorphous felodipine binary mixtures over a range of composition (0–70% drug loading), showing the ability to inhibit re-crystallisation and to increase the dissolution rate of poorly soluble felodipine [23–27]. The physical mixture of crystalline felodipine and copovidone VA64 has been shown instead to have a small increase in dissolution rate when compared to pure crystalline felodipine, further demonstrating how the physical state of the active ingredient (e.g. amorphous vs. crystalline) affects the whole dissolution performance regardless the presence or absence of the polymer in the formulation [8]. This work follows on from the recent paper by Langham et al., where the use of a combined spectrophotometric and magnetic resonance imaging technique to investigate the dissolution mechanisms of felodipine–copovidone spray-dried amorphous solid dispersions was described [8]. It was found that the dissolution behaviour of the high drug-loaded amorphous solid dispersions is governed by the low aqueous solubility of felodipine and by the re-crystallisation (confirmed by off-line XRPD) of the drug.

In the present work, we investigated formulations which have different drug loadings (5% and 50% w/w), with the aim of studying the effects of increasing the amount of active ingredient on the dissolution performance. Two different approaches were employed to probe the dissolution performance of amorphous solid dispersions. The first used Raman spectroscopy and the second uses a rotating disk dissolution rate (RDDR) test. Our RDDR method, with respect to conventional intrinsic dissolution rate (IDR) test described in the USP and in the European Pharmacopoeia, [12,28] employs HPLC to separate the drug from the polymer and ultimately allows us to measure the performance in aqueous media of multi-component systems.

The aim of this work is to investigate whether Raman spectroscopy provides additional chemical and spatial information regarding the

dissolution mechanisms that underpin amorphous solid dispersions, used in conjunction with RDDR dissolution test.

## 2. Materials and methods

### 2.1. Preparation of amorphous felodipine and extrudate solid dispersions

The amorphous form of felodipine was obtained by heating the drug as received (AstraZeneca, Macclesfield, United Kingdom) in the oven to 160 °C and, after melting, cooling back to room temperature. Visual inspection and Raman spectroscopy confirmed the formation of the amorphous form and the absence of crystalline material within the detection limits (ca. 0.5% or better). 5% and 50% drug-loaded amorphous solid dispersions of felodipine in copovidone (BASF, Ludwigshafen, Germany) were prepared using a co-rotating twin-screw extruder (Thermo Scientific HAAKE MiniLab II). Felodipine and copovidone were pre-mixed for 20 min in a Turbula T2F mixer (Willy A. Bachofen AG Mashinefabrik). The extruder was manually fed with the physical mixture. The screw speed was set to 150 rpm and the temperature to 160 °C. The extrudates with spaghetti shape were then collected, cooled to room temperature and manually milled to fine powder. X-ray powder diffraction confirmed the formation of the amorphous solid dispersion and the absence of crystalline material (Figure S1).

### 2.2. X-ray powder diffraction (XRPD)

XRPD patterns were obtained using a PANalytical CubiX PRO diffractometer. Samples were exposed to Cu-K $\alpha$  radiation at a voltage of 45 kV and a current of 40 mA. After being smeared onto the holder, samples were scanned from 2° to 40° 2 $\theta$ , with a step size of 0.02° 2 $\theta$ .

### 2.3. Rotating disk dissolution rate (RDDR)

RDDR testing was carried on using the rotating disk system, also known as 'Woods apparatus'. The die cavity has a diameter of 8 mm with subsequent exposed sample surface area of 0.5 cm<sup>2</sup>. About 250 mg of extrudate powder was compressed under a compression force of 2000 kg using a manual IR press (Specac). The experiment was performed in a Sotax AT7 semi-automated dissolution bath equipped with an automated sample collector. Compressed discs were immersed in 500 ml of deionised water at 37 °C ( $\pm$  0.5), at 100 rpm rotational speed. The automated sample collector removed aliquots of sample from the dissolution medium at regular time intervals over 120 min. The samples were then analysed by reverse phase high performance liquid chromatography (RP-HPLC). Both the experiments for 5 and 50% extrudates were performed in triplicate. HPLC analysis was carried out using an Agilent 1100 with UV detection at 210 nm, equipped with an Agilent PLRP-S 300 Å 3  $\mu$ m 50 mm column (polystyrene/divinylbenzene stationary phase). The flow rate was set to 1.0 ml/min and the temperature of the column was kept at 40 °C. A linear gradient elution was used starting at 40% acetonitrile/60% deionised water and ending at 90% acetonitrile/10% deionised water after 3.5 min, with chromatograms collected up to 5 min. A series of standard solutions of felodipine and copovidone were prepared to generate a calibration curve covering the concentration range of dissolved sample. The partial RDDR of both drug and polymer was calculated using linear regression analysis [12,28]. The partial RDDR of the substance tested was determined from the slope of the regression line.

### 2.4. Raman spectroscopy

We investigated the dissolution performance of compressed extrudate powder. Spherical compacts with a diameter of 5 mm and a weight of 50 mg were prepared with a manual IR press (Specac) using a compression force of ca. 20 kN. The dissolution test was performed in a flow cell, which is illustrated in Figure S2. Deionised water was

used as dissolution medium and the flow rate was set to 10 ml/min. The flow cell was placed under the objective of the Raman microscope and data were collected as function of time using a Horiba LabRAM HR confocal microscope/spectrometer. The system has an automated xyz stage (Märzhäuser) for mapping. In all the experiments, a near-IR laser (785 nm) of 250 mW power was employed. Spectra were acquired using a 50 × objective and a 300 μm confocal hole. A 600 lines/mm rotatable diffraction grating along a path length of 800 mm was used to simultaneously scan a range of frequencies. Raman spectra were collected using a SYNAPSE CCD detector (1024 pixels). During the dissolution experiment, before each map being acquired, the z-axis position of the sample was adjusted to maximise the Raman signal. For both formulations (5% and 50% felodipine), spectra were obtained mapping an area of 500 × 500 μm with a grid spacing of 50 μm along both x-axis and y-axis, a total of 121 spectra for map. As each individual spectrum was collected for 1 s, repeated once in order to automatically remove the cosmic rays, the whole map required only 5 min. For the 5% extrudate compact, eight maps were acquired across a 70 minute time frame in the spectral range from 1100 to 1750 cm<sup>-1</sup> (finger print region). For the 50% extrudate compact, eight maps were acquired over 1705 min (28 h25) in the phonon-mode (30–400 cm<sup>-1</sup>) and finger print (1100–1750 cm<sup>-1</sup>) regions using a fixed grating to allow relatively rapid mapping. In the latter case, the phonon-mode range was also scanned because it is extremely sensitive to the different solid forms (amorphous, crystalline, etc.) and therefore the potential drug re-crystallisation can be readily detected [18,19]. All the spectra from each map were integrated to produce a single averaged spectrum corresponding to each time point. In this way, it was possible to determine any spectral changes occurring during the dissolution test.

To obtain spatially-resolved information from the 50% extrudate compact, the dissolution experiment was repeated increasing significantly the spatial resolution. Seven maps were acquired over 1705 min (28 h25) in the spectral range between 1100 and 1750 cm<sup>-1</sup>, across a 500 × 1000 μm area at a grid spacing of 15 μm along the x-axis, and 30 μm along the y-axis, a total of 1156 spectra per map. As the data acquisition time was 2 s for each spectrum, repeated once, each map required

1 h and 30 min for acquisition. False colour maps were generated using multi-variate curve resolution (MCR). A single data matrix, comprising all the spectra collected across the entire dissolution experiment (8092 spectra), was produced in order to probe changes as a function of both xy-position and time. Numerical codes for statistical analyses were written in the 'R' language, which is open-source and freely available [29]. Data were scaled prior to analysis and plotting using variance scaling and mean centering standard methods, as per standard practice [20] to reduce the effect of variability in Raman scattering efficiency. For multi-variate curve resolution analysis, the 'ALS-MCR' module (alternating least-squares algorithm) was employed, while hierarchical agglomerative clustering is part of the standard package in R. All numerical routines along with the raw data are included in the supplementary material for information and reference.

### 2.5. Optical imaging

Photographic images of the compact during the dissolution were taken at regular time intervals using a CoolSNAP-Pro CF camera (Media Cybernetics) equipped with a Nikon AF Micro NIKKOR 60 mm lens. The same experimental setup described in the previous section was used, with the flow cell placed under the camera instead of the Raman microscope.

## 3. Results and discussion

### 3.1. Optical imaging

Before commencing a full discussion of the RDDR and Raman data, it is important to observe the optical images taken through the dissolution experiment for the 5% and 50% drug-loaded compacts (Fig. 1a and b). Prior to the dissolution test, both formulations appear similar, being yellowish compacts. It is important to notice the different experimental time-scales used for the two formulations. The 5% extrudate dissolution experiment was carried out for 80 min after which time the images show that the compact is completely dissolved. For the 50% drug-

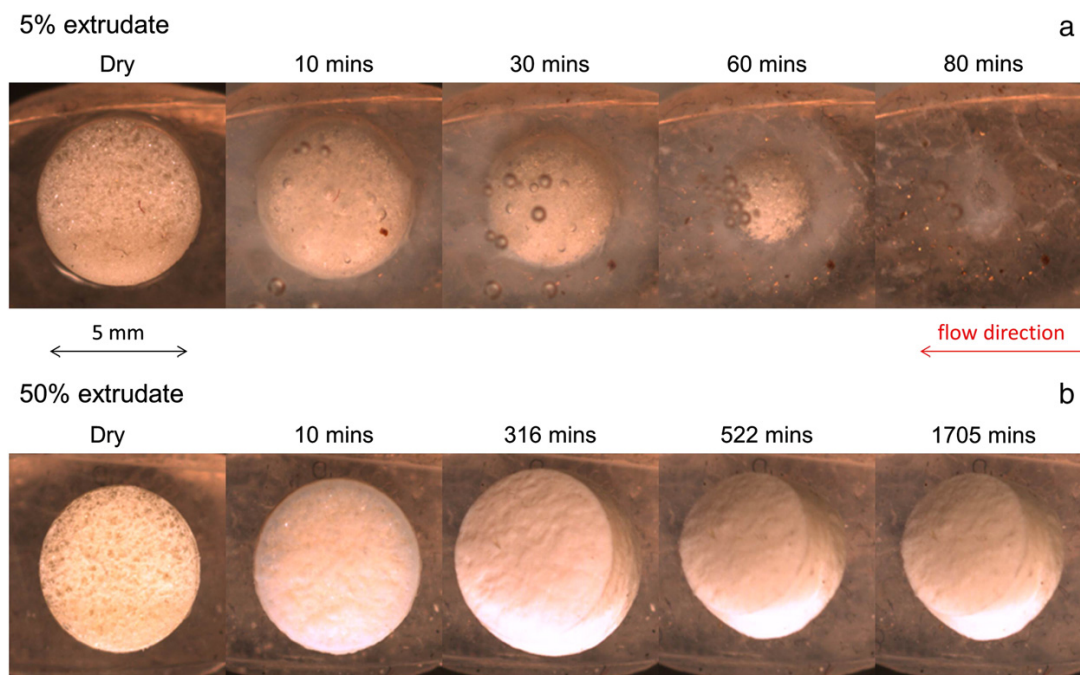


Fig. 1. Optical images taken through the dissolution experiment of the 5% extrudate (a) and 50% extrudate (b) compacts.

loaded formulation, the time-scale was significantly longer. In total, the compact was observed in the flow cell for 1705 min, remaining intact even after the end of this period. An in depth observation of the images from the 50% extrudate shows that the compact swells and increases in size during the first 316 min, then slightly reduces and remains intact until the end of the experiment. This suggests that the initial hydration leads to swelling of the compact rather than to dissolution/erosion, due to the high content of poorly soluble felodipine in the extrudate (images until 316 min). This behaviour was previously described by Langham et al [8]. In Fig. 7 of their paper, they reported MRI sequences showing that the 50% felodipine-loaded spray-dried material swells as a result of water ingress from the dissolution medium. The visual observation of the optical images relative to the 50% extrudate is confirmed by the kinetic trend generated by counting the number of pixels of the compact during the dissolution test (Figure S3). The trend is characterised by an increase in pixel number until 316 min, which corresponds to the observed increase in the compact size. Following this, the number of pixels decreases with the rate of decrease falling to near-zero between 1093 and 1705 min, confirming that the size of the compact reduces after an initial swelling. The reduction of the compact size after an initial swelling was not previously seen in the MRI images reported by Langham et al [8]. This change in behaviour may be related to the different conditions during preparation *via* hot melt extrusion compared to spray drying (e.g. high temperatures, absence of solvents, formulation bulk density, etc) which may affect the final physico-chemical properties of amorphous solid dispersions and thus their performance in aqueous media.

### 3.2. Rotating disk dissolution rate (RDDR)

The intrinsic dissolution rate (IDR) test has been widely used in biopharmaceutics for measuring the dissolution rate of pure active ingredients [30,31]. It is an important biopharmaceutics screening tool, and requires far less material than a traditional dissolution test. IDR measurements yield a dissolution rate normalised to the exposed surface area of the material. Formally, IDR applies only to pure drug substances [12]. Here we extend the IDR concept to formulations. By analogy with disk IDR, we define a 'rotating disc dissolution rate' RDDR. By simply coupling an IDR apparatus to a HPLC system, the partial RDDR of both the pure drug substance and the excipients (in the present case copovidone) can be measured and compared for different formulations. The partial RDDR for the drug and polymer in the different formulations are shown below to provide valuable information on the mechanism of drug release.

The dissolution rate values for the 5% and 50% drug-loaded formulations are summarised in Table 1. The dissolution profiles can be inspected in Figure S4 of the supplementary information. Partial RDDR was calculated using the first 20 minute time period, where the trend is relatively linear, in accordance with USP procedures [12]. Looking at the formulation with 5% drug loading, the partial RDDR value for felodipine is 0.17 mg/min/cm<sup>2</sup>, while the partial RDDR for copovidone is 3.10 mg/min/cm<sup>2</sup>. The intrinsic dissolution rate value of pure crystalline felodipine has been previously found to be 0.00064 mg/min/cm<sup>2</sup> in

**Table 1**

Partial RDDR values of felodipine and copovidone for the 5% and 50% extrudate formulations. The index of performance was obtained dividing the partial RDDR value of felodipine by the total RDDR value of formulation (felodipine plus copovidone) and then normalising by the felodipine mass fraction.

	RDDR (mg/min/cm <sup>2</sup> )				Index of performance <sup>a</sup>
	Time	Felodipine	Copovidone	Total	
5% extrudate	<20 min	0.17 (±0.02)	3.10 (±0.43)	3.26	1.0
50% extrudate	<20 min	0.01 (±0.01)	0.25 (±0.01)	0.26	0.07

<sup>a</sup> Index of performance = (Partial RDDR felodipine / Total RDDR) / drug mass fraction.

pH 6.5 FaSSIF medium, so in comparison the 5% extrudate exhibits approximately a 265 fold increase in dissolution rate [32]. The significant improvement in dissolution is in agreement with literature on felodipine amorphous solid dispersions [27,33]. The dissolution rate of the polymer allows calculation of an index of performance of the formulation which essentially shows how the two components of the amorphous solid dispersion behave during the dissolution process. The equation to calculate the index of performance is reported in Table 1. The index of performance for the low drug-loaded extrudate results in a value of 1, indicating that felodipine and copovidone have the same dissolution trend and thus they effectively dissolve as single entity, the molecular dispersion of felodipine in copovidone. Given the very low solubility of felodipine, the release of the 5% extrudate is clearly dependent on the high water solubility of the polymer.

Turning now to the formulation with high drug loading, it is immediately evident that both felodipine and copovidone have partial RDDR values significantly lower when compared to those calculated for the 5% extrudate (Table 1). The index of performance is also very low (0.07), indicating that the dissolution rates of felodipine and copovidone are in this case very different, suggesting that the two components of the formulation are not behaving as a single entity but as two separate components. Compared to the IDR value of pure extruded copovidone (5.20 mg/min/cm<sup>2</sup> in pH 6.8 blank FaSSIF medium, Figure S4), copovidone present in the 50% extrudate shows approximately a 21 fold decrease in dissolution rate. RDDR data suggest that the drug release is felodipine-dependent, where low solubility in water and high hydrophobicity of the drug contribute to decrease the wettability and to slow the water uptake in the formulation.

Summarising, the 5% drug-loaded extrudate showed polymer-dependent dissolution behaviour with felodipine dissolving simultaneously with copovidone. For the 50% extrudate, the rate of felodipine release is considerably lower than that observed for the 5% drug-loaded formulation. Although the RDDR test gives a comprehensive explanation about the dissolution trend observed for the low drug-loaded formulation, it does not clearly explain why felodipine shows a very low dissolution rate for the 50% extrudate. To obtain a better understanding of the chemical changes that occur during dissolution of the formulation, Raman spectroscopic imaging was used to interrogate the samples.

### 3.3. Raman spectroscopy

#### 3.3.1. Dry raw materials spectra: visual observation

The Raman spectra of the raw materials are shown in Fig. 2a (finger print) and 2b (phonon-mode). Starting with the pure components, it is evident that the spectrum of felodipine is characterised by sharp bands and a good signal/noise ratio, whereas the spectrum of copovidone shows less-defined bands. At first approximation, the amorphous solid dispersion spectra appear as a linear combination of melt quenched felodipine (amorphous reference form) and copovidone. In the 5% extrudate spectrum, copovidone bands are predominant, while in the 50% extrudate bands related to felodipine prevail. In the latter case two slight shifts appear when comparing to the spectrum of melt quenched felodipine: the band at 1209 cm<sup>-1</sup> moves to a lower wavenumber, while the band at 1497 cm<sup>-1</sup> appears at higher wavenumber. These changes can be ascribed to the formation of molecular interactions between the drug and the polymer coupled with minor conformational changes, as has been previously reported for amorphous solid dispersions of felodipine and PVP [11].

Turning now to the felodipine spectra, we can see significant differences between the amorphous (melt quenched felodipine) and the crystalline (felodipine as received) solid forms. Firstly, the bands of the crystalline form appear more intense and sharper than those of the amorphous form, due to the disorganised molecular environment of the amorphous solid state. Furthermore, a detailed observation highlights that the intra-molecular vibration bands at 1213, 1492 and 1645 cm<sup>-1</sup> of the amorphous form slightly shift to higher

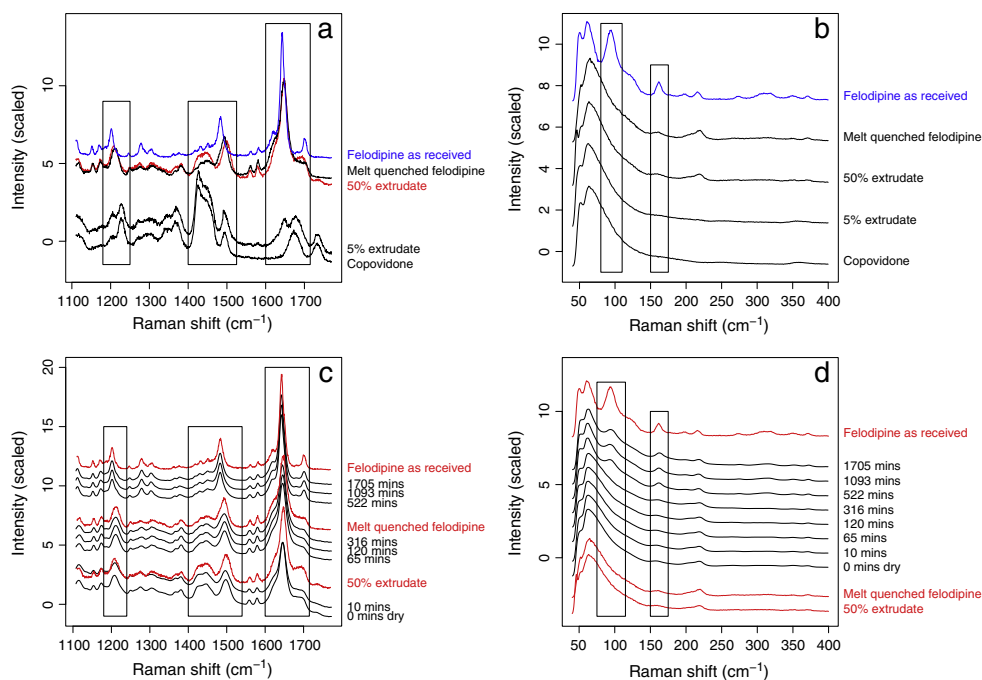


**Fig. 2.** Finger print (a) and phonon-mode (b) regions of raw materials spectra and finger print (c) and phonon-mode (d) regions of the averaged spectra relative to the dissolution of the 50% extrudate compact, with reference spectra in red. Y-Axis offsets were employed for presentational purposes and differ between panels.

wavenumber. In the phonon-mode region, which results from inter-molecular vibration, the two felodipine solid forms have different spectra. The amorphous form spectrum is characterised by broad bands and a continuous distribution of inter-molecular vibrations. In the crystalline form, sharp bands are present at 94 and 168  $\text{cm}^{-1}$ , due to the quantised nature of the inter-molecular vibrations in the crystalline material. Thus, as reported in literature, [18,19] the phonon-mode region represents an area of the Raman spectrum where it is possible to rapidly distinguish between different solid forms.

### 3.3.2. Dissolution experiments

**3.3.2.1. Averaged spectra: visual observation.** Raman averaged spectra for the 5% extrudate dissolution are presented in Figure S5. Examination of the data does not reveal significant changes in the spectra across the entire period covered by these data (0–70 min), beyond a reduction in spectral intensity as the compact dissolves (as seen in the optical images Fig. 1a). The ratio between the band of felodipine at 1650  $\text{cm}^{-1}$  and that of copovidone at 1426  $\text{cm}^{-1}$  is preserved throughout the whole dissolution process. The Raman data essentially show that felodipine and copovidone dissolve as a single entity rather than as two separate components. This is in accordance with the RDDR data, which illustrated that felodipine and copovidone dissolve with the same rate. Therefore, it seems reasonable to suggest that the dissolution occurs from the molecular dispersion, with the overall behaviour being dependent on the highly-soluble polymer.

Raman data of the 50% extrudate dissolution are shown in Fig. 2c (finger print region) and d (phonon-mode region). Raman data show that the spectrum does not change after 10 min (Fig. 2c, 10 min). Bands relative to felodipine (1497  $\text{cm}^{-1}$ ) and copovidone (1426  $\text{cm}^{-1}$ ) preserve the same ratio as in the spectrum of the compact 'Dry'. Proceeding with the analysis, after 65 min the intensity of copovidone band at 1426  $\text{cm}^{-1}$  appears to decrease in relation to that of felodipine at 1497  $\text{cm}^{-1}$ . A comparison with the '50% extrudate' reference spectrum reveals that the band at 1209  $\text{cm}^{-1}$  moves to slightly higher wavenumber

and that at 1497  $\text{cm}^{-1}$  shifts to lower wavenumber. Figure S6 presents 'difference spectra' obtained by subtracting each averaged spectrum corresponding to each time point from the averaged spectrum of the compact 'Dry', which was used in this case as reference spectrum. 'Difference spectra' between 65 and 316 min are characterised by negative bands at 1213 and 1492  $\text{cm}^{-1}$  which correspond to the observed shifts in Fig. 2c. These spectral shifts, which were previously denoted in the visual observation of the raw ingredients spectra (Fig. 2a), unambiguously indicate a strong correlation with the melt quenched (amorphous) felodipine spectrum. It is likely that the faster dissolution of copovidone with respect to felodipine from the drug:polymer dispersion leads to a build-up of felodipine-rich amorphous material on the surface of the compact. The second important change occurs at 522 min. It is immediately obvious that the averaged spectrum, after 522 min, corresponds to the crystalline form of felodipine. When compared to melt quenched felodipine, intra-molecular bands at 1202, 1484 and 1642  $\text{cm}^{-1}$  shift to lower wavenumber as well as they appear more intense and sharper. These spectral changes were previously seen in Fig. 2a, revealing the formation of crystalline felodipine. In the phonon-mode region (Fig. 2d), well-defined bands appear at 94 and 168  $\text{cm}^{-1}$  after 522 min, essentially confirming that amorphous felodipine begins to re-crystallise by this time-point.

**3.3.2.2. Averaged spectra: hierarchical agglomerative clustering (HAC).** In this section we describe the use of an objective statistical analysis method to validate our subjective interpretation of the Raman data. HAC is an automated method of cluster analysis which calculates a distance, also called 'degree of dissimilarity', between datasets, [34] including Raman spectra [19]. The dendrogram obtained applying HAC to the 21 datasets is shown in Fig. 3. It is immediately evident that the overall structure of the dendrogram is governed by two branches: spectra relative to the dissolution of the 5% extrudate with the 5% extrudate and copovidone reference spectra, and spectra relative to the dissolution of the 50% extrudate with the remaining reference spectra ('50% extrudate', 'Melt quenched felodipine' and 'Felodipine as received').

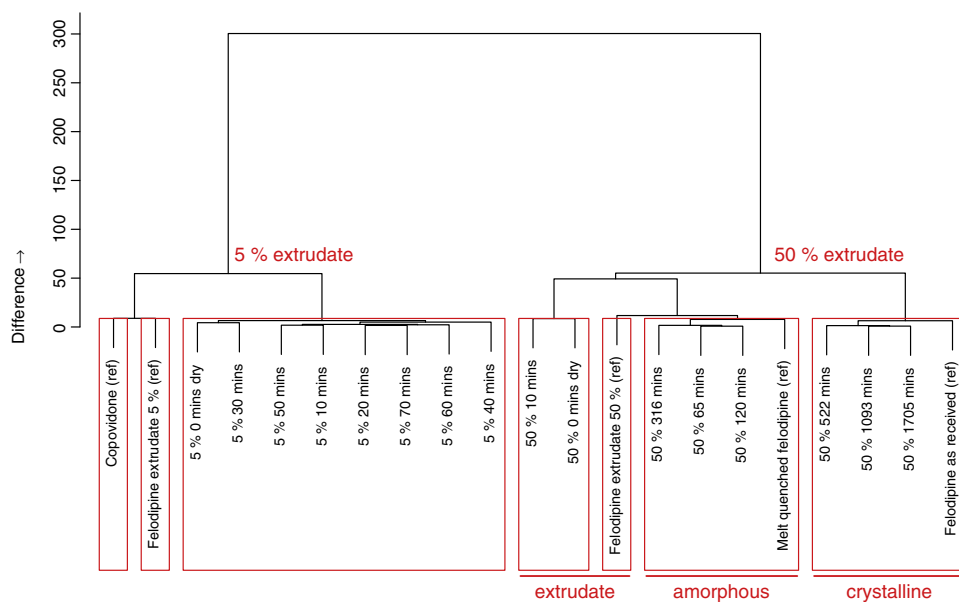


**Fig. 3.** Similarity dendrogram with clusters indicated by red boxes. Raw data were variance-scaled and mean-centred before performing HAC. The Euclidean distance measure was employed to define clusters.

Starting with the branch of the 5% extrudate (LHS of plot), it is clear that all the spectra relative to the dissolution can be classified by only one cluster, as they are characterised by a high degree of similarity. This trend is in a good agreement with the visual inspection of the data. As noted earlier (Figure S5), significant changes were not observed in the spectra collected during the dissolution of the 5% extrudate compact.

Turning now to the other portion of the dendrogram, that relative to the high drug-loaded formulation (RHS of plot), the presence of three main clusters is immediately apparent. The first includes '50% extrudate dry' and '50% extrudate 10 mins' spectra, which show high similarity for the 50% extrudate reference. The second cluster includes spectra collected between 65 and 361 min, with the reference spectrum of melt quenched (amorphous) felodipine. The last cluster includes spectra collected from 522 min until the end of the experiment along with the reference crystalline form of felodipine. Again, HAC confirms the visual inspection of the data, further demonstrating that two transformations occur during the dissolution of the high drug-loaded extrudate. The first involves the conversion, *via* dissolution of copovidone, of mixed extrudate into felodipine-rich amorphous material on the surface of the compact, indeed spectra collected between 65 and 361 min showed high similarity for the melt quenched reference form. The other is the re-crystallisation of the amorphous felodipine after 522 min. The first transformation clearly explains the extremely low partial RDDR values observed during the dissolution of the 50% extrudate. Copovidone cannot drive the dissolution of felodipine due to an insufficient polymer to drug ratio, resulting in formation of felodipine-rich hydrophobic amorphous areas on the compact surface. The disruption of the drug–polymer molecular dispersion system through loss of copovidone then induces the drug re-crystallisation.

We conclude by stating that HAC widely validated all our subjective observations of Raman data, adding to them an objective and impartial component.

**3.3.2.3. Multi-variate curve resolution (MCR).** We now discuss the spatially resolved images of the crystallisation event observed for felodipine present in the high drug-loaded formulation. Raman maps of the 50% extrudate compact, obtained by MCR analysis of all the spectra collected across the entire dissolution test (8092 spectra), are presented in Fig. 4.

MCR results can be presented as loadings which provide the spectral phase of a specific component, and score plots that illustrate the spatial distribution of the corresponding component. Three components were required to deconvolute the mapped data. Comparison with the reference spectra unambiguously indicates that the first component, MCR1, can be associated with the extrudate and the second, MCR2, with the crystalline form of felodipine. The excellent peak to peak correlation between loadings and reference spectra confirms the utility of MCR as the statistical method to analyse spatial–temporal Raman data. MCR3 mostly picked up the background noise which characterises areas where no compact is present. The score plots show that the extrudate (MCR1) is homogeneously distributed throughout the mapped compact surface before immersion in water. The corresponding MCR2 score plot indicated no traces of crystalline material in the mapped area of the dry compact. Then, the amount of crystalline felodipine (MCR2) rapidly increases at the expense of the extrudate (MCR1) after 316 min, and this is reflected by the re-crystallisation kinetic shown in Fig. 5. It is interesting to notice the complementarity of MCR1 and MCR2 score plots at 316 and 522 min, which denotes the coexistence of the extrudate and crystalline felodipine. Regions where the extrudate (MCR1) is present to its maximum are indicated by white or red colour, while the corresponding crystalline regions (MCR2) are characterised by blue colour, and *vice versa*. The re-crystallisation of amorphous felodipine evidently occurs at different rates in different regions of the compact surface, suggesting that the crystal growth stage follows an initial stage of heterogeneous nucleation. The nucleation/crystallisation process is likely linked with loss of copovidone from the extrudate. It is well known that the polymeric carrier in amorphous solid dispersion formulations not only has the function to improve the dissolution properties of poorly soluble drugs, but also inhibits crystal growth of the amorphous form, *via* antiplasticisation effect or hydrogen-bonding interactions between drug and polymer [25]. It is therefore likely that loss of copovidone during the first 316 min, previously observed in the averaged Raman spectra (Fig. 2c), promotes heterogeneous nucleation followed by crystallisation of felodipine-rich amorphous material in the compact surface.

At the end of the experiment, after 1705 min, the residue of the compact was recovered and analysed using Raman and XRPD. MCR maps of

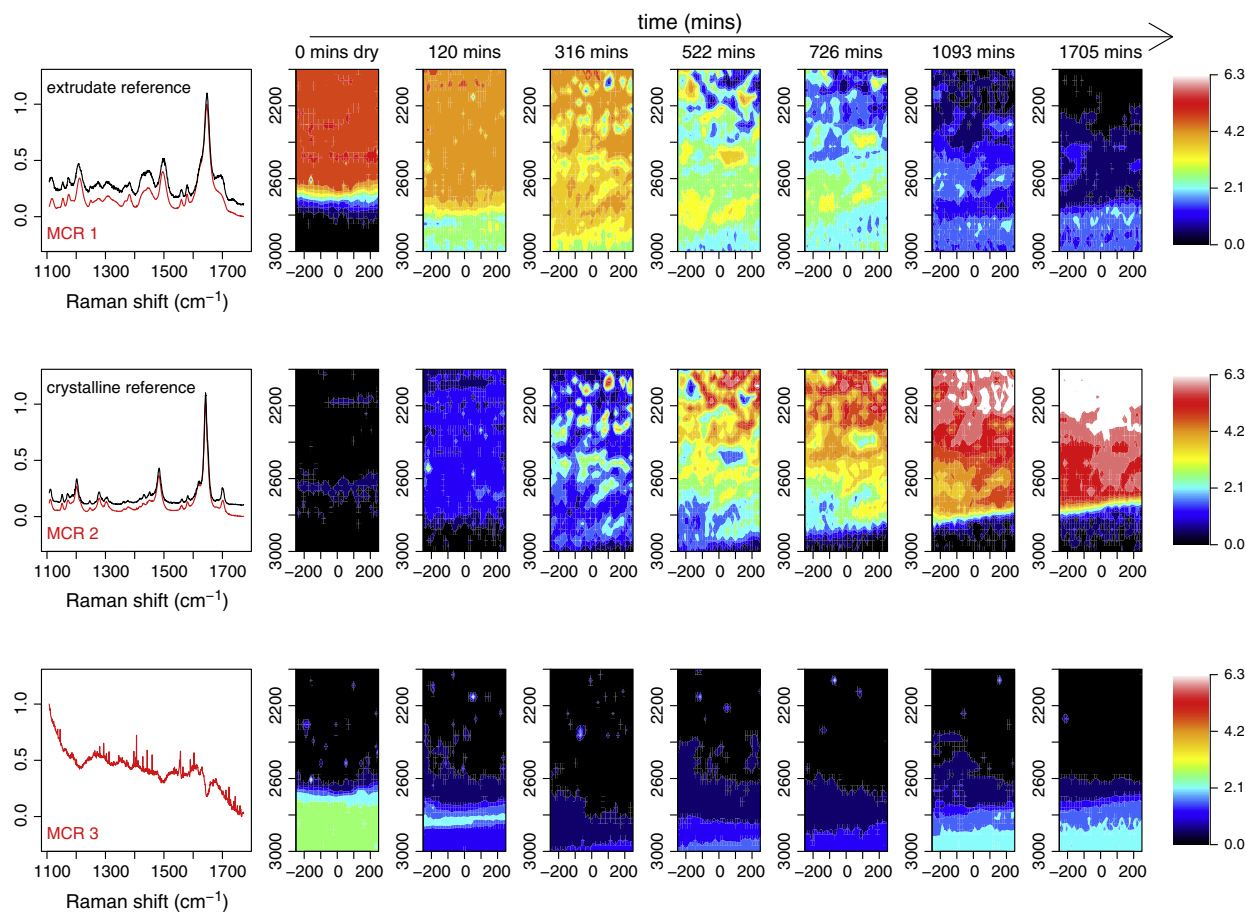


Fig. 4. Raman maps of the 50% extrudate compact as function of time, generated by MCR analysis.

the core (after breaking the compact into two parts) and surface are presented in Figure S7. Two components were required in this case to deconvolute the data, with the first component (MCR1) corresponding to amorphous felodipine and the second (MCR2) corresponding to crystalline felodipine. The score plots show that felodipine is predominantly amorphous in the core, whereas in the surface is completely crystalline.

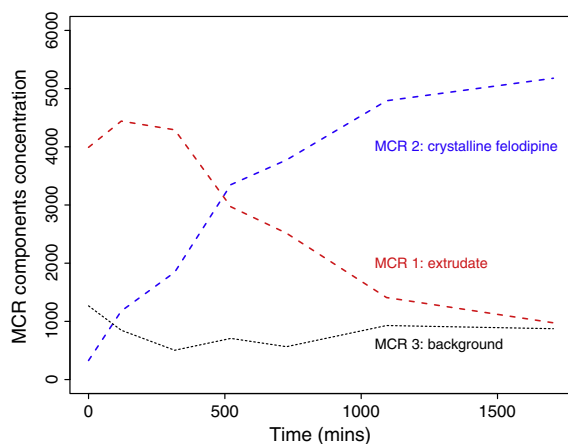


Fig. 5. Crystallisation kinetic generated by plotting the MCR component concentration in each map as function of time.

Raman data suggest that the crystallisation begins from the compact surface exposed to water and propagates towards the core, where only a little amount of crystalline drug was found. The XRPD pattern of the compact after grinding it into powder can be seen in the supplementary material (Figure S1). The pattern appears as a combination of sharp bands, typical of the crystalline materials, and a broad halo which characterises the amorphous materials. XRPD therefore indicates that felodipine sampled from the entire compact after the dissolution experiment is a mixture of crystalline and amorphous. This is in full agreement with Raman results, which indicated a crystalline outer section and an amorphous inner section of the compact.

#### 4. Conclusions

We have demonstrated that Raman imaging offers an appropriate method to investigate in real time the dissolution process and provides additional spatial information regarding the dissolution mechanisms that underpin amorphous solid dispersions, when compared to USP dissolution testing and classical Raman spectroscopy. We have successfully employed a RDDR method which allows us to track the dissolution profiles of both drug and polymer simultaneously and ultimately to measure the dissolution performance in multi-component systems. We have widely consolidated the previous findings described in Langham et al. work, [8] by generating spatially-resolved MCR Raman maps of the re-crystallisation of felodipine present in the 50% extrudate formulation. MCR Raman maps showed that amorphous felodipine crystallises at different rates in different regions of the compact surface,

indicating that crystallisation follows an initial stage of heterogeneous nucleation. The re-crystallisation of felodipine leads to large variations in the Raman spectrum and thus it is readily detectable. In particular in the phonon-mode region, the spectrum of the crystalline form is characterised by clear and sharp bands, while that of the amorphous form by a broad halo. The nucleation/crystallisation process proceeds from the surface towards the core and is likely linked to loss of copovidone from the extrudate. For the 5% drug-loaded extrudate, Raman spectroscopy did not show any significant changes in the spectra collected during the course of the dissolution test. This demonstrates that felodipine and copovidone dissolve as a single entity, in accordance with the RDDR data.

## 5. Acknowledgements

We thank AstraZeneca and EPSRC for funding through grant EP/I01375X/1 (via the joint Centre for Doctoral Training in Targeted Therapeutics and Formulation Sciences). We would like to thank Richard Hart, Caroline Roger and Zoe Langham (AstraZeneca) for their helpful suggestions on the work leading to these results. We thank Jamie Patient (University of Nottingham) for his contribution to the early stages of this work. The Nottingham Nanotechnology and Nanoscience Centre is gratefully acknowledged for the access to the Raman microscope.

## Appendix A. Supplementary data

Supplementary data to this article can be found online at <http://dx.doi.org/10.1016/j.jconrel.2014.05.061>.

## References

- [1] N.J. Babu, A. Nangia, Solubility advantage of amorphous drugs and pharmaceutical cocrystals, *Cryst. Growth Des.* 11 (7) (2011) 2662–2679.
- [2] C. Leuner, J. Dressman, Improving drug solubility for oral delivery using solid dispersions, *Eur. J. Pharm. Biopharm.* 50 (1) (2000) 47–60.
- [3] A.T.M. Serajuddin, Solid dispersion of poorly water-soluble drugs: early promises, subsequent problems, and recent breakthroughs, *J. Pharm. Sci.* 88 (10) (1999) 1058–1066.
- [4] A. Newman, G. Knipp, G. Zografi, Assessing the performance of amorphous solid dispersions, *J. Pharm. Sci.* 101 (4) (2012) 1355–1377.
- [5] B.C. Hancock, G. Zografi, Characteristics and significance of the amorphous state in pharmaceutical systems, *J. Pharm. Sci.* 86 (1) (1997) 1–12.
- [6] B.C. Hancock, M. Parks, What is the true solubility advantage for amorphous pharmaceuticals? *Pharm. Res.* 17 (4) (2000) 397–404.
- [7] D.Q.M. Craig, The mechanisms of drug release from solid dispersions in water-soluble polymers, *Int. J. Pharm.* 231 (2) (2002) 131–144.
- [8] Z.A. Langham, J. Booth, L.P. Hughes, G.K. Reynolds, S.A.C. Wren, Mechanistic insights into the dissolution of spray-dried amorphous solid dispersions, *J. Pharm. Sci.* 101 (8) (2012) 2798–2810.
- [9] D.E. Alonzo, G.G.Z. Zhang, D. Zhou, Y. Gao, L.S. Taylor, Understanding the behavior of amorphous pharmaceutical systems during dissolution, *Pharm. Res.* 27 (4) (2010) 608–618.
- [10] I. Tho, B. Liepold, J. Rosenberg, M. Maegerlein, M. Brandl, G. Fricker, Formation of nano/micro-dispersions with improved dissolution properties upon dispersion of ritonavir melt extrudate in aqueous media, *Eur. J. Pharm. Sci.* 40 (1) (2010) 25–32.
- [11] E. Karavas, G. Ktistis, A. Xenakis, E. Georarakis, Effect of hydrogen bonding interactions on the release mechanism of felodipine from nanodispersions with polyvinylpyrrolidone, *Eur. J. Pharm. Biopharm.* 63 (2) (2006) 103–114.
- [12] United States Pharmacopoeia 31 and National Formulary 26, The United States Pharmacopoeial Convention, Inc., Rockville, Md, 2008.
- [13] S.G. Kazarian, J. van der Weerd, Simultaneous FTIR spectroscopic imaging and visible photography to monitor tablet dissolution and drug release, *Pharm. Res.* 25 (4) (2008) 853–860.
- [14] P.S. Wray, G.S. Clarke, S.G. Kazarian, Dissolution of tablet-in-tablet formulations studied with ATR-FTIR spectroscopic imaging, *Eur. J. Pharm. Sci.* 48 (4–5) (2013) 748–757.
- [15] P. Avalle, S.R. Pygall, J. Pritchard, A. Jastrzemska, Interrogating erosion-based drug liberation phenomena from hydrophilic matrices using near infrared (NIR) spectroscopy, *Eur. J. Pharm. Sci.* 48 (1–2) (2013) 72–79.
- [16] W. Li, A. Woldu, L. Araba, D. Winstead, Determination of water penetration and drug concentration profiles in HPMC-based matrix tablets by near infrared chemical imaging, *J. Pharm. Sci.* 99 (7) (2010) 3081–3088.
- [17] Y.Y. Chen, L.P. Hughes, L.F. Gladden, M.D. Mantle, Quantitative ultra-fast MRI of HPMC swelling and dissolution, *J. Pharm. Sci.* 99 (8) (2010) 3462–3472.
- [18] S. Al-Dulaimi, A. Aina, J.C. Burley, Rapid polymorph screening on milligram quantities of pharmaceutical material using phonon-mode Raman spectroscopy, *CrystEngComm* 12 (4) (2010) 1038–1040.
- [19] A. Alkhalil, J. Babu Nanubolu, J.C. Burley, Analysis of phase transitions in molecular solids: quantitative assessment of phonon-mode vs intra-molecular spectral data, *RSC Adv.* 2 (1) (2012) 209–216.
- [20] S. Šašić, *Pharmaceutical Applications of Raman Spectroscopy*, Wiley-Interscience, Hoboken, New Jersey, 2007.
- [21] E. Karavas, E. Georarakis, M.P. Sigalas, K. Avgoustakis, D. Bikiaris, Investigation of the release mechanism of a sparingly water-soluble drug from solid dispersions in hydrophilic carriers based on physical state of drug, particle size distribution and drug-polymer interactions, *Eur. J. Pharm. Biopharm.* 66 (3) (2007) 334–347.
- [22] V. Bühler, *Kollidon® Polyvinylpyrrolidone excipients for the pharmaceutical industry*, 9th edition BASF, Ludwigshafen, Germany, 2008.
- [23] A.C.F. Rumondor, I. Ivanisevic, S. Bates, D.E. Alonzo, L.S. Taylor, Evaluation of drug-polymer miscibility in amorphous solid dispersion systems, *Pharm. Res.* 26 (11) (2009) 2523–2534.
- [24] P.J. Marsac, H. Konno, A.C.F. Rumondor, L.S. Taylor, Recrystallization of nifedipine and felodipine from amorphous molecular level solid dispersions containing poly(vinylpyrrolidone) and sorbed water, *Pharm. Res.* 25 (3) (2008) 647–656.
- [25] L.S. Taylor, G. Zografi, Spectroscopic characterization of interactions between PVP and indomethacin in amorphous molecular dispersions, *Pharm. Res.* 14 (12) (1997) 1691–1698.
- [26] A.L. Sarode, P. Wang, S. Obara, D.R. Worthen, Supersaturation, nucleation, and crystal growth during single- and biphasic dissolution of amorphous solid dispersions: polymer effects and implications for oral bioavailability enhancement of poorly water soluble drugs, *Eur. J. Pharm. Biopharm.* 86 (3) (2014) 351–360.
- [27] Y. Song, L. Wang, P. Yang, R.M. Wenslow, B. Tan, H. Zhang, Z. Deng, Physicochemical characterization of felodipine-kollidon VA64 amorphous solid dispersions prepared by hot-melt extrusion, *J. Pharm. Sci.* 102 (6) (2013) 1915–1923.
- [28] European Pharmacopoeia, Directorate for the Quality of Medicines and Healthcare of the Council of Europe, 6th edition, Council of Europe, Strasbourg, France, 2008.
- [29] R development core team, R: A Language and Environment for Statistical Computing, R Foundation for Statistical Computing, Vienna, Austria, 2011.
- [30] L.X. Yu, A.S. Carlin, G.L. Amidon, A.S. Hussain, Feasibility studies of utilizing disk intrinsic dissolution rate to classify drugs, *Int. J. Pharm.* 270 (1–2) (2004) 221–227.
- [31] P. Zakeri-Milani, M. Barzegar-Jalali, M. Azimi, H. Valizadeh, Biopharmaceutical classification of drugs using intrinsic dissolution rate (IDR) and rat intestinal permeability, *Eur. J. Pharm. Biopharm.* 73 (1) (2009) 102–106.
- [32] J.H. Fagerberg, O. Tsinman, N. Sun, K. Tsinman, A. Avdeef, C.A.S. Bergström, Dissolution rate and apparent solubility of poorly soluble drugs in biorelevant dissolution media, *Mol. Pharm.* 7 (5) (2010) 1419–1430.
- [33] E. Karavas, M. Georarakis, A. Docoslis, D. Bikiaris, Combining SEM, TEM, and micro-Raman techniques to differentiate between the amorphous molecular level dispersions and nanodispersions of a poorly water-soluble drug within a polymer matrix, *Int. J. Pharm.* 340 (1–2) (2007) 76–83.
- [34] F. Murtagh, A survey of recent advances in hierarchical clustering algorithms, *Comput. J.* 26 (4) (1983) 354–359.



## Monitoring the Dissolution Mechanisms of Amorphous Bicalutamide Solid Dispersions via Real-Time Raman Mapping

Francesco Tres,<sup>\*,†</sup> Jamie D. Patient,<sup>†</sup> Philip M. Williams,<sup>†</sup> Kevin Treacher,<sup>‡</sup> Jonathan Booth,<sup>‡</sup> Leslie P. Hughes,<sup>‡</sup> Stephen A. C. Wren,<sup>‡</sup> Jonathan W. Aylott,<sup>†</sup> and Jonathan C. Burley<sup>\*,†</sup>

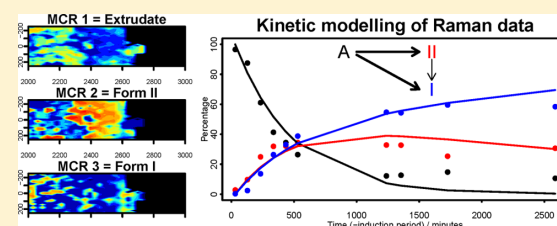
<sup>†</sup>School of Pharmacy, University of Nottingham, Boots Science Building, Nottingham NG7 2RD, United Kingdom

<sup>‡</sup>Pharmaceutical Development, AstraZeneca, Macclesfield SK10 2NA, United Kingdom

### Supporting Information

**ABSTRACT:** Real-time *in situ* Raman mapping has been employed to monitor, during dissolution, the crystallization transitions of amorphous bicalutamide formulated as a molecular dispersion in a copovidone VA64 matrix. The dissolution performance was also investigated using the rotating disc dissolution rate methodology, which allows simultaneous determination of the dissolution rate of both active ingredient and polymer. The dissolution behavior of two bicalutamide:copovidone VA64 dispersion formulations, containing 5% (w/w) and 50% (w/w) bicalutamide, respectively, was investigated, with the aim of exploring the effect of increasing the bicalutamide loading on the dissolution performance. Spatially time-resolved Raman maps generated using multivariate curve resolution indicated the simultaneous transformation of amorphous bicalutamide present in the 50% drug-loaded extrudate into metastable polymorphic form II and low-energy polymorphic form I. Fitting a kinetic model and spatially correlating the data extracted from the Raman maps also allowed us to understand the re-crystallization mechanisms by which the low-energy form I appears. Form I was shown to crystallize mainly directly from the amorphous solid dispersion, with crystallization from the metastable form II being a minor contribution.

**KEYWORDS:** bicalutamide, poorly soluble drugs, amorphous solid dispersions, dissolution, solid-state transformations, polymorphic changes, Raman mapping, multivariate curve resolution, kinetic modeling, spatial correlations



### 1. INTRODUCTION

An increasing number of drug candidates emerging from pharmaceutical development pipelines are characterized by poor dissolution and solubility profiles.<sup>1</sup> In light of this, there is a requirement for the pharmaceutical industry to develop innovative formulations to achieve the desired oral bioavailability and *in vivo* efficacy. A common strategy to improve the apparent solubility of poorly soluble drugs is to generate the amorphous form of the drug.<sup>2,3</sup> Amorphous solids consist of disordered arrangements of molecules and do not possess a distinguishable crystal lattice. As a result, the dissolution rate of the amorphous form is higher than in its crystalline counterpart.<sup>4</sup> However, the amorphous form is thermodynamically unstable and therefore tends to convert into the crystalline form over time, thereby compromising the drug bioavailability.<sup>5,6</sup> An increasingly popular strategy to stabilize the amorphous state is the use of solid dispersions and solid solutions in which the drug is molecularly mixed with a water-soluble or water-swellaable carrier, typically via hot melt extrusion or spray drying.<sup>7,8</sup>

Although the physical stability of amorphous solid dispersion formulations has been widely probed, particularly focusing on the use of different polymers to inhibit drug re-crystallization,<sup>9,10</sup> few studies have been conducted specifically to

understand their performance in a dynamic aqueous environment.<sup>11,12</sup> Drug release from amorphous solid dispersions has been classified as polymer-controlled or drug-controlled, depending on the chemical nature of the components and on the carrier-to-drug ratio.<sup>13</sup> Several processes have been demonstrated to be involved during the dissolution of amorphous solid dispersion formulations. The nucleation and crystallization of the drug either in the solid state or from a super-saturated state in solution, the generation of nano- and microparticles suspended in the dissolution medium, and the behavior of the carrier itself can significantly affect the overall dissolution performance.<sup>11,14–16</sup> Due to the number of processes involved, the dissolution mechanisms of amorphous solid dispersions are extremely difficult to deconvolute.

Classical methods of investigating drug release, such as the use of USP dissolution apparatuses, involve dissolving a tablet in water or other biorelevant media and measuring the drug content in solution as a function of time using UV spectroscopy or HPLC.<sup>17</sup> Data are not collected directly from the dosage

**Received:** December 12, 2014

**Revised:** March 31, 2015

**Accepted:** April 15, 2015

**Published:** April 15, 2015

form itself, and therefore solution-based methods do not offer any chemical or spatially resolved information on potential changes in the solid form during dissolution (e.g., recrystallization of the amorphous form, polymorphic transformations, or formation of hydrate states), which may be extremely important for developing reliable medicines with well-understood dissolution performance.

Given the limitations of classical solution-based methods, there have been a number of attempts to provide a full and clear picture of the drug release. Methods have included confocal fluorescence microscopy,<sup>18</sup> mid-infrared (mid-IR),<sup>19,20</sup> near-infrared (near-IR),<sup>21,22</sup> and magnetic resonance imaging (MRI).<sup>23,24</sup> The first three offer some chemical information, while MRI provides relatively low chemical specificity, but it is the only one of these methods that can provide three-dimensional information. Although near-IR and mid-IR are characterized by the highest chemical selectivity among the techniques mentioned ("multivariate data", one spectrum per pixel), their radiation is strongly absorbed by water molecules, which is not ideal for imaging in aqueous environments but can be worked around by integrating only bands for each component which appear distant from the absorption of water, as Kazarian et al. have shown.<sup>19,20,25</sup>

Raman mapping has been demonstrated to be a useful tool to investigate the distribution of multiple components in solid dosage forms during dissolution.<sup>26,27</sup> In a recent work, Strachan et al. employed coherent anti-Stokes Raman scattering (CARS) microscopy to image *in situ* the solid-state changes during dissolution in oral dosage forms containing theophylline anhydrate.<sup>28</sup> In CARS, compared to spontaneous Raman spectroscopy, two pulsed lasers are focused on the sample to generate a coherent anti-Stokes signal.<sup>28</sup> CARS requires very specialized equipment, while laboratory-based Raman requires only one laser and is therefore much more readily accessible. One of the key advantages of Raman spectroscopy is the access to the low-wavenumber region that has been demonstrated to be extremely sensitive to differences between amorphous and crystalline forms and among different polymorphic forms.<sup>12,29,30</sup> In addition, Raman spectroscopy can, in principle, achieve a spatial resolution at the sub-micrometer level, while the maximum spatial resolution possible with the IR and near-IR radiations is diffraction-limited to 0.5 and 1–2  $\mu\text{m}$ , respectively, although in practice it has been reported that the maximum spatial resolution for IR is 4  $\mu\text{m}$  and that for near-IR is 6  $\mu\text{m}$ .<sup>26</sup> In comparison to mid-IR and near-IR, Raman spectroscopy is relatively insensitive to water, offering therefore some potential advantages over the other state-of-the-art methods for investigating drug release from tablets in water.

Conventional Raman spectroscopic mapping was employed in the present work to deconvolute the dissolution mechanisms of bicalutamide:copovidone VA64 amorphous solid dispersions. Bicalutamide (Figure 1) is an important front-line treatment for prostate cancer. It is a non-steroidal anti-androgen that has an extremely low aqueous solubility (lower than 5 mg/L) and belongs to class II (low solubility, high intestinal permeability)

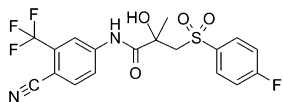


Figure 1. Molecular structure of bicalutamide.

of the biopharmaceutics classification system.<sup>31,32</sup> Bicalutamide exists in two known crystalline phases (polymorphs I and II): form I is currently marketed, whereas form II is metastable and therefore can convert into form I in appropriate conditions.<sup>33</sup> The polymorphic forms of bicalutamide have been thoroughly characterized by Vega et al.,<sup>34</sup> who reported single-crystal X-ray structures and showed that low-energy form I relates monotropically to metastable form II; i.e., under standard conditions form I is more stable than form II at all temperatures. Due to the different crystal structures, forms I and II have different physicochemical properties. The melting points have been found by Vega et al. to be 192 °C for form I and 189 °C for form II, and form II has been demonstrated to be 2.4 times more water-soluble than form I at room temperature.<sup>34</sup> Researchers have also characterized forms I and II using Raman spectroscopy. They observed several differences between the two polymorphic forms in the fingerprint region because the two polymorphs contain different conformations of bicalutamide. Copovidone VA64 is a highly water-soluble polymer (solubility higher than 100 mg/L) that has been widely used to prepare single-phase amorphous solid dispersions of poorly soluble drugs.<sup>11,12,35</sup>

The aim of the work presented below was to investigate the effects of increasing the amount of bicalutamide on the overall performance in water of the solid dispersion. For this reason, two bicalutamide:copovidone VA64 dispersions containing 5% (w/w) and 50% (w/w) bicalutamide were prepared. The rotating disc dissolution rate (RDDR) test, which is an extension of the standard intrinsic dissolution rate (IDR) test, was employed. The IDR test is an important biopharmaceutics screening tool to measure the dissolution rate normalized to the exposed surface area of a material.<sup>36</sup> Formally, IDR applies only to pure drug substances. By coupling an IDR apparatus to a HPLC system, the partial RDDR of both the drug substance and the excipients can be measured and compared for different formulations. The RDDR test has been recently demonstrated to be a useful tool for investigating the dissolution behavior of amorphous solid dispersions.<sup>12</sup> Real-time and *in situ* Raman mapping was also employed to monitor the solid-state transformations that occur during the dissolution of amorphous bicalutamide dispersions.

## 2. EXPERIMENTAL SECTION

**2.1. Materials and Methods.** Crystalline bicalutamide form I was provided by AstraZeneca (Macclesfield, United Kingdom). The polymorphic purity of form I was verified by Raman spectroscopy and XRPD. Copovidone (Kollidon VA64) was supplied by BASF (Ludwigshafen, Germany) and used as received, without any further purification.

**2.2. Preparation of Amorphous Form and Crystalline Bicalutamide Form II.** The amorphous form of bicalutamide was obtained by heating form I to 200 °C and quench-cooling the melt at room temperature. Raman spectroscopy and XRPD confirmed the formation of the amorphous form and the absence of crystalline material. Crystalline bicalutamide form II was produced according to patent, by heating the amorphous form to 175 °C.<sup>37</sup> Raman spectroscopy and XRPD confirmed the formation of polymorphic form II. Raman spectra and XRPD patterns from forms I and II and the amorphous form of bicalutamide are consistent with those previously reported by other workers.<sup>31–34</sup>

**2.3. Preparation of Bicalutamide:Copovidone Amorphous Solid Dispersions.** A co-rotating twin-screw extruder

(Thermo Scientific HAAKE MiniLab II) was used to prepare the amorphous solid dispersions of bicalutamide and copovidone (5% and 50% w/w bicalutamide). Bicalutamide as received (form I) and copovidone were pre-mixed for 20 min in a Turbula T2F mixer (Willy A. Bachofen AG Mashinefabrik). The physical mixture was extruded at a temperature of 170 °C and a screw speed of 150 rpm. The materials were then cooled to room temperature and manually milled with a T&G CrushGrind mill to fine powders. Raman spectroscopy and XRPD confirmed the formation of the amorphous form and the absence of crystalline material.

**2.4. X-ray Powder Diffraction (XRPD).** XRPD patterns were obtained using a PANalytical CubiX PRO diffractometer ( $\lambda = 1.5418 \text{ \AA}$ ). Samples were spun at 30 rpm and measured over the scan range from 2° to 40°  $2\theta$ , with a 25 s exposure per 0.02°  $2\theta$  increment. The X-rays were generated by a copper long-fine focus tube operated at a voltage of 45 kV and a current of 40 mA.

**2.5. Rotating Disc Dissolution Rate (RDDR) Measurements.** RDDR were determined using the “Woods apparatus” rotating disc system. The die cavity has a diameter of 8 mm with an exposed surface area of 0.5 cm<sup>2</sup>. Testing was carried out in a Sotax AT7 semi-automated dissolution bath. About 250 mg of each sample was compressed under a force of ca. 20 kN for 1 min using a Specac manual hydraulic press. Compressed discs were immersed in 500 mL of dissolution medium (pH 6.8 blank fasted state simulated intestinal fluid) at 37 °C ( $\pm 0.5$ ), and the rotational speed was set to 100 rpm. Samples were taken manually at regular time intervals over 120 min and then analyzed by reverse-phase high-performance liquid chromatography (RP-HPLC). All experiments were carried out in duplicate. All HPLC measurements were carried out on an HP Agilent 1100 instrument, equipped with an Agilent PLRP-S 300 Å/3  $\mu\text{m}$ /50 mm column (polystyrene/divinylbenzene stationary phase). The flow rate was 1 mL/min, the column temperature was 40 °C, and the UV detection wavelength was set to 210 nm. A linear gradient elution was used starting at 40% acetonitrile/60% deionized water and ending at 70% acetonitrile/30% deionized water after 2 min, with chromatograms collected for 3.5 min. A series of standard solutions were prepared in the relevant medium to generate a standard curve covering the concentration range of the dissolved sample. For each experiment, standards were analyzed alongside the RDDR samples. The partial RDDR of both drug and polymer was calculated using linear regression analysis. The partial RDDR of the material was obtained from the slope of the regression line. For the 5% extrudate RDDR was calculated using the first 20 min time period, where the trend is linear. For the 50% extrudate RDDR was obtained using the time interval between 40 and 120 min, where the trend of both bicalutamide and copovidone is linear, in accordance with Pharmacopoeia procedures.<sup>36,38</sup>

**2.6. Raman Spectroscopic Mapping.** The dissolution performance of compressed extrudate powders was investigated. Circular compacts with a diameter of 5 mm and a weight of 50 mg were prepared with a Specac manual hydraulic press using a force of ca. 20 kN. The dissolution test was carried out using a flow cell previously described by Tres et al.<sup>12</sup> Deionized water was used as dissolution medium with the flow rate set to 5 mL/min. Data were acquired as a function of time using a HORIBA Jobin Yvon LabRAM HR confocal microscope/spectrometer. The system is equipped with an automated xyz stage (Märzhäuser) to allow mapping. All

samples were illuminated with a near-IR (785 nm) laser. Spectra were collected using a 50× objective (Olympus BX51) and a 300  $\mu\text{m}$  confocal pinhole. All experiments used a 600 lines/mm rotatable diffraction grating along a path length of 800 mm to simultaneously scan a range of frequencies, and the spectra were detected using a SYNAPSE CCD detector (1024 pixels). The system was calibrated before collecting spectra with the Rayleigh line at 0 cm<sup>-1</sup>, as well as using a standard silicon band at 520.7 cm<sup>-1</sup>. For the raw materials, spectra were acquired in the wavenumber range from 30 to 4000 cm<sup>-1</sup>, with the lower limit corresponding to the cutoff of the Rayleigh rejection filter. During the dissolution tests, prior to each map being collected, the z-axis position of the sample (i.e., level of sample perpendicular to optical axis) was adjusted to maximize the Raman signal. The time frames, dimensions of the mapped areas, and acquisition times for the 5% and 50% experiments are depicted in Table 1.

**Table 1. Experimental Details for Raman Map Acquisition during the Dissolution Experiments of the 5% and 50% Extrudates**

	5% extrudate	50% extrudate
time frame, minutes	80	2946
total no. of maps	7	14
total no. of spectra per map	121	1156
acquisition time per spectrum, seconds	2	2
acquisition time per map, minutes	8	90
mapped area, $\mu\text{m}$	500 × 500	500 × 1000
grid spacing x-axis, $\mu\text{m}$	50	15
grid spacing y-axis, $\mu\text{m}$	50	30

For Raman data analysis two approaches were adopted. First, to rapidly evaluate any spectral changes occurring during the dissolution tests, all the spectra from each map were integrated to generate a single averaged spectrum corresponding to each time point. Second, to obtain spatial information for the 50% extrudate compact dissolution experiment, false color maps were generated using multivariate curve resolution (MCR). In order to monitor changes as a function of both time and x-y position, a single data matrix was generated which includes all the spectra collected across the entire dissolution experiment time scale (16 184 spectra). Statistical analyses were performed using R software, which is open-source and well-documented software for statistical computing and graphics.<sup>39</sup> For MCR, the separate alternating least-squares algorithm (ALS)-MCR library was employed, with raw data being scaled prior to analysis using variance-scaling and mean-centering standard methods. All the raw data along with the numerical routines written in the R language are included in the Supporting Information for reference. An interested reader should therefore be able to reproduce all the data analysis presented in this paper.

**2.7. Optical Imaging.** A CoolSNAP-Pro CF camera (Media Cybernetics) equipped with a Nikon AF Micro NIKKOR 60 mm lens was employed to collect the photographic images during the dissolution of the extrudate formulations. The same flow cell experimental conditions previously described for the dissolution tests using Raman mapping were employed. For the dissolution test of the 50% extrudate, the “imgThreshold” function part of “biOps” package in R was employed to count the number of pixels above a pre-defined color threshold of the images collected during the

dissolution experiment. This allowed us to focus only on the pixels of the compact and build a trend which shows how the surface area of the compact changes as a function of time. An example of a thresholded image can be seen in Figure S1 in the Supporting Information.

### 3. RESULTS AND DISCUSSION

#### 3.1. Optical Imaging and Rotating Disc Dissolution

**Rate.** Before commencing a full discussion of the results, a key point needs to be made. Extrinsic factors such as hydrodynamics (e.g., disc rotation speed and fluid flow) and test conditions (e.g., temperature and pH of the medium) certainly differ between the RDDR test and Raman/optical imaging experiments. The primary aim of the present work is simply to investigate whether or not the combination of these techniques can provide a full and clear understanding of the bicalutamide release from solid dispersions.

Figure 2 shows the optical images observed during the dissolution under flow of the 5% and 50% drug-loaded

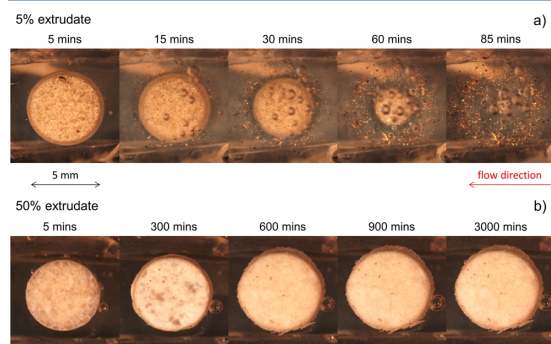


**Figure 2.** Optical images collected through the dissolution experiment for the 5% (a) and 50% (b) extrudate formulations.

extrudates. It is important to note the different time scales between the two experiments which is due to the difference in dissolution rates. The 5% extrudate formulation was completely dissolved after approximately 85 min, whereas the 50% drug-loaded extrudate remained intact after 3000 min. The optical imaging experiment does not provide any chemical information, but clearly shows that the two different drug loadings behave very differently in aqueous media. The 5% extrudate compact undergoes erosion and is completely dissolved by 85 min from the beginning of the experiment. The 50% extrudate compact swells during the first 600 min of the dissolution experiment and remains intact even after 3000 min. The initial swelling is confirmed by the kinetic trend generated by plotting the surface area of the compact vs time (Supporting Information, Figure S2). The swelling of a high drug-loaded extrudate has been

previously observed for amorphous solid dispersions of felodipine and copovidone.<sup>11,12</sup>

RDDR measurements were then carried out in order to determine the amount of drug and polymer released into solution as a function of time. The RDDR method, as described previously,<sup>12</sup> uses HPLC to separate the active ingredient from the polymer and track the dissolution trend of both entities. The dissolution profile of the polymeric carrier provides valuable information in the case of binary systems, as the carrier can significantly affect the dissolution performance of the poorly soluble active ingredient.<sup>2,3</sup> The dissolution rate of the polymer allows us to calculate an index of performance for the formulation, which illustrates how the drug and the polymer behave during the course of the dissolution experiment. The index of performance was defined by dividing the partial RDDR of bicalutamide by the total RDDR of the formulation (bicalutamide and copovidone) and then normalizing by the bicalutamide mass fraction. The equation to calculate the index of performance is reported in Table 2, along with the RDDR values for both 5% and 50% extrudates. Dissolution trends of the extrudates and pure crystalline form of bicalutamide are presented in the Supporting Information (Figures S3 and S4).

For the 5% extrudate, the partial RDDR value for bicalutamide is 0.24 mg/(min·cm<sup>2</sup>), and that for copovidone is 4.85 mg/(min·cm<sup>2</sup>). Compared to the IDR of pure crystalline bicalutamide (0.003 mg/(min·cm<sup>2</sup>), Figure S3), bicalutamide present in the 5% extrudate shows an 80-fold increase in dissolution rate. The index of performance results in a value close to unity, indicating that the two components have very similar dissolution trends and thus they dissolve simultaneously from the molecular dispersion. Given the low water solubility of bicalutamide, the overall behavior of the 5% bicalutamide-loaded solid dispersion is clearly dominated by water-soluble copovidone. Considering the 50% extrudate formulation, it is immediately apparent that the partial RDDR values of both bicalutamide and copovidone are much lower than those observed for the 5% extrudate. The partial RDDR of bicalutamide (0.008 mg/(min·cm<sup>2</sup>)) is comparable with the IDR of pure crystalline bicalutamide (0.003 mg/(min·cm<sup>2</sup>)). Optical images and RDDR data therefore suggest that the dissolution behavior of the 50% extrudate is dominated by the physicochemical properties of bicalutamide. The low water solubility and high hydrophobicity of the drug prevents the wetting and water uptake of the compact due to an insufficient ratio of copovidone to bicalutamide at the diffusion layer.<sup>32</sup> As a result, the dissolution of both bicalutamide and copovidone is very limited.

Summarizing, the overall dissolution performance of the 5% drug-loaded extrudate is clearly polymer-dependent, with bicalutamide dissolving simultaneously with the hydrophilic polymer. For the 50% extrudate, optical images and RDDR measurements indicate that the behavior in water of the amorphous solid dispersion is dependent on the physicochem-

**Table 2.** Partial RDDR Values along with the Index of Performance for 5% and 50% Extrudates

drug loading	RDDR, mg/(min·cm <sup>2</sup> )			index of performance <sup>a</sup>
	bicalutamide	copovidone	total	
5%	0.24(±0.005)	4.85(±0.127)	5.09(±0.127)	0.94(±0.030)
50%	0.008(±0.001)	0.025(±0.001)	0.033(±0.001)	0.48(±0.064)

<sup>a</sup>The index of performance was calculated by dividing the partial RDDR of bicalutamide by the total RDDR (bicalutamide plus copovidone) and then normalizing by the bicalutamide mass fraction: index of performance = (partial RDDR bicalutamide/total RDDR)/drug mass fraction.

ical properties of the hydrophobic bicalutamide. However, this does not clearly explain which processes occur during the course of the dissolution test, as data are not being collected directly from the dosage form, nor do the RDDR data provide any direct chemical explanation of the differences in dissolution rates between the 5% and 50% compacts. For this reason, real-time *in situ* Raman spectroscopic mapping along with off-line XRPD were used to investigate the samples.

**3.2. Raman Spectroscopy.** **3.2.1. Raman Spectra of "Dry" Raw Materials.** Raman spectra of the dry raw materials are available in Figure 3. The three solid forms of bicalutamide

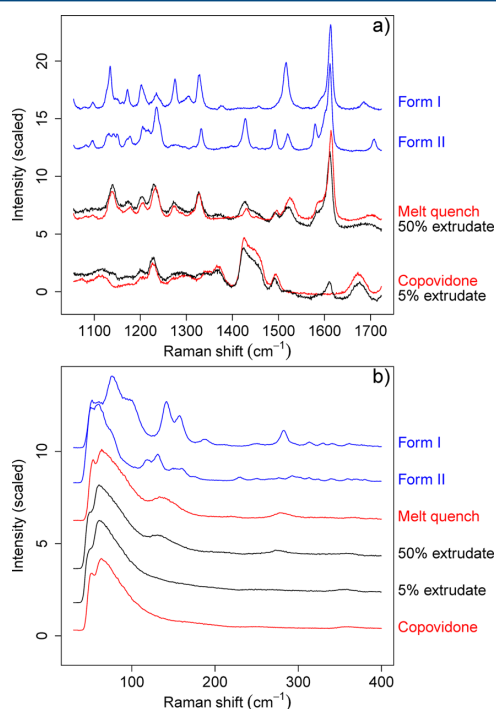


**Figure 3.** The 1055–1724  $\text{cm}^{-1}$  (a) and 40–400  $\text{cm}^{-1}$  (b) regions of the Raman spectra of "dry" raw materials. Data were variance-scaled and mean-centered before plotting. Y-offsets have been applied for presentation purpose and differ between the two panels.

present spectra with clear and obvious differences. Considering the region between 1055 and 1724  $\text{cm}^{-1}$  (Figure 3a), the differences between the crystalline forms are reasonable, given that they are known to be conformational polymorphs. The band deriving from the stretching mode of the carbonyl group moves to higher wavenumber in form II (1709  $\text{cm}^{-1}$ ) compared to form I (1686  $\text{cm}^{-1}$ ). Due to the different conformation of forms I and II, the oxygen of the carbonyl group is involved in different intramolecular hydrogen bond interactions, which lead to the observed peak shift. Atoms are also involved in intermolecular interactions. The hydrogen bonding between the N–H of the amide group and one of the oxygen atoms of the sulfonyl group determines the formation of a dimer in the molecules of form II. This interaction would explain why an intense single band at 1517  $\text{cm}^{-1}$  corresponding to the N–H bending and C–N stretching modes of the amide group is replaced by three peaks with inferior intensity appearing at 1428, 1493, and 1520  $\text{cm}^{-1}$  in form II. In

addition, the particular conformation of form II enables  $\pi$ – $\pi$  stacking interactions between the two rings. Due to this extra interaction form II presents a small peak at 1579  $\text{cm}^{-1}$  (ring stretching mode) which is not present in the spectrum of form I. The schematic of the structural conformations of forms I and II is shown in the Supporting Information (Figure S5).

The amorphous (melt quench) form presents a spectrum more similar to that of crystalline form II than form I (e.g., bands at 1428 and 1493  $\text{cm}^{-1}$  are present in the amorphous spectrum and the form II spectrum but not in the form I spectrum). This spectral similarity with form II suggests that the molecular conformation of the amorphous form is more similar to that of the metastable form II than that of highly stable form I. The amorphous form also exhibits greater peak widths than for the crystalline forms I and II, which is expected due to the molecular disorder inherent in the amorphous form but not present in the two crystalline forms. The spectra for the two extrudates are at first approximation simply a linear combination of the spectra for the amorphous drug and the polymer. A detailed inspection reveals some subtle differences, including a shift of the bands of the N–H bending mode at 1490 and 1516  $\text{cm}^{-1}$  for the 50% extrudate, and at 1490  $\text{cm}^{-1}$  for the 5% extrudate. These likely arise from the intermolecular hydrogen-bonding interactions between the amide of bicalutamide (N–H, proton donor) and the oxygen atoms of the carbonyl groups of copovidone (proton acceptor).<sup>32</sup>

In the low-wavenumber region between 40 and 400  $\text{cm}^{-1}$  (Figure 3b), the two crystalline forms of bicalutamide present clear, well-resolved bands, and the spectra are easily distinguishable from each other. This is wholly consistent with previous work by ourselves and other workers on low-wavenumber Raman spectroscopy applied to polymorphs.<sup>29,30</sup> The melt-quenched bicalutamide, the two extrudates, and the pure polymer exhibit the typical broad boson peak at low wavenumber expected for amorphous materials,<sup>29,30</sup> with the differences between these amorphous forms being subtle in this spectral region.

In summary, the various pure forms of bicalutamide and the extrudates can be distinguished using the reference Raman spectra, especially the region from 1055 to 1724  $\text{cm}^{-1}$ . The low-wavenumber data (40–400  $\text{cm}^{-1}$ ) allow the crystalline forms to be distinguished both from each other and from the various amorphous forms. Bicalutamide form II and the amorphous form present similar spectra in the region between 1055 and 1724  $\text{cm}^{-1}$ , and all amorphous forms (pure bicalutamide and the extrudates) exhibit similar spectra at low wavenumber.

**3.2.2. Raman Spectroscopic Mapping.** In order to gain good chemical and spatial detail on the dissolution processes in the compacts, Raman mapping was undertaken as a function of time in the region between 1055 and 1724  $\text{cm}^{-1}$ . The data for the 5% extrudate are presented in the Supporting Information (Figure S6). No changes were observed during the dissolution beyond a reduction in the overall Raman intensity, which may result from the presence of the medium, loss of focus, and the surface changing from flat and even to relatively rounded and uneven as the dissolution proceeds. These factors will reduce the amount of sample in the Raman confocal plane and lead to a reduction in signal.

For the 50% compact, analysis indicated that significant changes occurred in the Raman spectra as the dissolution progressed. A univariate analysis (e.g., one peak intensity) is difficult due to the similarity in the bicalutamide spectra already noted between forms II and the amorphous form, as well as due

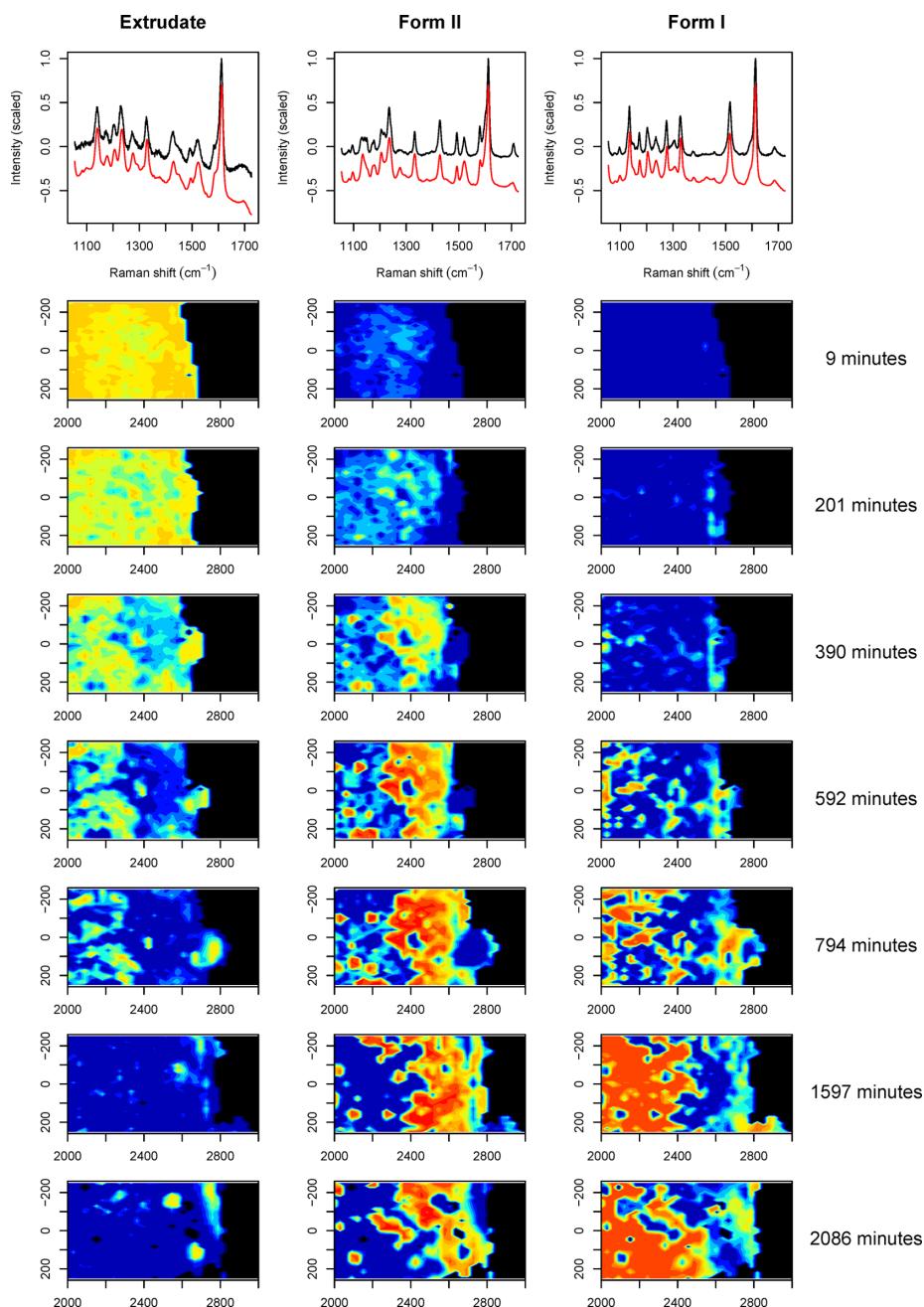


**Figure 4.** MCR Raman maps collected as a function of time through the dissolution experiment for the 50% extrudate formulation. Here presented are the loadings (with reference spectra in black) and the scores plots for the first three MCR components. White/red colors indicate areas where a particular phase is present to its maximum, while black/blue colors represent areas where it is present at its minimum. Areas with variable weighting of that phase are indicated by a continuum of white-red-orange-yellow-cyan-blue-black colors. Raw data were variance-scaled and mean-centered before MCR analysis was performed.

to the multicomponent nature of the formulation. To spatially and spectrally deconvolute the changes in the patterns for the 50% compact, we therefore employed MCR, which is a very well-established component analysis method and has been employed to resolve ToF-SIMS, IR, near-IR, and Raman data

from pharmaceutical samples.<sup>40–43</sup> MCR requires input of a body of spectral data in a matrix format, each spectrum being tagged with a set of labels (e.g.,  $x, y$  position), which is resolved by the MCR method into a number of components. The only user input is the requested number of components; i.e., MCR is

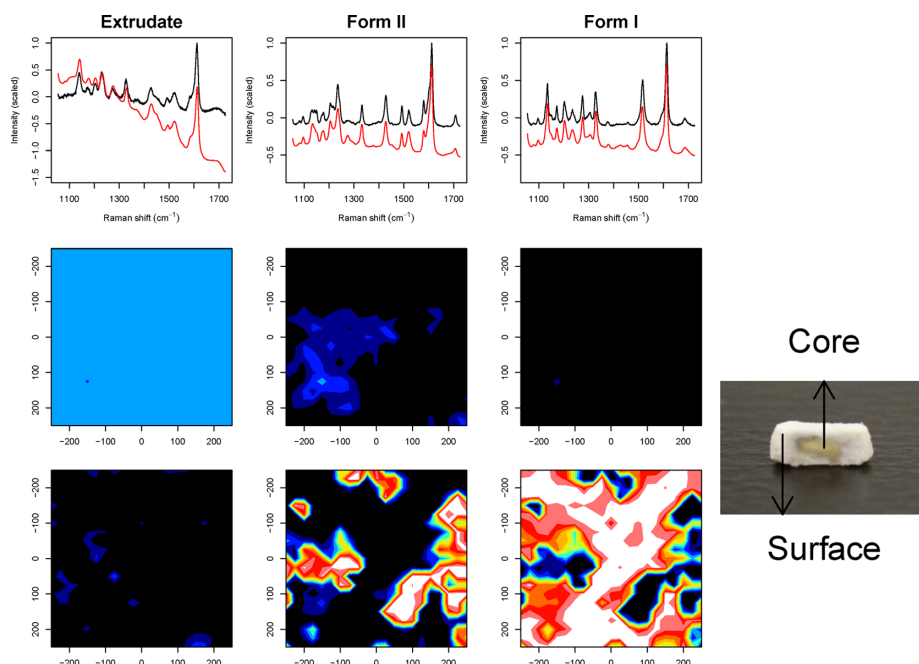


**Figure 5.** MCR Raman maps of the inner and outer sections of the compact. Here presented are the loadings (with reference spectra in black) and the scores plots of the first three MCR components, with data being variance-scaled and mean-centered prior to plotting.

a model-free method. Outputs from MCR include loadings (which in the present case correspond to Raman spectra of the resolved components) and scores (which provide the spectral weighting of a given component for the relevant unique set of labels). Labels typically comprise  $x$  and  $y$  positions, but there is no reason why they cannot include more information. To include time in our analysis, we simply concatenated all  $xy$  spectral maps together and included a time label for each input spectrum, in addition to the usual  $x$  and  $y$  labels. Our MCR results are reproducible for multiple runs, despite a different randomly generated set of numbers being employed as a starting model for each run. This provides confidence that our results are robust, which is important in the context of the well-known rotational ambiguities present in the MCR methodology.<sup>44,45</sup> In our analysis, trial runs indicated that a suitable choice for number of components was three, and intensity thresholding was employed so that only the spectra from the compact were included in the analysis; i.e., the surrounding solution was excluded.

The results of our MCR analysis are presented graphically in Figure 4. Note that half the maps are shown for reasons of space, i.e., every second one starting at 9 min; however, the analysis included all maps, and the remaining time-point maps can be found in Supporting Information (Figure S7). Comparison of MCR loadings with reference spectra clearly indicates that the data have been resolved into components which correspond remarkably well with crystalline bicalutamide forms I and II, and the bicalutamide:copovidone extrudate. The variation in the scores as a function of space (within each map) and time (between maps, vertically descending) indicates that the starting material—the extrudate—decreases in weighting as time passes. In the early stages of the experiment, crystalline form II appears and grows in weighting, while after

approximately the 592 min time point the weighting of form I increases. Form I continues to increase in weighting at the expense of both the extrudate and form II, with the latter reducing in weighting after 889 min. The crystallization of amorphous bicalutamide into form II has been reported previously,<sup>33,34</sup> and the hypothetical sequence amorphous  $\rightarrow$  metastable form II  $\rightarrow$  stable form I is in accord with the long-standing Ostwald's rule of stages. We note, however, that the results presented so far do not allow us to distinguish between the linear pathway amorphous  $\rightarrow$  form II  $\rightarrow$  form I and an alternative parallel pathway whereby amorphous  $\rightarrow$  form II and amorphous  $\rightarrow$  form I occur independently, with the crystallization to form I having a longer induction period than the crystallization to form II.

At the end of the experiment, the remaining compact was removed from the flow cell, cut through the center, and analyzed by Raman spectroscopy and visually. Data are presented in Figure 5. The recrystallization of the drug to a mixture of forms I (dominant at the end of the experiment) and form II occurs from the outside of the compact, with the interior being unchanged bicalutamide:copovidone extrudate. XRPD data from a powdered compact (Supporting Information, Figure S8) are in full accord with these *ex situ* Raman data.

The Raman mapping results, for the 50% extrudate, considered alongside the RDDR analysis, clearly indicate the hydrophilic polymer preferentially dissolves from the exterior of the compact. This leaves a drug-rich (therefore hydrophobic) shell on the outside of the compact, which is initially amorphous. The decrease in polymer concentration and increase in (amorphous) drug naturally leads to a crystallization of the drug. To address directly the question of the crystallization mechanism, we undertook a kinetic analysis of the crystallization processes, which we now outline.

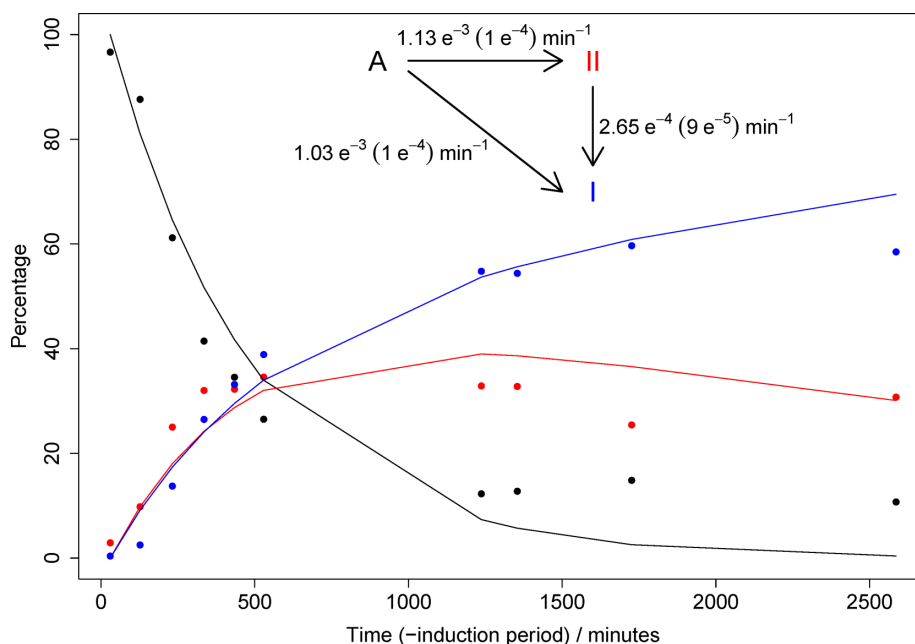


**Figure 6.** Experimental (dotted plots) and fitted (line plots) data of the three-step kinetic model. The induction period represents the first 360 min of the experiment. Estimated uncertainties are shown in parentheses.

While the MCR results are very useful for gaining a qualitative understanding of the spectral changes occurring, they are less useful for a quantitative analysis as the proportion of the spectral weighting cannot be related to the actual concentration without suitable standards. We therefore undertook a simple three-level classification procedure and assigned each spectrum at every  $xy$  time point to extrudate, form I, or form II, based upon the calculated correlations between the three reference spectra and the relevant experimental spectrum with its unique  $xy$  time labels. To remove the effect of the compact expanding/moving, the results are reported as percentages. Only the area corresponding to the compact was included in this analysis.

Results for the kinetic analysis are presented in Figure 6 both for the classification (i.e., experimental data) and for the kinetic model. The kinetic model included first-order rate constants for the processes  $A \rightarrow II$ ,  $A \rightarrow I$ , and  $II \rightarrow I$ , which were adjusted according to the least-squares method until an optimized model was arrived at. To summarize, the rates of conversion  $A \rightarrow II$  and  $A \rightarrow I$  are similar, both being around  $10^{-3} \text{ min}^{-1}$ . The rate of conversion  $II \rightarrow I$  is found to be approximately an order of magnitude lower, and therefore the analysis distinctly points toward a mixed crystallization mechanism. The appearance of form I directly from the amorphous form is favored compared to the conversion  $II \rightarrow I$ . The robustness of the analysis was cross-checked by constraining the rate constant for  $A \rightarrow I$  to be  $0 \text{ min}^{-1}$ , and the resulting model (Figure S9) is clearly far inferior to the unconstrained model in which the rate constant for  $A \rightarrow I$  is found to be of order  $10^{-3} \text{ min}^{-1}$ . We can therefore conclude that the parallel crystallization mechanism is dominant compared to the serial one in terms of kinetics.

Spatial correlations were then employed to fully understand the re-crystallization mechanism by which form I appears. Theory suggests that the serial route ( $A \rightarrow II \rightarrow I$ ) should

involve a strong spatial correlation between form II and form I, and a strong anti-correlation between amorphous and form I.<sup>46</sup> The parallel route ( $A \rightarrow II$  and  $A \rightarrow I$ ) is expected to be random nucleation and growth of both forms II and I from amorphous. Each nearest “tablet” neighbor pixel to each “tablet” pixel has been classified (A/II/I) and counted as a function of time, so that transformations in polymorph can be monitored. To model the parallel route (random nucleation of forms I and II) a similar analysis was performed, differing only in that the neighboring pixels were replaced one-for-one by pixels selected randomly from across the compact (excluding the specific pixel of interest) at the relevant time point. The number of pixels with neighbors of which sort they are (A/II/I) at each time point is presented in Figure 7. The experimentally determined number of neighbors of each type is in good agreement with the modeled “random nucleation”, i.e., in accord with a predominantly parallel crystallization mechanism ( $A \rightarrow II$  and  $A \rightarrow I$  rather than  $A \rightarrow II \rightarrow I$ ).

To summarize, both kinetic modeling of the classification data and detailed spatial analysis point toward the predominance of a non-Ostwald “parallel” crystallization mechanism, in which crystalline form I bicalutamide nucleates directly from the amorphous extrudate rather than from form II. Given that the amount of form II decreases after 889 min the pathway  $II \rightarrow I$  clearly has some importance, but the main route for formation of form I appears to be direct random nucleation from the amorphous extrudate.

#### 4. CONCLUSIONS

We have employed optical observation, rotating disc dissolution rate, and real-time Raman mapping to investigate the dissolution of bicalutamide:copovidone compacts for 5% and 50% drug loadings. The 5% sample dissolution mechanism involves the hydrophilic polymer and the hydrophobic drug

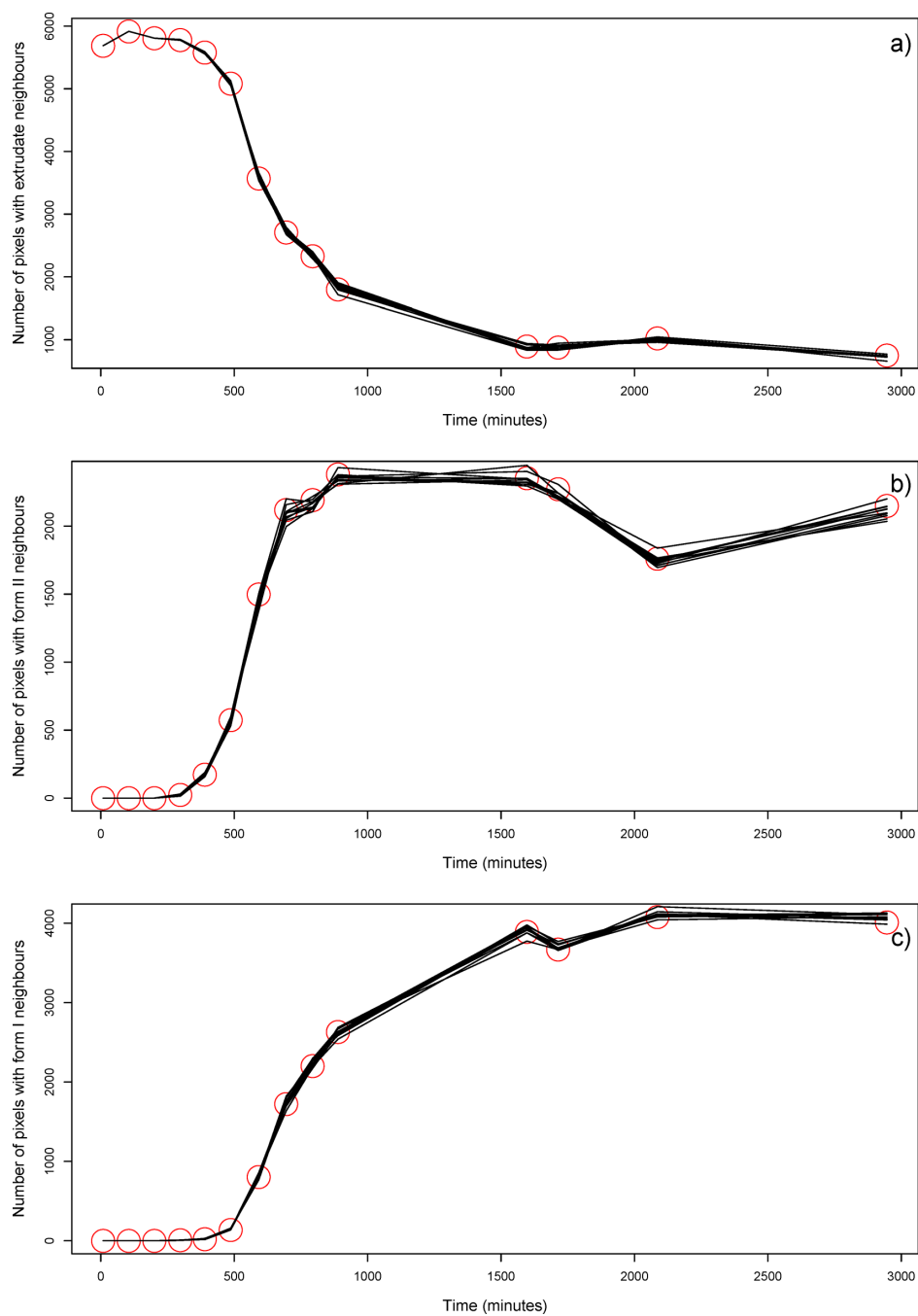


**Figure 7.** Spatial correlations between the “tablet” pixels and (a) amorphous, (b) form II, and (c) form I neighbors. The red circles indicate the experimental data, the black lines a set of 10 analyses in which neighbor spectra are replaced one-for-one by randomly selected pixels from that time map.

dissolving at the same rate, and the compact is completely dissolved after 85 min. In contrast, the 50% sample remains intact even after 3000 min. This is shown to be due to preferential dissolution of the hydrophilic polymer, which, we hypothesize, leads to a shell of amorphous hydrophobic drug

around the exterior of the compact. Our data indicate that this shell transforms first to metastable crystalline form II and then stable form I. Form I crystallizes preferentially from the amorphous form in a random nucleation mechanism, rather than from the crystalline form II. The interior of the compact is

protected from water ingress by the shell of hydrophobic drug and remains a copovidone:bicalutamide molecular dispersion, even after ca. 50 h immersion in flowing water. The dissolution behavior observed here and the hypothesized water-resistant “hydrophobic shell” of drug are likely to have significant implications for drug delivery and bioavailability optimization, and are likely to apply to a wide range of molecular dispersion formulations.

## ■ ASSOCIATED CONTENT

### 📄 Supporting Information

Example of a thresholded image, kinetic trend showing how the surface area of the 50% extrudate changes during dissolution, RDDR and IDR trends, schematic of the structural conformations of forms I and II, averaged spectra of the dissolution of the 5% extrudate, remaining time-point maps of the 50% extrudate, XRPD data, kinetic model obtained by constraining the rate constant for  $A \rightarrow I$  to be  $0 \text{ min}^{-1}$ , and raw data and numerical routines. This material is available free of charge via the Internet at <http://pubs.acs.org>.

## ■ AUTHOR INFORMATION

### Corresponding Authors

\*Phone: +44 (0) 1158468357. Fax: +44 (0) 1159515102. E-mail: francesco.tres@nottingham.ac.uk.

\*E-mail: jonathan.burley@nottingham.ac.uk.

### Notes

The authors declare no competing financial interest.

## ■ ACKNOWLEDGMENTS

Support from AstraZeneca and EPSRC through grant EP/I01375X/1 (via the joint Centre for Doctoral Training in Targeted Therapeutics and Formulation Sciences) is kindly acknowledged. We also thank the Nottingham Nanotechnology and Nanoscience Centre for the access to the Raman system.

## ■ REFERENCES

- (1) Babu, N. J.; Nangia, A. Solubility Advantage of Amorphous Drugs and Pharmaceutical Cocrystals. *Cryst. Growth Des.* **2011**, *11*, 2662–2679.
- (2) Hancock, B. C.; Parks, M. What is the True Solubility Advantage for Amorphous Pharmaceuticals? *Pharm. Res.* **2000**, *17*, 397–404.
- (3) Hancock, B. C.; Zografi, G. Characteristics and significance of the amorphous state in pharmaceutical systems. *J. Pharm. Sci.* **1997**, *86*, 1–12.
- (4) Murdande, S. B.; Pikal, M. J.; Shanker, R. M.; Bogner, R. H. Solubility advantage of amorphous pharmaceuticals: I. A thermodynamic analysis. *J. Pharm. Sci.* **2010**, *99*, 1254–1264.
- (5) Greenhalgh, D. J.; Williams, A. C.; Timmins, P.; York, P. Solubility parameters as predictors of miscibility in solid dispersions. *J. Pharm. Sci.* **1999**, *88*, 1182–1190.
- (6) Marsac, P. J.; Shamblin, S. L.; Taylor, L. S. Theoretical and Practical Approaches for Prediction of Drug–Polymer Miscibility and Solubility. *Pharm. Res.* **2006**, *23*, 2417–2426.
- (7) Leuner, C.; Dressman, J. Improving drug solubility for oral delivery using solid dispersions. *Eur. J. Pharm. Biopharm.* **2000**, *50*, 47–60.
- (8) Serajuddin, A. T. M. Solid dispersion of poorly water-soluble drugs: Early promises, subsequent problems, and recent breakthroughs. *J. Pharm. Sci.* **1999**, *88*, 1058–1066.
- (9) Yang, J.; Grey, K.; Doney, J. An improved kinetics approach to describe the physical stability of amorphous solid dispersions. *Int. J. Pharm.* **2010**, *384*, 24–31.
- (10) Ivanisevic, I. Physical stability studies of miscible amorphous solid dispersions. *J. Pharm. Sci.* **2010**, *99*, 4005–4012.
- (11) Langham, Z. A.; Booth, J.; Hughes, L. P.; Reynolds, G. K.; Wren, S. A. C. Mechanistic insights into the dissolution of spray-dried amorphous solid dispersions. *J. Pharm. Sci.* **2012**, *101*, 2798–2810.
- (12) Tres, F.; Treacher, K.; Booth, J.; Hughes, L. P.; Wren, S. A. C.; Aylott, J. W.; Burley, J. C. Real time Raman imaging to understand dissolution performance of amorphous solid dispersions. *J. Controlled Release* **2014**, *188*, 53–60.
- (13) Craig, D. Q. M. The mechanisms of drug release from solid dispersions in water-soluble polymers. *Int. J. Pharm.* **2002**, *231*, 131–144.
- (14) Alonzo, D. E.; Zhang, G. G. Z.; Zhou, D.; Gao, Y.; Taylor, L. S. Understanding the Behavior of Amorphous Pharmaceutical Systems during Dissolution. *Pharm. Res.* **2010**, *27*, 608–618.
- (15) Tho, L.; Liepold, B.; Rosenberg, J.; Maegerlein, M.; Brandl, M.; Fricker, G. Formation of nano/micro-dispersions with improved dissolution properties upon dispersion of ritonavir melt extrudate in aqueous media. *Eur. J. Pharm. Sci.* **2010**, *40*, 25–32.
- (16) Karavas, E.; Ktistis, G.; Xenakis, A.; Georgarakis, E. Effect of hydrogen bonding interactions on the release mechanism of felodipine from nanodispersions with polyvinylpyrrolidone. *Eur. J. Pharm. Biopharm.* **2006**, *63*, 103–114.
- (17) Gray, V.; Kelly, G.; Xia, M.; Butler, C.; Thomas, S.; Mayock, S. The Science of USP 1 and 2 Dissolution: Present Challenges and Future Relevance. *Pharm. Res.* **2009**, *26*, 1289–1302.
- (18) Pygall, S. R.; Whetstone, J.; Timmins, P.; Melia, C. D. Pharmaceutical applications of confocal laser scanning microscopy: The physical characterisation of pharmaceutical systems. *Adv. Drug Delivery Rev.* **2007**, *59*, 1434–1452.
- (19) van der Weerd, J.; Kazarian, S. G. Release of poorly soluble drugs from HPMC tablets studied by FTIR imaging and flow-through dissolution tests. *J. Pharm. Sci.* **2005**, *94*, 2096–2109.
- (20) Wray, P. S.; Clarke, G. S.; Kazarian, S. G. Dissolution of tablet-in-tablet formulations studied with ATR-FTIR spectroscopic imaging. *Eur. J. Pharm. Sci.* **2013**, *48*, 748–757.
- (21) Avalle, P.; Pygall, S. R.; Gower, N.; Midwinter, A. The use of in situ near infrared spectroscopy to provide mechanistic insights into gel layer development in HPMC hydrophilic matrices. *Eur. J. Pharm. Sci.* **2011**, *43*, 400–408.
- (22) Avalle, P.; Pygall, S. R.; Pritchard, J.; Jastrzemska, A. Interrogating erosion-based drug liberation phenomena from hydrophilic matrices using near infrared (NIR) spectroscopy. *Eur. J. Pharm. Sci.* **2013**, *48*, 72–79.
- (23) Chen, Y. Y.; Hughes, L. P.; Gladden, L. F.; Mantle, M. D. Quantitative ultra-fast MRI of HPMC swelling and dissolution. *J. Pharm. Sci.* **2010**, *99*, 3462–3472.
- (24) Richardson, J. C.; Bowtell, R. W.; Mäder, K.; Melia, C. D. Pharmaceutical applications of magnetic resonance imaging (MRI). *Adv. Drug Delivery Rev.* **2005**, *57*, 1191–1209.
- (25) Chan, K. L. A.; Kazarian, S. G. FTIR Spectroscopic Imaging of Dissolution of a Solid Dispersion of Nifedipine in Poly(ethylene glycol). *Mol. Pharmaceutics* **2004**, *1*, 331–335.
- (26) Windbergs, M.; Haaser, M.; McGoverin, C. M.; Gordon, K. C.; Kleinebudde, P.; Strachan, C. J. Investigating the relationship between drug distribution in solid lipid matrices and dissolution behaviour using Raman spectroscopy and mapping. *J. Pharm. Sci.* **2010**, *99*, 1464–1475.
- (27) Haaser, M.; Windbergs, M.; McGoverin, C. M.; Kleinebudde, P.; Rades, T.; Gordon, K. C.; Strachan, C. J. Analysis of matrix dosage forms during dissolution testing using raman microscopy. *J. Pharm. Sci.* **2011**, *100*, 4452–4459.
- (28) Fussell, A.; Garbacik, E.; Offerhaus, H.; Kleinebudde, P.; Strachan, C. In situ dissolution analysis using coherent anti-Stokes Raman scattering (CARS) and hyperspectral CARS microscopy. *Eur. J. Pharm. Biopharm.* **2013**, *85*, 1141–1147.
- (29) Brillante, A.; Bilotti, I.; della Valle, R. G.; Venuti, E.; Girlando, A. Probing polymorphs of organic semiconductors by lattice phonon Raman microscopy. *CrystEngComm* **2008**, *10*, 937–946.
- (30) Al-Dulaimi, S.; Aina, A.; Burley, J. C. Rapid polymorph screening on milligram quantities of pharmaceutical material using

phonon-mode Raman spectroscopy. *CrystEngComm* **2010**, *12*, 1038–1040.

(31) Abu-Diak, O. A.; Jones, D. S.; Andrews, G. P. Understanding the performance of melt-extruded poly(ethylene oxide)–bicalutamide solid dispersions: Characterisation of microstructural properties using thermal, spectroscopic and drug release methods. *J. Pharm. Sci.* **2012**, *101*, 200–213.

(32) Andrews, G. P.; AbuDiak, O. A.; Jones, D. S. Physicochemical characterization of hot melt extruded bicalutamide–polyvinylpyrrolidone solid dispersions. *J. Pharm. Sci.* **2010**, *99*, 1322–1335.

(33) Németh, Z.; Sztatisz, J.; Demeter, A. Polymorph transitions of bicalutamide: A remarkable example of mechanical activation. *J. Pharm. Sci.* **2008**, *97*, 3222–3232.

(34) Vega, D. R.; Polla, G.; Martinez, A.; Mendioroz, E.; Reinoso, M. Conformational polymorphism in bicalutamide. *Int. J. Pharm.* **2007**, *328*, 112–118.

(35) Breitenbach, J. Melt extrusion can bring new benefits to HIV therapy. *Am. J. Drug Delivery* **2006**, *4*, 61–64.

(36) *United States Pharmacopoeia 31 and National Formulary 26*; The United States Pharmacopoeial Convention, Inc.: Rockville, Md, 2008.

(37) Westheim, R. Bicalutamide forms. U.S. Patent 20040063782, 2004.

(38) *European Pharmacopoeia*, 6th ed.; Directorate for the Quality of Medicines and Healthcare of the Council of Europe: Strasbourg, France, 2008.

(39) R Development Core Team. *R: A language and environment for statistical computing*; R Foundation for Statistical Computing: Vienna, Austria, 2011.

(40) Gendrin, C.; Roggo, Y.; Collet, C. Pharmaceutical applications of vibrational chemical imaging and chemometrics: A review. *J. Pharm. Biomed. Anal.* **2008**, *48*, 533–553.

(41) Gallagher, N. B.; Shaver, J. M.; Martin, E. B.; Morris, J.; Wise, B. M.; Windig, W. Curve resolution for multivariate images with applications to TOF-SIMS and Raman. *Chemometr. Intell. Lab. Syst.* **2004**, *73*, 105–117.

(42) Duponchel, L.; Elmi-Rayaleh, W.; Ruckebusch, C.; Huvenne, J. P. Multivariate Curve Resolution Methods in Imaging Spectroscopy: Influence of Extraction Methods and Instrumental Perturbations. *J. Chem. Inf. Comput. Sci.* **2003**, *43*, 2057–2067.

(43) Awa, K.; Okumura, T.; Shinzawa, H.; Otsuka, M.; Ozaki, Y. Self-modeling curve resolution (SMCR) analysis of near-infrared (NIR) imaging data of pharmaceutical tablets. *Anal. Chim. Acta* **2008**, *619*, 81–86.

(44) Rutan, S.; de Juan, A.; Tauler, R. Introduction to Multivariate Curve Resolution. *Comprehensive Chemometrics*; Elsevier: Oxford, 2009; Vol. 2, Chapter 2.15, pp 249–259.

(45) de Juan, A.; Rutan, S.; Tauler, R. Two-Way Data Analysis: Multivariate Curve Resolution—Iterative Resolution Methods. *Comprehensive Chemometrics*; Elsevier: Oxford, 2009; Vol. 2, Chapter 2.19, pp 325–344.

(46) Snyder, V.; Alkemper, J.; Voorhees, P. The development of spatial correlations during Ostwald ripening: a test of theory. *Acta Mater.* **2000**, *48*, 2689–2701.

Article

## Investigating the Dissolution Performance of Amorphous Solid Dispersions Using Magnetic Resonance Imaging and Proton NMR

Francesco Tres <sup>1,\*</sup>, Steven R. Coombes <sup>2</sup>, Andrew R. Phillips <sup>2</sup>, Leslie P. Hughes <sup>2</sup>,  
Stephen A. C. Wren <sup>2</sup>, Jonathan W. Aylott <sup>1</sup> and Jonathan C. Burley <sup>1,\*</sup>

<sup>1</sup> School of Pharmacy, Boots Science Building, University of Nottingham, Nottingham NG7 2RD, UK;

E-Mail: Jon.Aylott@nottingham.ac.uk

<sup>2</sup> Pharmaceutical Development, AstraZeneca, Macclesfield SK10 2NA, UK;

E-Mails: Steven.Coombes@astrazeneca.com (S.R.C.); andrew.r.phillips@astrazeneca.com (A.R.P.);

Les.Hughes2@astrazeneca.com (L.P.H.); Stephen.Wren@astrazeneca.com (S.A.C.W.)

\* Authors to whom correspondence should be addressed;

E-Mails: francesco.tres@nottingham.ac.uk (F.T.); jonathan.burley@nottingham.ac.uk (J.C.B.);

Tel.: +44-7429-424-935 (F.T.); +44-115-846-8357 (J.C.B.); Fax: +44-115-951-5102 (J.C.B.).

Academic Editors: Thomas Rades, Holger Grohganz and Korbinian LÄübmann

Received: 9 July 2015 / Accepted: 2 September 2015 / Published: 10 September 2015

---

**Abstract:** We have investigated the dissolution performance of amorphous solid dispersions of poorly water-soluble bicalutamide in a Kollidon VA64 polymeric matrix as a function of the drug loading (5% vs. 30% bicalutamide). A combined suite of state-of-the-art analytical techniques were employed to obtain a clear picture of the drug release, including an integrated magnetic resonance imaging UV-Vis flow cell system and <sup>1</sup>H-NMR. Off-line <sup>1</sup>H-NMR was used for the first time to simultaneously measure the dissolution profiles and rates of both the drug and the polymer from a solid dispersion. MRI and <sup>1</sup>H-NMR data showed that the 5% drug loading compact erodes linearly, and that bicalutamide and Kollidon VA64 are released at approximately the same rate from the molecular dispersion. For the 30% extrudate, data indicated a slower water ingress into the compact which corresponds to a slower dissolution rate of both bicalutamide and Kollidon VA64.

**Keywords:** bicalutamide; poorly soluble drugs; amorphous solid dispersions; hot melt extrusion; solid-state transformations; magnetic resonance imaging; suppressed water  $^1\text{H-NMR}$

---

## 1. Introduction

Due to an increasing number of poorly water-soluble molecules emerging from pharmaceutical pipelines, there is a continual drive to develop formulations for the delivery of such compounds [1,2]. Conventional formulations using the crystalline form of the drug often do not achieve the desired oral bioavailability and pharmacological effects. An alternative strategy is to exploit the higher apparent solubility and dissolution rate of the amorphous form. However, this may convert into the crystalline form over time as it is thermodynamically unstable [3,4]. A popular strategy to stabilise the amorphous form is to use amorphous solid dispersions in which the drug is molecularly dispersed in a water-soluble or water-swallowable polymer. These are typically prepared by fusion (e.g., hot melt extrusion) or solvent evaporation (e.g., spray drying) methods [5,6].

In recent years, a number of studies have been conducted to understand the performance of amorphous solid dispersions during manufacturing, storage and *in vitro* dissolution [7–10]. The understanding of the formulation performance during dissolution is of particular interest as it underpins the *in vivo* efficacy. The dissolution mechanisms of amorphous solid dispersions are extremely difficult to deconvolute as a number of processes are involved [11]. Dissolution can be classified as drug-controlled or polymer-controlled depending on the physicochemical properties of the drug and the polymer, and the drug-to-polymer ratio [11]. The dissolution behaviour of amorphous solid dispersions can therefore be dependent on the polymeric carrier itself. The re-crystallisation of the drug in the solid state or from a super-saturated solution and the formation of drug nano- and micro-particles can also contribute to the final dissolution performance [9,10,12,13].

To gain a more complete picture of the drug release from amorphous solid dispersions, a number of solid-state analytical methods have been developed and employed, with a strong focus on how the solid state properties of the drug and polymer affect the drug release. These include ultraviolet (UV) imaging [14,15], infrared (IR) and Raman spectroscopy [10,12,16,17], magnetic resonance imaging (MRI) [9,18],  $^1\text{H-NMR}$  [19] and particle analysis (e.g., dynamic image analysis to monitor particle size and number during dissolution) [20]. UV imaging provides spatially and temporally resolved information, and in addition enables real time dissolution rates to be obtained. UV imaging has been employed to monitor in real time the drug re-crystallisation processes of several poorly soluble drugs [14,15]. IR and Raman spectroscopy can provide high chemical specificity (multi-variate data, one spectrum per xy position) [10,12,16,17]. Raman spectroscopy, compared to IR, is relatively insensitive to water which is clearly an advantage for imaging in aqueous environments. In addition, the low-wavenumber data of the Raman spectrum allows easy differentiation between amorphous and crystalline forms and between different polymorphic forms [10,21,22]. Coherent anti-Stokes Raman scattering (CARS), a particular form of Raman spectroscopy which uses two pulsed lasers focused

on the sample to generate a signal, has also been employed to image the solid-state changes during dissolution of theophylline anhydrate [23]. In contrast, MRI offers relatively low chemical selectivity, but can provide three-dimensional information on molecular mobility. In recent work by Langham *et al.* magnetic resonance images were used to determine the erosion rates of a compact during dissolution [9].

Solution-state  $^1\text{H-NMR}$  has also recently been demonstrated to be a useful tool to monitor the dissolution of pharmaceutical products [19], especially for chemical species lacking a UV chromophore (e.g., soluble fillers), or medicines containing more than one active ingredient where quantification can be challenging using UV absorbance data.  $^1\text{H-NMR}$  offers a high chemical selectivity and therefore is capable of resolving signals from components through differences in their chemical shifts. In addition, as  $^1\text{H-NMR}$  spectra obtained from a dissolution test can be referenced against a spectrum of a solution with known concentration, quantification is possible [24,25].

While each of these techniques have been used to study the formulation dissolution performance, a better understanding of drug release can be achieved when techniques are used in combination.

We have previously investigated the dissolution performance of 5% and 50% drug-loaded bicalutamide-Kollidon VA64 extrudates using Raman mapping [12]. Bicalutamide (Figure 1) is an anti-androgen used for the treatment of prostate cancer and belongs to class II of the biopharmaceutics classification system (BCS), *i.e.*, it is characterised by low water solubility (less than  $5 \mu\text{g}\cdot\text{mL}^{-1}$ ) and high intestinal permeability [26,27]. Raman data indicated that amorphous bicalutamide present in the 50% extrudate re-crystallised into polymorphic forms II and I. As a result, the dissolution profiles of both bicalutamide and Kollidon VA64 (coPVP) were found to be extremely limited. We have also hypothesised that the re-crystallisation event follows the formation of an amorphous drug-rich shell due to the preferential dissolution of the hydrophilic polymer. In contrast, the dissolution performance of the 5% extrudate indicated the hydrophilic polymer and the hydrophobic drug dissolving at the same rate.

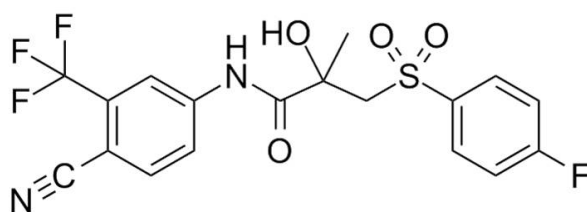


**Figure 1.** Molecular structure of bicalutamide.

In the present paper we further explore the dissolution performance of bicalutamide: coPVP amorphous solid dispersions using a suite of analytical techniques. We investigated the 5% extrudate (low drug loading) and this time the 30% extrudate (intermediate drug loading), with the aim of obtaining additional information on how the drug amount affects the dissolution performance. A combined MRI/UV-Vis flow cell system was used, allowing changes in dissolution profile to be related to physical changes occurring in the solid material. Off-line  $^1\text{H-NMR}$  was also employed for the first time to simultaneously measure the dissolution profiles and rates of both the drug and the polymer from the molecular dispersion.

## 2. Results and Discussion

### 2.1. Solution-State Assays

#### 2.1.1. UV-Vis Flow Cell Experiments

The UV-Vis dissolution profiles of the 5% and 30% extrudates are presented in Figure 2. The experiments were repeated twice for each drug loading to obtain an indication of the reproducibility in dissolution performance. A good reproducibility was observed in the two experiments of the 5% extrudate. Both profiles are characterised by two regions which correspond to the dissolving bicalutamide followed by the drug precipitation. In contrast, the two dissolution profiles of the 30% extrudate appear highly non-reproducible, *i.e.*, they are characterised by a different number of regions, but both show two pronounced “turning points” at 350 and 700 min (first experiment) and 250 and 500 min (second experiment) where the rate of drug dissolution increases. Overall, the UV-Vis data indicate a lack of controlled release for the 30% extrudate compared to the 5% extrudate.

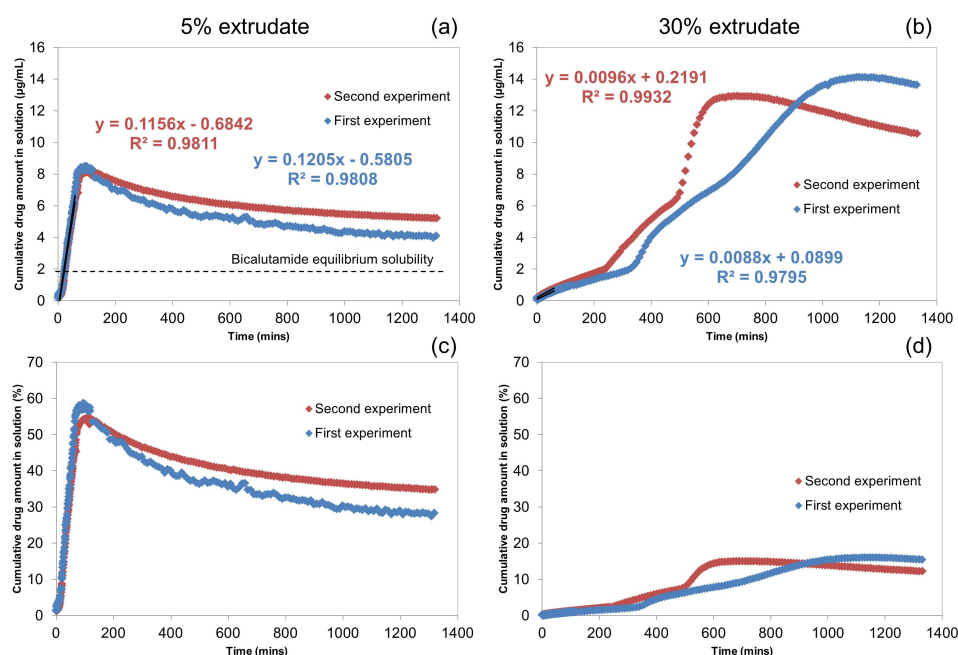


**Figure 2.** UV-Vis dissolution profiles of bicalutamide released from the 5% and 30% extrudates. (a,c) Drug release for the 5% extrudate expressed in Cumulative drug amount in solution ( $\mu\text{g}\cdot\text{mL}^{-1}$ ) and Cumulative drug amount in solution (%) respectively; (b,d) Drug release for the 30% extrudate expressed in Cumulative drug amount in solution ( $\mu\text{g}\cdot\text{mL}^{-1}$ ) and Cumulative drug amount in solution (%) respectively. The dissolution rates of the initial time-points were calculated using linear regression analysis. Linear best fits for the 5% and 30% dissolution experiments are included.

These data indicate that there is a significant difference in dissolution behaviour between the two drug loadings. For example in the first experiment the 5% extrudate reaches a maximum concentration

of  $8.5 \mu\text{g} \cdot \text{mL}^{-1}$  (which corresponds to approximately 59% of total release) at 95 min, with an initial dissolution rate of  $0.12 \mu\text{g} \cdot \text{mL}^{-1} \cdot \text{min}^{-1}$ . The 30% extrudate achieves a maximum concentration in solution of  $14.1 \mu\text{g} \cdot \text{mL}^{-1}$  ( $\approx 16\%$  of total release) at 1179 min and an initial dissolution rate of  $0.01 \mu\text{g} \cdot \text{mL}^{-1} \cdot \text{min}^{-1}$ . For both drug loadings, the concentration of bicalutamide in solution declines after reaching the maximum concentration. The final measured concentration at 1319 min is  $4.1 \mu\text{g} \cdot \text{mL}^{-1}$  ( $\approx 28\%$  of total release) and  $13.6 \mu\text{g} \cdot \text{mL}^{-1}$  ( $\approx 15\%$  of total release) for the 5% extrudate and 30% extrudate respectively.

In accordance with previous work, the dissolution behaviour of the bicalutamide extrudates is clearly dependent on the drug loading [9,10,12]. At low drug loading (*i.e.*, 5% extrudate), the performance is dependent on the high aqueous solubility of the polymer. The drug is quickly released and the maximum concentration corresponding to approximately 59% of total release is reached within 95 min. For the extrudate containing a higher proportion of bicalutamide (*i.e.*, 30% extrudate), the dissolution performance is dominated by the physicochemical properties of the drug (e.g., low aqueous solubility and high hydrophobicity). As a result, the initial dissolution rate is approximately one order of magnitude lower ( $0.01 \mu\text{g} \cdot \text{mL}^{-1} \cdot \text{min}^{-1}$  vs.  $0.12 \mu\text{g} \cdot \text{mL}^{-1} \cdot \text{min}^{-1}$ ) and the maximum concentration corresponding to 16% of total release is achieved only after 1179 min.

The UV-Vis data also show that the bicalutamide content in solution for both the 5% and 30% extrudates decreases after achieving the maximum concentration at 95 and 1179 min respectively, indicating that the drug super-saturation in solution is not maintained by the presence of coPVP across the entire dissolution test. In addition, in both experiments this reduction is accompanied by an increase of the absorbance at 350 nm (Figure S1 of SI), which is related to the scattering as well as absorption contributions of insoluble particles [13]. The formation of these particles, which cause the subsequent reduction in solution concentration, has been previously observed also for amorphous spray-dried solid dispersions of felodipine and coPVP [9].

It is also important to note that the 30% bicalutamide extrudate exhibited a markedly superior dissolution profile compared to the corresponding drug loading of amorphous spray-dried solid dispersions of felodipine and coPVP [9]. This can be attributed to the higher aqueous solubility of bicalutamide over felodipine [10,12], although the manufacturing route (hot melt extrusion vs. spray drying) may also be a factor.

### 2.1.2. Off-Line $^1\text{H-NMR}$

In this section we employ off-line  $^1\text{H-NMR}$  to complement the UV-Vis data for understanding the dissolution performance of the bicalutamide extrudates. With respect to standard UV-Vis measurements,  $^1\text{H-NMR}$  allows us to simultaneously determine the amount of drug and polymer in solution. As the dissolution performance of poorly soluble drugs can be largely dependent on that of the polymeric carrier, quantitative measurements of the latter provide valuable information [3,4]. In addition, similarly to the previously employed rotating disk dissolution rate (RDDR) methodology which uses HPLC to separate and therefore track the dissolution trends of both drug and polymer, the dissolution rate of the polymer allows us to determine an index of dissolution performance of the extrudate [10,12]. The index of performance shows how the drug and polymer behave during the dissolution test and it is defined by dividing the dissolution rate of bicalutamide by the total rate of the extrudate (bicalutamide

plus coPVP) and normalising by the bicalutamide mass fraction (e.g., 0.05 for the 5% extrudate). The temporal evolution of NMR spectra for the 5% and 30% extrudates are presented in Figure 3, while the spectra from the reference solutions are shown in Figure S2 of SI. For each spectrum, two integrals from bicalutamide and coPVP were generated and then scaled to integrals obtained from the reference solutions of known concentration. The spectra from the reference solutions were obtained using identical experimental conditions. The release profiles of the individual species are shown in Figure 4.

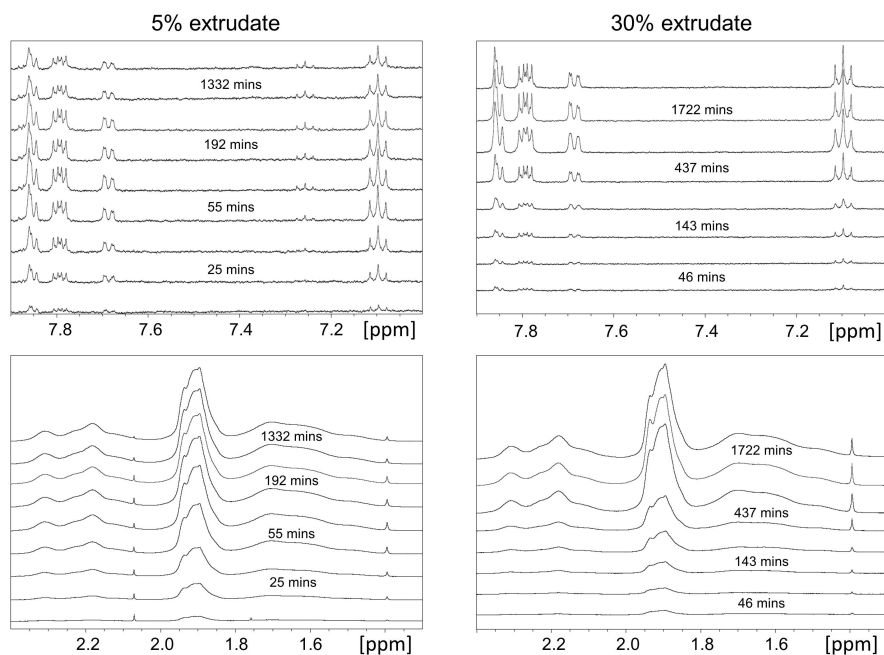


**Figure 3.** Portions of the  $^1\text{H-NMR}$  spectra acquired during the dissolution of the 5% and 30% extrudates. Bicalutamide and coPVP data were obtained from single integrals at 7.06–7.14 ppm (two aromatic protons of fluorobenzene) and 1.2–2.6 ppm (protons of pyrrolidone ring and methylene chains) respectively.

For the 5% extrudate (e.g., first experiment), bicalutamide exhibits an initial dissolution rate of  $0.16 \mu\text{g} \cdot \text{mL}^{-1} \cdot \text{min}^{-1}$  and that of coPVP is  $3.84 \mu\text{g} \cdot \text{mL}^{-1} \cdot \text{min}^{-1}$ . The index of performance resulted in a value of 0.8, indicating that the drug and polymer dissolve approximately with the same rate from the dispersion. The index of performance obtained from the  $^1\text{H-NMR}$  system is similar to that previously obtained from the RDDR test (value of 0.94) [12].

For the 30% extrudate, the dissolution rates of both bicalutamide and coPVP are lower with values of  $0.009 \mu\text{g} \cdot \text{mL}^{-1} \cdot \text{min}^{-1}$  and  $0.18 \mu\text{g} \cdot \text{mL}^{-1} \cdot \text{min}^{-1}$  respectively. In agreement with these data, the dissolution rates of bicalutamide and coPVP from the 50% extrudate were also found extremely low using the RDDR test [12]. The index of performance of the 30% extrudate is also far inferior (0.15) compared to that of the 5% extrudate, indicating that for this drug loading the higher content of bicalutamide limits the dissolution performance of both bicalutamide and coPVP.

The dissolution rates of bicalutamide obtained from the  $^1\text{H-NMR}$  experiments ( $0.16 \text{ mL}^{-1} \cdot \text{min}^{-1}$  for the 5% extrudate and  $0.009 \text{ mL}^{-1} \cdot \text{min}^{-1}$  for the 30% extrudate) are in a good agreement with those

obtained from the UV-Vis ( $0.12 \text{ mL}^{-1} \cdot \text{min}^{-1}$  for the 5% extrudate and  $0.009 \text{ mL}^{-1} \cdot \text{min}^{-1}$  for the 30% extrudate).

From Figure 4 it is also apparent that for both the 5% and 30% extrudates, whilst coPVP achieves a dissolution release plateau, the bicalutamide concentration declines after reaching a maximum. In addition, for the 5% extrudate the bicalutamide precipitation begins before the coPVP dissolution is complete. This, in agreement with the previous UV-Vis data, clearly indicates that the super-saturation of the drug is not maintained by the polymer across the entire dissolution test.

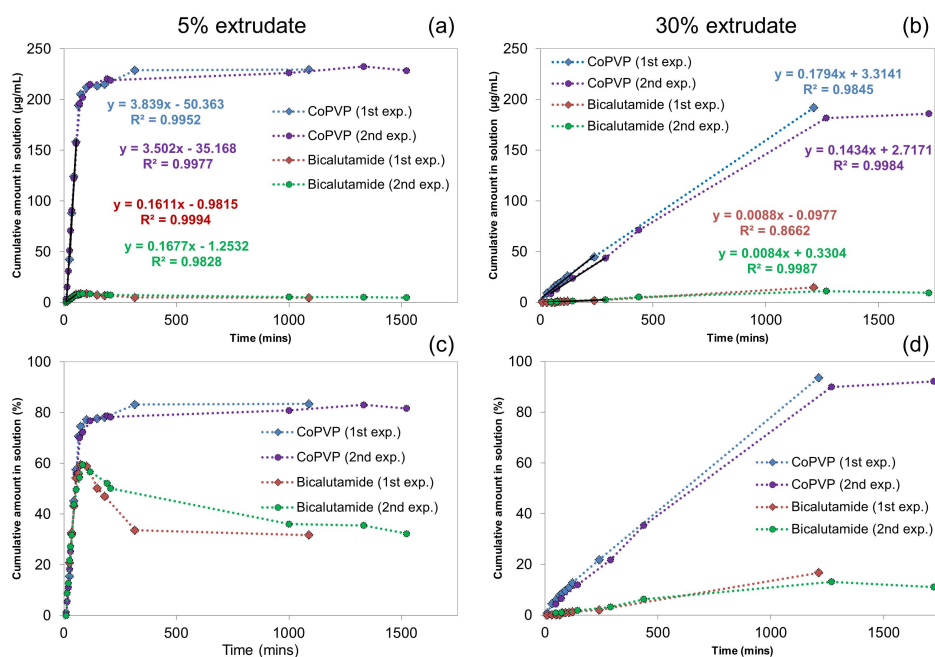


**Figure 4.** Release profiles obtained from the  $^1\text{H-NMR}$  spectra of bicalutamide and coPVP from the 5% and 30% extrudates. (a,c) Release for the 5% extrudate expressed in Cumulative drug amount in solution ( $\mu\text{g} \cdot \text{mL}^{-1}$ ) and Cumulative drug amount in solution (%) respectively; (b,d) Release for the 30% extrudate expressed in Cumulative drug amount in solution ( $\mu\text{g} \cdot \text{mL}^{-1}$ ) and Cumulative drug amount in solution (%) respectively. Data were scaled using the reference standard solutions. Linear best fits for the dissolution profiles of the 5% and 30% extrudates are included.

## 2.2. Solid-State Assays

### MRI Flow Cell Experiments

The solution-state measurements obtained from the UV-Vis and  $^1\text{H-NMR}$  data are then complemented with solid-state measurements, *i.e.*, magnetic resonance imaging. The magnetic resonance images showing the temporal changes in one cross sectional slice of the 5% and 30% extrudates during the dissolution test are shown in Figure 5 (first experiment) and Figure S3 of SI (second experiment). The measured dimensions of the compacts as a function of time are presented in Figure 6. In this MRI

experiment the image contrast is due to differences in molecular mobility. As a result, protons in a solid environment have a faster  $T_2$  relaxation time and therefore the solid materials appear dark in the images. Protons in solution have a significantly slower  $T_2$  relaxation time and thereby they generate a bright image, while, for example, protons in a hydrating gel give an intermediate brightness [9].

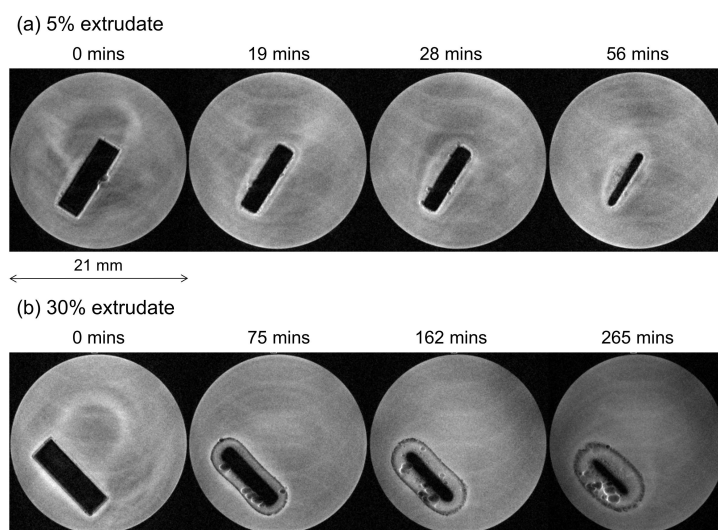


**Figure 5.** Magnetic resonance images (first experiment) showing the changes as a function of time in one cross sectional slice of the extrudates containing 5% (a) and 30% (b) of bicalutamide.

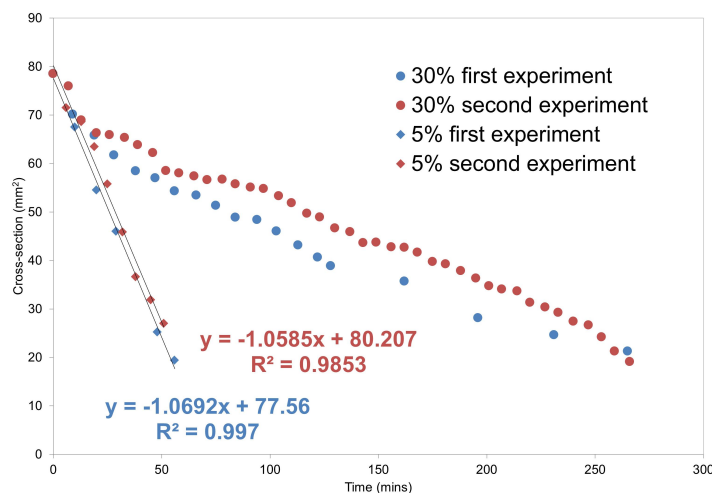


**Figure 6.** Evolution of the compact dimensions as a function of time for the 5% extrudate and 30% extrudate. Linear best fit to the data for the 5% extrudate is included. For the 30% extrudate, to facilitate the comparison with the 5% extrudate, the dimensions of the compact core (solid material) without considering those of the hydrated layer were measured. Data were collected only up to approximately 300 min due to the compact falling off from the support and being out of the instrumental field of view after this time-point.

The images presented in Figure 5, for example, show significantly different dissolution behaviours for the 5% extrudate (Figure 5a) and 30% extrudate (Figure 5b). The 5% extrudate undergoes erosion and it is almost entirely dissolved over a period of 56 min, while the 30% extrudate swells and remains intact after 265 min (it is then no longer attached to the support due to its swelling and expansion and as a consequence it is out of the instrumental field of view). These results are in full accord with the UV-Vis and  $^1\text{H-NMR}$  solution-state data.

Throughout the experiments, the 30% extrudate exhibits a well-defined region of intermediate MRI contrast, which is either not present, or hardly present, in the 5% extrudate (Figure 7). This region is due to water ingress into the compact. It is clear that for the 5% sample the rates of water ingress and dissolution are similar, which prevents the formation of the intermediate contrast region, whereas for the 30% compact dissolution is markedly slower than water ingress. Our previous Raman spectroscopy studies on a 50% sample [12] indicated that the preferential dissolution of coPVP led to formation of a drug-rich shell which crystallised and appeared to strongly inhibit further erosion and dissolution of the compact. We therefore suggest that this region of intermediate contrast in the magnetic resonance images of the 30% sample is due to water partially dissolved in the coPVP matrix, which does not lead to dissolution and drug release due to a drug-rich, likely crystalline shell which prevents further water ingress and thus greatly reduces the dissolution rate of the compact. Formation of a gel-layer can be ruled out on the basis of the optical images previously collected during the dissolution test of the 50% drug loading [12]. The drug re-crystallisation is likely to be one of the main factors which determines lack of controlled release observed in the UV-Vis profiles for the 30% drug loading.

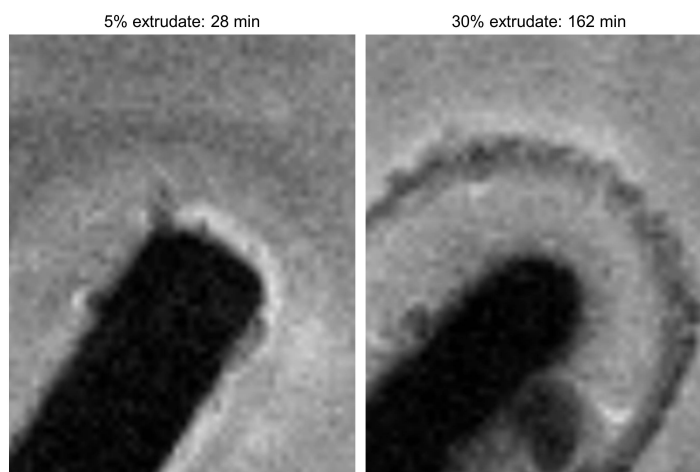


**Figure 7.** Zoom of the images collected for the 5% extrudate (28 min) and 30% extrudate (162 min) to highlight the well-defined region of intermediate MRI contrast present in the 30% extrudate.

It is important to note that the images in Figure 5 show some ghosting artefacts which are a likely consequence of the wash in/wash out effect of the flowing medium with nuclei moving between two consecutive spatially selective RF excitations. The artefacts do not interfere with the determination of the compact dimensions. The overall contrast of the flowing bulk dissolution medium seems to gradually

decrease for the 30% loading sample and this is thought to be a consequence of the wash in/wash out effects of the flowing medium rather than due to any change in its mobility. If the intensity of the bulk medium in the initial image of 5% extrudate is compared with that for the 30% compact at 265 min they are similar. As the dissolution experiment proceeds, however, the difference in mobility and hence contrast between the hydrated compact and the bulk medium is reduced. In addition, bright halos on the outer edges of the compact as well as air bubbles are visible in the images of Figure 5. The origins of these are not fully understood but are likely to be due to magnetic susceptibility effects which are known to occur at interfaces. These effects are often observed with gradient echo imaging based sequences such as FLASH, which has been used in this work, and result in spatial mis-mapping of the MR signal, often presented as regions of very bright signal resulting from “piling up” of signal at the interface.

The difference in dissolution performance between the two drug loadings is reflected in Figure 6. The 5% extrudate quickly erodes with a linear erosion rate of  $1.1 \text{ mm}^2 \cdot \text{min}^{-1}$ , while the erosion rate for the 30% extrudate is slower and not linear due to the presence of the hydrating layer.

At the end of the dissolution test of the 30% extrudate (approximately after 1700 min), we noted abundant presence of undissolved material in the flow cell. This residue was removed from the flow cell and shown by Raman spectroscopy to contain crystalline bicalutamide form I (Figure S4), pointing to the drug re-crystallisation.

The MRI images are in agreement the UV-Vis and  $^1\text{H-NMR}$  data, indicating that for the 5% extrudate the release of bicalutamide is a polymer-controlled process whereby the dissolution is governed by the fast hydration of the highly water-soluble coPVP. For the 30% extrudate, the dissolution is dependent on the physicochemical properties of bicalutamide. The low aqueous solubility and high hydrophobicity of the drug contribute to a slower water uptake into the compact which corresponds to a slower dissolution rate of both bicalutamide and coPVP.

### 3. Experimental Section

#### 3.1. Materials

Bicalutamide was provided by AstraZeneca (Macclesfield, UK) and shown to be polymorphic form I by Raman spectroscopy and X-ray powder diffraction (XRPD). Kollidon VA64 (coPVP) was supplied by BASF (Ludwigshafen, Germany). All materials were used as received and without any further purification.

#### 3.2. Sample Preparation

##### 3.2.1. Preparation of the Amorphous Reference form of Bicalutamide

The amorphous form of bicalutamide was prepared by heating form I to  $200 \text{ }^\circ\text{C}$  and quench cooling the melt to room temperature [12]. The formation of the amorphous form was confirmed by Raman spectroscopy and XRPD (Figures S4 and S5 of SI).

### 3.2.2. Preparation of the Bicalutamide: coPVP Extrudates

Extrudates of bicalutamide in coPVP (5% and 30% w/w bicalutamide) were prepared using a co-rotating twin-screw extruder (Thermo Scientific HAAKE MiniLab II). Bicalutamide form I and coPVP were pre-mixed for 20 min in a Turbula T2F mixer (Willy A. Bachofen AG Mashinefabrik). The materials were extruded at a screw speed of 150 rpm and a temperature of 170 °C, then cooled to room temperature and manually milled with a T & G CrushGrind mill to fine powders. The formation of the amorphous form was confirmed by Raman spectroscopy and XRPD (Figures S4 and S5 of SI).

## 3.3. Analytical Methods

### 3.3.1. Raman Spectroscopy

Data were acquired on a HORIBA Jobin Yvon LabRAM HR confocal microscope/spectrometer. A near-IR (785 nm) laser was employed to illuminate the samples, and spectra were collected using a 50× objective and a 300 µm confocal pinhole. A 600 lines·mm<sup>-1</sup> rotatable diffraction grating along a path length of 800 mm was used to simultaneously scan a range of Raman shifts, and spectra were detected using a SYNAPSE CCD detector (1024 pixels). Spectra were collected in the range from 1055 to 1725 cm<sup>-1</sup>.

### 3.3.2. X-ray Powder Diffraction (XRPD)

X-ray powder diffraction data were collected on a PANalytical CubiX PRO diffractometer ( $\lambda = 1.5418 \text{ \AA}$ ). Powders were smeared onto zero-background silicon wafer sample holders and measured over the scan range from 2° to 40° 2 $\theta$ , with a 25 s exposure per 0.02° 2 $\theta$  increment. Samples were spun at 30 rpm and exposed to a radiation generated by a copper long-fine focus tube operated at a voltage of 45 kV and a current of 40 mA.

### 3.3.3. MRI UV-Vis Flow Cell System

The dissolution performance of circular compacts with a diameter of 10 mm and a weight of approximately 290 mg was investigated. Powders were compressed using a Specac manual hydraulic press using a compression force of *ca.* 50 kN. The dissolution tests were performed in a USP IV-type flow cell previously described by Langham *et al.* [9]. 1 L of pH 6.5 phosphate buffer dissolution medium maintained at a temperature of 37 °C using a temperature-controlled water bath was circulated continuously at a flow rate of 15 mL·min<sup>-1</sup>.

The dissolution profile of bicalutamide was obtained by recording the absorbance of the unfiltered dissolution medium at 275 nm (wavelength maxima of bicalutamide) and 350 nm (no observed absorbance, for correction for any suspended particles) at regular time intervals using a Agilent 8453 UV-Vis spectrophotometer with a 10 mm quartz flow cell (Starna Scientific, Ilford, UK). The dissolution data were calibrated against the absorbance of a series of standard solutions of bicalutamide in water–acetonitrile 75/25 (v/v).

The flow cell was sited in the probe of a 400 MHz Bruker Avance NMR spectrometer fitted with a Micro2.5 imaging accessory fitted with a 25 mm O.D. RF coil. The images were collected as a function of time using a FLASH (Fast Low Angle Shot) protocol to generate  $16 \times 1 \text{ mm}^2$  concatenated axial slices with a field of view of 25 mm. The echo time was 3.0 ms and the repetition time was 500 ms giving a scan time of 1 min 4 s for each 16 slice experiment. A data matrix size of  $128 \times 128$  pixels was recorded giving a resolution of 0.0195 cm/pixel in the read direction. Data were processed using ParaVision™ software v4.0. Changes in the size of the compacts were followed by measuring the dimensions of a single slice as a function of time.

#### 3.3.4. $^1\text{H}$ -NMR Spectroscopy

All NMR measurements were performed on a Bruker Avance III 500 MHz NMR spectrometer fitted with a 5 mm QCI cryoprobe. The spectra from the dissolution samples and the reference solutions were acquired at 300.0 K with a spectral width of 10 kHz, with 64 k data points in the time domain. A recycle delay of 4 s was used and the peak due to water was suppressed using a 1D NOESY pulse program with presaturation and spoil gradients (noesygprr1d) and with irradiation at the water frequency during the recycle and mixing time delays. The receiver gain was set to 128 and kept the same for each experiment. Data were processed using the Bruker Topspin 3.0 software. Interactive zero order phase correction was applied to all the spectra and the “Use lastscale for calibration” functionality was employed to directly compare integrals across multiple spectra.

## 4. Conclusions

A combination of solution-state and solid-state analytical techniques were employed to fully understand the dissolution performance of amorphous bicalutamide solid dispersions at two different drug loadings (5% and 30% bicalutamide). The integrated MRI UV-Vis system enabled us to relate changes in dissolution profile to physical changes occurring to the solid material. The MRI data indicated that the 5% extrudate erodes linearly, while for the 30% extrudate the water ingress is significantly slower which corresponds to a slower dissolution of both bicalutamide and coPVP. We also employed for the first time  $^1\text{H}$ -NMR spectroscopy to simultaneously measure the dissolution profiles and rates of both drug and polymer.  $^1\text{H}$ -NMR has been demonstrated to be a valid alternative to the previously employed rotating disk dissolution rate (RDDR) methodology for tracking the dissolution profiles in multi-component systems.  $^1\text{H}$ -NMR data showed that for the 5% extrudate, bicalutamide and coPVP dissolve with approximately the same rate pointing to a matrix-controlled release, while for the 30% drug loading they dissolve very differently and at a significantly lower rate. For the 30% extrudate the dissolution performance is dominated by the physicochemical properties of the drug.

## Supplementary Materials

Supplementary materials can be accessed at: <http://www.mdpi.com/1420-3049/20/09/16404/s1>.

## Acknowledgments

AstraZeneca and EPSRC are acknowledged for funding through grant EP/I01375X/1 (via the joint Center for Doctoral Training in Targeted Therapeutics and Formulations Sciences).

## Author Contributions

All the authors conceived and designed the experiments. F.T., S.R.C., A.R.P., L.P.H. and S.A.C.W. performed the experiments. F.T., S.A.C.W., J.W.A. and J.C.B. analysed the UV-Vis and Raman data. F.T., S.R.C., A.R.P., L.P.H. and S.A.C.W. analysed the <sup>1</sup>H-NMR data. F.T. and L.P.H. analysed the MRI images. F.T. wrote the paper. All the authors revised the manuscript and approved the final version.

## Conflicts of Interest

The authors declare no conflict of interest.

## References

1. Babu, N.J.; Nangia, A. Solubility advantage of amorphous drugs and pharmaceutical cocrystals. *Cryst. Growth Des.* **2011**, *11*, 2662–2679.
2. Di, L.; Fish, P.V.; Mano, T. Bridging solubility between drug discovery and development. *Drug Discov. Today* **2012**, *17*, 486–495.
3. Hancock, B.C.; Parks, M. What is the true solubility advantage for amorphous pharmaceuticals? *Pharm. Res.* **2000**, *17*, 397–404.
4. Hancock, B.C.; Zografi, G. Characteristics and significance of the amorphous state in pharmaceutical systems. *J. Pharm. Sci.* **1997**, *86*, 1–12.
5. Leuner, C.; Dressman, J. Improving drug solubility for oral delivery using solid dispersions. *Eur. J. Pharm. Biopharm.* **2000**, *50*, 47–60.
6. Serajuddin, A.T.M. Solid dispersion of poorly water-soluble drugs: Early promises, subsequent problems, and recent breakthroughs. *J. Pharm. Sci.* **1999**, *88*, 1058–1066.
7. Ivanisevic, I. Physical stability studies of miscible amorphous solid dispersions. *J. Pharm. Sci.* **2010**, *99*, 4005–4012.
8. Van den Mooter, G.; Wuyts, M.; Blaton, N.; Busson, R.; Grobet, P.; Augustijns, P.; Kinget, R. Physical stabilisation of amorphous ketoconazole in solid dispersions with polyvinylpyrrolidone K25. *Eur. J. Pharm. Sci.* **2001**, *12*, 261–269.
9. Langham, Z.A.; Booth, J.; Hughes, L.P.; Reynolds, G.K.; Wren, S.A.C. Mechanistic insights into the dissolution of spray-dried amorphous solid dispersions. *J. Pharm. Sci.* **2012**, *101*, 2798–2810.
10. Tres, F.; Treacher, K.; Booth, J.; Hughes, L.P.; Wren, S.A.C.; Aylott, J.W.; Burley, J.C. Real time Raman imaging to understand dissolution performance of amorphous solid dispersions. *J. Control. Release* **2014**, *188*, 53–60.

11. Craig, D.Q.M. The mechanisms of drug release from solid dispersions in water-soluble polymers. *Int. J. Pharm.* **2002**, *231*, 131–144.
12. Tres, F.; Patient, J.D.; Williams, P.M.; Treacher, K.; Booth, J.; Hughes, L.P.; Wren, S.A.C.; Aylott, J.W.; Burley, J.C. Monitoring the dissolution mechanisms of amorphous bicalutamide solid dispersions via real-time raman mapping. *Mol. Pharm.* **2015**, *12*, 1512–1522.
13. Van Eerdenbrugh, B.; Alonzo, D.; Taylor, L. Influence of particle size on the ultraviolet spectrum of particulate-containing solutions: Implications for *in-situ* concentration monitoring using UV/vis fiber-optic probes. *Pharm. Res.* **2011**, *28*, 1643–1652.
14. Boetker, J.P.; Savolainen, M.; Koradia, V.; Tian, F.; Rades, T.; Müllertz, A.; Cornett, C.; Rantanen, J.; Østergaard, J. Insights into the early dissolution events of amlodipine using UV imaging and raman spectroscopy. *Mol. Pharm.* **2011**, *8*, 1372–1380.
15. Nielsen, L.H.; Gordon, S.; Pajander, J.P.; Østergaard, J.; Rades, T.; Müllertz, A. Biorelevant characterisation of amorphous furosemide salt exhibits conversion to a furosemide hydrate during dissolution. *Int. J. Pharm.* **2013**, *457*, 14–24.
16. Chan, K.L.A.; Kazarian, S.G. FTIR spectroscopic imaging of dissolution of a solid dispersion of nifedipine in poly(ethylene glycol). *Mol. Pharm.* **2004**, *1*, 331–335.
17. Wray, P.S.; Clarke, G.S.; Kazarian, S.G. Dissolution of tablet-in-tablet formulations studied with ATR-FTIR spectroscopic imaging. *Eur. J. Pharm. Sci.* **2013**, *48*, 748–757.
18. Chen, Y.Y.; Hughes, L.P.; Gladden, L.F.; Mantle, M.D. Quantitative ultra-fast MRI of HPMC swelling and dissolution. *J. Pharm. Sci.* **2010**, *99*, 3462–3472.
19. Coombes, S.R.; Hughes, L.P.; Phillips, A.R.; Wren, S.A.C. Proton NMR: A new tool for understanding dissolution. *Anal. Chem.* **2014**, *86*, 2474–2480.
20. Wilson, D.; Wren, S.; Reynolds, G. Linking dissolution to disintegration in immediate release tablets using image analysis and a population balance modelling approach. *Pharm. Res.* **2012**, *29*, 198–208.
21. Brillante, A.; Bilotti, I.; Della Valle, R.G.; Venuti, E.; Girlando, A. Probing polymorphs of organic semiconductors by lattice phonon Raman microscopy. *CrystEngComm* **2008**, *10*, 937–946.
22. Al-Dulaimi, S.; Aina, A.; Burley, J.C. Rapid polymorph screening on milligram quantities of pharmaceutical material using phonon-mode Raman spectroscopy. *CrystEngComm* **2010**, *12*, 1038–1040.
23. Fussell, A.; Garbacik, E.; Offerhaus, H.; Kleinebudde, P.; Strachan, C. *In situ* dissolution analysis using coherent anti-Stokes Raman scattering (CARS) and hyperspectral CARS microscopy. *Eur. J. Pharm. Biopharm.* **2013**, *85*, 1141–1147.
24. Bharti, S.K.; Roy, R. Quantitative <sup>1</sup>H-NMR spectroscopy. *Trends Anal. Chem.* **2012**, *35*, 5–26.
25. Dalitz, F.; Cudaj, M.; Maiwald, M.; Guthausen, G. Process and reaction monitoring by low-field NMR spectroscopy. *Prog. Nucl. Magn. Reson. Spectrosc.* **2012**, *60*, 52–70.
26. Abu-Diak, O.A.; Jones, D.S.; Andrews, G.P. Understanding the performance of melt-extruded poly(ethylene oxide)-bicalutamide solid dispersions: Characterisation of microstructural properties using thermal, spectroscopic and drug release methods. *J. Pharm. Sci.* **2012**, *101*, 200–213.

27. Andrews, G.P.; AbuDiak, O.A.; Jones, D.S. Physicochemical characterization of hot melt extruded bicalutamide-polyvinylpyrrolidone solid dispersions. *J. Pharm. Sci.* **2010**, *99*, 1322–1335.

*Sample Availability:* Samples of the compounds used in this study are available from the authors.

© 2015 by the authors; licensee MDPI, Basel, Switzerland. This article is an open access article distributed under the terms and conditions of the Creative Commons Attribution license (<http://creativecommons.org/licenses/by/4.0/>).